THE EUROPEAN
PHYSICAL JOURNAL C

Review

HHH whitepaper

Hamza Abouabid[1], **Abdesslam Arhrib**[1], **Hannah Arnold**[2], **Duarte Azevedo**[3], **Vuko Brigljevic**[4], **Maggie Chen**[5], **Daniel Diaz**[6], **Javier Duarte**[6], **Tristan du Pree**[7,8], **Jaouad El Falaki**[9], **Dinko Ferencek**[4], **Pedro. M. Ferreira**[10,11], **Benjamin Fuks**[12], **Sanmay Ganguly**[13,14], **Osama Karkout**[7,8], **Marina Kolosova**[15], **Jacobo Konigsberg**[15], **Greg Landsberg**[16], **Bingxuan Liu**[17,18], **Brian Moser**[19], **Margarete Mühlleitner**[3], **Andreas Papaefstathiou**[20], **Roman Pasechnik**[21], **Tania Robens**[4,a], **Rui Santos**[10,11], **Brian Sheldon**[6], **Gregory Soyez**[22], **Marko Stamenkovic**[16], **Panagiotis Stylianou**[23], **Tatjana Susa**[4], **Gilberto Tetlalmatzi-Xolocotzi**[24,25], **Georg Weiglein**[23,26], **Giulia Zanderighi**[27,28], **Rui Zhang**[29]

[1] Faculty of Sciences and Techniques, Abdelmalek Essaadi University, Ancienne Route de l'aéroport, Ziaten, B.P. 416, Tangier, Morocco
[2] Stony Brook University, Stony Brook, New York, USA
[3] Institute for Theoretical Physics, Karlsruhe Institute of Technology, Wolfgang-Gaede-Str. 1, 76131 Karlsruhe, Germany
[4] Rudjer Boskovic Institute, Zagreb, Croatia
[5] University of Oxford, Oxford OX1 2JD, UK
[6] Department of Physics, University of California San Diego, La Jolla, CA 92093, USA
[7] Nikhef-National Institute for Subatomic Physics, Science Park 105, 1098 XG Amsterdam, Netherlands
[8] University of Twente, Drienerlolaan 5, 7522 NB Enschede, Netherlands
[9] LPTHE, Physics Department, Faculty of Sciences, Ibnou Zohr University, P.O.B. 8106, Agadir, Morocco
[10] ISEL-Instituto Superior de Engenharia de Lisboa, Instituto Politécnico de Lisboa, 1959-007 Lisbon, Portugal
[11] Centro de Física Teórica e Computacional, Faculdade de Ciências, Universidade de Lisboa, Campo Grande, Edifício C8, 1749-016 Lisbon, Portugal
[12] Laboratoire de Physique Théorique et Hautes Énergies (LPTHE), UMR 7589, Sorbonne Université et CNRS, 4 Place Jussieu, 75252 Paris Cedex 05, France
[13] Indian Institute of Technology Kanpur, Kalyanpur, Kanpur, Uttar Pradesh 208016, India
[14] ICEPP, The University of Tokyo, Hongo, Bunkyo-ku, Tokyo 113-0033, Japan
[15] Department of Physics, University of Florida, Gainesville, FL, USA
[16] Department of Physics, Brown University, 182 Hope St., Providence, RI 02912, USA
[17] Department of Physics, Simon Fraser University, Burnaby, BC V5A 1S6, Canada
[18] School of Science, Shenzhen Campus of Sun Yat-sen University, No. 66 Gongchang Road, Guangming District, Shenzhen 518107, China
[19] EP Department, CERN, Geneva, Switzerland
[20] Department of Physics, Kennesaw State University, 830 Polytechnic Lane, Marietta, GA 30060, USA
[21] Department of Physics, Lund University, SE-223 62 Lund, Sweden
[22] Université Paris-Saclay, CNRS, CEA, Institut de Physique Théorique, 91191 Gif-sur-Yvette, France
[23] Deutsches Elektronen-Synchrotron DESY, Notkestr. 85, 22607 Hamburg, Germany
[24] Theoretische Physik 1, Center for Particle Physics Siegen (CPPS), Universität Siegen, Walter- Flex-Str. 3, 57068 Siegen, Germany
[25] Université Paris-Saclay, CNRS/IN2P3, IJCLab, 91405 Orsay, France
[26] Institut für Theoretische Physik, Universität Hamburg, Luruper Chaussee 149, 22761 Hamburg, Germany
[27] Max-Planck-Institut für Physik, Boltzmannstraße 8, 85748 Garching, Germany
[28] Technische Universität München, James-Franck-Strasse 1, 85748 Garching, Germany
[29] Department of Physics, University of Wisconsin, Madison, WI 53706, USA

Abstract We here report on the progress of the HHH Workshop, that took place in Dubrovnik in July 2023. After the discovery of a particle that complies with the properties of the Higgs boson of the Standard Model, all Standard Model (SM) parameters are in principle determined. However, in order to verify or falsify the model, the full form of the potential has to be determined. This includes the measurement of the triple and quartic scalar couplings.

We here report on ongoing progress of measurements for multi-scalar final states, with an emphasis on three SM-like scalar bosons at 125 GeV, but also mentioning other options. We discuss both experimental progress and challenges as well as theoretical studies and models that can enhance such rates with respect to the SM predictions.

[a] e-mail: trobens@irb.hr (corresponding author)

Springer

Contents

Introduction

V. Brigljevic, D. Ferencek, G. Landsberg, T. Robens, M. Stamenkovic, T. Susa

In October 2022 we were contacted and asked about the possibility to hold the first triple Higgs workshop in Dubrovnik in the Summer of 2023. A few months earlier, in June of 2022, Dubrovnik hosted the 2022 Higgs Pairs Workshop (https://indico.cern.ch/e/HH2022). While adding only one letter (H) to the workshop topic, this seemed a daring step forward in many respects. The HHH process itself seemed quite beyond the LHC reach. While the expected Standard Model (SM) cross section for HH production (~ 30 fb) makes it barely observable with the full expected luminosity at the LHC, the expected SM cross section for HHH production (~ 0.1 fb) is lower by more than two orders of magnitude, making its observation completely beyond reach at the LHC. The study of Double Higgs production at the LHC is also a very well established research topic, with many theoretical and experimental results available, which was manifested in the rich program of the 2022 workshop filling almost five full days of interesting talks and discussions. On the other side, the study of HHH production is still a largely uncharted territory. While several theoretical studies and calculations already exist, there is no experimental result on searches for such processes yet.

There are, however, several common aspects closely connecting HH and HHH production and their studies: both processes provide unique handles to explore the Higgs potential and in particular the Higgs self-couplings. Also, many of the analysis tools and techniques developed for non-resonant or resonant HH analyses are expected to be of great importance for tackling HHH final states. Both are also sensitive to similar beyond the Standard Model (BSM) models and in

particular to extensions of the SM scalar sector, which could in some cases largely enhance their production cross sections and make even HHH production experimentally reachable at the LHC.

Bringing together interested theorists and experimentalists to discuss this very new topic represented an exciting challenge. As the local HEP community in Croatia was itself directly involved, both on the experimental and theoretical side, in some of the first HHH studies, accepting to host it became an easy decision, resulting in the organization of the first HHH workshop in Dubrovnik from July 14 to 16 2023 at the Inter-University Centre Dubrovnik.

We certainly did not regret the decision as the workshop really provided a very stimulating atmosphere and exchange of ideas. We would like to thank all participants for contributing with excellent talks and lively and very open discussions. We have good hope that it will serve as a catalyst for future work on HHH production, hopefully soon leading to the first experimental search results on HHH production.

The Inter-University Centre Dubrovnik provided an excellent environment and infrastructure and we would like to acknowledge the friendly and very efficient support of their staff, notably Nada, Nikolina and Tomi. They greatly contributed to making the workshop a success and a very pleasant experience for all participants. They have enthusiastically welcomed all CERN-related academic events and let us feel very welcome, leading us to come back again and again to IUC as our preferred venue for the organization of scientific meetings in Croatia. Of course, the city of Dubrovnik with its rich history and unique old town and natural surroundings did its part too.

At the end of the workshop there was a clear consensus among workshop participants that the discussions started in Dubrovnik should continue and that this should only be the first HHH workshop. Consensus also emerged to reconvene in Dubrovnik with the hope to see the first experimental results from HHH searches at the LHC. This second workshop is likely to take place in the fall of 2025. Stay tuned!

To facilitate and trigger further work, the participants agreed that a written track of the presented results and ideas should be kept, resulting in the decision to write this White Paper. We hope it will serve as a useful overview of current results and a catalyst for both theoretical and experimental future work on HHH production.

This manuscript is structured loosely around the contributions to the HHH workshop, where we tried to group similar topics into common sections. For some topics, we also enhanced the content presented in talks in order to render a more complete overview on the current state of the art as well as future prospects and challenges.

This manuscript is organized as follows. In Sect. 1, we give a short overview on the current status of theory predictions in both the Standard Model and New Physics scenarios, with

relevant references to subsequent sections if feasible. Section 2 addresses the important topic of predictions within the SM, with a focus on topics arizing from QCD corrections, jet definitions, and scale uncertainties. In Sect. 3, we discuss possible lessons that can be learned from the investigation of DiHiggs final states for the study of multi scalar final states. This is further elaborated on in Sect. 4, where we discuss current experimental prospects and challenges for such searches. In Sect. 5, we present an example of a study that addresses diHiggs final states using machine learning. Section 6 we give an overview on the current state of the art for flavour tagging, focussing on ATLAS and CMS. In Sect. 7, we touch upon the broad range of new physics models that can render enhanced triple scalar final states. We address the simulation of such new physics scenarios in a possible simplified approach in Sect. 8. Conclusions and outlook are presented in Sect. 9.

Vuko Brigljevic, RBI (Zagreb)
on behalf of the local organizers:
V.B., Bhakti Chitroda, Dinko Ferenček, Tania Robens and Tatjana Šuša

1 A window on Standard Model physics and beyond with triple-Higgs production

B. Fuks

The discovery of a Higgs boson with a mass of about 125GeV at the LHC [1,2] has been one of the most important developments in high-energy physics over the last decade. It provided the first crucial insights into the nature of the electroweak symmetry breaking mechanism, the generation of fermion masses, as well as into establishing the Standard-Model nature of the observed new state. Since then, extensive efforts have been undertaken to unravel its properties. In particular, both the ATLAS [3] and CMS [4] collaborations have meticulously investigated its tree-level Yukawa couplings with third-generation fermions and weak gauge bosons, as well as its loop-induced couplings with gluons and photons. Measurements have consistently shown excellent agreement with the predictions of the Standard Model, albeit within the present experimental and theoretical uncertainties.

However, to definitely ascertain whether the observed Higgs state aligns with the predictions of the Standard Model, it is imperative to gather information on the shape of the Higgs potential. This necessitates independent measurements of the Higgs cubic, quartic and even higher-order self-couplings. Presently, available data only loosely constrains some of these parameters, allowing for the possibility of significant deviations from the Standard Model [4,5]. This is especially motivating for new physics scenarios incorporating an extended scalar sector with additional scalar fields. Moreover, understanding the intricacies of the Higgs

potential is crucial for the exploration of the mechanisms underlying the electroweak phase transition and the matter–antimatter asymmetry in the universe. Therefore, regardless of a potential discovery of physics beyond the Standard Model in the future, measuring the Higgs cubic and quartic self-couplings stands out as one of the primary objectives of the physics programme at current and future high-energy colliders [6–9].

In the Standard Model, the Higgs potential reads

$$V(\Phi) = -\mu^2 \Phi^\dagger \Phi + \lambda \left(\Phi^\dagger \Phi\right)^2, \tag{1}$$

where Φ represents the weak Higgs doublet, and μ and λ denote the typical Higgs quadratic and quartic interaction terms, respectively. After electroweak symmetry breaking, the neutral component of the Higgs doublet acquires a vacuum expectation value v. Consequently, the potential can be reformulated in terms of the physical Higgs field, h, as

$$V(h) = \frac{1}{2} m_h^2 h^2 + \lambda_{hhh} v h^3 + \frac{1}{4} \lambda_{hhhh} h^4 \quad \text{with}$$

$$\lambda_{hhh} = \lambda_{hhhh} = \frac{m_h^2}{2v}. \tag{2}$$

The Higgs self-couplings λ_{hhh} and λ_{hhhh} are thus inherently linked to both the Higgs mass m_h and the vacuum expectation value v. While predictions for these couplings can be derived from existing experimental knowledge, ($v \simeq 246$ GeV and $m_h \simeq 125$ GeV), direct measurements are crucial for independent confirmation. Legacy LHC measurements are anticipated to provide an $\mathcal{O}(1)$ estimate of the triple-Higgs coupling λ_{hhh} relative to its Standard Model value [8,9]. However, significant direct information on λ_{hhhh} is not expected [10,11]. Therefore, substantial deviations from these values may persist for the foreseeable future, particularly in scenarios where all other Higgs properties align with Standard Model predictions.

Accordingly, various studies have explored the potential of both existing and proposed proton-proton colliders to constrain the two Higgs self-couplings through potentially innovative strategies. These investigations typically interpret their findings following one of two approaches, and utilise either the so-called 'κ-framework' [12,13] or well-defined models of physics beyond the Standard Model. The latter usually incorporate an extended scalar sector with additional weak Higgs singlets and doublets [14–20], and hence rely on a possibly complex parameter space and a very different scalar potential embedding a Standard-Model-like component. In contrast, the kappa framework represents the simplest and most effective method to include new physics effects into the Higgs potential, and it relies on the introduction of two new physics parameters, κ_3 and κ_4. These quantities act as modifiers of the cubic and quartic Higgs couplings from their Standard model values. Consequently, the potential (2) can be expressed as

$$V(h) = \frac{1}{2}m_h^2 h^2 + \lambda_{hhh}(1 + \kappa_3)vh^3 + \frac{1}{4}\lambda_{hhhh}(1 + \kappa_4)h^4,$$

(3)

with the Standard Model configuration defined by $\kappa_3 = \kappa_4 = 0$.

The first step in the exploration of the Higgs potential involves the study of the trilinear Higgs self-coupling. A primary avenue for investigating this coupling is through the production of Higgs-boson pairs at hadron colliders [21]. In the Standard Model, this process is associated with substantial cross section reaching approximately $\sigma_{hh} \simeq 31$fb and 38fb for LHC centre-of-mass energies of $\sqrt{s} = 13$ TeV and 14 TeV, respectively, and increasing to 4.4pb at $\sqrt{s} = 100$ TeV. These cross sections, that reach a percent-level precision, correspond to state-of-the-art predictions that incorporate next-to-next-to-next-to-leading-order corrections in QCD and soft-gluon resummation at the next-to-next-to-next-to-leading-logarithmic accuracy [22]. Such a high production rate, that could even be higher in new physics scenarios less sensitive to destructive interference between diagrams, allows for the investigation of various final states to probe the Higgs cubic coupling, with the most promising signatures arising from final state systems composed of four b-jets, or a pair of photons combined with either a pair of b-jets or a pair of tau leptons [23–25]. Modern machine-learning techniques have been proven to be highly efficient to extract the signal from the overwhelming background, and their prospects for the future is quite encouraging, as quantitatively assessed in Sect. 5. Additionally, the triple Higgs coupling indirectly influences single Higgs production, where it arises through self-energy and vertex higher-order loop-corrections [26–29]. Recently, the ATLAS collaboration exploited this and jointly utilised measurements originating from both di-Higgs and single-Higgs studies to impose the most stringent constraints to date on κ_3 [5], which must satisfy:

$$\kappa_3 \in [-0.4, 6.3].$$

(4)

The impact of the different final states relevant to di-Higgs production at the LHC Run 2 is discussed in further detail in Sect. 3.

Similarly, the quartic Higgs self-coupling, which represents the second key factor in determining the shape of the Higgs potential, can be directly examined through triple-Higgs production and indirectly through loop-corrections in di-Higgs production. In the Standard Model, triple-Higgs production suffers from extremely low cross sections because of large destructive interference between the representative diagrams shown in Fig. 1, rendering any expectation at the LHC unrealistic. The total rate at a centre-of-mass energy $\sqrt{s} = 14$ TeV is indeed as low as $\sigma_{hhh} \simeq 0.05$fb$^{+31\%}_{-22\%}$, thus exhibiting additionally a large theory uncertainty [30]. However, the prospects for a future proton-proton collider oper-

ating at $\sqrt{s} = 100$ TeV are much more promising, particularly in scenarios involving new physics where the cross section could be substantially enhanced. This requires controlling the associated SM background, a task still lying at the frontier of the state of the art for theoretical predictions, not only because of the problematic of jet flavour tagging in an infrared-safe way and the treatment of the mass of the b quark, but also because of the final-state multiplicity of relevant SM background processes challenging our computing capabilities of achieving precise predictions. These issues are addressed in detail in Sect. 2. On the other hand, probing the quartic Higgs coupling with di-Higgs and triple-Higgs probes also poses various experimental challenges. Notably, this concerns the choice of the best final state and kinematic configuration to be studied, that both impact our abilities to decipher the relevance of the different diagrams shown in Fig. 1 as a function of phase space. This is further discussed in Sect. 4. Moreover, heavy-flavour tagging is also instrumental to maximise the potential experimental outcome. In this respect, huge progresses have been realised in the last decade, as detailed in Sect. 6.

From now on, we specifically discuss existing studies aiming to assess the prospects of triple Higgs production at present and future colliders. Within the κ-framework, $pp \to hhh$ production rates could potentially be several times larger. This is illustrated in Fig. 2 where the left panel depicts the ratio between the triple-Higgs production cross section with non-zero κ_3 and κ_4 values and the Standard Model predictions (with $\kappa_3 = \kappa_4 = 0$). Theory calculations are state-of-the-art, and incorporate corrections at the next-to-next-to-leading order modelled through form factors expressed in the heavy-top limit so that theory uncertainties are reduced to 5–10% [30]. As κ_3 values are negative and decrease, new physics contributions to the total rate become increasingly dominant, leading to enhancement of 1–5 for $-5 \lesssim \kappa_3 \lesssim -1$. The right panel of the figure presents instead exact leading-order predictions for a wider range of κ_3 values [31], demonstrating that the cross section can increase by 1 or 2 orders of magnitude for moderately sized κ_3 values well below those acceptable by perturbative unitarity [32]. While these perspectives are promising for observing a triple-Higgs signal at a future collider operating at 100 TeV, the dependence of the cross section on modifications of the quartic Higgs coupling (through a non-zero κ_4 parameter) is less pronounced. Moreover, in the unlucky situation in which both κ_3 and κ_4 parameters are positive, the cross section suffers for even more destructive interference as in the Standard Model, rendering the situation even more challenging.

Consequently, associated measurements could offer additional insight into κ_3, which could then be used in combination with the aforementioned di-Higgs searches to refine its determination. However, obtaining the first constraints on the κ_4 coupling modifier is not straightforward and will require
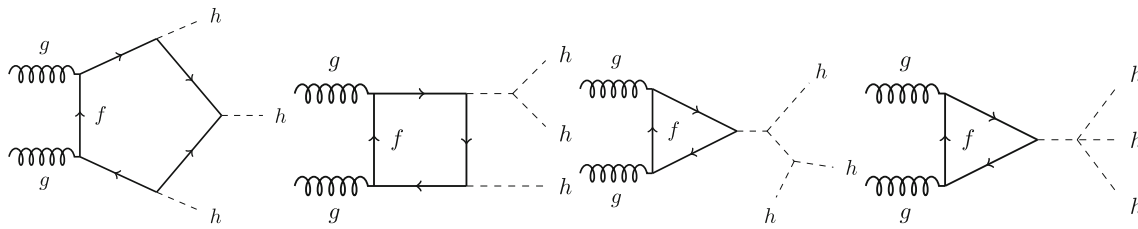
Fig. 1 Representative leading-order Feynman diagrams for triple-Higgs production in proton-proton collisions
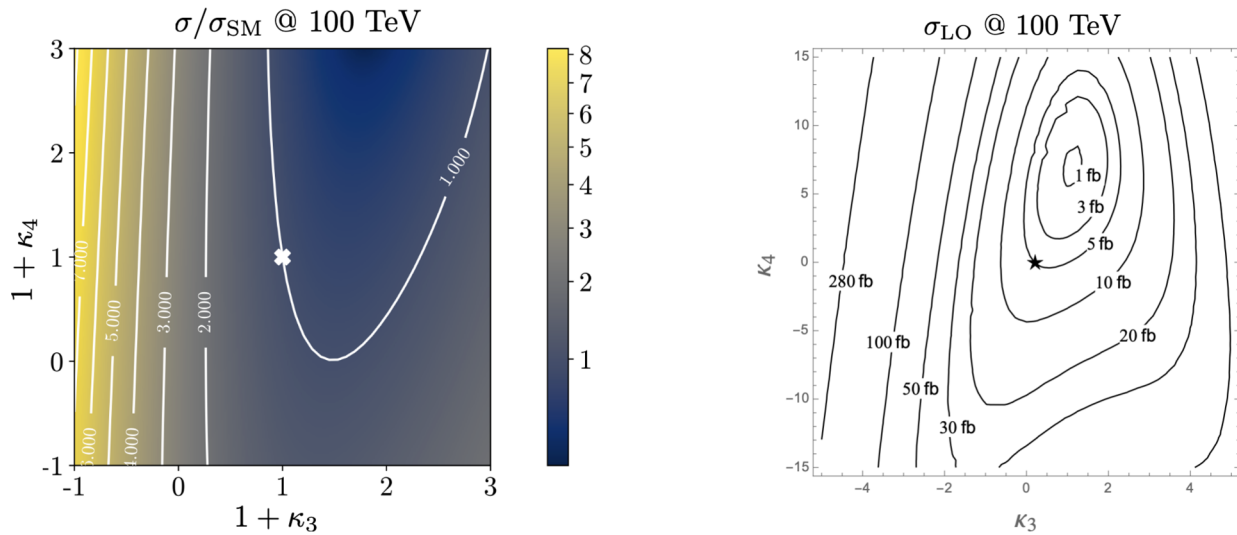

Fig. 2 Triple-Higgs production cross section at a proton-proton collider operating at a centre-of-mass energy of 100 TeV. We present predictions normalised with respect to the Standard Model cross section and with next-to-next-to-leading order corrections in the heavy-top limit included (left, figure adapted from [30]), as well as at leading order without any approximation (right, taken from [31]). The star and cross represent the SM scenario

comprehensive phenomenological studies going beyond simple analyses of the total production rates, and where κ_3 effects must be correlated with κ_4 effects. This will then have to be confronted to a precise examination of di-Higgs production, where κ_4 impacts higher-order virtual corrections (similar to κ_3 for single Higgs production). Such an approach is expected to yield complementary constraints, enabling a more precise determination of κ_4 [33,34]. For instance, for 30 ab^{-1} of pp collisions at centre-of-mass energy of 100 TeV, the parameter κ_4 can be constrained to a range of $[-3, 13]$ by profiling over κ_3. On the other hand, studies in the κ-framework are not the whole story; investigations in the context of well-defined ultraviolet (UV)-complete models are also necessary as they could involve resonant contributions that significantly alter rates and distributions.

Once Higgs-boson decays are taken into account, triple-Higgs production can give rise to a wide variety of final-state signatures. However, due to the diverse magnitude of the different Higgs branching ratios and the expected background levels, only a select few final states have been studied thus far in light of their potentially significant signal-to-

background ratios and feasibility for detection. They include cases where all three Higgs bosons decay into bottom quarks [35] ($hhh \rightarrow bbbbbb$ with a triple-Higgs branching ratio of approximately 19.5%), topologies in which two Higgs bosons decay into bottom quarks and the third decays into either a pair of photons [31,36,37] ($hhh \rightarrow bbbb\gamma\gamma$ with a triple-Higgs branching ratio of about 0.23%) or a pair of hadronically-decaying tau leptons [38] ($hhh \rightarrow bbbb\tau\tau$ with a triple-Higgs branching ratio of approximately 6.5%), and a configuration in which two Higgs bosons decay into a pair of W-bosons and the third into bottom quarks [39] ($hhh \rightarrow WWWWbb$ with a triple-Higgs branching ratio of around 0.9%).

All past studies on triple-Higgs production in proton-proton collisions at a centre-of-mass energy of 100 TeV have significantly influenced the design requirements for future detectors at such colliders. It has been consistently emphasised, irrespective of the considered hhh decay channel, that excellent b-tagging performance is indispensable. This entails achieving a low mistagging rate, even at the expense of a lower tagging efficiency, and ensuring good coverage of the

forward region of the detector given that any produced systems tend to be more forward when they originate from collisions at higher centre-of-mass energies. Furthermore, the exploitation of the $hhh \rightarrow 4b2\gamma$ mode necessitates a high photon resolution to enable the possible selection of a narrow mass window around the true Higgs mass, minimising hence background contamination. Similarly, the $hhh \rightarrow 4b2\tau$ mode should leverage excellent double-tau-tagging performance, as currently achieved in di-Higgs searches at the LHC. Additionally, efficient reconstruction of boosted-Higgs systems, where the Higgs boson decays into a pair of collimated bottom quarks, is crucial for several signatures. This is essential for disentangling the signal from the overwhelming QCD background featuring light jets. Finally, the incorporation of high-level variables in the analysis, such as the m_{T2} variable [40,41] or the $m_{\tau\tau}^{\text{Higgs-bound}}$ and m_T^{True} variables [42–44], could provide excellent handles to discriminate signal and backgrounds.

In Fig. 3, we evaluate the capability of detecting a triple-Higgs signal in proton-proton collisions at $\sqrt{s} = 100$ TeV for the three most promising final states. The results, obtained from state-of-the-art Monte Carlo simulations, are presented in the κ-framework. Technical details and analysis description can be found in [31,35,38]. The left panel of the figure showcases the sensitivity to an $hhh \rightarrow 6b$ signal in terms of standard deviations, and illustrates its dependence on the two κ-parameters across a wide range of values. Similarly, the central panel focuses on the $hhh \rightarrow 4b2\gamma$ mode. Despite potentially aggressive and not always conservative assumptions on detector parametrisation, both analyses demonstrate similar sensitivity. Notably, these pioneering studies indicate that the Standard Model configuration, defined by $\kappa_3 = \kappa_4 = 0$, is theoretically attainable at a 2σ level. Furthermore, the right panel considers the $hhh \rightarrow 4b2\tau$ channel. However, the results are this time displayed in terms of the luminosity required to achieve a 2σ exclusion for each point in the (κ_3, κ_4) parameter space. Specifically, we can note that a target luminosity of 30ab^{-1} ensures a 2σ exclusion for the Standard Model point. These results underscore the potential of combining all modes, mirroring current practice for single Higgs and di-Higgs experimental studies at the LHC. Finally, we recall that we can leverage the same hhh studies to get additional handles of non-standard couplings of the Higgs boson to the top quark, as depicted in Sect. 7.5 when the (κ_3, κ_4) parameter space is generalised to include new physics modifiers to the coupling of a top-antitop pair to one, two and even three Higgs bosons.

Beyond the κ-framework, triple-Higgs production can be also enhanced through extra diagrams incorporating new physics contributions. Prime examples include models featuring multiple scalars, such as those explored in Sect. 7. In these scenarios, the enhancement arises from Higgs-to-Higgs

cascade decays [20,45–51]. For instance, one or two heavier Higgs bosons could be initially produced and subsequently decay into a set of Standard-Model-like Higgs bosons, potentially leading to abundant production of triple-Higgs systems beyond the Standard Model. This configuration is realised easily in a model with three Higgs-like particles (h, h_2, h_3), where the heavier h_2 and h_3 correspond to new physics Higgs states. Well-studied frameworks exhibiting such states is the so-called 'Two Real Singlet Model' (TRSM) [20,52] further explored in Sects. 7.1 and 7.2, as well as the complex two-Higgs Doublet Model [53–57], Next-to-Two-Higgs-Doublet Model [58–60] and the Non-Minimal Supersymmetric Standard Model [61–72] discussed in Sect. 7.3. A triple-Higgs system can then be produced through the production and decay sequence of sub-processes

$$pp \rightarrow h_3 \rightarrow h_2 h \rightarrow h h h. \tag{5}$$

These decay processes here occur due to multi-Higgs interactions included in the scalar potential.

This phenomenon is particularly relevant at the LHC, not only for the planned high-luminosity operations but also for the much closer upcoming Run 3. However, in models featuring additional scalars, the parameter space is often vast and contains numerous free parameters relevant to the Higgs sector. Nonetheless, studies in the TRSM [50], also detailed in Sect. 7.1, have demonstrated that typical scenarios consistent with current constraints on extended scalar sectors, including additional Higgs bosons with masses in the 200–500 GeV range, could yield observable signals at the LHC Run 3 with significance ranging from 2σ over to 5σ. Furthermore, with an expected accumulated luminosity of 3ab^{-1} at the high-luminosity LHC, any representative benchmark scenario exhibits a significance exceeding 5 standard deviations. These findings leverage the presence of intermediate resonance effects in triple-Higgs production, and the ability to fully reconstruct the resonant states through kinematic fits of the final state. Consequently, undertaking triple-Higgs searches at the LHC presents promising avenues and there is no need to wait for a future collider that could operate in a few decades from now. In addition, such analyses involving intermediate scalar resonances and Higgs-to-Higgs cascades could be facilitated by utilising a simplified-model approach, such as the one proposed in Sect. 8.

These promising results should prompt a reevaluation of triple-Higgs phenomenology within the κ-framework at the LHC, particularly considering that perturbative unitarity allows for κ_3 and κ_4 values much larger than those considered in pioneering studies at future colliders, with acceptable values of $|\kappa_3| < 10$ and $|\kappa_4| < 65$ using partial wave expansion at the tree level and the optical theorem [32]. However, despite the larger signal cross sections for more extreme κ parameter values, they remain insufficient to ensure potential observations across wide parts of the parameter space. Lever-
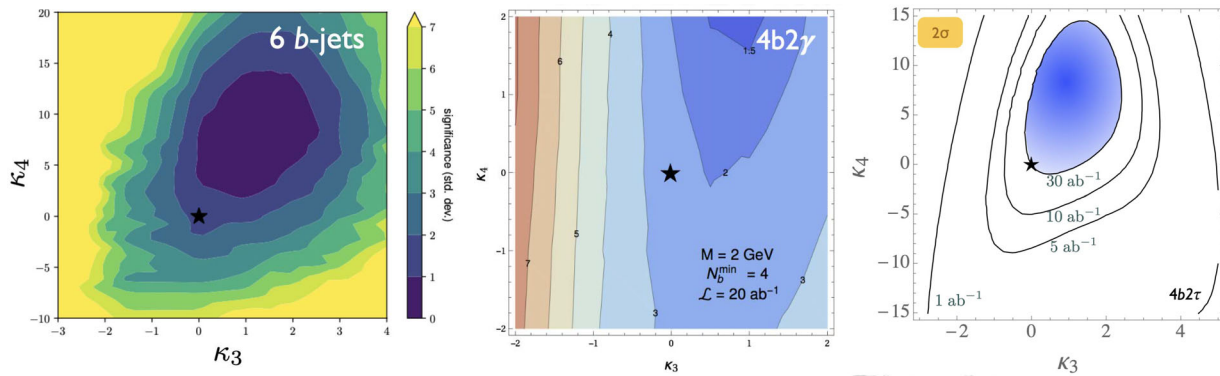
Fig. 3 Sensitivity to a triple-Higgs signal at a proton-proton collider operating at a centre-of-mass energy of 100 TeV. The figure presents the sensitivity in terms of standard deviations for the $hhh \to 6b$ final state (left, figure adapted from [35]) and for the $hhh \to 4b2\gamma$ final state (centre, figure adapted from [31]), as well as in terms of the luminosity required to achieve a 2σ sensitivity for the $hhh \to 4b2\tau$ mode (right, figure adapted from [38]). The star represents the SM scenario
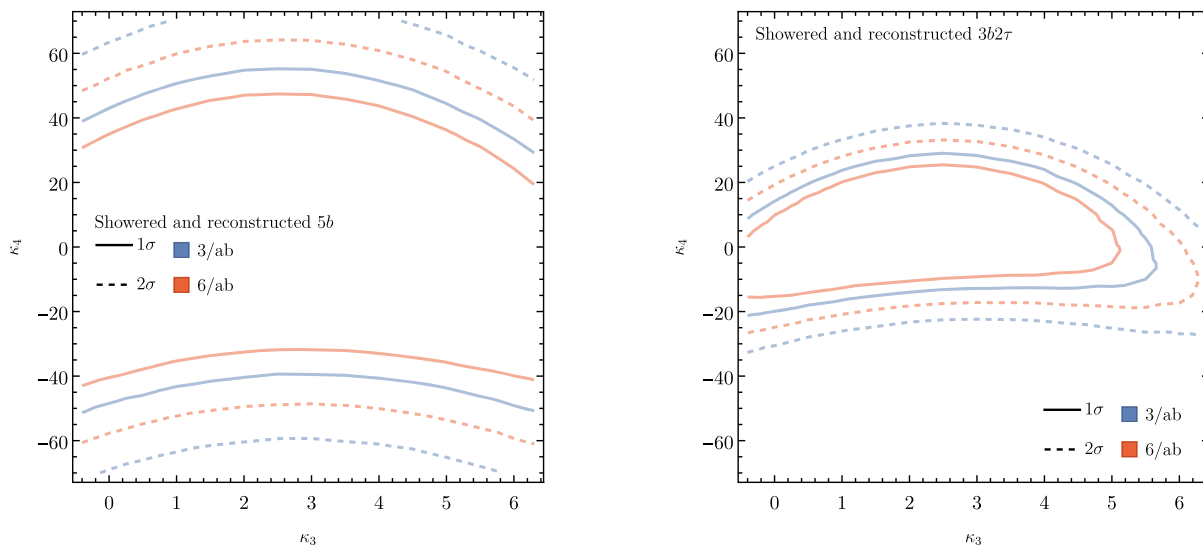
Fig. 4 Sensitivity to a triple-Higgs signal at the high-luminosity LHC, after the analysis of signal and backgrounds for the $hhh \to 6b$ final state (left, figure taken from [32]) and for the $hhh \to 4b2\tau$ mode (right, figure taken from [32])

aging advanced machine learning techniques and assuming excellent detector performance for the high-luminosity LHC, along with an aggressive choice for the systematics, it is however possible to show that certain regions of the (κ_3, κ_4) parameter space are excluded at 95% confidence level with a luminosity of 3ab^{-1}, or even of 6ab^{-1} when combinations from both the ATLAS and CMS experiments are considered. This is depicted in Fig. 4 for the $hhh \to 6b$ and $hhh \to 4b2\tau$ channels, the only two modes showing significant potential at the LHC due to their large-enough production cross section (including relevant branching ratio factors), as well as more comprehensively discussed in Sect. 7.4. Consequently, scenarios with extreme values for the κ_4 parameter can be possibly excluded, providing further motivation for investigating triple-Higgs production at the LHC.

Throughout our discussion, we delved into the significance of triple-Higgs production in the context of high-energy colliders, particularly focusing on its implications for understanding the Higgs potential and probing physics beyond the Standard Model. We emphasised the importance of the κ-framework as a mean to both probe the Standard-Model nature of the Higgs self-couplings and provide insights into new physics scenarios. While studies at future colliders indicate promising prospects for observing triple-Higgs events, we highlighted the potential for reevaluating triple-Higgs phenomenology at the LHC both within the κ-framework and in new physics models with additional scalars. As also further detailed in the next chapters of this work, despite challenges posed, advanced machine learning techniques, high-level variables and excellent detector per-

formance could offer avenues for excluding certain regions of the parameter spaces. Collider studies should however always try to exploit best any complementary source of information. For instance, as detailed in Sect. 7.6, gravitational wave properties that are now measured sufficiently well could be interpreted as constraints on the Higgs potential. In conclusion, undertaking such searches at the LHC could hold the promise of shedding light on fundamental aspects of particle physics, advancing our understanding of the Higgs mechanism and its implications for physics beyond the Standard Model.

2 QCD overview and possible challenges

G. Soyez, G. Zanderighi

The investigation of the triple Higgs final state in the SM as well as possible new physics scenarios highly relies on an accurate understanding of the corresponding theoretical predictions for both signal and dominant SM background, related higher-order corrections and scale uncertainties, as well as available tools to describe the corresponding differential contributions as accurately as possible. In addition, it is important to understand the differences in predictions depending on the chosen flavour scheme. We briefly address these issues in this section by describing current state of the art as well as open questions and possible challenges that appear in the investigation of triple Higgs final states at current and future hadron colliders.

2.1 Jet flavour

As extensively discussed in Sect. 1, the investigation of triple-Higgs production and the endeavor to extract the quartic coupling are extremely challenging due to the tiny cross sections for the production of three Higgs bosons. These cross sections are strongly suppressed not only because of the large invariant mass of the final state but also due to the destructive interference between diagrams involving the triple and the quartic Higgs coupling. Such destructive interference may persist in models of physics beyond the SM or could be alleviated, potentially making the signals accessible. However, even if the signal involving the quartic Higgs coupling were to be significantly amplified, precisely determining the quartic Higgs coupling would remain exceedingly challenging due to the overwhelming background processes to this signal.

As already noted in Sect. 1, the tiny cross-section for the signal process necessitates a focus on decay channels with the largest branching ratio of the Higgs boson, notably final states involving three pairs of $b\bar{b}$ quarks, two $b\bar{b}$-pairs and one 2τ, or $4b + 2\gamma$. All these decay channels feature at least four b quarks in the final state. However, b quarks are abundantly produced at the LHC in numerous processes unrelated

to Higgs bosons, such as gluon splitting or the decay of top quarks, Z-bosons, or W-bosons. At high energies, b quarks typically result in b-jets, making the study of the quartic Higgs coupling inseparable from the challenge of understanding and optimizing b-tagging and assigning bottom-flavor to jets.

While the development of infrared (IR) safe jet algorithms is a solved problem for unflavored jets, incorporating flavor information into jet definitions poses challenges. Traditionally, a flavored-jet is identified by the presence of at least one flavor tag, such as a B or D meson, above a specified transverse momentum threshold. However, due to collinear or soft wide-angle $g \to Q\bar{Q}$ splittings, where Q represents a quark with the flavor of interest, this definition lacks collinear and infrared safety whenever the quarks are treated as massless. In a calculation which keeps the finite mass of the heavy flavour, even though infrared-and-collinear safety is technically restored, the infrared sensitivity still manifests itself as large logarithms in the ratio of the small mass of the flavoured quark over the hard scale of the process. As extensively discussed in Ref. [73], defining jet flavor in perturbation theory is extremely delicate. Notably, defining a b-jet as a jet containing at least a b-quark yields non-infrared finite cross-sections in the case of calculations performed in the massless limit, and results logarithmically sensitive to the quark mass, when this is kept finite in the calculations. The formulation of a k_t-like algorithm ensuring infrared safety to all orders was attempted in Ref. [73], predating the anti-k_t algorithm [74]. Key elements of this definition include a mechanism preventing soft flavored quarks from contaminating the flavor of hard flavorless jets and labeling jets containing more than one b-quark as flavorless jets.

This first flavour-algorithm was formulated to address a discrepancy between data and theory in the context of heavy-flavor production at the Tevatron [73,75]. However, the proposed jet-algorithm based on the k_t algorithm was impractical for experimental implementations and its use was primarily limited to the development of perturbative predictions involving heavy-flavor.

Recent years have witnessed renewed interest in providing an infrared safe and practical definition of flavored jets. Given the widespread use of the anti-k_t algorithm in experimental studies, recent endeavors have focused on formulating algorithms maintaining the anti-k_t kinematics of jets while ensuring infrared safety, at least to some high order in the perturbation theory, and enabling flavor assignment [76–78].

Nevertheless, addressing this problem has proven more complex than anticipated. A recent breakthrough was achieved with the development of infrared-safe anti-k_t-like jets, accomplished through the introduction of an interleaved flavor neutralization procedure [79]. However, experimental challenges related to the identification and separation of two B hadrons which are very close to each other remain. Further-

more, an unfolding procedure will be indispensable to convert experimental measurements of flavor-k_t jets into a format directly comparable with theoretical predictions. Further research in this direction is undoubtedly needed to accurately describe the signals and backgrounds involving multiple b-jets, which is needed to study signal events with two or three Higgs bosons, and their irreducible backgrounds. It is interesting to point out that the approach of Ref. [79] is also suited for use with the Cambridge/Aachen algorithm. This helps jet flavour tagging for a large family of jet substructure tools which could also be relevant for multi-Higgs tagging (see below).

2.2 Perturbative challenges

In addition to the challenges posed by b-tagging and flavored jets, the complexity of the high multiplicity final states resulting from the production of two or three Higgs bosons presents other significant challenges.

Advancements in perturbative calculations over the past two decades have enabled the development of publicly available codes [80–82], which allow the automatic computation of one-loop amplitudes for final states with a high particle multiplicity. For a long time the availability of one-loop amplitudes constituted the bottleneck to obtain next-to-leading order (NLO) accurate predictions for these processes. Nowadays, the primary obstacles in obtaining NLO predictions lie in issues of numerical stability and computational time rather than theoretical limitations. Processes featuring six particles in the final state, such as the production of three $b\bar{b}$-pairs, while feasible, still present numerical challenges for NLO calculations. These calculations can be further refined by matching them with all-order parton shower effects using methods like POWHEG [83] or MC@NLO [84].

Despite the progress made, the precision of NLO calculations remains limited, especially for pure QCD processes involving a high particle multiplicity. For instance, in the QCD production of three pairs of bottom quarks, the leading-order contributions involve a high power (6th power) of the strong coupling constant. In such a case, determining a preferred renormalization and factorization scale is not straightforward. Consequently, uncertainties due to missing higher orders below 10–20% are not reachable based solely on pure NLO predictions (see e.g. Ref. [81]). The frontier of next-to-next-to-leading order (NNLO) calculations now extends, for selected processes, to cross sections with three particles in the final state. Processes known today at NNLO include three photon production [85,86], two photons and one jet [87], two jets and one photon [88], three-jets [89], $Wb\bar{b}$ production [90,91], ttH [92] and $t\bar{t}W$ [93].

However, it is currently unrealistic to expect NNLO calculations for processes with six particles in the final state in the near future, which is the typical multiplicity of backgrounds relevant to triple-Higgs production.

Various approaches are routinely employed to address this issue. One widely used experimental-driven approach involves extracting precise estimates of background processes directly from experimental data using regions which are devoid of signal to normalize the background, and subsequently extrapolating these backgrounds to the signal region of interest. These techniques, and extensions thereof, have been highly successful in searches for new physics, particularly in excluding regions of parameter space for new physics models. However, their application to precision measurements is more challenging due to the difficulty in estimating the uncertainty associated with the extrapolation from the signal-free region to the region of interest. This, coupled with the challenges related to flavor assignment discussed earlier, makes it particularly challenging to assign solid theory uncertainties to theory predictions of high multiplicity processes such as the production of 4 b-jets, 4 b-jets and two photons, or 6 b-jets.

Several theory-based approaches exist to improve upon NLO calculations. One widely used and generic approach is the multi-jet merging of NLO calculations involving different multiplicities [94–97]. This approach is known to work well in practice, particularly concerning the shapes of distributions. Alternatively, it is sometimes feasible to include a well-defined subset of NNLO corrections, such as form factor corrections. Another approximation is to work in the leading-color approximation, which typically captures the bulk of the NNLO corrections. In some cases, such as the production of top-quarks decaying to W and bottom quarks or the production of other resonances, it is possible to consider only factorizing corrections [98], i.e. to separate the corrections to production and decay, thereby simplifying the structure of higher-order corrections. This simplification is justified by the observation that non-factorizable corrections are typically suppressed by the small width over the heavy mass of the resonant particles. Other interesting approximations include, for instance, employing the soft Higgs approximation in the two-loop virtual corrections. This method bears resemblance to the soft-gluon approximation widely used in perturbative QCD, albeit tailored specifically to the Higgs boson. Recently, it has been employed to provide an accurate estimate of the NNLO cross-section for ttH production [92] and $t\bar{t}W$ [93]. In these cases, it is possible to validate the soft-boson approximation at one-loop. Since the predicted two-loop hard coefficient is found to be very small, even when assigning a very conservative error to it, the resulting theory uncertainty remains small. Another approach to obtaining massive amplitudes involves starting from massless ones and then incorporating masses through a massification procedure [99–103]. It is worth noting that in the case of $t\bar{t}W$, the massification procedure of the quarks, or the soft approx-

imation of the W, yield approximate two-loop results that are consistent with one another. This observation is particularly intriguing because both approximations are, in principle, utilized beyond their region of validity, and the two approaches are conceptually very different. Yet another standard approximation for the two-loop virtual is to use Padé approximants [104,105], which essentially determines a best estimate of the missing higher-orders based on previous orders. To name a few examples, Padé approximants were used in Ref. [106] to estimate higher-order effects in the decays of Higgs to $b\bar{b}$ and Higgs to two gluons, in Ref. [107] Padè approximants are constructed from the expansions of the amplitude for large top mass and around the top threshold to estimate the top-quark mass effects in the Higgs-interference contribution to Z-boson pair production in gluon fusion and in Ref. [108] the approximation is used to estimate the three-loop corrections to the Higgs boson-gluon form factor, incorporating the top quark mass dependence. In general, these approximations and their practical efficiency can only be assessed on a case-by-case basis.

Overall, these and other approximate higher-order results are likely to drive the progress of theory predictions to achieve the desired precision for the dominant background processes relevant to the study of triple Higgs production in different decay channels, while full NNLO corrections are likely to remain unavailable in the foreseeable future.

2.3 Four- versus five-flavour scheme

When dealing with processes involving bottom quarks,[1] two commonly used approaches are the four-flavor scheme (4FS) and the five-flavor scheme (5FS). Each scheme offers distinct advantages and drawbacks. For a discussion of these see e.g. Ref. [109]. In the 4FS, the b-quark is treated as a massive object at the level of short-distance matrix elements, and never explicitly appears in the initial state. Cross-sections in the 4FS typically contain large logarithms of the ratio of the bottom mass to the hard scale of the scattering process. Conversely, in the 5FS, b-quarks are treated as light partons in short-distance matrix elements. They are generated at a scale $\mu \sim m_b$ in the Dokshitzer–Gribov–Lipatov–Altarelli–Parisi (DGLAP) evolution of initial state PDFs, and resummation of large logarithms is achieved through the DGLAP evolution equations of the bottom PDF.

While resummation of large logarithms is not possible in the 4FS, and large logarithms are included only at fixed order. This resummation, included in the 5FS, typically translates into a better perturbative convergence for the latter scheme. Computing higher-order effects is also more challenging in the 4FS due to the larger multiplicity and inclusion of massive quarks in the Born process. On the other hand in the 4FS scheme, mass effects are included exactly, at the order at which the calculation is carried out. Implementing 4FS calculations in a Monte Carlo framework is straightforward, whereas in the 5FS particular care is needed when dealing with gluon splittings to bottom quarks.

When mass effects are significant and the resummation of collinear logarithms is important, a combination of both schemes is necessary. The FONLL (Fixed Order plus Next-to-Leading Logarithms) approach [110] successfully combines the strengths of both schemes to obtain a best estimate of total cross sections. Essentially, this involves adding the cross-sections computed in the 4FS and 5FS and subtracting the double-counting at fixed order. The only subtlety is that, in order to consistently remove the double-counting, one needs to express both 4FS and 5FS cross-sections in terms of the same coupling (i.e. involving the same number of flavours) and the same PDF. Although technically cumbersome, this procedure is well-understood and has been widely applied in various contexts.

Having FONLL-matched predictions available for all ranges of signals and backgrounds relevant to double and triple Higgs production at the LHC would be highly desirable for more accurate theoretical predictions and comparisons with experimental data. This would enable a better understanding of the underlying physics and aid in the measurements or constraints of triple and quartic Higgs coupling.

2.4 Monte Carlo predictions

While perturbative fixed-order calculations provide the best estimates for inclusive measurements, Monte Carlo (MC) tools are essential for the description of more exclusive observables and for a full interpretation of LHC data. The sophistication of Monte Carlo tools has improved over the years, and it is not uncommon to find examples where, for instance, Pythia outperforms full matrix element generators even in regions dominated by hard radiation, which should theoretically be described less accurately by Monte Carlo generators. However, since Monte Carlos rely on several approximations, particularly in the generation of the parton shower in soft and collinear limits, one issue in comparing data to Monte Carlo predictions is the lack of clarity in assigning a theory uncertainty to MC predictions.

Over the past few years, a significant effort has been directed towards improving generic-purpose Monte Carlo event generators. In particular, several new parton shower algorithms have been introduced. In this context, considerable progress has been made to formally validate the (logarithmic) accuracy of parton showers by comparing their output to analytic resummation for specific classes of observables. Concretely, several groups (see e.g. [111–115]) have reported next-to-leading (NLL) logarithmic accuracy for broad classes of observables, or even higher accuracy for non-

---

[1] Similar arguments apply to charm quarks.

global observables [116]. Additionally a substantial progress has been made to include subleading-colour contributions in dipole-based parton showers (see, for example, Refs. [117–119]) We refer to Ref. [120], and references therein, for a broader overview of recent improvements.

Such progress in Monte-Carlo generators (together with steady progress in analytic resummations) can be viewed as complementary to the fixed-order perturbative considerations highlighted in the last two sections. In the context of multi-Higgs production, combining improvements in fixed-order perturbation theory, all-order resummations (analytically or by means of parton shower algorithms), and non-perturbative corrections, would largely help the study of both signals and backgrounds. It could, in particular, impact the modelling of backgrounds in experimental context.

2.5 Boosted versus non-boosted

As a final set of remarks, we wish to comment on possible scenarios where one or more Higgs bosons are produced with a transverse momentum much larger than its mass. This could for example happen in situations where a more massive intermediate new particle decays into a pair of Higgs bosons.

In such a boosted-Higgs case, the angle between the b and $\bar{b}$ quarks becomes small and the Higgs is reconstructed as a single fat jet. The event reconstruction therefore has to rely on jet substructure techniques. While the boosted regime often comes with low, kinematically-suppressed, cross-sections, it can offer several advantages that we briefly discuss here.

First of all, jet substructure techniques have seen a large amount of development over the past decade, establishing themselves as a powerful approach to study complex final-states. A wealth of techniques have been proposed and can be used to enhance specific aspects of the signal. The recent years have also seen the rise of deep-learning-based tools which excel at separating signals from backgrounds in boosted jets. This is particularly relevant in a discovery context where boosted Higgses would appear in a BSM scenario.

From an event reconstruction perspective, situations with one or more boosted Higgs(es) would suffer less from combinatorial issues than non-boosted cases.

It is beyond the scope of this document to dive into specific jet substructure tools. We can however redirect the reader to review articles, and references therein, for a generic overview of theoretical and machine-learning aspects [121], for experimental aspects [122], and for a generic introduction with emphasis on analytic aspects in QCD [123].

We also note that several jet substructure methods of broad interest have been introduced since these reports have been written. This includes, for example, techniques based on the Lund Jet Plane [124], or on energy correlators (see e.g. [125]). When it comes to using Machine learning algorithms to tag boosted objects, techniques such as the ones from Refs.

[126–128] have shown good overall performance in different physics scenarios.

A final set of remark concerns the relation between the boosted regime and the perturbative QCD aspects discussed in the previous sections. Some substructure techniques are amenable to precision calculations. This could lead to situations where analytic predictions, obtained through a combination of (approximate) NNLO, analytic resummations and parton shower developments allow for better, simplified, theoretical control over QCD backgrounds. A word of caution is however needed when relying on machine-learning techniques. These would typically involve training a neural network on Monte Carlo samples. In such a case, aspects of the physics which are not accurately described by the Monte Carlo generator would be "learned" by the neural network, resulting in potentially spurious discriminating power. Besides being aware of this fact when using Deep learning techniques, this again points towards pursuing the effort of improving the theoretical description of both the multi-Higgs signals and the associated backgrounds.

3 Experimental lessons from HH

T. du Pree, M. Stamenkovic

The self-interactions of the Higgs boson are determined by the shape of the Higgs field potential, which can be written as a polynomial function of the Higgs field h:

$$V(h) = \frac{1}{2}m_H^2 h^2 + \lambda_3 v h^3 + \frac{1}{4}\lambda_4 h^4, \tag{6}$$

where m_H is the Higgs boson mass, v is the vacuum expectation value of the Higgs field, and λ_3 and λ_4 are the coefficients of the cubic and quartic terms, respectively. These coefficients are also known as the trilinear and quartic couplings for the Higgs boson, and they encode the strength of the interactions among three and four Higgs bosons, respectively. In the Standard Model, these couplings are fixed by the Higgs boson mass and the electroweak parameters, and their values are $\lambda_3 = \lambda_4 = m_H^2/(2v^2) \approx 0.13$. The shape of the Higgs potential is a crucial ingredient of the theory that describes the origin and nature of the Higgs boson and its interactions. However, this shape is not predicted by the theory, but rather assumed as an input. It is essential to test this assumption experimentally and measure the shape of the Higgs potential.

Figure 5 illustrates how the shape of the Higgs potential depends on the values of the trilinear and quartic couplings of the Higgs boson, denoted by λ_3 and λ_4, respectively. Deviations of these couplings from their expected values in the SM would indicate the presence of new physics beyond the SM. Therefore, measuring these couplings precisely is a powerful way to search for new physics phenomena and to understand
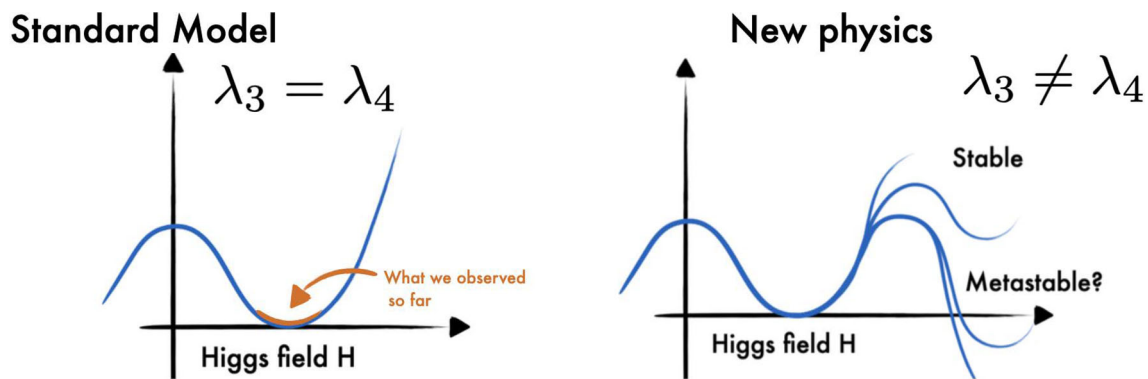
Fig. 5 Illustration of the shape of the Higgs field potential for the Standard Model ($\lambda_3 = \lambda_4$) and for new physics scenarios where the trilinear and quartic self-coupling are not equal ($\lambda_3 \neq \lambda_4$)

the fundamental nature of the Higgs boson and its role in the universe.

The Higgs boson is a key element of the SM of particle physics, responsible for the mass generation of elementary particles. The ATLAS and CMS experiments at the Large Hadron Collider (LHC) have confirmed the existence of the Higgs boson and measured its interactions with gauge bosons and the third-generation fermions. They have also found evidence for its interactions with the second-generation charged leptons [3,4]. However, the self-interactions of the Higgs boson, which are related to the shape of the Higgs potential, remain untested. The ATLAS and CMS experiments have searched for the production of two Higgs bosons (HH), but no significant signal has been observed yet. No results have been reported so far on the HHH production at the LHC.

The Feynman diagrams for both the HH and HHH production at hadron colliders are shown in Fig. 6. While the HH production is mostly sensitive to the trilinear coupling λ_3, the quartic coupling λ_4 contributes at the next-to-leading order. The HHH production, however, is dominated by both the trilinear and quartic couplings at leading order.

From an experimental point of view, the measurement of the Higgs self-coupling as well as the shape of the potential can only be fully determined from a combined measurement of the HH and HHH processes.

3.1 Cross-sections and branching ratios

At proton-proton colliders, the dominant production mode for the HH and HHH processes is the gluon-gluon fusion production mode. The theoretical and experimental status of the HH production searches, and of the direct and indirect constraints on the Higgs boson self-coupling is extensively discussed in [21]. The cross-sections for both the HH and HHH gluon-gluon fusion production mode, calculated at a center-of-mass $\sqrt{s} = 14$ TeV at NNLO, are shown in Table 1. The cross-section of the HH production is approximately

300 times larger than the cross-section of the HHH production.

Under the SM hypothesis, the dominant branching ratios the HH and HHH decay modes are shown in Fig. 7 for a mass $m_H = 125.25$ GeV. Due to the largest branching fraction of the $H \to b\bar{b}$ decay mode, the largest branching ratio for the HH process is the $HH \to b\bar{b}\, b\bar{b}$ decay mode. In the case of the HHH process, the largest branching ratios are the $HHH \to b\bar{b}\, b\bar{b}\, WW$ and $HHH \to b\bar{b}\, b\bar{b}\, b\bar{b}$. Furthermore, in the case of HHH, about 60% of the total cross-section is accessible via the $HHH \to b\bar{b}\, b\bar{b}\, YY$ decay modes, where $YY = b\bar{b}, WW, gg, \tau\tau, ZZ, yy$. The HH and HHH processes have similar decay modes, kinematics and backgrounds. Therefore, the experimental techniques and results obtained from the HH searches can provide useful guidance and input for the HHH searches.

3.2 Sensitivities to SM HH

From an experimental point of view, the three HH channels with the highest sensitivity are:

– $HH \to b\bar{b}\, b\bar{b}$: largest branching ratio (33.4%) but large contamination from QCD multi-jet background,
– $HH \to b\bar{b}\, \tau\tau$: sizable branching ratio (7.2%) with lower background contamination,
– $HH \to b\bar{b}\, yy$: small branching ratio (0.3%) but low background contamination and better energy resolution on photons.

The $HH \to b\bar{b}\, b\bar{b}$ final state is the most probable decay mode for the HH production, but it also poses several experimental challenges. One of them is the identification of b-jets, which requires efficient and precise tagging algorithms to discriminate them from light-flavor jets. Another challenge is the reliable modelling of the dominant background, which is the QCD multi-jet production. This background has a large
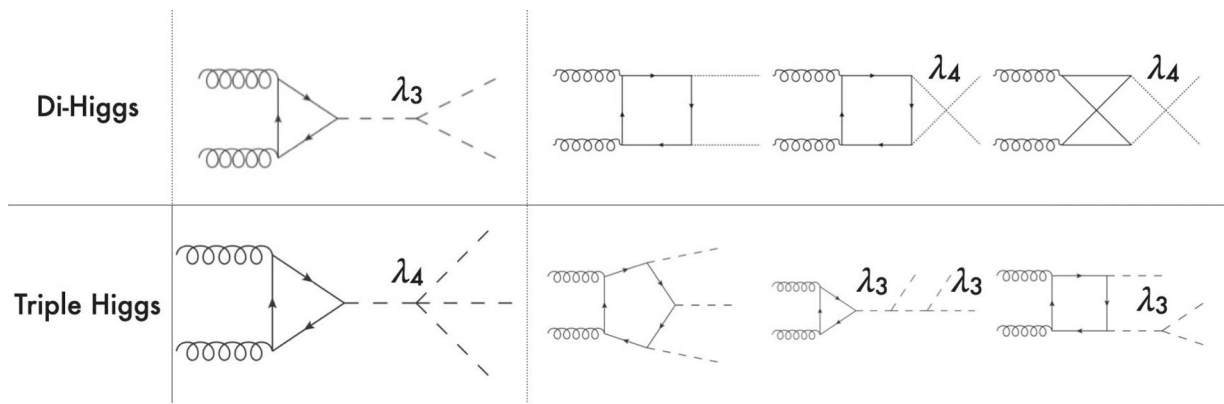
Fig. 6 Feynman diagram for the gluon-gluon fusion di-Higgs HH and triple Higgs HHH productions at hadron colliders

Table 1 Cross-section of the gluon-gluon fusion production mode for HH [129–131] and HHH [30] production at NNLO at a center-of-mass $\sqrt{s} = 14$ TeV. The uncertainties include the available QCD corrections, as well as the renormalisation and factorisation scales set to $m_{HH}/2$ and $m_{HHH}/2$

	HH	HHH
σ_{NNLO} at $\sqrt{s} = 14$ TeV [fb]	$36.69^{+2.1\%}_{-4.9\%} \pm 3.0\%$	$0.103^{+5\%}_{-8\%} \pm 15\%$

cross section and is computationally costly to simulate for the ATLAS and CMS experiments. Therefore, data-driven methods are often employed to estimate the QCD multi-jet background from control regions in data and extrapolate it to the signal region.

A further complication arises from the jet pairing problem, which refers to the ambiguity in assigning the b-jets to the Higgs boson candidates. To resolve this problem, a pairing algorithm based on the minimal distance between the invariant masses of the b-jet pairs, where the signal uniquely converges to the same mass. This algorithm does not shape the QCD multi-jet background around the Higgs boson mass peak, however the probability to correctly reconstruct the pairs is often lower than in the non-ambiguous decay modes. The jet pairing algorithm is even more important for the $HHH \rightarrow b\bar{b}\,b\bar{b}\,b\bar{b}$ process, where the additional jets increase the number of possible combinations and therefore degrades the reconstruction efficiency. The usage of modern machine learning methods, such as attention networks [132], or algorithms based on the minimal distance between the jets will be necessary to improve the sensitivity to the HHH processes.

The loss of performance arising from the jet pairing can be mitigated with the usage of a boosted category where the two Higgs boson candidates, recoiling against each other, are reconstructed within a large-radius jets with a transverse momentum of 300 GeV. By exploiting from the recent improvement in boosted Higgs boson tagging, such as Parti-

cleNet [127], the QCD multi-jet background can be reduced and the sensitivity largely improved. Boosted reconstruction techniques can play a large role in the search for HHH.

The $HH \rightarrow b\bar{b}\,\tau\tau$ final state requires both flavour tagging and τ-identification algorithms. While the branching ratio is lower than in the $HH \rightarrow b\bar{b}\,b\bar{b}$ final state, the presence of $2\,\tau$-leptons allows to efficiently reduce the background contamination from the QCD multi-jet process. The dominant background is therefore the $t\bar{t}$ process, for which the Monte-Carlo simulation can be used to describe the data accurately. The sensitivity of the analysis is further improved by splitting the signal region in categories depending on the decays of the τ-leptons: $e\tau_{hadronic}$, $\mu\tau_{hadronic}$ and $\tau_{hadronic}\tau_{hadronic}$. The $\tau_{hadronic}\tau_{hadronic}$ channel has the advantage of having a lower contamination from jets from the QCD background misidentified as a τ-lepton, which in turns improves the sensitivity. It is interesting to note that the $HHH \rightarrow b\bar{b}\,b\bar{b}\,\tau\tau$ final state will benefit from the same advantages as the $HH \rightarrow b\bar{b}\,\tau\tau$. In this case, the branching ratio difference with respect to the final state with 6 b-quarks is lower than the difference in HH, a hint that this channel will play a crucial role in the search for HHH.

The $HH \rightarrow b\bar{b}\,yy$ final state has a lower branching ratio but benefits from the energy resolution of the ATLAS and CMS experiments, which is of the order of $\mathcal{O}(1)$ GeV with respect to the jets energy resolution of $\mathcal{O}(10)$ GeV. The analysis is designed to measure a narrow resonance in the invariant mass distribution m_{yy}, where the dominant background yy+jets is estimated from a parametric fit to the sideband. Due to the more precise resolution of the invariant mass of the Higgs candidate, this final state benefits the most from the increased statistics obtained over the years. Regarding $HHH \rightarrow b\bar{b}\,b\bar{b}\,yy$, the branching ratio is 0.228%, resulting in about 1 event produced by the end of the High-Luminosity LHC. This channel therefore constitutes an interesting probe for new physics phenomena.
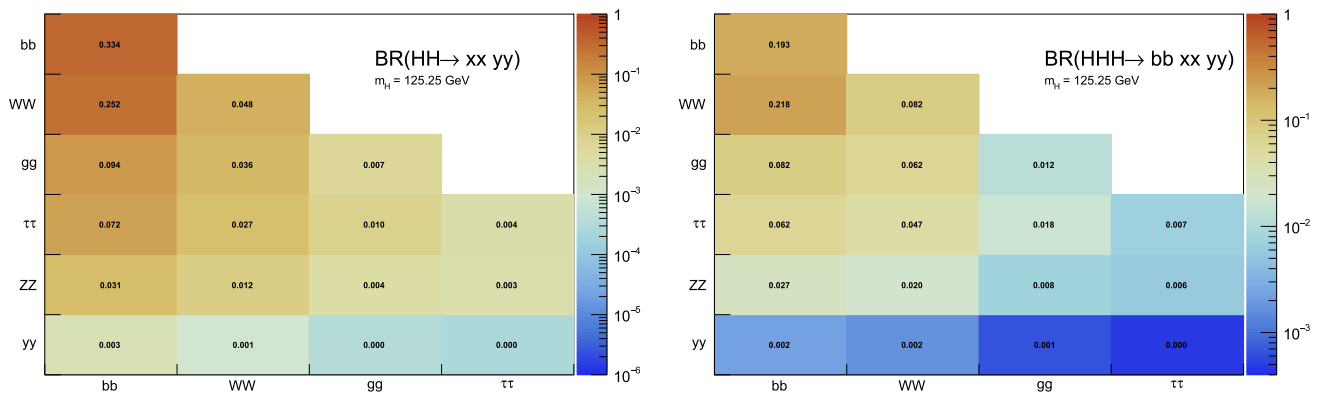
Fig. 7 Branching ratios for the largest decay mode of the $HH \to XX\,YY$ and $HHH \to b\bar{b}\,XX\,YY$ final states assuming a Higgs boson with a mass of 125.25 GeV, rounded to the third decimal

Table 2 Observed (expected) limit on the signal strength $\mu = \frac{\sigma \times br}{\sigma_{SM} \times br_{SM}}$ to the SM HH process from the ATLAS and CMS experiments, under the background only hypothesis $\mu_{HH} = 0$

Final state	ATLAS	CMS
Resolved $HH \to b\bar{b}\,b\bar{b}$	$\mu_{HH} < 5.4$ (8.1) [133]	$\mu_{HH} < 3.9$ (7.8) [134]
Boosted $HH \to b\bar{b}\,b\bar{b}$	-	$\mu_{HH} < 9.9$ (5.1) [135]
Combined $HH \to b\bar{b}\,b\bar{b}$	-	$\mu_{HH} < 6.4$ (4.0) [4]
$HH \to b\bar{b}\,\tau\tau$	$\mu_{HH} < 5.9$ (3.1) [136]	$\mu_{HH} < 3.3$ (5.2) [137]
$HH \to b\bar{b}\,yy$	$\mu_{HH} < 4.0$ (5.0) [138]	$\mu_{HH} < 7.7$ (5.2) [139]

The limits at 95% confidence level on the signal strength $\mu = \frac{\sigma \times br}{\sigma_{SM} \times br_{SM}}$, under the assumption that there is no SM Higgs self-coupling $\mu = 0$, are shown in Table 2. In CMS, the combined measurement of the $HH \to b\bar{b}\,b\bar{b}$ analyses results in the highest expected sensitivity. This mostly relies on the inclusion of a category where both the Higgs bosons are reconstructed in a large-radius jet with a transverse momentum of $p_T > 300$ GeV and exploits the ParticleNet machine learning algorithm to select Higgs-like jets and remove the background arising from QCD multijets. This unique signature, where two Higgs bosons recoil again each other, measured in a decay channel with the highest branching ratio, drives the sensitivity to the HH process. The other channels exhibit a similar sensitivity to this boosted category.

In ATLAS, the decay channel $HH \to b\bar{b}\,\tau\tau$ results in the best sensitivity and drives the search for the HH process. In particular, the category where the two τ-leptons decay hadronically shows the best performance within the analysis. This result outperforms the other leading channels, taken separately, in both ATLAS and CMS by 60–70% and is therefore one of the most promising channel for HHH as well. The gain in signal acceptance outperforms the increase in the dominant $t\bar{t}$ background relevant for this channel. The difference with respect to the CMS result is partly due to the trigger requirements, where the ATLAS experiment recorded signal events more efficiently during Run 2. The Run 3 analyses, which will benefit from optimised strategies in terms

of trigger as well as improved machine learning tools for the identification of b-jets and τ-lepton, will lead to even better constraints on the HH search and the Higgs self-coupling.

These results are interpreted in terms of Higgs self-coupling modifications κ_λ and reported in Table 3, where $\kappa_\lambda = 1$ corresponds to the SM self-coupling. In terms of constraints on the self-coupling, it is interesting to note that the $HH \to b\bar{b}\,yy$ channel drives the sensitivity. This is due to the trigger requirement, which selects events with two photons and allows to record events in the low part of the invariant mass $m_{HH} < 450$ GeV, where the large modifications of the κ_λ coupling are dominant. Under the current assumptions, only coupling modifications to the trilinear κ_{λ_3} coupling are considered and the modifications to the quartic coupling are currently neglected. In order to relax these assumptions, the combined measurement of HH and HHH will provide complementary constraints.

Finally, the combination of the main HH analyses allows to set the most stringent constraint on the κ_λ coupling modification, as reported by both the ATLAS and CMS experiments in Fig. 8. A similar combination for the dominant HHH channels is expected to yield in the most stringent constraint on both λ_3 and λ_4 and probe further the potential of the Higgs field.

In summary, while the cross-section of the HHH process is ≈ 300 times smaller than the cross-section of the HH process, this unexplored process at the LHC will allow to

Table 3 Observed (expected) limit on coupling modifier of κ_λ from the ATLAS and CMS experiments. References for each measurements can be found in Table 2

Final state	ATLAS	CMS
Resolved $HH \to b\bar{b}\,b\bar{b}$	$-3.5(-5.4) < \kappa_\lambda < 11.3(11.4)$	$-2.3(-5.0) < \kappa_\lambda < 9.4(12)$
Boosted $HH \to b\bar{b}\,b\bar{b}$	-	$-9.9(-5.1) < \kappa_\lambda < 16.9(12.2)$
$HH \to b\bar{b}\,\tau\tau$	$-3.2(-2.5) < \kappa_\lambda < 9.1(9.2)$	$-1.7(-2.9) < \kappa_\lambda < 8.7(9.8)$
$HH \to b\bar{b}\,yy$	$-1.4(-2.8) < \kappa_\lambda < 7.8(6.9)$	$-3.3(-2.5) < \kappa_\lambda < 8.5(8.2)$
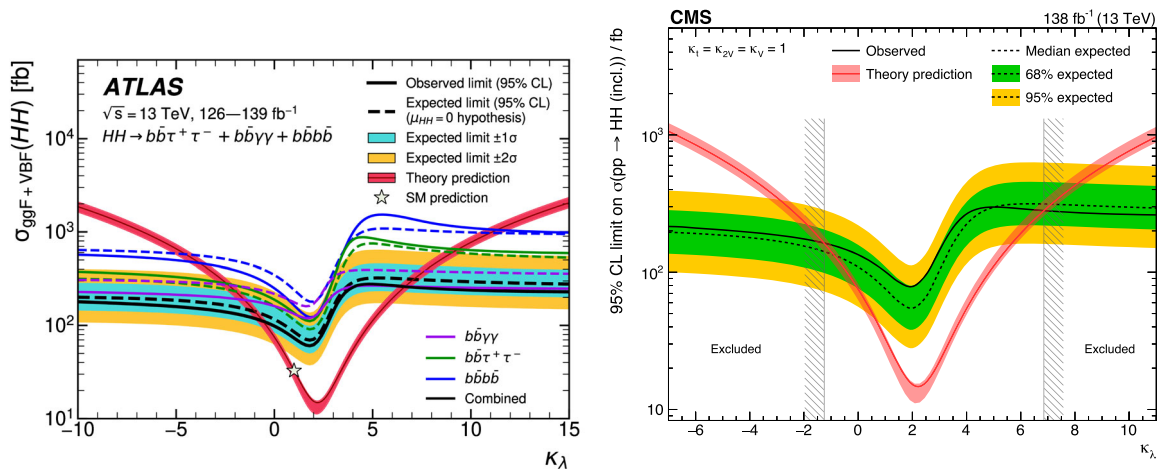
Fig. 8 Combined measurements of $HH \to b\bar{b}b\bar{b}$, $HH \to b\bar{b}\tau\tau$ and $HH \to b\bar{b}yy$ interpreted in terms of constraints on the coupling modifier κ_λ for ATLAS and CMS [3,4]

test the shape of the Higgs field potential. As both processes depend on the trilinear λ_3 and quartic λ_4 couplings, the most promising probe of the self-coupling will be obtained from a combined measurement. From an experimental point of view, the lessons learned during the HH search are the importance of boosted reconstruction techniques to select $H \to b\bar{b}$ and $H \to \tau\tau$ signatures in large-radius jets. In addition, signatures including τ-leptons provide a high signal acceptance for a lower background contamination, which in turns result in a large sensitivity. Finally, decay channels including photons y, while subject to a small branching ratio, provide excellent probes to test anomalous self-couplings of the Higgs boson, in both HH and HHH.

4 Experimental prospects and challenges

H. Arnold, G. Landsberg, B. Moser, M. Stamenkovic

4.1 Experimental thoughts

In this section, we offer a few thoughts on the best ways of tackling various experimental challenges in a search for HHH production, with the focus on LHC and HL LHC.

4.1.1 Diagrammatics

At leading order, there are exactly 100 Feynman diagrams contributing to the standard model like $pp \to HHH$ production: 50 involving the top quark mediated loops and another 50 involving the b quark mediated loops. Ignoring the latter as subdominant contributions, we could focus on the former 50 diagrams. Here by SM-like production, we mean production with SM-like diagrams, i.e., the ones that do not involve new particles, but not necessarily with the SM value of Higgs self-couplings. This is non-resonant HHH production, which results in generally falling HHH invariant mass spectrum.

These 50 diagrams can be arranged in four broad classes, as shown in Fig. 9: 24 pentagon, 18 box, 6 triangle, and 2 quartic diagrams, which generally destructively interfere with each other. The pentagon diagrams constitute the irreducible SM background, as they do not involve either trilinear (λ_3) or quartic (λ_4) Higgs self-coupling. In contrast, we will refer to the diagrams that are sensitive to either trilinear or quartic Higgs self-coupling as signal diagrams. The matrix elements of these diagrams are $\mathcal{M} \sim y_t^3$, where y_t is the top quark Yukawa coupling. The box (triangle) diagram matrix elements are $\mathcal{M} \sim y_t^2\lambda_3$ ($\mathcal{M} \sim y_t\lambda_3^2$), while the quartic diagrams matrix elements are $\mathcal{M} \sim y_t\lambda_4$. The box and
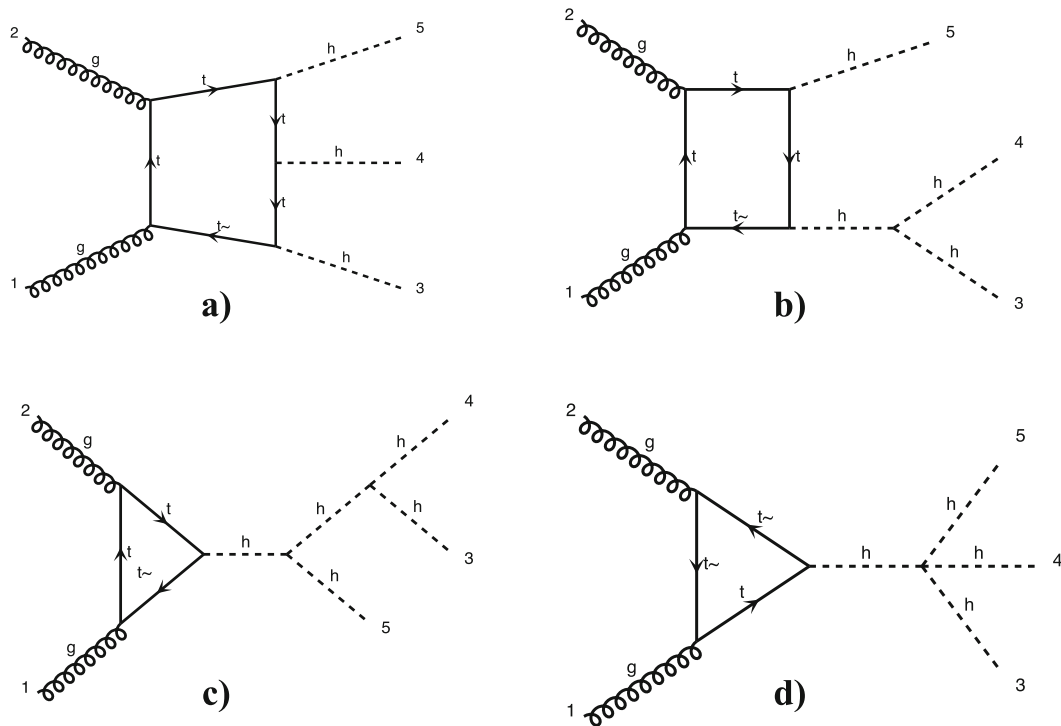
Fig. 9 Examples of four classes of leading-order diagrams contributing to the $pp \rightarrow HHH$ production: (**a**) pentagon; (**b**) box; (**c**) triangle; and (**d**) quartic

triangle diagrams interfere destructively with the SM background diagrams, while the quartic diagrams to first order do not interfere with the other three classes. Given that in the SM $\lambda_3 = \lambda_4 \approx 0.13$, the pentagon background diagrams dominate, but this is not necessarily the case when λ_3 and/or λ_4 are large. We note that while there are only 2 diagrams involving λ_4, there are 24 diagrams involving λ_3, which makes HHH production an excellent laboratory to study trilinear Higgs self-coupling.

An experimental challenge is to identify the region of phase space where box and triangular diagram contributions dominate, which could improve sensitivity to Higgs self-couplings by not only suppressing the irreducible SM background but also removing the unwanted negative interference with it.

4.2 Branching fractions

An obvious experimental question is which channels of the HHH system decay are most promising to explore at the (HL-) LHC.

Here we will use the following values of branching fractions for the major Higgs boson decay modes [140], assuming the Higgs boson mass of 125.25 GeV [141]:

– $\mathcal{B}_1 = \mathcal{B}(H \rightarrow b\bar{b}) = 57.8\%$;

– $\mathcal{B}_2 = \mathcal{B}(H \rightarrow WW) = 21.8\%$;
– $\mathcal{B}_3 = (H \rightarrow gg) = 8.17\%$;
– $\mathcal{B}_4 = \mathcal{B}(H \rightarrow \tau^+\tau^-) = 6.23\%$;
– $\mathcal{B}_5 = \mathcal{B}(H \rightarrow ZZ) = 2.68\%$; and
– $\mathcal{B}_6 = \mathcal{B}(H \rightarrow \gamma\gamma) = 0.227\%$.

First, we focus on the existing LHC data from Run 2 and assume that we are aiming at probing the HHH cross section at ~ 100 times the SM value. The next-to-next-to-leading order (NNLO) cross section for triple Higgs production was evaluated at 14 TeV [30] as ≈ 100 ab; within the precision we are interested in here, we will assume that this value also applies to the 13 TeV Run 2 center-of-mass energy. That implies that in Run 2, one would expect to produce ~ 1000 HHH events per experiment at 100 times the SM cross section, which would correspond to about 100 events after the acceptance and reconstruction efficiency in a typical decay channel (based on a typical efficiency of the HH analyses [134,137]). Even if one manages to completely suppress the background, in order to set a 95% confidence level limit on the HHH cross section, one needs an expectation of at least three observed events. That implies that any decay channel with a branching fraction of less than $\sim 3\%$ is not useful in setting such a limit with the present data set. While these channels may play an important role at the HL-LHC with a

Table 4 Leading branching fraction of the HHH system decay modes

$HHH \rightarrow 3(b\bar{b})$	$\mathcal{B}_1^3$	19.3%
$HHH \rightarrow 2(b\bar{b})\tau^+\tau^-$	$3\mathcal{B}_1^2\mathcal{B}_4$	6.24%
$HHH \rightarrow 2(b\bar{b})\tau_h\tau_h$	$3\mathcal{B}_1^2\mathcal{B}_4\mathcal{B}(\tau_h)^2$	2.62%
$HHH \rightarrow 2(b\bar{b})W^+W^-$	$3\mathcal{B}_1^2\mathcal{B}_2$	21.8%
$HHH \rightarrow 2(b\bar{b})W_hW_h$	$3\mathcal{B}_1^2\mathcal{B}_2\mathcal{B}(W_h)^2$	9.93%
$HHH \rightarrow 2(b\bar{b})W_hW_\ell$	$6\mathcal{B}_1^2\mathcal{B}_2\mathcal{B}(W_h)\mathcal{B}(W_\ell)$	6.36%
$HHH \rightarrow 2(b\bar{b})gg$	$3\mathcal{B}_1^2\mathcal{B}_4$	8.19%
$HHH \rightarrow b\bar{b}W^+W^-\tau^+\tau^-$	$3!\mathcal{B}_1\mathcal{B}_2\mathcal{B}_4$	4.7%
$HHH \rightarrow b\bar{b}W_hW_h\tau_h\tau_h$	$3!\mathcal{B}_1\mathcal{B}_2\mathcal{B}_4\mathcal{B}(W_h)^2\mathcal{B}(\tau_h)^2$	0.898%
$HHH \rightarrow b\bar{b}gg\tau^+\tau^-$	$3!\mathcal{B}_1\mathcal{B}_3\mathcal{B}_4$	1.77%
$HHH \rightarrow b\bar{b}gg\tau_h\tau_h$	$3!\mathcal{B}_1\mathcal{B}_3\mathcal{B}_4\mathcal{B}(\tau_h)^2$	0.741%
$HHH \rightarrow 2(b\bar{b})ZZ$	$3\mathcal{B}_1^2\mathcal{B}_5$	2.69%
$HHH \rightarrow 2(b\bar{b})Z_hZ_h$	$3\mathcal{B}_1^2\mathcal{B}_5\mathcal{B}(Z_h)^2$	1.31%
$HHH \rightarrow b\bar{b}gggg$	$3\mathcal{B}_1\mathcal{B}_3^2$	1.16%
$HHH \rightarrow b\bar{b}2(\tau^+\tau^-)$	$3\mathcal{B}_1\mathcal{B}_4^2$	0.673%
$HHH \rightarrow 2(b\bar{b})\gamma\gamma$	$3\mathcal{B}_1^2\mathcal{B}_6$	0.228%

full 3 ab^{-1} data set, for practical purposes, we will ignore such channels for now.

Table 4 lists leading branching fractions of various experimentally feasible HHH decays. We will use the following branching fractions for the dominant decays of the τ leptons, and W and Z bosons: $\mathcal{B}(\tau_h) = \mathcal{B}(\tau \rightarrow \text{hadrons}) = 64.8\%$, $\mathcal{B}(W_h) = \mathcal{B}(W \rightarrow q\bar{q}') = 67.4\%$, $\mathcal{B}(W_\ell) = \mathcal{B}(W \rightarrow e^+e^- + \mu^+\mu^-) = 21.6\%$, and $\mathcal{B}(Z_h) = \mathcal{B}(Z \rightarrow q\bar{q}) = 69.9\%$.

It is quite obvious from this table that the decay modes with two photons, two Z bosons, or four τ leptons are hopeless with the currently available data. It is further clear that one should instead focus on the all-hadronic channels, as those are the only ones that have sufficiently high branching fraction. The only exception is the $HHH \rightarrow 2(b\bar{b})W_hW_\ell$ channel that has a branching fraction of 6.36%, but unfortunately this channel does not have a mass peak in the invariant mass distribution of the visible part of the W^+W^- system decay, so it would be quite challenging (but perhaps worth a second look!). Focusing only on the all-hadronic channels, one can see that it is completely dominated by the $4b+$ jets decays, which comprise 40% of all HHH decays. This is a great news, as we recover 40% of possible decays in the channel that has been experimentally proven to be feasible through the $pp \rightarrow HH \rightarrow bb\bar{b}\bar{b}$ searches. Requiring at least two extra jets (and further splitting into categories with extra jets being b- or τ_h-tagged) is certainly a less challenging signature with lower backgrounds than the inclusive $bb\bar{b}\bar{b}$ channel, so one could use the background suppression and evaluation techniques developed in the $H(b\bar{b})H(b\bar{b})$ analyses to search for triple Higgs boson production with high efficiency and acceptance.

Thus, the all-hadronic $bb\bar{b}\bar{b}+$ jets channels is most promising to establish first limits on the HHH production with Run 2 and Run 3 data.

4.2.1 Boost or bust!

We now focus on the $HHH \rightarrow 3(b\bar{b})$ channel, which comprises about half of the inclusive $bb\bar{b}\bar{b}+$ jets branching fraction. In this case, the combinatorics related to pairing of 6 b-tagged jets to match the three Higgs boson candidates becomes quite tedious. The number of possible pairings of 6 b-tagged jets is equal to $C_6^2 C_4^2 C_2^2/3! = 15 \times 6 \times 1/6 = 15$ combinations, making it hard to reconstruct individual Higgs bosons reliably.

This is where the jet merging comes to rescue! It turns out that the Higgs bosons in the HHH production are produced with quite significant transverse momentum p_T, as shown in Fig. 10. The distributions for the two leading Higgs boson peak well above 100 GeV, and even for the trailing Higgs boson the median is about 100 GeV. (This is not surprising, as the signal diagrams with trilinear coupling are t-channel-like with either the Higgs boson or the top quark as a t-channel propagator, so the characteristic p_T of the leading Higgs boson or the recoiling di-Higgs system on the other side is of order of the mass of the propagator, i.e., ~ 150 GeV.) This implies that it is very likely that at least one of the Higgs bosons within the HHH system has a significant Lorentz boost, resulting in its decay products (a b quark-antiquark pair) to be reconstructed as a single, merged jet, J. Indeed, on average, the opening angle between the two decay products of a Lorentz-boosted resonance is given by $\theta = 2/\gamma$, where γ is the Lorentz boost. For a Higgs boson with a $p_T^H = 250$ GeV, the γ factor is 2, so the opening angle is 1 radian. This is similar to a radius parameter of the jet reconstruction used for merged jet analyses (between 0.8 and 1.5).
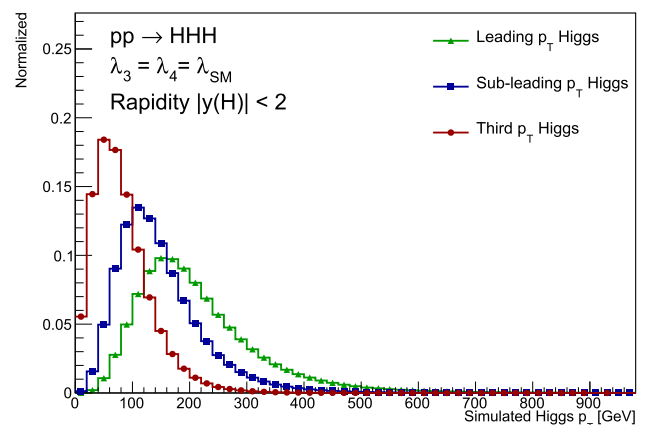

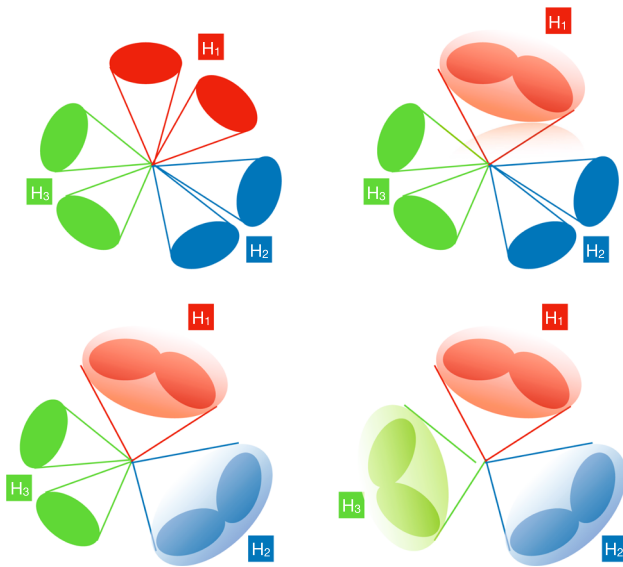**Fig. 10** Transverse momentum p_T^H spectrum of the Higgs bosons in SM triple Higgs boson production

Fig. 11 Schematics of the reconstruction of the $HHH \to 3(b\bar{b})$ system with (upper left to lower right) 0, 1, 2, and 3 Higgs boson decaying into a merged jet topology

In the last decade or so, a number of powerful techniques to distinguish such merged jets with a distinct two-prong substructure from regular QCD jets have been developed, which allow for an effective reduction of backgrounds in a boosted topology. (Indeed, the boosted topology is shown to be the most sensitive in the $HH \to bb\bar{b}\bar{b}$ searches [4].) In addition to a powerful background suppression, the boosted topology in the HHH case carries additional benefits: if just one of the Higgs bosons decays into a merged jet, the number of possible jet permutations decreases from 15 to $C_4^2 C_2^2 / 2! = 6 \times 1/2 = 3$, and if at least two Higgs bosons are reconstructed as merged jets, there is only one possible permutation, as illustrated in Fig. 11 (as long as we do not distinguish the individual Higgs bosons)!

The situation becomes even more advantageous for the beyond-the-SM scenarios where the HHH system is produced via resonance decays. For example, in a two real singlet extension of the SM [50], the following process results in a triple Higgs boson production: $pp \to h_3 \to h_2 h_1 \to h_1 h_1 h_1$, where h_1 is the SM Higgs boson ($h_1 = H$) and $h_{2,3}$ are the extra scalars. For a typical benchmark with the h_3 mass of 500 GeV and h_2 mass of 300 GeV, the $pp \to HHH$ production cross section is enhanced by 2.5 orders of magnitude to ~ 40 fb, while the relatively high mass of h_3 guarantees a large Lorentz boost of the produced Higgs bosons!

As a side remark, generally this and related extensions of the SM should result in resonant production of HHH, VHH, and VVH systems, with $V = W$ or Z boson. At the LHC, the program of searches for triple-boson resonances is still in its infancy, so it would be very advantageous to mount a broad search for resonant decays into VHH and

VHH topologies, in addition to the HHH studies, which are the focus of this paper.

Requiring one or two of the Higgs bosons to be reconstructed as merged jets with two-prong b jet substructure by employing a large-radius jet algorithm with the radius parameter of about 1.0 offers a powerful way to deal with combinatorics in the $HHH \to 3(b\bar{b})$ decays.

4.3 HHH estimated sensitivities at the LHC

The current consensus in the ATLAS and CMS collaborations is that a measurement of the quartic coupling is out of reach. As a consequence, there is currently no estimate of the sensitivity to the triple Higgs production at the LHC. However, from various studies performed by theorists for future colliders, one can estimate the sensitivity range for HHH. The predictions at future colliders assume a center of mass energy of $\sqrt{s} = 100$ TeV and each prediction focuses on a specific decay mode such as $HHH \to b\bar{b}b\bar{b}b\bar{b}$ [142], $HHH \to b\bar{b}b\bar{b}\gamma\gamma$ [143] and $HHH \to b\bar{b}b\bar{b}\tau^+\tau^-$ [144]. A basic event selection is applied, usually similar to the ones used in experimental measurements.

In order to obtain an estimated result at the LHC, the significance is scaled with respect to the luminosity ratio and the difference in the predictions of the cross-sections. The difference in the cross-section of the signal is a factor $\sigma(HHH)_{13\text{TeV}} / \sigma(HHH)_{100\text{TeV}} = 1/60$ [145]. As the background processes for these different modes can vary, two scenarios are investigated: an optimistic scaling using the same reduction as the signal (1/60) and a pessimistic scaling assuming a reduction factor of 1/10 for the background processes only, which corresponds to the ratio of cross-sections for the QCD multi-jet production with 6 b-quarks in the final state. This assumption is not optimal for the $HHH \to b\bar{b}b\bar{b}\gamma\gamma$ and $HHH \to b\bar{b}b\bar{b}\tau^+\tau^-$ decay modes but it captures the general trend that the background production should be lower at $\sqrt{s} = 13$ TeV.

A sensitivity estimate at the LHC is presented in the Table 5 for the main decay modes as well as a potential combination. The combination leads to a sensitivity of 60–150 times the SM prediction. In order to obtain this result, several challenges will have to be resolved. In particular the choice of the trigger, the control and reduction of the background processes as well as the estimation of the systematic uncertainties will need to be studied in details.

While the result of the combination indicates that the evidence for the HHH production might be achieved at a future collider, this result can be improved with more sophisticated analyses techniques than the simple selections applied in the theory studies. These measurements could strongly benefit continuous improvement in b-jets and τ-leptons identification as well as analyses design relying on modern machine learning developments. The projections assuming a scaling

Table 5 Extrapolation of the main triple Higgs decay modes to the Large Hadron Collider. The results are presented in terms of the limit on the signal strength at 95% confidence level. The pessimistic scaling assumes a reduction of a factor 10 in the background similar to the reduction of the cross-section of the multijets process with 6 b-quarks. The optimistic scaling assumes a reduction of 60 similar to the signal

Channel	$\mathcal{L}$ at 100 TeV	Significance	$\mathcal{L}$ at 13 TeV	Pessimistic	Optimistic
$HHH \rightarrow b\bar{b}b\bar{b}b\bar{b}$ [142]	20 ab^{-1}	1.6σ	139 fb^{-1}	285$\times$ SM	120$\times$ SM
$HHH \rightarrow b\bar{b}b\bar{b}\gamma\gamma$ [143]	20 ab^{-1}	2.1σ	139 fb^{-1}	220$\times$ SM	90$\times$ SM
$HHH \rightarrow b\bar{b}b\bar{b}\tau^+\tau^-$ [144]	30 ab^{-1}	2.0σ	139 fb^{-1}	280$\times$ SM	115$\times$ SM
Combination	20 ab^{-1}	2.9σ	139 fb^{-1}	150$\times$ SM	64$\times$ SM

Table 6 Estimated limit on the triple Higgs production from a combination of the $HHH \rightarrow b\bar{b}b\bar{b}b\bar{b}$, $HHH \rightarrow b\bar{b}b\bar{b}\tau^+\tau^-$ and $HHH \rightarrow b\bar{b}b\bar{b}\gamma\gamma$ at 95% confidence level for different luminosities at a center-of-mass energy of $\sqrt{s} = 13$ TeV

$\mathcal{L}$ at 13 TeV	Pessimistic	Optimistic
139 fb^{-1}	150$\times$ SM	64$\times$ SM
300 fb^{-1}	100$\times$ SM	40$\times$ SM
500 fb^{-1}	80$\times$ SM	35$\times$ SM
3000 fb^{-1}	30$\times$ SM	15$\times$ SM

with the luminosity expected to be achieved in Run 2, Run 3 and the High-Luminosity LHC is shown in Table 6. The ATLAS and CMS experiments at the LHC are the only detectors in the world capable of probing electro-weak symmetry breaking through searches for the HHH process.

4.4 Complementary between ongoing HH searches and future HHH searches

As shown in Sect. 3, for multi Higgs boson production, the connection between Higgs boson multiplicity and contributing coupling modifiers is non-trivial: HH and HHH production are both affected by the trilinear coupling modifier κ_3 and the quartic coupling modifier κ_4. A combined experimental picture is therefore desirable.

Through a combination of multiple search channels, the ATLAS experiment limits the signal strength of HH production μ_{HH} to be <2.4 times the SM prediction at the 95% confidence level, where 2.9$\times$SM is expected [5]. The CMS experiment reaches similar sensitivity with an observed limit of $\mu_{HH} < 3.4\times$SM where 2.5$\times$SM is expected in the absence of any signal [4].

In this section we present expected limits on κ_3 and κ_4 based on extrapolations of the expected ATLAS HH results, scaled to an integrated luminosity of 450 fb^{-1}. For HHH production, limits have been estimated extrapolating existing phenomenological studies [31,35,37] to LHC energies, similar to the previous section. The κ limits presented in this section are purely based on re-interpretations of the signal strength limits and neglect any change in the event kinematics

induced by anomalous κ_3 and κ_4 values. In the case of κ_3 and HH production for example, this assumption has its limitations as large values of κ_3 make the m_{HH} spectrum softer and the signal-to-background ratio is lower at low m_{HH} [21,146]. Therefore the results in this section are to be seen as qualitative statements. The purpose of these studies is to highlight the complementary between the two channels and to advocate for a more thorough study within the experiments, taking the kinematic changes fully into account.

To calculate likelihood values, the HH and HHH signal strengths are parameterised as a function of $\Delta\kappa_3 = (\kappa_3 - 1)$ and $\Delta\kappa_4 = (\kappa_4 - 1)$ based on [33,147]:

$$
\begin{aligned}
\mu_{HH}^{14\,\mathrm{TeV}} &= 1 - 0.867(\Delta\kappa_3) + 1.48 \cdot 10^{-3}(\Delta\kappa_4) + 0.329(\Delta\kappa_3)^2 \\
&\quad + 7.80 \cdot 10^{-4}(\Delta\kappa_3\Delta\kappa_4) + 2.73 \cdot 10^{-5}(\Delta\kappa_4)^2 \\
&\quad - 1.57 \cdot 10^{-3}(\Delta\kappa_3)^2(\Delta\kappa_4) \\
&\quad - 1.90 \cdot 10^{-5}(\Delta\kappa_3)(\Delta\kappa_4)^2 + 9.74 \cdot 10^{-6}(\Delta\kappa_3)^2(\Delta\kappa_4)^2 \\
\mu_{HHH}^{14\,\mathrm{TeV}} &= 1 - 0.921(\Delta\kappa_3) + 0.091(\Delta\kappa_4) + 0.860(\Delta\kappa_3)^2 \\
&\quad - 0.168(\Delta\kappa_3\Delta\kappa_4) + 1.71 \times 10^{-2}(\Delta\kappa_4)^2 - 0.258(\Delta\kappa_3)^3 \\
&\quad + 4.91 \times 10^{-2}(\Delta\kappa_3)^2\Delta\kappa_4 + 4.13 \times 10^{-2}(\Delta\kappa_3)^4 \quad .
\end{aligned}
$$

As can be seen, the HH signal strength, for example, depends only weakly on the quartic coupling as it intervenes at a two-loop level. While the absolute cross-section values are $\sqrt{s}$ dependent, the signal strength parameterisations show little dependence on the assumed $\sqrt{s}$. The estimated constraints are shown in Fig. 12 in the two-dimensional κ_3-κ_4 plane. The plot highlights the complementary between the two searches.

One dimensional likelihood contours are shown for κ_3 in Fig. 13 and for κ_4 in Fig. 14. For each of those contours the coupling modifier that is not shown is profiled over. By taking into account also the effect of κ_4 on HH production, one can derive limits on κ_3 that do not rely on any assumption on the relationship between κ_3 and κ_4 and therefore gain model independence. Furthermore, a $HH + HHH$ combination adds information to the constraint on κ_3. This is even more so the case for κ_4, where the combination significantly improves over the constraints from HHH production alone when κ_3 is profiled over.
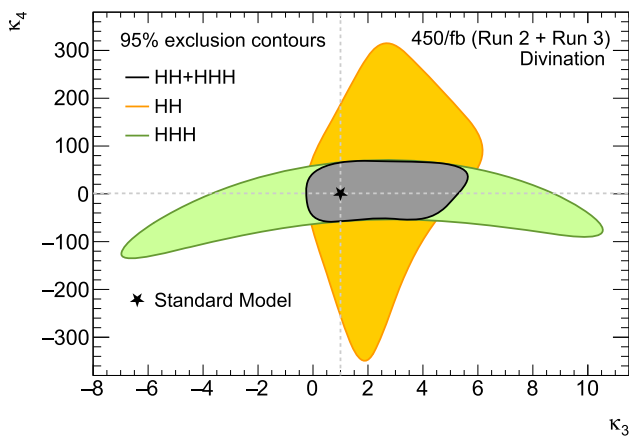
Fig. 12 Estimated likelihood contours at the 95% confidence level in the κ_3 and κ_4 plane from searches for HH, HHH, and a combination
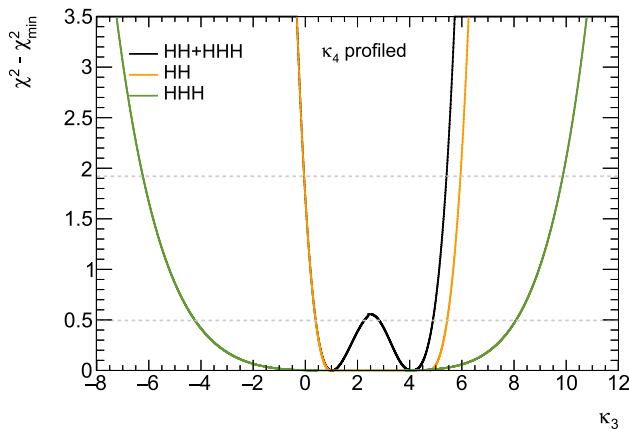

Fig. 13 Projected constraints on κ_3 without assumptions on κ_4 from searches for HH, HHH, and a combination of both searches. The estimates are based on a total integrated luminosity of 450 fb^{-1} at $\sqrt{s} = 14$ TeV
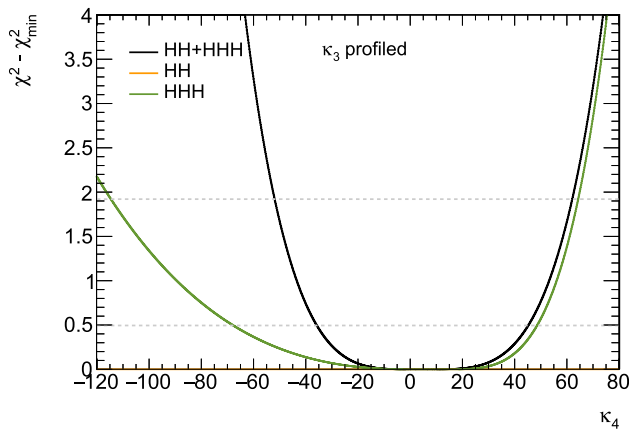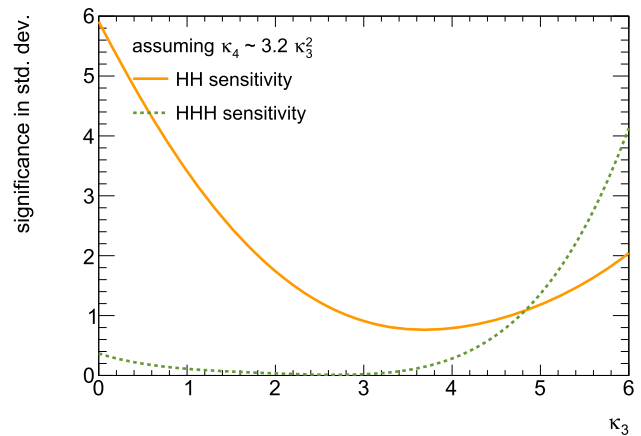

Fig. 14 Projected constraints on κ_4 without assumptions on κ_3 from searches for HH, HHH, and a combination of both searches. The estimates are based on a total integrated luminosity of 450 fb^{-1} at $\sqrt{s} = 14$ TeV

Fig. 15 Estimated sensitivity of HH and HHH searches to a model where $\kappa_4 = 3.2\kappa_3^2$ as a function of κ_3. The estimates are based on a total integrated luminosity of 450 fb^{-1} at $\sqrt{s} = 14$ TeV

The complementary between HH and HHH searches is further illustrated by looking at scenarios where κ_3 and κ_4 follow a specific relation, in this case assuming $\kappa_4 = 3.2\,\kappa_3^2$. Such a relation would not violate vacuum stability conditions requiring $\kappa_4 \leq \tfrac{9}{8}\,\kappa_3^2$ [148]. Figure 15 shows the estimated significance with which such a model would show up in HH and HHH searches, respectively. In this scenario, a search for HHH would be equally sensitive as a HH search for larger values of κ_3 that are currently not yet excluded by experiment.

In conclusion, the complementarity between HH and HHH searches in constraining the trilinear and quartic Higgs boson self-coupling calls for a combination that will allow to determine the shape of the Higgs potential more precisely and with less assumptions. With these studies we hope to trigger more realistic sensitivity estimations, taking into account also signal kinematic changes and refined background contamination estimates. The dependence of HH on κ_3 and κ_4, for example, can be simulated with publicly available POWHEG code from Ref. [147].

5 Machine learning prospects in di-Higgs events

D. Diaz, J. Duarte, S. Ganguly, B. Sheldon

5.1 Introduction

The di-Higgs production via vector boson fusion (VBF) processes at hadron colliders has been broadly studied in the theory literature [8,149–153], and only recently investigated experimentally [135,154]. Current projections [155] achieve an expected significance of approximately $4.0\,\sigma$ from CMS and ATLAS combined for the full HL-LHC data set. Measurements of Higgs boson pair production face the difficulty

of the small expected event yields even for the mode with the largest branching fraction ($b\bar{b}b\bar{b}$) as well as the presence of similar reconstructed QCD multijet events, which occur far more often. However, these projections do not include dedicated analyses of highly boosted hadronic final states, which may be especially sensitive to the SM and anomalous Higgs couplings [156].

If the Higgs boson is highly Lorentz boosted, its hadronic decay products can be reconstructed as one single jet and the jet can be tagged using jet substructure techniques [121, 122, 157, 158]. Moreover, several machine learning methods have also been demonstrated to be extremely efficient in jet tagging and jet reconstruction [159]. In the present work, we adopt ML algorithms to analyze boosted di-Higgs production in the four-bottom-quark final state at the FCC-hh, which is expected to produce hadron-hadron collisions at $\sqrt{s} = 100$ TeV and to deliver an ultimate integrated luminosity of 30 ab^{-1}. We compare our ML-based event selection to a reference cut-based selection [160] to demonstrate potential gains in sensitivity. The rest of the section is organized as follows. In Sects. 5.2 and 5.3, we illustrate the potential of boosted Higgs channels based on the expected yields and introduce the ML methods. In Sect. 5.4, we describe the reference cut-based analysis and in Sect. 5.5, we explain our ML-based analysis. Finally, we provide a summary and outlook in Sect. 5.6.

5.2 Boosted Higgs

The hadronic final states of the Higgs boson are attractive because of their large branching fractions relative to other channels. While the $b\bar{b}\gamma\gamma$ "golden channel" has a 0.26% branching fraction, the $b\bar{b}b\bar{b}$ and $b\bar{b}WW$ channels have a combined 58.8% branching fraction, which often produce a fully hadronic final state. At low transverse momentum (p_T), these final states are difficult to disentangle from the background, but at high p_T, the decay products merge into a single jet, which new ML methods can identify with exceptionally high accuracy. Even with a requirement on the p_T of the Higgs boson, the hadronic final states are still appealing in terms of signal acceptance. The efficiency of the $p_T > 400$ GeV requirement on both Higgs bosons is about 4% at the LHC. Thus, the boosted $b\bar{b}b\bar{b}$ ($b\bar{b}WW$) channel with $p_T > 400$ GeV has 5.2 times (4.3 times) more signal events than the "golden" $b\bar{b}\gamma\gamma$ channel at the LHC. Given the higher center-of-mass energy of the FCC-hh, the boosted fraction would increase.

Based on our preliminary investigations and existing LHC Run 2 results, these boosted channels are competitive with the $b\bar{b}\gamma\gamma$ channel, which corresponds to an expected significance of 2.7 standard deviations (σ) with the full ATLAS and CMS HL-LHC data set. As such, exploring these additional

final states with new methods will be crucial to achieving the best possible sensitivity to the Higgs self-coupling.

5.3 Machine learning for di-Higgs searches

Emerging ML techniques, including convolutional neural networks (CNNs) and graph neural networks (GNNs) [161–163], have enabled better identification of these boosted Higgs boson jets while reducing the backgrounds [127, 164–168]. CNNs treat the jet input data as either a list of particle properties or as an image. In the image representation case, CNNs leverage the symmetries of an image, namely translation invariance, in their structure. Deeper CNNs are able to learn more abstract features of the input image in order to classify them correctly. GNNs are also well-suited to these tasks because of their structure, and have enjoyed widespread success in particle physics [169–171]. GNNs treat the jet as an unordered graph of interconnected constituents (nodes) and learn relationships between pairs of these connected nodes. These relationships then update the features of the nodes in a *message-passing* [172] or *edge convolution* [163] step. Afterward, the collective updated information of the graph nodes can be used to infer properties of the graph, such as whether it constitutes a Higgs boson jet. In this way, GNNs learn pairwise relationships among particles and use this information to predict properties of the jet.

Significantly, it has been shown that these ML methods can identify several classes of boosted jets better than previous methods. For instance these methods have been used to search for highly boosted H($b\bar{b}$) [173] and VH($c\bar{c}$) [174] in CMS. Most recently, they have also been shown to enable the best sensitivity to the SM HH production cross section and to the quartic VVHH coupling in CMS using the LHC Run 2 data set [175]. In this work, we study the impact of the use of these ML algorithms in future colliders like the FCC-hh.

5.4 Reference cut-based event selection

For the cut-based reference selection, we follow Refs. [160, 176]. In particular, we study the configuration in which the Higgs boson pair recoils against one or more jets. We use the DELPHES-based [177] signal and background samples from Ref. [178]. The signal sample of HH+jet is generated taking into account the full top quark mass dependence at leading order (LO) with the jet p_T greater than 200 GeV. Higher-order QCD corrections are accounted for with a K-factor $K = 1.95$ applied to the signal samples [176], leading to $\sigma_{HHj} = 38$ fb for jet $p_T > 200$ GeV and $\kappa_\lambda = 1$. The main background includes at least four b-jets, where the two $b\bar{b}$ pairs come from QCD multijet production, mainly from gluon splitting g $\to$ $b\bar{b}$. The LO background cross section for jet $p_T > 200$ GeV is given by $\sigma_{b\bar{b}b\bar{b}j}$ (QCD) = 443.1 pb.

Jets are reconstructed with the anti-k_T [74,179] algorithm with a radius parameter $R = 0.8$ (AK8) and $R = 0.4$ (AK4). The AK8 jets are formed from calorimeter energy clusters whereas the AK4 jets are formed from track elements.

We require two AK8 jets with $p_T > 300$ GeV and $|\eta| < 2.5$. The AK8 jets are considered double b-tagged if they contain two b-tagged AK4 subjets. This AK4 b-tagging emulation corresponds to a conservative signal efficiency of 70%. The two highest p_T double b-tagged AK8 jets constitute the Higgs boson candidates. We further require the AK8 dijet system to be sufficiently boosted, $p_T^{jj} > 250$ GeV, and the leading jet to have a $p_T > 400$ GeV. The jet p_T and soft-drop mass m_{SD} [180] distributions are shown in Fig. 16, along with the N-subjettiness ratio $\tau_{21} = \tau_2/\tau_1$ [181]. The two Higgs boson candidate AK8 jets are tagged by selecting jets with $\tau_{21} < 0.35$ and $100 < m_{SD} < 130$ GeV.

After the selections, the expected signal (S) and background (B) yields for 30 ab^{-1} are 12,700 and 49,900,000 events, yielding an approximate significance $S/\sqrt{B} = 1.8$. The signal and background efficiencies of the cut-based selection are 1.7% and 0.53%, respectively.

5.5 Graph neural network event selection

We build a boosted HH $\to$ b$\bar{\text{b}}$b$\bar{\text{b}}$ event classifier using a GNN based on the features of all the AK4 and AK8 jet constituents (tracks and calorimeter clusters, respectively) in the event, as well as additional jet features. We stress that this approach, an event-level classifier using the information provided in the FCC-hh samples, is conservative as we expect the largest gains in signal-to-background discrimination to arise from including lower-level detector information, including tracking and vertexing information. Nonetheless, we can still compare this approach with a cut-based selection with access to similar information.

To define the input graph data structure or *point cloud*, each of the jet constituents is treated as a node with its associated pseudorapidity (η) and azimuthal angle (ϕ) as coordinates. The event can then be thought of as a two-dimensional point cloud. A graph is then formed using the k-nearest neighbor (kNN) algorithm in the η-ϕ plane. Each node has four features, namely the four components of the energy–momentum Lorentz vector. We augment this node representation with three additional variables related to the jet as a whole. In particular, we include the two- and one-subjettiness (τ_2 and τ_1) as well as b-tagging probability. Hence this construction associates a feature vector of size 7 to each node.

For the GNN architecture operation, we use the dynamic edge convolution. The original idea was proposed for shape classification [163], and was also used for jet classification [127]. The message-passing (MP) operation, referred to as *EdgeConv*, from layer ℓ to layer $\ell+1$ consists of the following operations

$$x_i^{\ell+1} = \max_{j \in \mathcal{N}(i)} \left(\Theta_x(x_j^\ell - x_i^\ell) \right) + \Phi_x(x_i^\ell), \tag{7}$$

$$e_i^{\ell+1} = \frac{1}{|\mathcal{N}(i)|} \left(\sum_{j \in \mathcal{N}(i)} \Theta_e(e_j^\ell - e_i^\ell) \right) + \Phi_e(e_i^\ell), \tag{8}$$

where $\mathcal{N}(i)$ is the neighborhood of objects connected to object i, $|\mathcal{N}(i)|$ is the number of neighboring objects, x_i^ℓ are the features of node i at layer ℓ, and e_i^ℓ are the features of edge i at layer ℓ.

The implemented model has four such MP layers. The output dimensions of the x coordinate after each layers are 3, 5, 4, and 2, respectively, whereas the dimensions of the variable e are chosen to be 4, 5, 6, and 8, respectively. The energy outputs of each layers are concatenated and passed though a MLP block to predict the output probability of the given event. The model is trained using a binary crossentropy loss for the classification task. The signal events correspond to simulated HH(b$\bar{\text{b}}$b$\bar{\text{b}}$) events, while background events are from simulated QCD multijet production with four bottom quarks. The optimizer used is Adam [182] with a fixed learning rate of 10^{-3}. For training purposes we have used 50k events for training data and 10k events for validation data with batch size of five.

The output of the trained network is evaluated on an independent test sample of signal and background and the logarithm of the signal-like event probability is shown in Fig. 17. The distribution demonstrates that a trained network can separate the signal from background. The level of discrimination is quantified by the receiver operating characteristic (ROC) curve shown in Fig. 18. This preliminary training can identify signal with 40% efficiency at the background efficiency level of 9%. Compared to the cut-based selection, the event-level GNN can identify HH(b$\bar{\text{b}}$b$\bar{\text{b}}$) signal events with an efficiency of about 6.1% for the same background efficiency of 0.53%, corresponding to a factor of 3 improvement. This leads to a signal efficiency $S/\sqrt{B} = 8.3$.

5.6 Summary and outlook

In summary, we have investigated the feasibility of observing the production of a pair of boosted Higgs bosons in hadronic final states at the Future Circular Collider in hadron mode (FCC-hh) and improving the sensitivity with ML techniques. The data sets simulated with DELPHES corresponds to a center-of-mass energy $\sqrt{s} = 100$ TeV and an integrated luminosity of 30 ab^{-1} We focused on the four-bottom-quark final state, in which the each b$\bar{\text{b}}$ pair is reconstructed as a large-radius jet. We have studied the sensitivity using a traditional cut-based analysis as well as a selection based on an event classifier built using a graph neural network (GNN), as
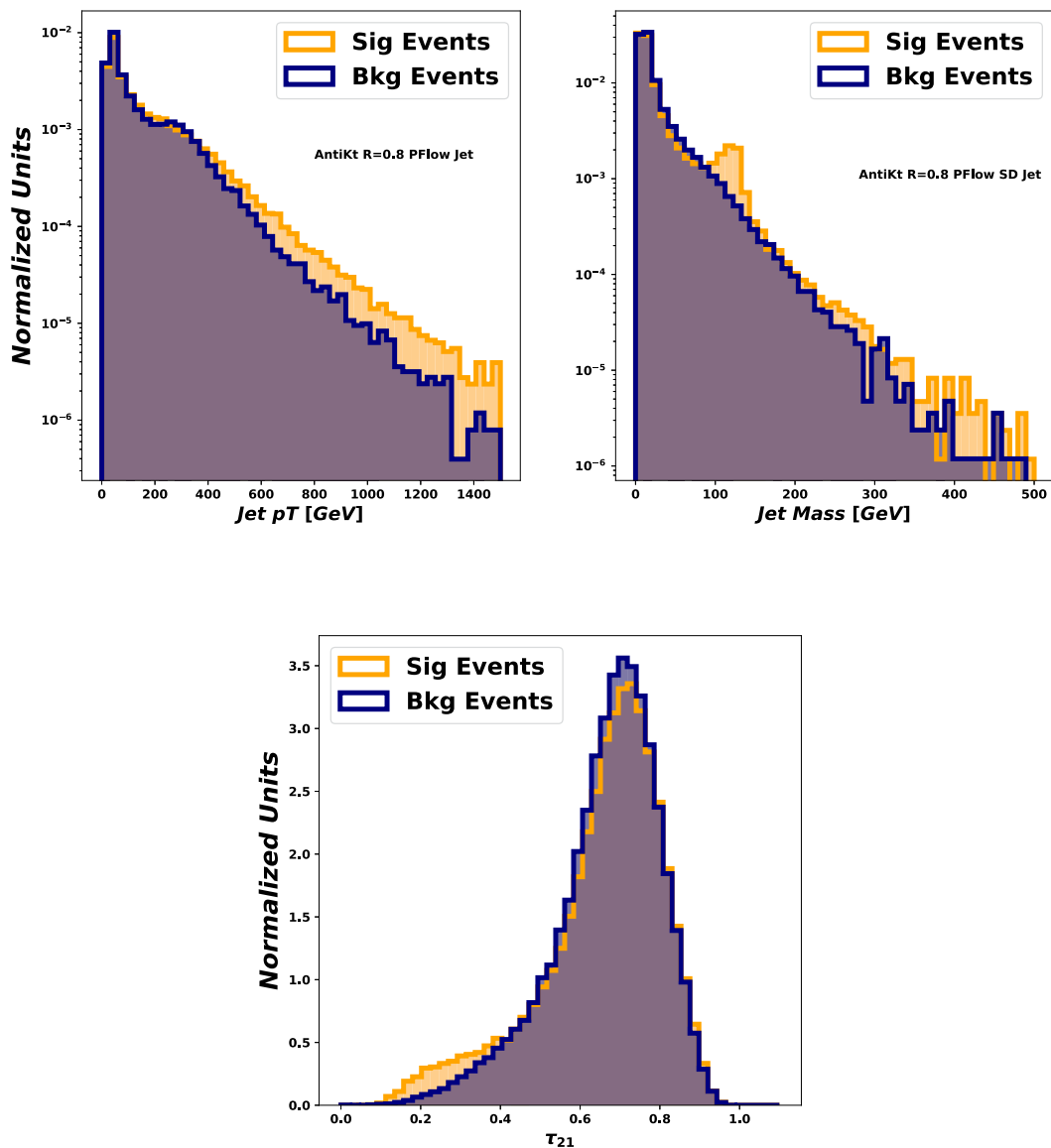
Fig. 16 Jet p_T (upper left), soft-drop mass (upper right), τ_{21} (bottom) and distribution of anti-k_T $R = 0.8$ PF jets for signal and background events. The shape difference plays a crucial role in identifying signal events over background

described in Sect. 5.5. For the cut-based analysis, we leveraged the jet kinematics, substructure variables, and b-tagging for the two leading jets in the event. For the GNN, we used lower level information, such as the jet constituents' four-momenta, as well as high-level jet substructure and b-tagging variables. We established that a better sensitivity by a factor of 3 is achievable using the GNN as shown in Fig. 18.

Higgs boson pair production is a crucial process to characterize and measure precisely at future colliders. In order to do so with the best precision possible, it is important to exploit all possible production and decay modes. This includes the high-p_T hadronic final states, such as $b\bar{b}b\bar{b}$, $W(q\bar{q})W(q\bar{q})b\bar{b}$, $W(q\bar{q})W(\ell\nu)b\bar{b}$, and $b\bar{b}\gamma\gamma$, whose sensitivity can be improved with ML methods. Beyond H jet clas-

sification, particle reconstruction [183–185], and jet reconstruction [186], and jet mass regression [187] algorithms can also be improved with ML.

Fully quantifying the impact of ML for these final states on the ultimate sensitivity achievable for the HH cross section, H self-coupling, trilinear VVH coupling, and quartic VVHH coupling are important goals of future work. Another important future deliverable is to consider how these ML methods may impact optimal detector design. In this context, explainable AI methods [188] can be developed to understand the physics learned by the networks, and fully exploit this in future detector design. Future work can also explore the impact of using symmetry-equivariant networks [189,190] for Higgs boson property measurements at future colliders.
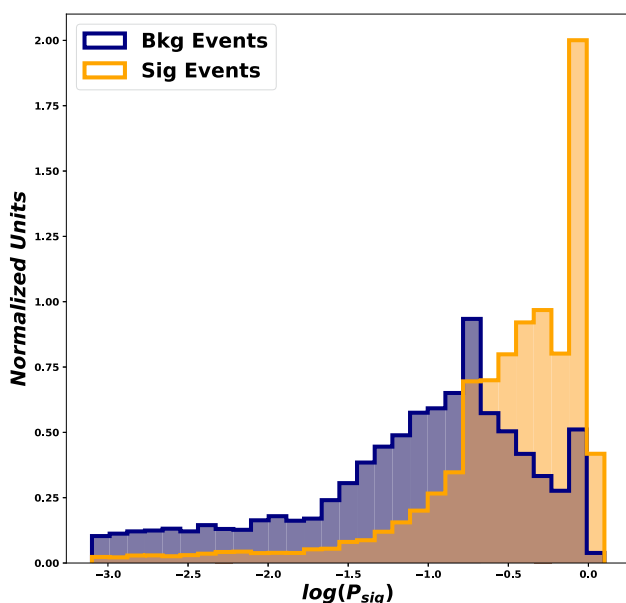
Fig. 17 The distribution of natural logarithm of the events of being signal like, evaluated on the signal and background samples, respectively
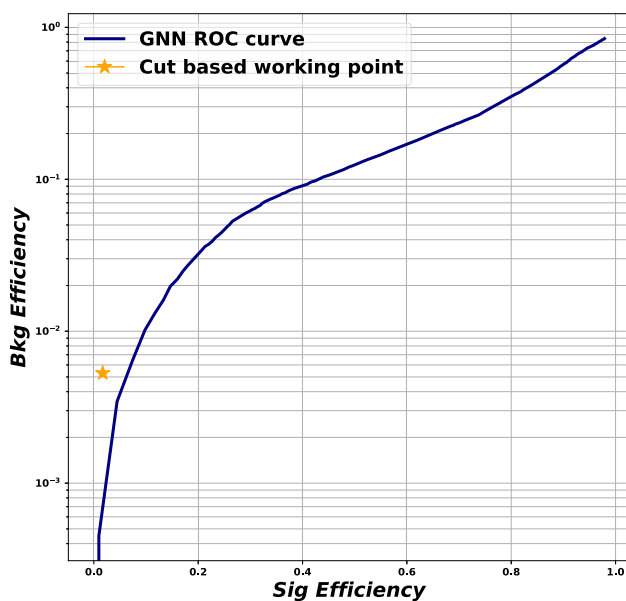
Fig. 18 The ROC curve showing the ability of the NN to discriminate between signal and background. With the preliminary study we achieve a signal efficiency of around 40% for a background efficiency of 9%

Future colliders will be able to probe the quartic interaction vertex of SM Higgs by producing three on-shell Higgs boson in the final state. In presence of dominant background, reconstruction of three individual Higgs boson candidates is a complex combinatorial task. The GNN methods, discussed in this section, can be of particular usage for this case. As in the case of HH, the events from HHH decay can be represented as a graph as well. Henceforth, the methods we demonstrated

in this section are equally applicable for the reconstruction of HHH events. There are ample opportunities to venture hetero-graph methods in the context of HHH event reconstructions, where each H can decay into a particular mode and different nodes of the heterograph may represent different physics objects (like jets, γ, leptons etc.). In case of semi-boosted or boosted event topologies with partial overlaps of these objects, sub-graph based methods have further potential which needs to be ventured. GNN based methods are already playing a mainstream role in HH searches and bound to take the center-stage in all upcoming HHH searches.

6 Flavour tagging

M. Chen, O. Karkout, M. Kolosova, B. Liu

6.1 Introduction

As discussed in Sect. 4.2, channels involving $H \rightarrow b\bar{b}$ decays give rise to the most promising channels to search for multiple Higgs-like particles, due to the much larger branching ratios. Therefore, the technique to identify jets containing b-hadrons is instrumental for this search programme.

Compared to lighter hadrons, b-hadron decays have very distinguishable characteristics. A b-hadron can travel for up to a few millimeters in the detector before decaying, because of its longer lifetime and the typical Lorentz boost expected at the LHC. It results in tracks and vertices that are away from the interaction point. They are referred to as "displaced tracks" and "displaced vertices". Because of its heavier mass, there is a larger number of tracks from b-hadron decays. In addition, a b-hadron can decay to a c-hadron that subsequently travels for an additional distance in the detector before decaying. Therefore, typically one expects a Secondary Vertex (SV) from b-hadron decay and a tertiary vertex from the c-hadron decay. Last but not the least, the semileptonic branching ratio of b-hadrons is larger than that of lighter hadrons, leading to a higher probability of having a lepton in the decay chain.

A flavour tagging algorithm explores the above unique features of b-hadron decays, aiming at identifying jets containing b-hadrons, i.e. b-jets. It therefore depends on the jet reconstruction algorithm. Two major types of algorithms have been extensively explored in ATLAS and CMS, one concentrated on jets with a smaller radius ($R = 0.4$) containing one b-hadron, and one considering jets with a larger radius ($R = 1.0$) with two b-hadrons inside. The former is referred to as the "single-b tagging", while the latter is referred to as the "double-b tagging". In this section, we will summarize the state-of-the-art flavour tagging algorithms developed in ATLAS and CMS, and discuss what can be further improved in the context of searching for multiple Higgs-like particles.

6.2 Single-*b* tagging in ATLAS

The small-R jets considered in most recent ATLAS analyses are reconstructed by the particle flow (PFlow) algorithm with the radius set to 0.4 [191]. A two-step approach is constructed to tag the small-R PFlow jets. As a first step, various dedicated taggers are designed to explore the above characteristics of *b*-hadron decays, such as the displaced tracks and the secondary vertices. The *b*-tagging algorithm developed for small-R jets is suitable for any physics processes as long as the jets only contain one *b*-hadron. Their outputs are then fed into a feedforward neural network, DL1r. Considering jets with 20 GeV $< p_{\text{T}} <$ 250 GeV in a $t\bar{t}$ sample, the rejection factor for charm (light) jets is 12 (625), while achieving a 70% efficiency for *b*-jets [192]. Before DL1r, the MV2 tagger family was widely used in early and partial Run 2 ATLAS analyses, where the dedicated taggers were fed into a boost decision tree instead. The DL1d tagger, an updated version of DL1r, replacing the recurrent neural network impact parameter tagger (RNNIP) with a deep impact parameter set tagger (DIPS) [193], is used in ATLAS early Run 3 analyses [194]. The performance of DL1d is increased by 30% at a *b*-tagging efficiency of 60%, compared to that of DL1r, as shown in Fig. 19. The rejection factor of a given type of background jets, which is defined as the multiplicative inverse of its mis-tagging rate, is used as the metric in ATLAS to quantify the performance.

The most state-of-the-art flavour tagging algorithm in ATLAS is the recently developed GN2 tagger, a transformer based algorithm [196]. The previous version, GN1, a graph neural network based algorithm, was also optimised for the HL-LHC conditions [197]. As opposed to the DL1r architecture, both GN2 and GN1 eliminate the use of intermediate taggers by utilising tracks as the input directly, as illustrated in Fig. 20. Vertex prediction and track origin prediction are realised via auxiliary tasks to improve the performance of jet flavour identification [198]. The flexibility of this architecture makes it straightforward to be adopted for different tasks as discussed in Sect. 6.4.

Figure 21 shows how the flavour tagging performance in ATLAS has improved in recent years. The charm (light) rejection power is increased by a factor of 4.1 (4.2) for a fixed 70% *b*-jet tagging efficiency, compared to the DL1 tagger. The multi-Higgs related searches will benefit significantly from the much improved flavour tagging performance.

For the HL-LHC, ATLAS will have a full silicon inner tracker (ITK) to cover the pseudo-rapidity range up to 4.0. Consequently, the scope of flavour tagging will be extended to a much larger kinematic region. Figure 22 compares the performance of various taggers in the forward region (2.5 < |η| < 4.0). The charm (light) rejection power of GN1 is a factor of 2 (3) better [197]. It is reasonable to expect the
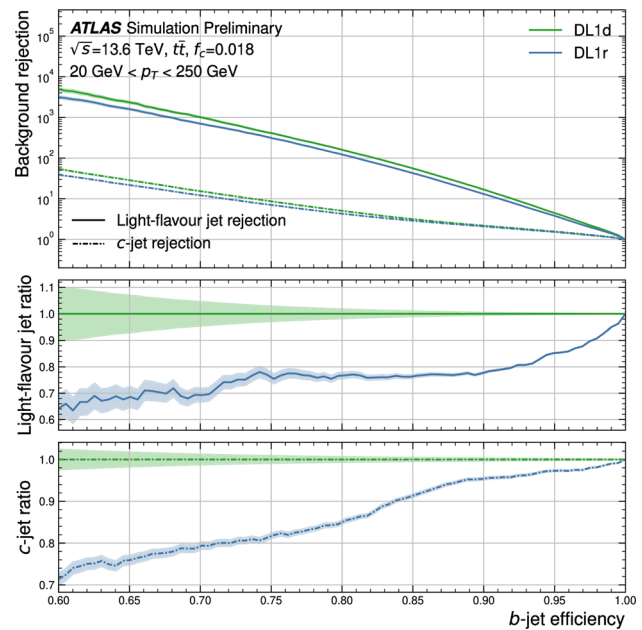

Fig. 19 The light-flavour jet (solid line) and charm-jet (dashed line) rejection factor for the latest DL1r and DL1d algorithms. The taggers are re-optimised on reprocessed Run 2 simulation. The x-axis corresponds to the *b*-jet efficiency, while the y-axis corresponds to the background rejection in the upper panel. The middle panel shows the ratio of the light-flavour jet rejection while the lower panel shows the ratio of the charm-jet rejection. The uncertainty bands correspond to the statistical uncertainties associated with the test sample [195]

performance to be further improved with GN2 and larger training samples.

6.3 Single-*b* tagging in CMS

Within the CMS experiment, heavy flavour tagging on small-R jets has been widely performed during Run 2 using the DNN-based multi-classifier DeepJet [199]. The DeepJet model utilises a total of 650 input variables, including global event variables, charged and neutral particle flow candidate features, and information regarding SVs associated with the small-R jet. DeepJet is a fully connected neural network consisting of 1×1 convolutional layers, which perform some automatic feature preprossesing on each type of jet constituents and SVs. Each of the convolutional layers is followed by a recurrent layer (of LSTM type) which combine the information for each sequence of constituents. The RNN outputs are combined with the global event variables with the use of fully connected layers. DeepJet has 6 output nodes, which can be used for b, c, and quark/gluon tagging. A schematic of the DeepJet architecture is shown in Fig. 23.

DeepJet is trained and tested using simulated small-R jets from QCD-multijet and fully hadronic $t\bar{t}$ events. Figure 24 shows the performance of DeepJet [200] in comparison with its predecessor, the CMS b-tagger DeepCSV [201], in a sim-
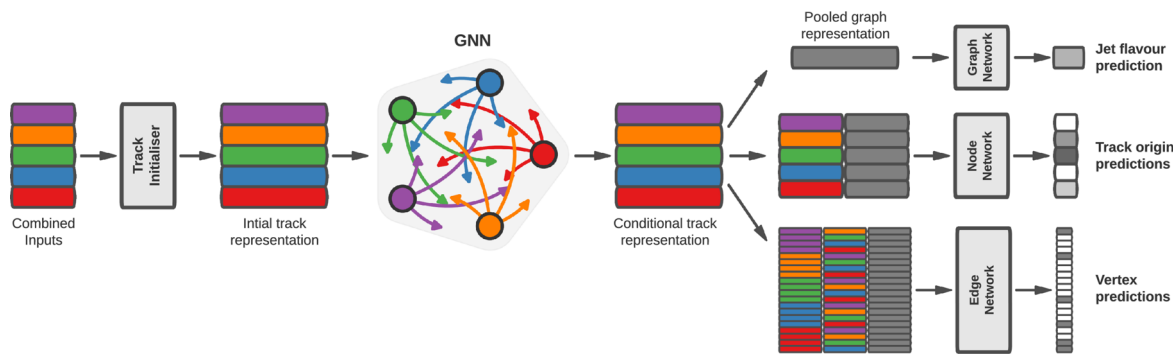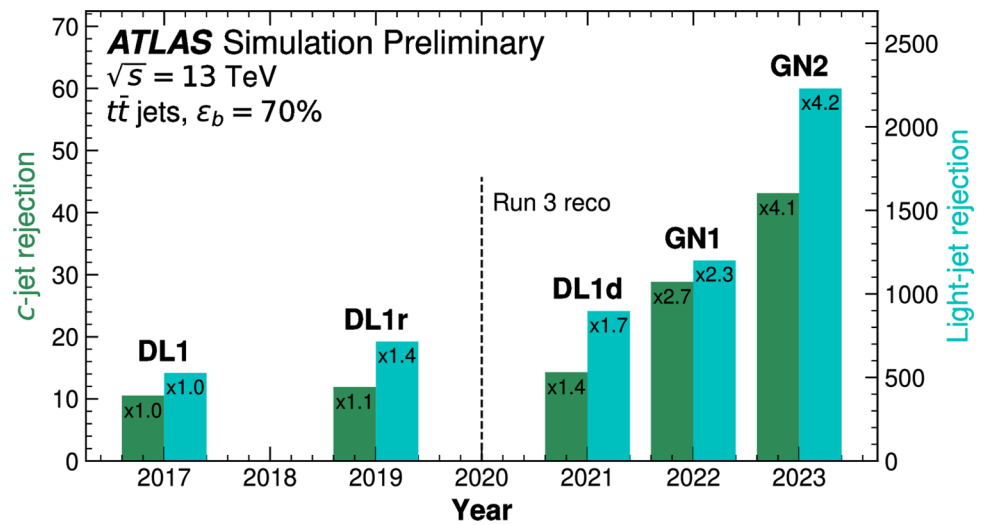
Fig. 20 Schematic diagram of the GN1 (GN2) tagger [198]

Fig. 21 Evolution of the ATLAS flavour tagging performance since 2017 [196]

ulated $t\bar{t}$ sample containing small-R jets with $p_T > 30$ GeV and $|\eta| < 2.5$. For both algorithms, the b jet identification efficiency is not the same in data and simulation. To account for this difference data-to-simulation correction factors are applied in simulated events.

Differences in the heavy-flavor tagging performance in data and simulation are observed and must be calibrated against. A recent development [202] introduces an adversarial training to the model with the scope of reducing any observed discrepancies between data and simulation

before any calibration is applied. This technique improves the robustness of the model, meaning that the model has two tasks to solve simultaneously: optimize classification and hold out against mismodellings that can mimic systematic uncertainties. This is done by applying adversarial attacks (small systematic disturbances) on the input features. Adversarial inputs are generated by the Fast Gradient Sign Method (FSGM) [203,204], which modifies the input features (x_{raw}) in a systematic way in order to increase the loss function,

Fig. 22 The charm-jet (left) and light-flavour jet (right) rejection factors as a function of the b-jet tagging efficiency for jets in the $t\bar{t}$ sample with $p_T > 20$ GeV and $2.5 < |\eta| < 4$. The uncertainty bands correspond to the statistical uncertainties associated with the test sample [197]
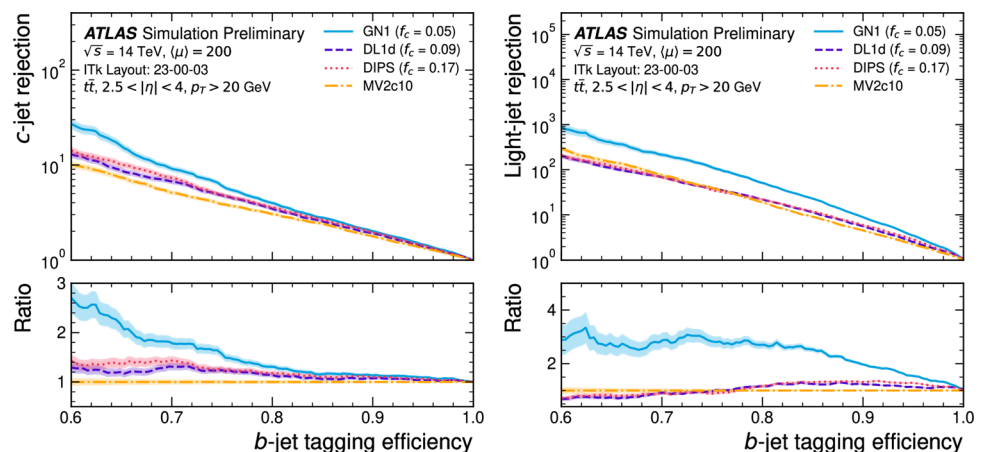
Fig. 23 Schematic diagram of the DeepJet tagger [199]
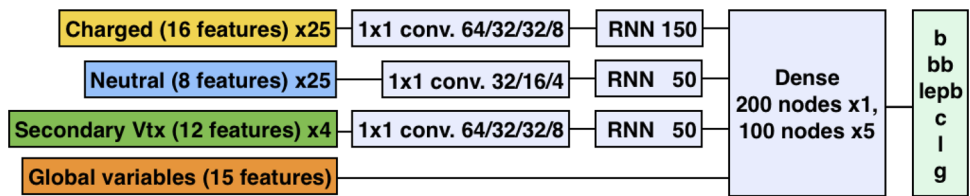
$(J(x_{raw}, y):$

$$x_{FGSM} = x_{raw} + \varepsilon \cdot sgn(\nabla_{x_{raw}} J(x_{raw}, y)), \qquad (9)$$

where ε is the (small) distortion parameter, y is the target and $sgn(\alpha)$ stands for the sign of α. The FSGM attacks are applied in all DeepJet input features (excluding integer and defaulted values), in every step of the training. Figure 25 shows the performance in discriminating b from light jets of the nominal and adversarial models with (dashed lines) and without (solid lines) the FSGM-attacks in the input features with a distortion parameter of $\varepsilon = 0.01$ and a shift of x_{raw} not more that 20% of its original value. The adversarial model not only shows similar performance with the nominal DeepJet training but also provides higher robustness. The hyperparameter optimization is performed based on where the focus is put on: higher performance or higher robustness. Figure 26 shows the data over simulation agreement for the b versus light DeepJet tagger for the nominal (left) and adversarial training (right) in events with at least two well isolated and oppositely charged muons with an invariant mass close to the Z boson mass [205]. While data over simulation agreement using the nominal training shows some oscillations, the

adversarial training provides a better agreement at a similar performance.

The latest development in heavy flavor tagging at the CMS experiment is the Particle Transformer (ParT) [206]. ParT has a Transformer-based architecture which incorporates pairwise particle interactions in a tailored attention mechanism [207]. It takes as input information from all jet constituent particles, such as the 4-vector (E, p_x, p_y, p_z), electric charge, particle identity as determined by the experiment detector and information on the trajectory displacements. The training is performed on a large dataset containing 100 M jets, called JETCLASS which includes 10 types of jets: H→ $b\bar{b}$, H→ $c\bar{c}$, H→gg, H→4q, H → $\ell\nu q\bar{q}'$, t → bqq', t→ $b\ell\nu$, W → qq', Z → qq', representing the signal jets and q/g, representing the background jets. A comparison of the performance of ParT and DeepJet b-tagging algorithms [208] is shown on the left (right) plot of Fig. 27, which shows the probability of misidentifying non-b (non-c) jets as b jets (c jets) with respect to correctly identifying b jets (c jets). ParT shows significant improvements compared to DeepJet and its promising performance makes it a good candidate for becom-
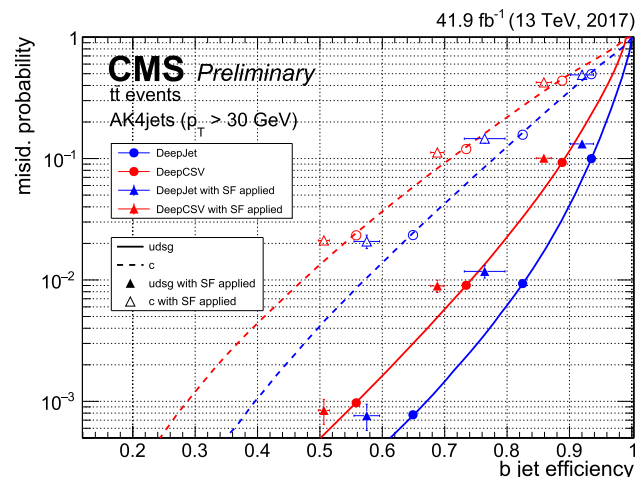

Fig. 24 The receiver operating characteristic curve (ROC) of the CMS DeepJet (blue) and DeepCSV (red) b-tagging algorithms. The probability of misidentifying non-b jets as b jets is shown with respect to the efficiency of correctly identifying b jets for three working points: loose, medium and tight (represented by the circular markers). A b jet efficiency and a misidentification probability equal to one corresponds to no selection on the b discriminant score. The performance of the algorithms is also shown after the application of the data-to-simulation correction factors (represented by the triangle symbols) [200]
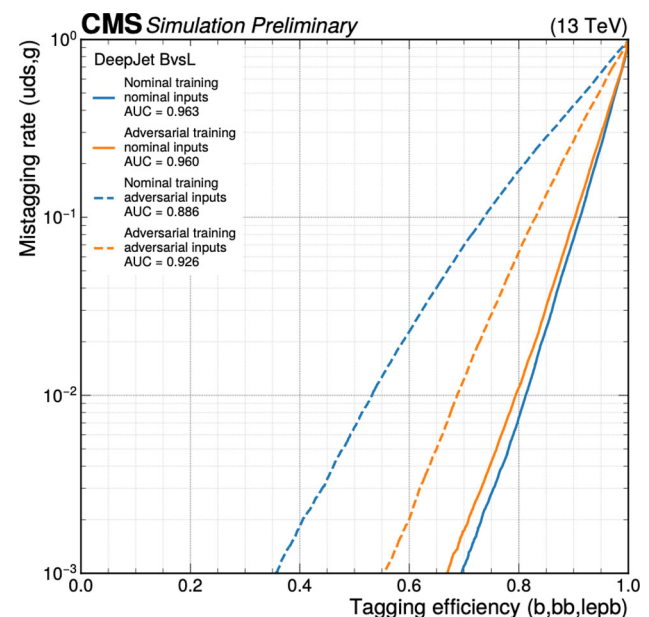

Fig. 25 Performance of DeepJet b versus light (BvsL) tagger for the nominal and adversarial models as derived from simulated QCD-multijet and $t\bar{t}$ events. The b tagging performance of the nominal (non FSGM-attacked) models are represented with solid lines, while the performance of the FSGM-attacked models are shown with dashed lines. [202]
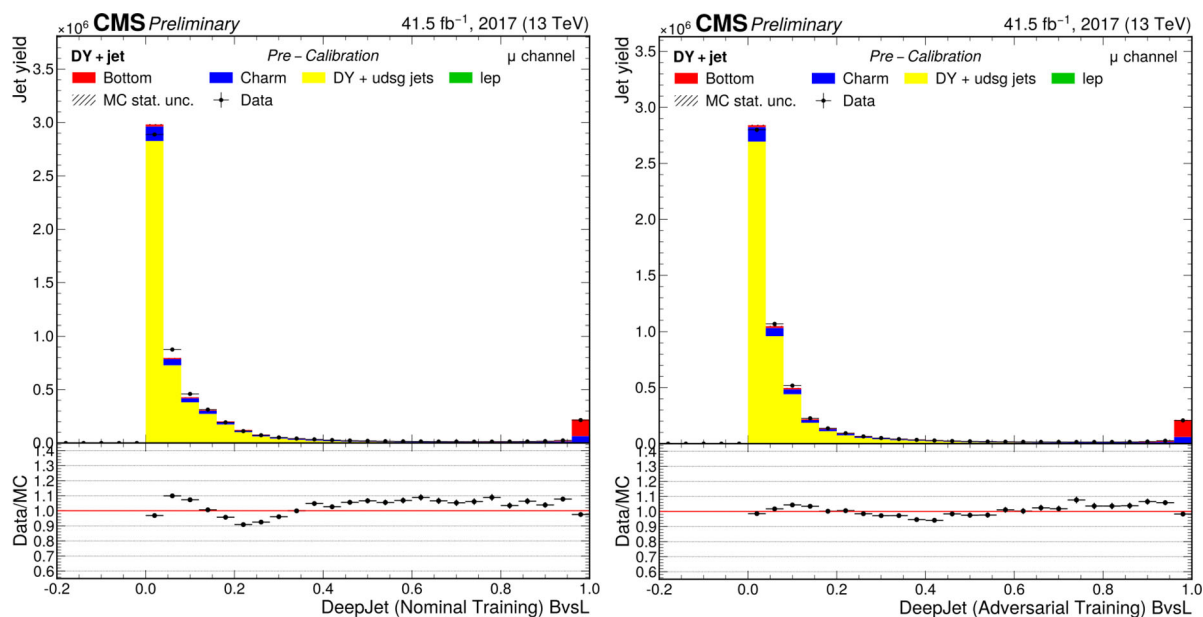
Fig. 26 Data-to-simulation agreement for the DeepJet b versus light discriminator in a light flavor-enriched selection using the nominal (left) and adversarial (right) trainings [202]

ing the state-of-the-art heavy flavor tagger for CMS during the Run-3 data-taking period of the LHC.

6.4 Double-*b* tagging in ATLAS

The double-*b* tagging algorithm in ATLAS shares the same architecture as that of the single-*b* tagging algorithm. The first method developed is to apply the single-*b* tagging algorithm directly on the subjets, requiring the two subjets to be identified as *b*-jets. The subjets are reconstructed using a variable radius (VR) algorithm considering tracks only [209] that can be associated with the large-R jets reconstructed using local calorimeter topological clusters (LCTopo). As a consequence, it is referred to as the "2-VR" method. The first dedicated double-*b* tagging algorithm, D_{Xbb} [210], is a feed forward neural network using the kinematic information of the large-R jet and the DL1r outputs evaluated on up to three subjets as the input. The DL1r tagger was retrained using the VR track jets in a $t\bar{t}$ sample. In the boosted regime, the major background consists of jets from multijet and top events. So the performance is represented in terms of multijet and top jet rejection factors. Figure 28 compares the D_{Xbb} tagger and the 2-VR method. The dedicated algorithm clearly outperforms the latter, especially when the $H \rightarrow b\bar{b}$ efficiency is high.

The flexible architecture of GN2 allows ATLAS to further unify both the single-*b* and double-*b* tagging algorithms. As seen in Fig. 20, the algorithm is agnostic to the jet reconstruction algorithms. The most state-of-the-art double-*b* tagging also uses the GN2 architecture but considering the large-R jets reconstructed using the united flow objects (UFO)

[211]. The baseline model, D_{Hbb}^{GN2X}, similar to the single-*b* version, only explores the kinematic information of the large-R jets and the associated tracks. Figure 29 compares the performance of GN2X to that of D_{Xbb}. Both the multi-jet and top rejection factors are improved by a factor of two when the $H \rightarrow b\bar{b}$ efficiency is 60%. In addition, the 2-VR method using GN2 is added as a reference, showing similar performance as that of D_{Xbb} [212].

Two additional variations are also considered by either adding calorimeter or subjet information. As seen in Fig. 30, adding both the charged and neutral calorimeter information, i.e. the flow objects, improves the multijet (top) rejection factor by 50% (80%). When the kinematic and GN2 output of the VR subjets are included, the top rejection factor is two times higher while the multijet rejection factor is up to 60% smaller when the $H \rightarrow b\bar{b}$ tagging efficiency is below 90%. The GN2X performance can be further improved by exploring the above variations [212].

6.5 Double-*b* tagging in CMS

Several machine-learning based algorithms have been developed in CMS to identify highly Lorentz-boosted massive particles. These algorithms utilise high level inputs, such as jet substructure observables, and lower level inputs, such as PF candidates or information from secondary vertices associated with the AK8 jets (PF candidates are clustered with the anti-k_T algorithm [74] with a distance parameter of 0.8).

An example of such algorithm is the DeepAK8 [213], a multi-class particle identification algorithm able to discrim-
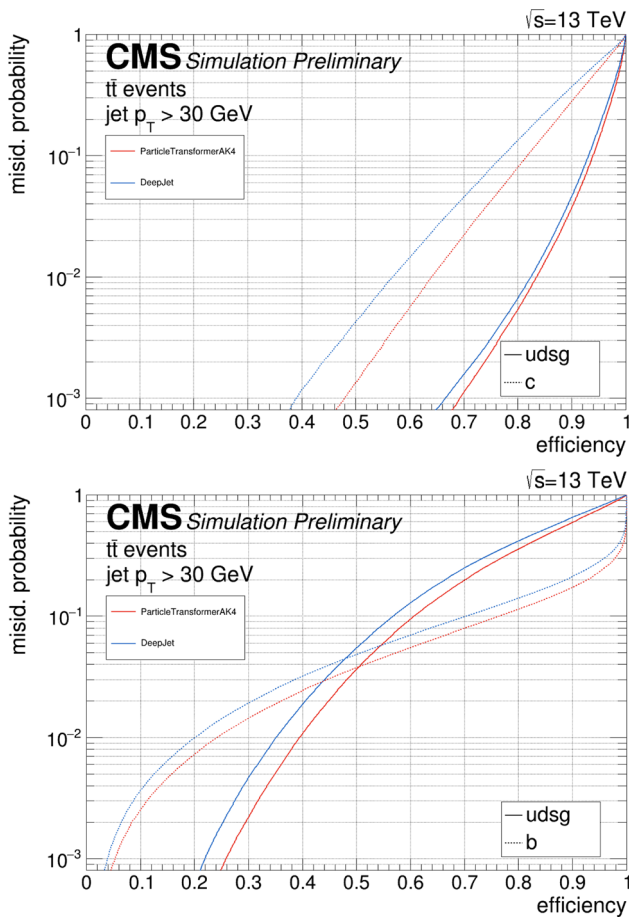
Fig. 27 Performance of DeepJet (blue) and ParT (red) b-tagging algorithms for identifying small-R jets with $p_T > 30$ GeV and $|\eta| < 2.5$, as measured in simulated $t\bar{t}$ events. Dashed lines correspond to the misidentification rate of udsg jets, while solid lines correspond to the misidentification rate of c (upper) or b (lower) jets [208]
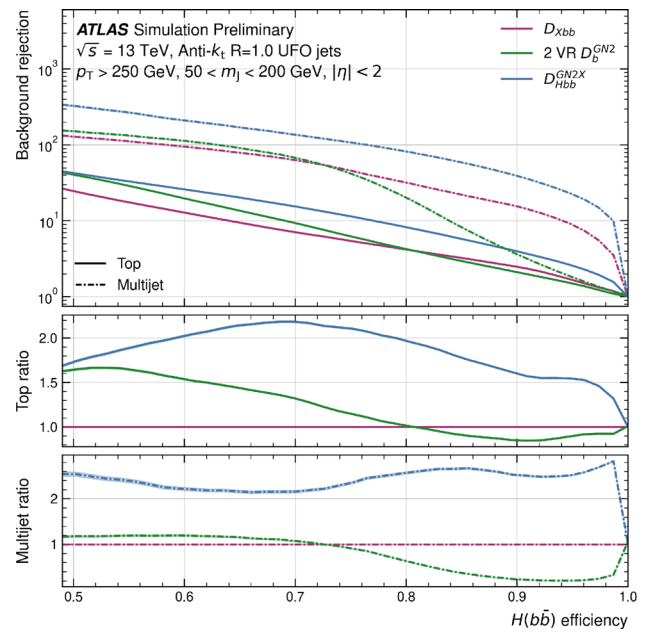

Fig. 29 Top and multijet rejection factors as a function of the $H \to b\bar{b}$ tagging efficiency for jets with $p_T > 250$ GeV and mass (50 GeV $< m_J < 200$ GeV). Performance of the GN2X algorithm is compared to the D_{Xbb} and VR subjets baselines [212]

inate heavy hadronically decaying particles into five categories: W, Z, H, top, or other, and the classes are further subdivided into decay modes (i.e. $b\bar{b}$, $c\bar{c}$, $q\bar{q}$). The DeepAK8 algorithm takes as input up to 100 jet constituent particles, sorted by decreasing p_T and utilises their properties, such as the p_T, charge, energy deposit, etc., and information regarding the SVs of the event. The DeepAK8 architecture consists of two parts. The first part consists of two one-dimensional convolutional neural networks (CNNs) which are applied to the particle and SV lists. The CNNs transform the inputs
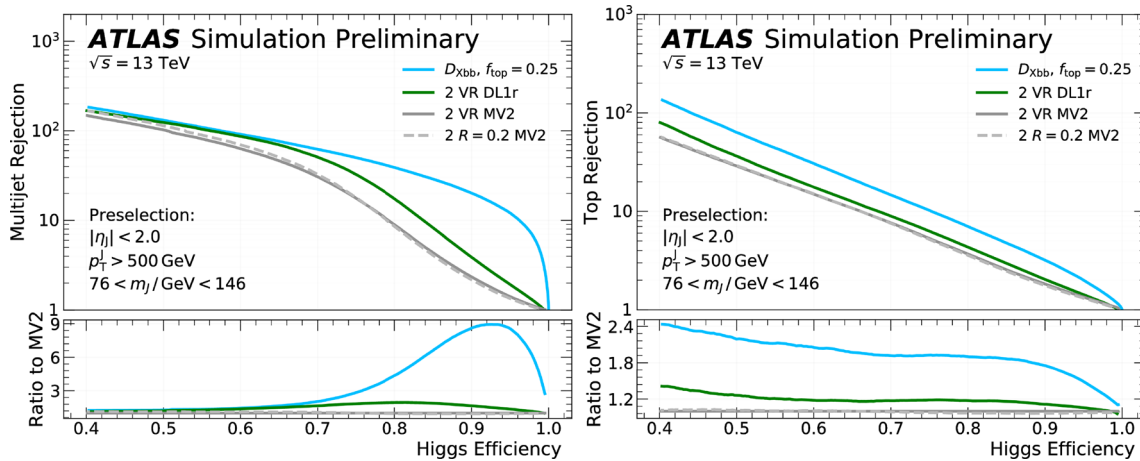

Fig. 28 Multijet (left) and top jet (right) rejection factors as a function of the $H \to b\bar{b}$ tagging efficiency, for large-R jet $p_T > 500$ GeV. Performance of the D_{Xbb} algorithm is compared to 2-VR DL1r and 2-VR MV2. Another variant of the 2-VR MV2 that considers fixed radius (R = 0.2) track jets is also included
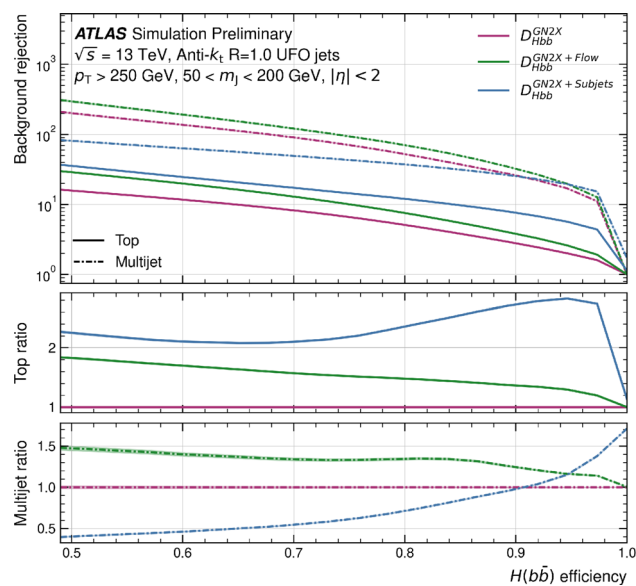
Fig. 30 The top and multijet background rejection factors as a function of the $H \to b\bar{b}$ tagging efficiency for the two heterogeneous input type architectures compared to the baseline GN2X model [212]

and provide useful features that are in turn processed by the second step, which is a simple fully connected network performing the jet classification. The architecture of DeepAK8 is illustrated in Fig. 31.

A jet mass decorrelated version of DeepAK8 is developed, namely DeepAK8-MD. This alternative network is using the same input features as the nominal one and its training samples are reweighted in order to yield a flat transverse momentum and mass distributions. DeepAK8-MD is able to preserve the discrimination power of the original DeepAK8 algorithm using adversarial training [214]. An additional network, called mass prediction, is added during the training phase and predicts the jet mass from the CNN output. The accuracy of the mass prediction network is subsequently used as a penalty to prevent the tagger from learning specific features correlated with the mass. A different approach towards jet mass decorrelation is based on the Designing Decorrelated Taggers (DDT) method [215]. In this method, the output of DeepAK8 is transformed as a function of a dimensionless scaling variable $\rho = ln(m_{SD}^2/p_T^2)$ and the jet p_T, where m_{SD} is the groomed jet mass derived from the soft-drop algorithm [180] with $\beta = 0$ and $z_{cut} = 0.1$. The resulting output score of DeepAK8-DDT yields into a flat QCD-multijet efficiency across the m_{SD} and the transverse momentum spectra. Two DeepAK8-DDT models are trained, corresponding to 2% and 5% flat background efficiency.

A more recent development is ParticleNet [127], a multi-classification algorithm that treats jet constituents as a permutation invariant set of particles (*point cloud*) rather than an ordered structure. ParticleNet is based on customised

dynamic graph convolutional neutral network (DGCNN) [216] and its key building block is the edge convolution (EdgeConv). The EdgeConv represents each point cloud as a graph with each point being the vertex, while the edges of the graph are constructed as connections between each point and its $k-$nearest neighbor. The EdgeConv operation can be stacked allowing to form a deep network where local and global structures are learned in a hierarchical way. The architecture of ParticleNet, shown in Fig. 32 consists of three EdgeConv blocks where the first one uses the spatial coordinates in the $\eta - \phi$ plane to compute the distances, while the next two blocks use the learned vectors as the new coordinates. Following the EdgeConv blocks, a global average pooling operation is performed in order to aggregate the output features over all point clouds. Subsequently, there are two fully connected layers of 256 and 2 units, and a softmax function which is used to generate the output of the classifier. As input features, ParticleNet utilises the same inputs as the DeepAK8 algorithm.

A mass-decorrelated (MD) version of ParticleNet that utilises the same inputs and architecture is used to identify highly Lorentz-boosted heavy particles (X) decaying hadronically. The mass decorrelation is achieved by training the network with a simulated signal sample containing Lorentz-boosted spin-0 particles of a flat mass in the range between 15 and 250 GeV and decay into a quark-antiquark pair. As background, a QCD-multijet sample is used. Both signal and background training samples are subject to reweighting in transverse momentum and mass.

Figure 33 shows the performance of the aforementioned machine learning algorithms on identifying highly Lorentz-boosted Higgs bosons into a pair of bottom quarks [217]. The performance is derived after a selection on the mass of the large-R jets is made, requiring $90 < m_{SD} < 140$ GeV. For simulated SM H$\to b\bar{b}$ signal (QCD-multijet background) events, the generated Higgs boson (quarks and gluons) candidates are required to have $500 < p_T < 1000$ GeV and $|\eta| < 2.4$. In the case of background, the efficiency is defined as the ratio of the reconstructed Higgs boson candidates satisfying the selection, over all Higgs boson candidates. ParticleNet shows significant improvements with respect to the previous highly Lorentz-boosted particle taggers.

6.6 Flavour tagging in ATLAS trigger

Trigger performance is vital in the tri-Higgs search programme. In certain low mass region, applying flavour tagging in the high level trigger (HLT), i.e. *b*-jet trigger, is the only viable approach. Unlike the offline environment, the stringent computational requirement for triggers prevents reconstructing all tracks in the event. Therefore, the overall *b*-jet trigger has the same workflow as the offline reconstruction except the fact that two dedicated track reconstruction iterations are

Fig. 31 The network architecture of the DeepAK8 multi-classifier [213]
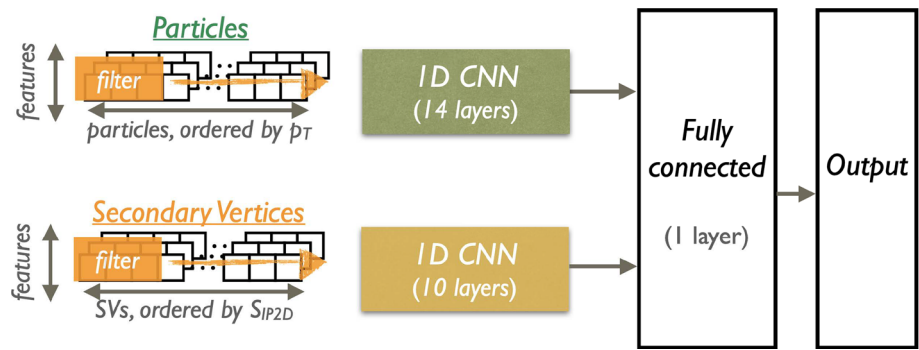
performed within given regions of interest (ROI). A fast track finding (FTF) step is employed using the super-ROIs defined by trigger jets with $p_T > 30$ GeV, and the tracks are used to reconstruct primary vertices. Jets passing further kinematic selections define the ROIs for the precision tracking iteration, and the resulting tracks are used to perform the flavour tagging algorithms. A simplified flow diagram is shown on the left side of Fig. 34. The MV2 tagger family was adopted in the b-jet triggers during Run 2 data-taking. A detailed documentation can be found in ref. [218].

Significant improvements have been introduced to the Run 3 b-jet triggers. New taggers such as DL1d and GN1 were implemented into the trigger, and have been collecting data efficiently. In addition, a fast b-tagging sequence using the tracks from FTF iteration is introduced to further reduce the rate. It applies a similar structure as the DIPS tagger so that it is referred to as the "fastDIPS" algorithm. The right side of Fig. 34 illustrates the new b-jet trigger workflow. Nearly all high rate b-jet triggers include the "fastDIPS" preselection step [193]. Figure 35 compares the performance of various b-jet trigger algorithms. The GN1 b-jet trigger has a charm (light) jet rejection larger than 20 (1000) when the b-jet tagging efficiency is 70% [219].
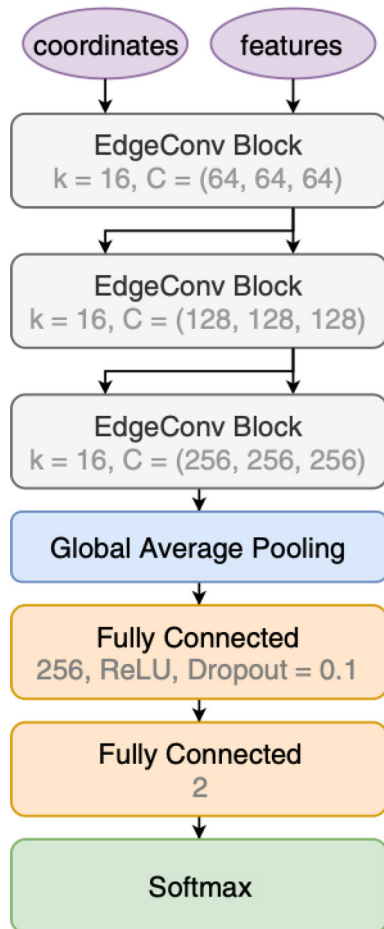
6.7 Flavour tagging in CMS trigger

The ParticleNet model was deployed online for the first time in Run 3 2022 with the score of identifying highly Lorentz-boosted heavy particles decaying into a pair of bottom quarks,
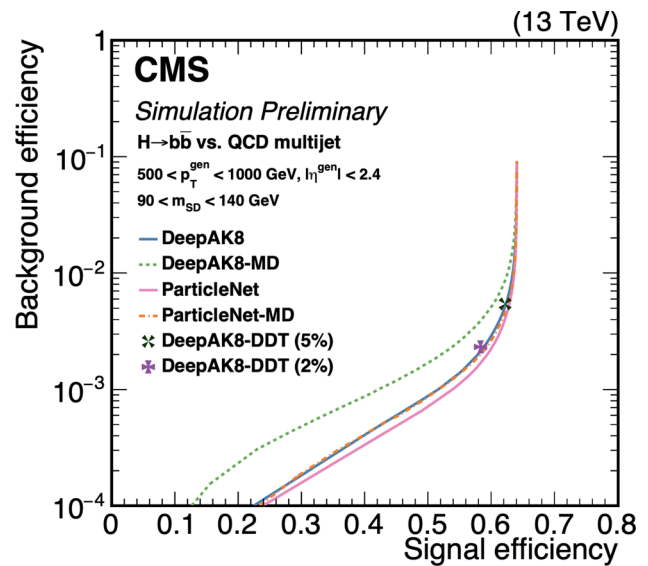

Fig. 32 The ParticleNet architecture [127]

Fig. 33 Performance of tagging algorithms identifying Higgs bosons decaying into a pair of bottom quarks, as measured in simulated SM H→ $b\bar{b}$ (signal efficiency) and QCD-multijet (background efficiency) events [217]

Fig. 34 Simplified schematic descriptions of the *b*-jet trigger selections in two different ATLAS trigger implementations: the Run 2 implementation on the left, and the Run 3 implementation on the right [193]
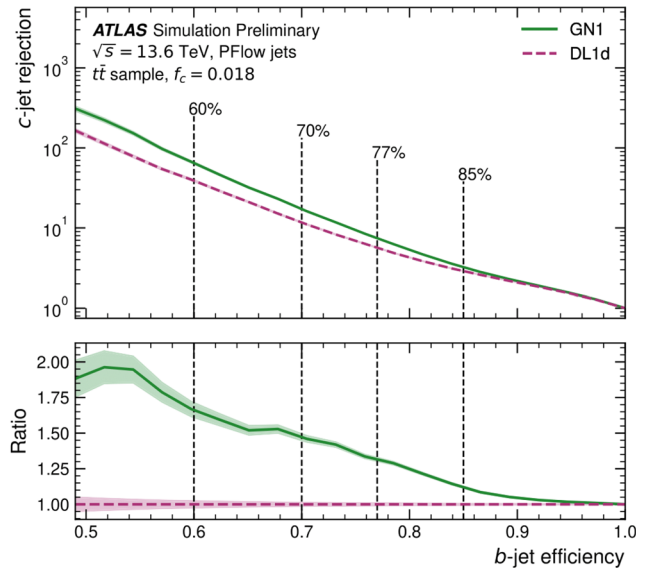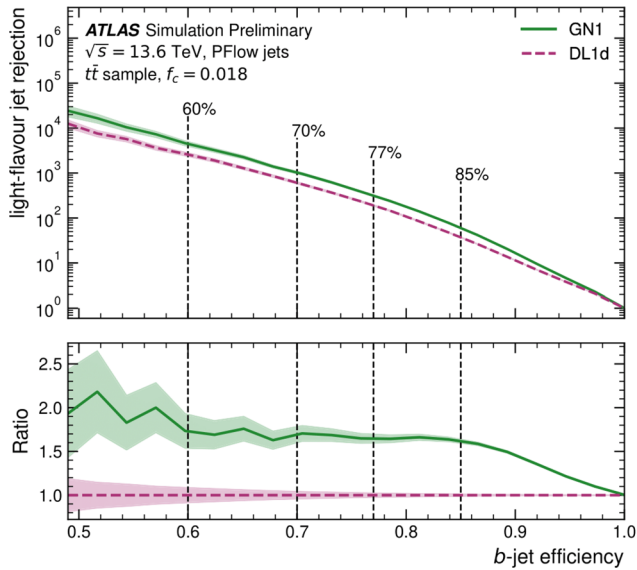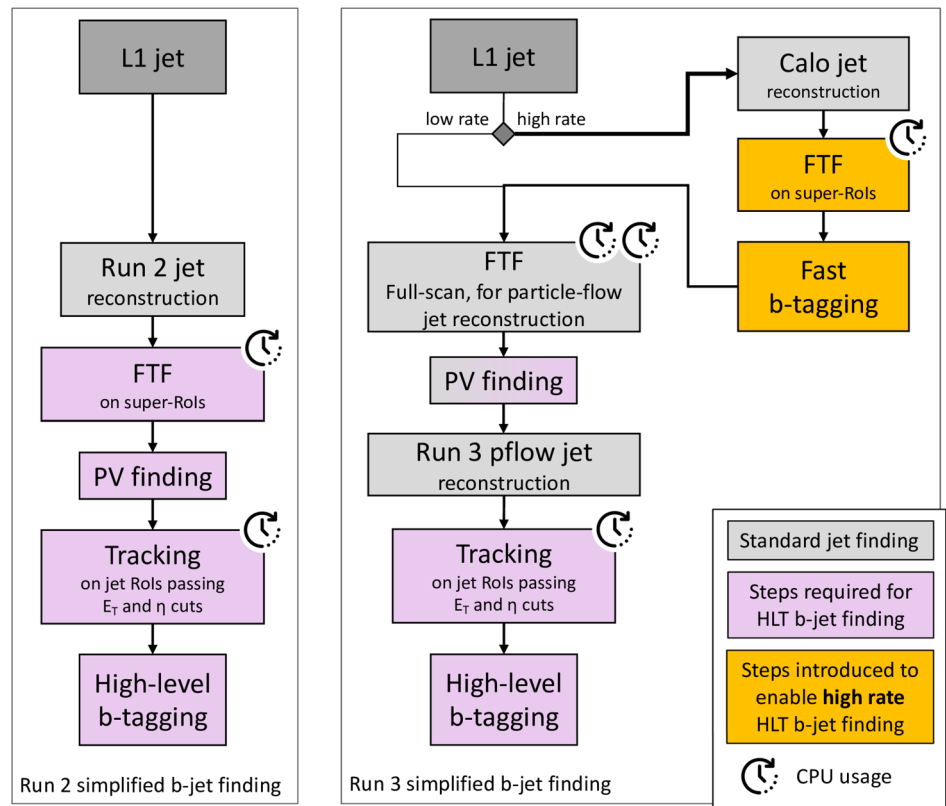

Fig. 35 Light-flavour jet rejection as a function of *b*-jet efficiency of the GN1 algorithm (green) in comparison to the benchmark DL1d algorithm (purple) which uses the DL1 architecture, evaluated on HLT Par-

ticle Flow jets in a $t\bar{t}$ sample. The 60%, 70%, 77% and 85% *b*-jet efficiency operating points are indicated by vertical black lines [219]
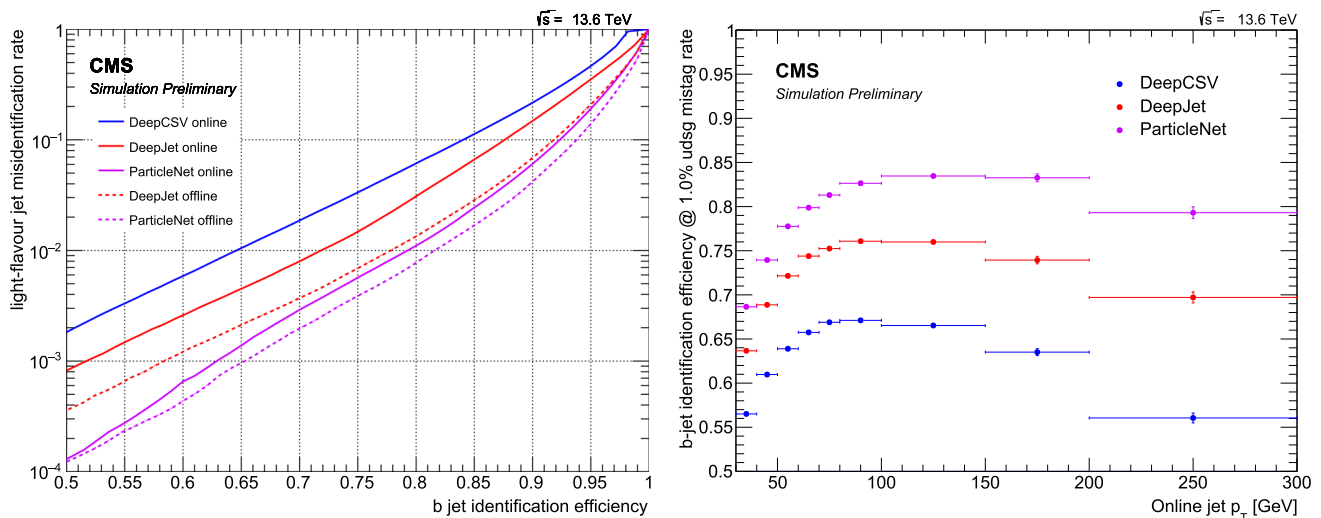
Fig. 36 Left: light flavour jet misidentification rate as a function of the efficiency of correctly identifying b jets for the b-taggers DeepCSV (blue), DeepJet (red), and ParticleNet (purple). Solid lines represent the performance for simulated HLT-level jets with $p_T > 30$ GeV and $|\eta| < 2.5$ matched to an offline reconstructed jet with $p_T > 25$ GeV.

Dashed lines correspond to the offline tagging performance on the matched offline jets. Right: online b jet identification efficiency at 1% light flavour jet misidentification rate as a function of the HLT-level jet p_T [220]

as well as identifying signatures with b jets (small-R) in the final state. Figure 36 shows the performance of ParticleNet b-tagger [220] compared to DeepJet and DeepCSV CMS b-taggers, for HLT-level jets with $p_T > 30$ GeV and geometrically matched to offline jets. The ParticleNet online b-tagger shows a substantial improvement compared to the previous online DeepJet and DeepCSV b-taggers and its performance approaches that of the offline. Figure 36 right, compares the three online b-taggers at a 1% light-flavour jet misidentification rate, showing that ParticleNet achieves up to 10% improvement throughout the jet p_T range.

Since the beginning of Run 3 data-taking period, the CMS experiment has exploited the recent improvements in heavy flavour tagging for online HLT-jets [220] and deployed online a new trigger strategy [221] to record di-Higgs and tri-Higgs production in events with b jets in the final state. In 2022, the trigger targeting HH→4b production (mentioned below as Run 3 2022 HH trigger) had a rate of around 60 Hz at an instantaneous luminosity of $2 \times 10^{34} cm^{-2} s^{-1}$ and required at least four small-R HLT-jets with $p_T > 70, 50, 40$, and 35 GeV for the four leading-in-p_T jets and the average score of the two jets with the highest b-tagging score tagged with the ParticleNet online b-tagger to be above 0.65. In 2023, the an updated version of the HH→4b trigger was deployed in the delayed stream, allowing a higher rate and acceptance at the cost of a delayed event reconstruction. This new trigger (mentioned below as Run 3 2023 HH trigger) recorded events at a maximum rate of 180 Hz at $2 \times 10^{34} cm^{-2} s^{-1}$ and required events to have at least 4 HLT-jets with $p_T > 30$ GeV, the scalar sum of p_T of all HLT-jets with p_T above 30 GeV

(H_T) to be above 280 GeV, and the average score of the two leading-in-b-tagging score jets to be at least 0.55. The L1 trigger requirement was also relaxed to allow events with H_T above 280 GeV instead of the 2022 threshold of 360 GeV. Figure 37 shows the trigger efficiency as a function of the reconstructed invariant mass of the di-Higgs (m_{HH}^{Reco}) candidate in simulated SM HH→4b events with $\kappa_\lambda = 1$ (left) and $\kappa_\lambda = 5$ (right). The trigger efficiency is defined as:

$$\varepsilon = \frac{N_{events}(\text{pass trigger and event selection})}{N_{events}(\text{pass event selection})}, \qquad (10)$$

where event selection corresponds to the requirement of at least 4 small-R jets with $p_T > 30$ GeV and $|\eta| < 2.5$. The di-Higgs candidate is reconstructed from the four small-R jets with the highest b-tagging score. The performance of the Run 3 2022 (2023) HH trigger is shown with blue (orange). For comparison, the Run 2 HH trigger [222,223] is also shown with the black line. The aforementioned trigger, which operated at around 8 Hz at $2 \times 10^{34} cm^{-2} s^{-1}$, required an event $H_T > 340$ GeV and at least four small-R jets with $p_T > 75, 60, 45$, and 40 GeV, where at least three of those jets were tagged online with the DeepCSV online b-tagger with a working point of 0.24. The overall trigger efficiency achieved by the 2023 trigger strategy for the HH→4b process with $\kappa_\lambda = 1$ ($\kappa_\lambda = 5$) reaches 82% (64%), improved by 20% (30%) with respect to the 2022 trigger strategy and by 57% (78%) with respect to the 2018 one. The Run 3 2023 HH trigger results in higher efficiency on the full m_{HH}^{Reco} spectrum.

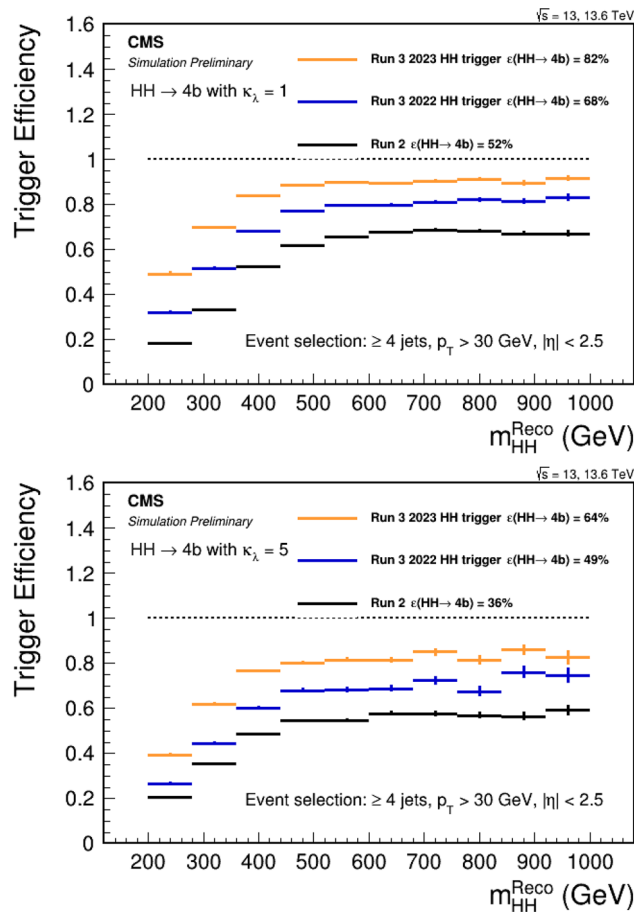The novel Run 3 2023 HH trigger is also used to recover HH→2b2τ_{had}-like events that are not recorded by triggers

Fig. 37 Trigger efficiency as a function of the invariant mass of the di-Higgs system (m_{HH}^{Reco}) for the simulated SM HH→4b process with $\kappa_\lambda = 1$ (upper) and κ_λ=5 (lower), shown for Run 2 (black), Run 3 2022 (blue) and Run 3 2023 (orange) HH triggers [221]

Fig. 38 Upper: trigger efficiency as a function of the reconstructed invariant mass of the di-Higgs system (m_{HH}^{Reco}) for the simulated SM HH→ $2b2\tau_{had}$ process with $\kappa_\lambda = 1$ for the Run 3 hadronic τ trigger (dark blue), the Run 3 missing transverse momentum trigger (light blue), the Run 3 2023 HH trigger (orange) and the logical OR of all triggers (green). Lower: the m_{HH}^{Reco} distribution with and without (black) any trigger requirement applied [221]

requiring hadronicaly decaying tau leptons (τ_{had}) or missing transverse energy (E_T^{miss}). The Run 3 τ_{had} triggers [224] have a rate ranging from 17 Hz up to 50 Hz at $2\times10^{34} cm^{-2}s^{-1}$ and require the presence of at least two τ_{had} with $p_T > 35$ GeV and $|\eta| < 2.1$ satisfying the Medium operating point of the DeepTau [225] algorithm, or two τ_{had} with $p_T > 30$ GeV and $|\eta| < 2.1$, satisfying the Medium operating point of DeepTau and the presence of an HLT-jet with $p_T > 60$ GeV, or at least one τ_{had} with $p_T > 180$ GeV and $|\eta| < 2.1$ and satisfying the loose DeepTau working point. The Run 3 E_T^{miss} trigger [226] operates at around 42 Hz at $2\times10^{34} cm^{-2}s^{-1}$ and requires an event E_T^{miss} of at least 120 GeV. The left plot of Fig. 38 shows the trigger efficiency as a function of the m_{HH}^{Reco} in simulated SM HH→$2b2\tau_{had}$ with $\kappa_\lambda = 1$ for the Run 3 τ_{had} triggers (dark blue), the Run 3 E_T^{miss} (light blue), the Run 3 2023 HH trigger (orange) and the logical OR of all trigges (green). The trigger efficiency is defined by Eq. 10 and the event selection requires the presence of at least 2 hadronic small-R jets with $p_T > 20$ GeV, $|\eta| < 2.5$ and identified as b jets with the loose operating point of DeepJet,
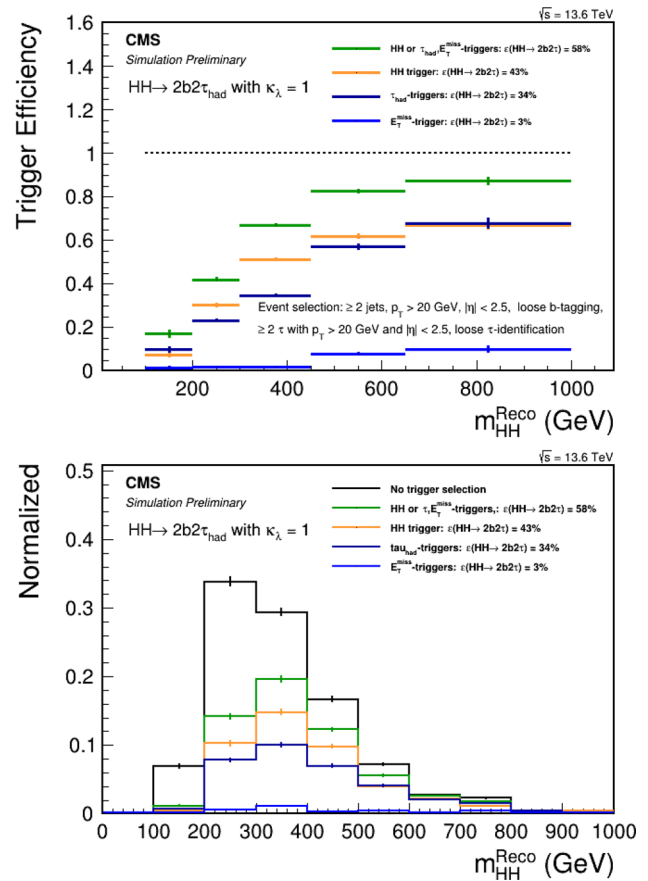
corresponding to 10% light-flavor jet misidentification rate, and at least 2 τ_{had} with $p_T > 20$ GeV and $|\eta| < 2.5$ with loose identification criteria using the DeepTau algorithm. The di-Higgs candidate is reconstructed using the two b jets and τ_{had} candidates. The right plot of Fig. 38 shows that the Run 3 2023 HH trigger is able to recover HH→$2b2\tau_{had}$ events in the full m_{HH}^{Reco} spectrum and provides an overall efficiency of 43%. For values of m_{HH}^{Reco} above 650 GeV, the Run 3 2023 HH trigger reaches the one of Run 2 τ_{had}-triggers. When combined in logical OR with the τ_{had}- and E_T^{miss}-triggers the overall efficiency reaches 58%, while the efficiency plateaus at an efficiency of around 85%.

The Run 3 2023 HH triggers can also be used to record almost all events from triple Higgs boson production in the $4b2\tau_{had}$ and 6b final states. Figure 39 shows the trigger efficiencies as a function of the reconstructed invariant mass of the tri-Higgs system for simulated SM HHH→$4b2\tau_{had}$ (left) and HHH→6b (right), both with $\kappa_\lambda = 1$. In the case of the
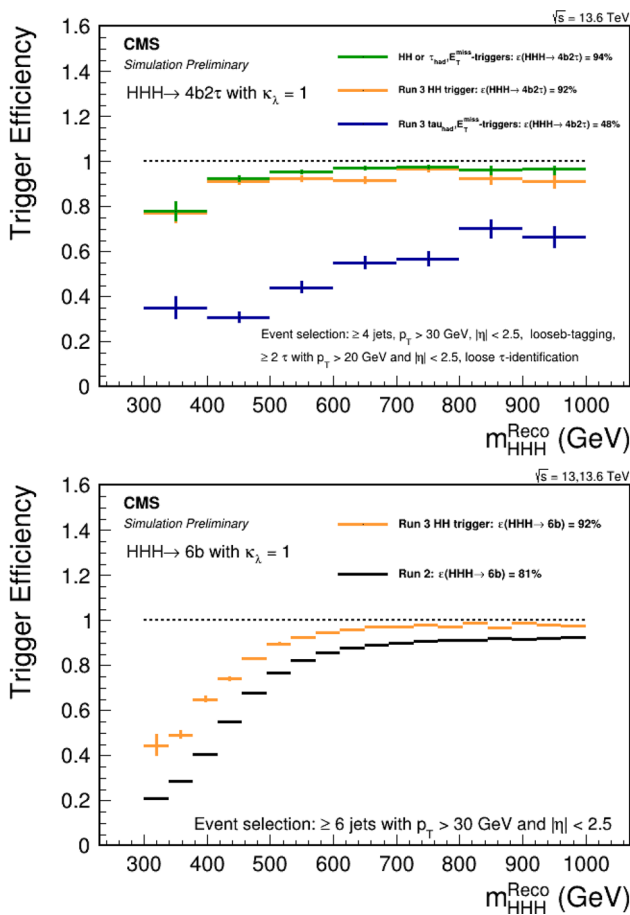
Fig. 39 Trigger efficiency as a function of the reconstructed invariant mass of the tri-Higgs system (m_{HHH}^{Reco}) for the simulated SM HHH→4b2τ_{had} (upper) and HHH→6b (lower) processes. [221]

SM HHH→4b2τ_{had} signal, the Run 3 2023 HH trigger can record 92% of all the events satisfying selection of at least four small-R jets with $p_T > 30$ GeV, $|\eta| < 2.5$ and satisfying the loose DeepJet working point, and at least 2 τ_{had} with $p_T > 20$ GeV and $|\eta| < 2.5$ and satisfying a loose DeepTau criterion. When combined with the Run 3 τ_{had}-triggers the efficiency reaches 94%. For the SM HHH→6b signal, the Run 3 2023 HH trigger can record around 92% of all events satisfying a basic selection of 6 jets with $p_T > 30$ GeV and $|\eta| < 2.5$. Compared to the Run 2 HH trigger, the new trigger strategy improves the acceptance by 14%.

6.8 Flavour tagging: outlook

Both ATLAS and CMS collaborations have demonstrated the great potential of a unified end-to-end heavy-flavour tagging architecture. The graph neural network approaches have been successfully deployed both online and offline. Both the single-b and double-b tagging performance have been enhanced significantly compared to Run 2 methods. The tri-Higgs search programme can already greatly benefit from the

state-of-the-art taggers. However their final impacts on the physics analyses also depend on the precision of their calibrations in MC. The author would also like to emphasize the importance of such calibration work. Due to the rich phase space of the tri-Higgs models, the search programme will be further extended if the flavour tagging algorithms are optimised for certain scenarios. In this section, the authors try to offer some discussion points.

Jets with low momenta play a vital role in certain phase space as seen before. It is experimentally challenging to identify b-jets with low momenta. The primary reason is that the main characteristics of b-hadron decays such as displaced tracks and secondary vertices diminish when the Lorentz boost is small. Improving the flavour tagging performance on low-p_T jets will be appreciated by the tri-Higgs search programme.

Because of the various mass hierarchies and splits, the boosted scenario is enriched. For instance, decay products of two low mass particles can be collimated, resulting in jets containing more than two b-hadrons. Expanding the current scope of the double-b tagging algorithms allows the tri-Higgs search programme to obtain optimal sensitivity.

It is also important to note that the $H \rightarrow gg$ decay channel should be investigated. The feasibility depends on the performance of quark-gluon tagging. So far, the quark-gluon tagging techniques are mainly studied in the single particle case. A double-gluon tagging algorithm analogous to the double-b tagging is another possible new avenue.

7 Theory studies and models, prospects at current and future hadron colliders

7.1 The TRSM and triple Higgs production

A. Papaefstathiou, T. Robens, G. Tetlalmatzi-Xolocotzi

We now turn to studies that investigate triple Higgs production in specific beyond the Standard Model realizations. As a first example, we consider a model where the SM scalar sector is enhanced by two additional real scalars. We consider here the "Two Real Singlet Model" [20,52], where the SM scalar sector is augmented by two additional scalar fields that transform as singlets under the SM gauge group. In addition, two $\mathbb{Z}_2$ symmetries are imposed, leading to a reduction of the available number of degrees of freedom.

The TRSM is characterized by the following scalar potential

$$V(\Phi, X, S) = \mu_\Phi^2 \Phi^\dagger \Phi + \lambda_\Phi \left(\Phi^\dagger \Phi\right)^2 + \mu_S^2 S^2$$
$$+ \lambda_S S^4 + \mu_X^2 X^2 + \lambda_X X^4$$
$$+ \lambda_{\Phi S} \Phi^\dagger \Phi S^2 + \lambda_{\Phi X} \Phi^\dagger \Phi X^2 + \lambda_{SX} S^2 X^2,$$
(11)

which contains nine real couplings $\mu_\Phi, \lambda_\Phi, \mu_S, \lambda_S, \mu_X, \lambda_X,$ $\lambda_{\Phi S}, \lambda_{\Phi X}, \lambda_{XS}$. All fields are assumed to acquire a vacuum expectation value (VEV). The physical gauge-eigenstates $\phi_{h,S,X}$ then follow from expanding around these according to:

$$\Phi = \begin{pmatrix} 0 \\ \frac{\phi_h + v}{\sqrt{2}} \end{pmatrix}, \quad S = \frac{\phi_S + v_S}{\sqrt{2}}, \quad X = \frac{\phi_X + v_X}{\sqrt{2}}. \quad (12)$$

The scalars ϕ_h, ϕ_S, ϕ_X mix into the physical states h_1, h_2 and h_3 according to

$$\begin{pmatrix} h_1 \\ h_2 \\ h_3 \end{pmatrix} = R \begin{pmatrix} \phi_h \\ \phi_S \\ \phi_X \end{pmatrix}, \quad (13)$$

with the rotation matrix R characterized by the angles

$$-\frac{\pi}{2} < \theta_{hS}, \theta_{hX}, \theta_{SX} < \frac{\pi}{2}. \quad (14)$$

In our scenario h_1 is identified with the SM-like Higgs boson, and h_2 and h_3 are two new physical *heavier* scalars obeying the mass hierarchy

$$M_1 \le M_2 \le M_3. \quad (15)$$

The identification of h_1 as the SM-like scalar fixes

$$M_1 \simeq 125\,\text{GeV},$$
$$v \simeq 246\,\text{GeV}. \quad (16)$$

This leaves us with 7 independent parameters, which we chose as

$$M_2, M_3, \theta_{hS}, \theta_{hX}, \theta_{SX}, v_S, v_X. \quad (17)$$

As this model contains three CP even neutral scalars, double resonance enhanced production of $h_1 h_1 h_1$ is possible and can be realized according to

$$pp \to h_3 \to h_2 h_1 \to h_1 h_1 h_1, \quad (18)$$

where $h_{1,2,3}$ are the physical scalar states of a model with an extended scalar sector. Depending on the values that the free parameters of Eq. (17) assume, different realisations of the TRSM are possible, yielding a rich phenomenology at colliders. Here we concentrate on the "Benchmark Plane 3" (**BP3**) addressed in [20], which was carefully tailored to allow for a large region in the (M_2, M_3) plane which obeys all current theoretical and experimental constraints, while at the same time allowing for a large $h_1 h_1 h_1$ decay rate. **BP3** is characterised by the numerical values of the parameters shown in Table 7.

The values of the cross sections in the plane $[M_2, M_3]$ are given in Fig. 40. It can be seen that the regions with maximal values occur when h_2 and h_3 are produced on-shell.

Note that several regions in that plane are already ruled out by current LHC data, as e.g. $h_{2/3} \to h_1 h_1$ [227–230], $h_3 \to ZZ$ [231], as well as $h_3 \to h_1 h_2$ searches [232],

Table 7 The numerical values for the independent parameter values of Eq. (17) that characterise **BP3**. The Higgs doublet VEV, v, is fixed to 246 GeV. The κ_i values correspond to the rescaling parameters of the SM-like couplings for the respective scalars and are derived quantities

Parameter	Value
M_1	125.09 GeV
M_2	[125, 500] GeV
M_3	[255, 650] GeV
θ_{hS}	−0.129
θ_{hX}	0.226
θ_{SX}	−0.899
v_S	140 GeV
v_X	100 GeV

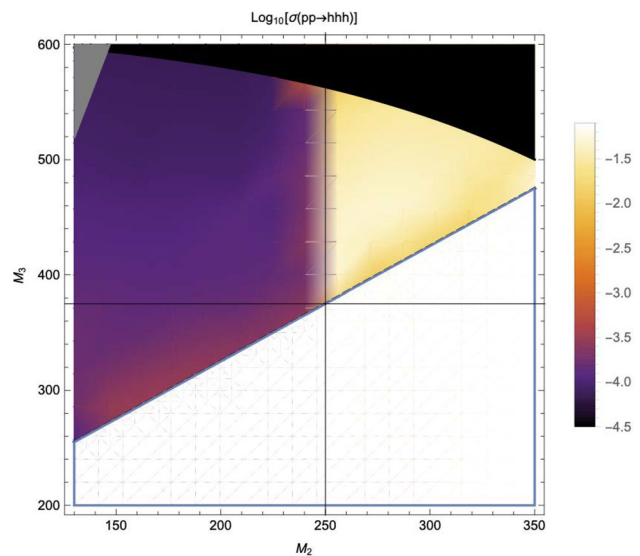**Fig. 40** The total leading-order gluon-fusion production cross sections for the $pp \to h_1 h_1 h_1$ process at a 14 TeV LHC. No cuts have been imposed. We also show the region excluded by constraints coming from perturbative unitarity in the dark upper part and boundedness from below in the gray wedge. In the allowed region, the leading-order predictions reach cross-section values of up to ~ 50 fb

see e.g. [233,234]. Concerned are regions for which $M_3 \lesssim 350 - 450$ GeV or $M_2 \lesssim 140$ GeV.

The results presented here have been presented in [35], to which we refer the reader for more details on the model as well as analysis setup. For reference, we here briefly list the most important details.

An event is analysed if it contains at least 6 b-tagged jets with a transverse momentum of at least $p_{T min,b} = 25$ GeV and a pseudo-rapidity no greater than $|\eta_{b,max}| = 2.5$. These initial cuts are further optimised for each of our signal samples, which are characterised by different combinations of M_2 and M_3.

We then select the 6 b-tagged jets with the highest transverse momentum and form pairs in different combinations,

Table 8 The resulting selection efficiencies, $\varepsilon_{\text{Sig.}}$ and $\varepsilon_{\text{Bkg.}}$, number of events, S and B for the signal and background, respectively. A b-tagging efficiency of 0.7 has been assumed. The number of signal and background events are provided at an integrated luminosity of 300 fb^{-1}.

Results for 3000 fb^{-1} are obtained via simple extrapolation. The significance is given at both values of the integrated luminosity excluding (including) systematic errors in the background. Table taken from [35]

Label	(M_2, M_3) [GeV]	$\varepsilon_{\text{Sig.}}$	$S\vert_{300\text{fb}^{-1}}$	$\varepsilon_{\text{Bkg.}}$	$B\vert_{300\text{fb}^{-1}}$	sig$\vert_{300\text{fb}^{-1}}$ (syst.)	sig$\vert_{3000\text{fb}^{-1}}$ (syst.)
A	(255, 504)	0.025	14.12	8.50×10^{-4}	19.16	2.92 (2.63)	9.23 (5.07)
B	(263, 455)	0.019	17.03	3.60×10^{-5}	8.12	4.78 (4.50)	15.10 (10.14)
C	(287, 502)	0.030	20.71	9.13×10^{-5}	20.60	4.01 (3.56)	12.68 (6.67)
D	(290, 454)	0.044	37.32	1.96×10^{-4}	44.19	5.02 (4.03)	15.86 (6.25)
E	(320, 503)	0.051	31.74	2.73×10^{-4}	61.55	3.76 (2.87)	11.88 (4.18)
F	(264, 504)	0.028	18.18	9.13×10^{-5}	20.60	3.56 (3.18)	11.27 (5.98)
G	(280, 455)	0.044	38.70	1.96×10^{-4}	44.19	5.18 (4.16)	16.39 (6.45)
H	(300, 475)	0.054	41.27	2.95×10^{-4}	66.46	4.64 (3.47)	14.68 (4.94)
I	(310, 500)	0.063	41.43	3.97×10^{-4}	89.59	4.09 (2.88)	12.94 (3.87)
J	(280, 500)	0.029	20.67	9.14×10^{-5}	20.60	4.00 (3.56)	12.65 (6.66)

with the aim of first reconstructing individual SM-like Higgs bosons, h_1, and subsequently the two scalars h_2 and h_3. Thus, we introduce two observables:

$$\chi^{2,(4)} = \sum_{qr \in I} \left(M_{qr} - M_1 \right)^2, \tag{19}$$

$$\chi^{2,(6)} = \sum_{qr \in J} \left(M_{qr} - M_1 \right)^2, \tag{20}$$

where we have defined the sets $I = \{i_1 i_2, i_3 i_4\}$ and $J = \{j_1 j_2, j_3 j_4, j_5 j_6\}$, constructed from different pairings of 4 and 6 b-tagged jets, respectively. Moreover, M_{qr} denotes the invariant mass of the respective pairing, qr. It should be understood that each jet can appear only in a single arrangement inside I and J. We select the combinations of b-tagged jets entering in I and J based on the minimisation of the sum

$$\chi^{2,(6)} + \chi^{2,(4)}. \tag{21}$$

The optimisation of the analysis is based on the sequential application of cuts on the different observables including $p_{Tmin,b}$, $|\eta_b|$, $\chi^{2,(6)}$, $\chi^{2,(4)}$, m_{6b}^{inv}, m_{4b}^{inv}. In addition we consider observables affecting the pairings of b-jets which define the combinations of six and four elements: (v) $p_T(h_1^i)$, (vi) $(\Delta m_{\text{min, med, max}})$, (vii) $\Delta R(h_1^i, h_1^j)$, (viii) $\Delta R_{bb}(h_1^i)$. We optimize for cuts on the different observables by constructing a grid over each one of them and exploring sequentially combinations of cuts which deliver the maximum rejection of the background while maintaining the highest acceptance for the signal. The specific values for the cuts depend on the combination of masses for the physical scalars h_2 and h_3.

We show the results after these selection cuts in Table 8. Note that we show significances with and without taking systematic uncertainties into account. For more details on the actual selection process, we refer the reader to [35].

We also provide some distributions for the b-jets $p_\perp$ and pseudorapidity in Fig. 41. Events have been generated using the TRSM model file available at [235], with leading order event generation using Madgraph [236]. Distributions have been obtained within the Madanalysis framework [237].

Another important question is whether the benchmark points discussed above could already be tested by other channels at the HL-LHC, e.g. via heavy resonance production decaying into a pair of (vector)-bosons. For this, we have extrapolated various analyses assessing the heavy Higgs boson prospects of the HL-LHC in final states originating from $h_i \rightarrow h_1 h_1$ [238,239], $h_i \rightarrow ZZ$ [8,240] and $h_i \rightarrow W^+W^-$ [241,242], for $i = 2, 3$, and combined these with extrapolations of results from 13 TeV where appropriate. We display the results in Fig. 42.

In particular ZZ final states can probe nearly all of the available parameter space. However, such searches do investigate different parts of the potential, and therefore can be seen as complementary.

7.2 Other theory scenarios

T. Robens

We here briefly discuss other scenarios that lead to triple scalar final states within the TRSM, as well as other new physics scenarios that can lead to triple scalar final states. TRSM benchmark planes follow the discussion in [20,52], with more recent updates available in [233,234].

In addition to the benchmark plane discussed above, two more scenarios can render interesting triple scalar final states. The first one is BP1, where the heaviest scalar is associated with the 125 GeV resonance at the LHC. For this parameter plane, the input parameters are specified in Table 9.
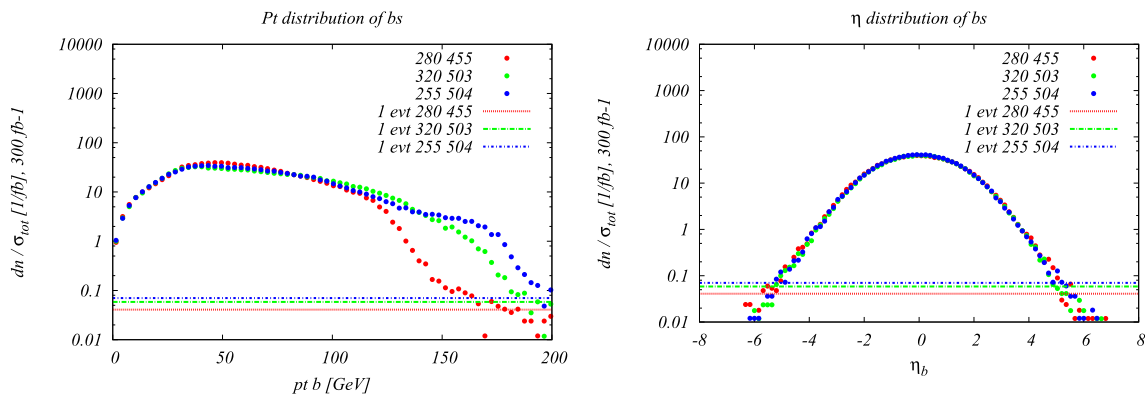
Fig. 41 For various benchmark points from Table 8, we show the $p_\perp$ distribution *(left)* as well as η_b distribution *(right)* of the b-jets, normalized to the respective production cross sections at 13 TeV. Shown are points G (280,455) *(red)*, E (320,503) *(green)*, and A (255,504) *(blue)*.

Also displayed are lines that would represent 1 event for an integrated luminosity of $300\,\text{fb}^{-1}$. While the rapidity distributions do not display significant differences, the $p_\perp$ distributions show large differences, with a major dependence on the absolute scale M_3
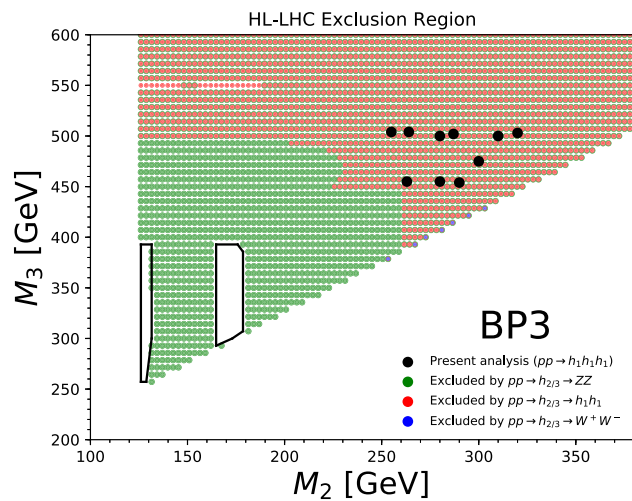

Fig. 42 Constraints on the (M_2, M_3) plane from extrapolation of other searches at the HL-LHC from extrapolation (see text for details). Taken from [50]
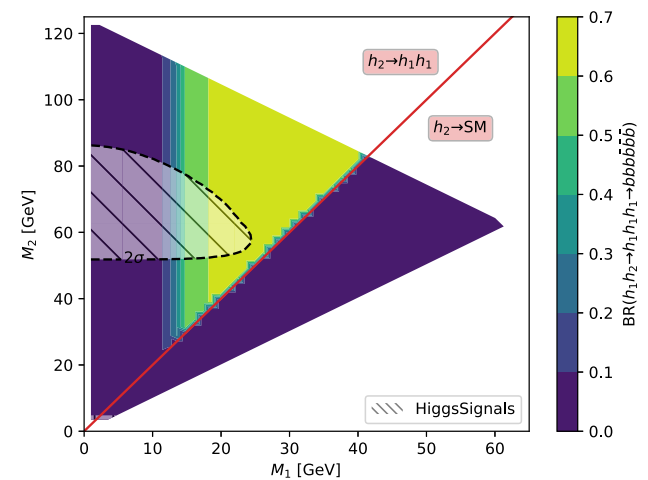

Fig. 43 Branching ratio into $6\,b$ final states for BP1, with triple light scalar productions. Cross sections can reach up to around 2 pb. Dominant constraints stem from signal strength measurements. Figure taken from [20]

Table 9 Input parameter values and coupling scale factors, κ_a ($a = 1, 2, 3$), for the three benchmark scenarios discussed here. The doublet VEV is set to $v = 246$ GeV for all scenarios. Table adapted from [20]

Parameter	Benchmark scenario		
	BP1	**BP3**	**BP6**
M_1 [GeV]	[1, 62]	125.09	125.09
M_2 [GeV]	[1, 124]	[126, 500]	[126, 500]
M_3 [GeV]	125.09	[255, 650]	[255, 1000]
θ_{hs}	1.435	−0.129	0.207
θ_{hx}	−0.908	0.226	0.146
θ_{sx}	−1.456	−0.899	0.782
v_s [GeV]	630	140	220
v_x [GeV]	700	100	150
κ_1	0.083	0.966	0.968
κ_2	0.007	0.094	0.045
κ_3	−0.997	0.239	0.246

For the BP1, we show the allowed benchmark plane in Fig. 43, where we have already included the branching ratio to $6\,b$ final states that can reach up to 70% depending on the specific mass range. Note that here due to the BP assumptions light scalars have masses $\lesssim 40$ GeV, leading to relatively soft decay products that might be difficult to trigger. Production cross section for the h_{125} GeV scalar is around 48 pb at 13 TeV.

Another point of interest is BP6, which was targeted for the $p\,p \rightarrow h_3 \rightarrow h_2\,h_2$ production and subsequent decays, where $M_{2,3} \geq 125$ GeV. We display the allowed parameter space in Fig. 44, and parameters are again defined in Table 9.

For this mass plane, production cross sections can reach up to 0.5 pb in the low mass region. As soon as the decay $h_2 \rightarrow$
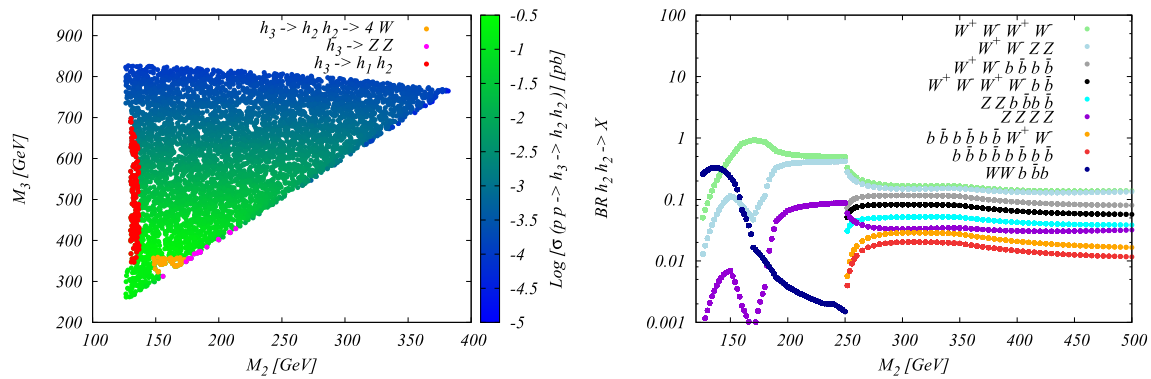
Fig. 44 Left: total rate for the $h_2 h_2$ final state at 13 TeV in BP6. Exclusions stem from 4W [243], ZZ [231], and $h_1 h_2$ [232] searches. Right: branching ratios of the $h_2 h_2$ final state as a function of M_2. Figures taken from [52,233]
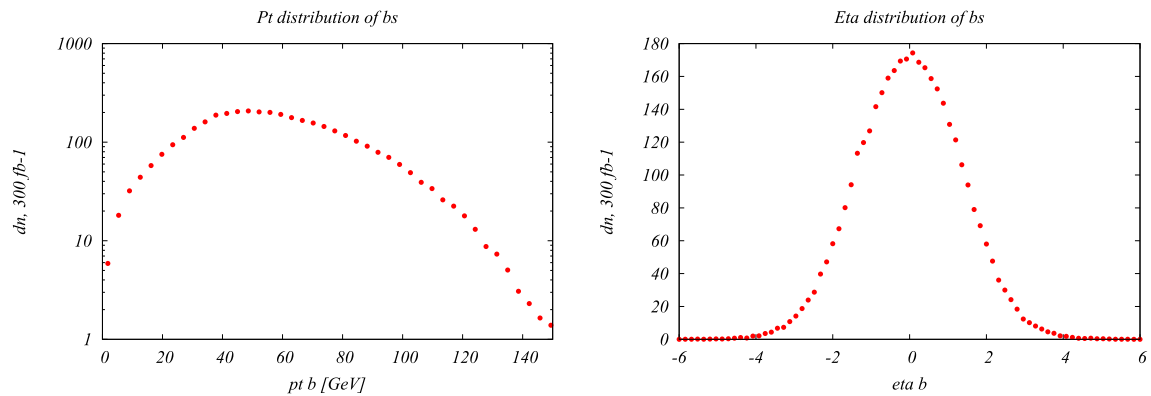

Fig. 45 Distributions of the b-jets for the process $p\,p \rightarrow h_3 \rightarrow h_2, h_2 \rightarrow h_2\,h_1\,h_1 \rightarrow W^+ W^- b\,\bar{b}\,b\,\bar{b}$

$h_1 h_1$ is kinematically allowed, interesting novel final states are possible, as e.g. $W^+ W^- b\,\bar{b}\,b\,\bar{b}$ or $W^+ W^- W^+ W^- b\,\bar{b}$.

In Fig. 45, we furthermore provide the distributions for the b-jets for a sample point where $M_2 = 279$ GeV, $M_3 = 583$ GeV, and $\sigma_{h_1 h_2} = 185$ fb, and where we consider the $W^+ W^- b\,\bar{b}\,b\,\bar{b}$ final state with a total rate ~ 21 fb.

7.3 Cascade Higgs-to-Higgs decays in the C2HDM, N2HDM and NMSSM

H. Abouabid, A. Arhrib, D. Azevedo, J. El Falaki, P. Ferreira, M. Mühlleitner, R. Santos

In non-minimal Higgs models multi-Higgs final states may arise from cascade Higgs-to-Higgs decays (see for instance a recent study of Ref. [244]). In some models, the cross sections can still be probed during the next LHC run. Moreover, there are scenarios where double Higgs production becomes more relevant than single Higgs production. We will discuss three extensions of the Standard Model where these processes are relevant: the complex two-Higgs Doublet Model (C2HDM), the Next-to-2HDM (N2HDM) and the Non-Minimal Supersymmetric extension of the SM (NMSSM). A discussion of the models can be found in [245]

where a thorough discussion on double Higgs production in these models is presented. Here we will just present very briefly the models and the constraints they are subject to.

The NMSSM [61–72] solves the little hierarchy problem and more easily complies with the discovered SM-like Higgs mass after inclusion of the higher-order corrections [246]. The Higgs sector consists of two Higgs doublets to which a complex singlet superfield is added so that after electroweak symmetry breaking (EWSB) we have three neutral CP-even, two neutral CP-odd and two charged Higgs bosons in the spectrum. Supersymmetric (SUSY) relations constrain the Higgs potential parameters in a different way than non-SUSY models. Therefore, we also investigate non-SUSY Higgs sector extensions where the trilinear couplings are less constrained from a theoretical point of view. This way we make sure not to miss some possibly interesting di-Higgs signatures. We start with one of the most popular extensions complying with $\rho = 1$ at tree level, the C2HDM [53–57] where a second Higgs doublet is added to the SM sector. Incorporating a minimal set of BSM Higgs bosons (five in total, three neutral and two charged ones) allows for resonant di-Higgs enhancement [247]. In this model there are three CP-mixed and two charged Higgs bosons. In this case the SM-like Higgs

Table 10 Four left rows: the four Yukawa types of the $\mathbb{Z}_2$-symmetric 2HDM, stating which Higgs doublet couples to the different fermion types. Five right columns: corresponding $\mathbb{Z}_2$ assignment for the quark doublet Q, the up-type quark singlet u_R, the down-type quark singlet d_R, the lepton doublet L, and the lepton singlet l_R

	u-type	d-type	Leptons	Q	u_R	d_R	L	l_R
Type I	Φ_2	Φ_2	Φ_2	$+$	$-$	$-$	$+$	$-$
Type II	Φ_2	Φ_1	Φ_1	$+$	$-$	$+$	$+$	$-$
Flipped (FL)	Φ_2	Φ_1	Φ_2	$+$	$-$	$-$	$+$	$+$
Lepton-specific (LS)	Φ_2	Φ_2	Φ_1	$+$	$-$	$+$	$+$	$-$

couplings can be diluted by CP admixture, the same happens through singlet admixture. Thus, light Higgs bosons may not be excluded yet because they may have escaped discovery through small couplings to the SM particles. Such a singlet admixture is realized in the next-to-2HDM (N2HDM) [58–60] as well as in the complex-singlet extensions of 2HDM with anomaly-free U(1) [248,249]. By adding, for instance, a real singlet field to the 2HDM Higgs sector the Higgs spectrum then consists of three neutral CP-even Higgs bosons, one neutral CP-odd and two charged Higgs bosons, allowing for the possibility of Higgs-to-Higgs cascade decays. This is also possible in the C2HDM and the NMSSM. For simplicity, we will focus on the type I and II versions of the C2HDM and N2HDM.

7.3.1 Models and scans

In this section we just briefly review the models and refer to Ref. [245] for details.

The real and complex 2HDM

The 2HDM was first proposed by Lee in 1973 [53] to provide an extra source of CP violation via spontaneous symmetry breaking. The version considered here has a softly broken discrete $\mathbb{Z}_2$ symmetry under $\Phi_1 \rightarrow \Phi_1$ and $\Phi_2 \rightarrow -\Phi_2$. In terms of the two $SU(2)_L$ Higgs doublets $\Phi_{1,2}$ with hypercharge $Y = +1$, the most general scalar potential which is $SU(2)_L \times U(1)_Y$ invariant and possesses a softly broken $\mathbb{Z}_2$ symmetry is given by

$$
\begin{aligned}
V_{\text{(C)2HDM}} = {} & m_{11}^2 |\Phi_1|^2 + m_{22}^2 |\Phi_2|^2 - m_{12}^2 (\Phi_1^\dagger \Phi_2 + h.c.) \\
& + \frac{\lambda_1}{2} (\Phi_1^\dagger \Phi_1)^2 + \frac{\lambda_2}{2} (\Phi_2^\dagger \Phi_2)^2 \\
& + \lambda_3 (\Phi_1^\dagger \Phi_1)(\Phi_2^\dagger \Phi_2) + \lambda_4 (\Phi_1^\dagger \Phi_2)(\Phi_2^\dagger \Phi_1) \\
& + \left[\frac{\lambda_5}{2} (\Phi_1^\dagger \Phi_2)^2 + H.c. \right].
\end{aligned} \tag{22}
$$

The $\mathbb{Z}_2$ symmetry is introduced in the model in order to avoid tree-level flavour-changing neutral currents (FCNCs) mediated by the neutral scalar. Since the $\mathbb{Z}_2$ symmetry is extended to the fermion sector, it will force all families of same-charge fermions to couple to a single doublet which eliminates tree-

level FCNCs [15,250]. This implies four different types of doublet couplings to the fermions listed in Table 10.

In the CP-violating version of the 2HDM, the C2HDM, the parameters m_{12}^2 and λ_5 can be complex. The two complex doublet fields can be parametrised as

$$
\Phi_i = \begin{pmatrix} \phi_i^+ \\ \frac{1}{\sqrt{2}}(v_i + \rho_i + i\eta_i) \end{pmatrix}, \quad i = 1, 2, \tag{23}
$$

with $v_{1,2}$ being the vacuum expectation values (VEVs) of the two doublets $\Phi_{1,2}$. After EWSB three of the eight degrees of freedom initially present in $\Phi_{1,2}$ are taken by the Goldstone bosons to give masses to the gauge bosons $W^\pm$ and Z, and we are left with five physical Higgs bosons. In the C2HDM, the three neutral Higgs bosons mix, resulting in three neutral Higgs mass eigenstates H_i ($i = 1, 2, 3$) with no definite CP quantum number and which by convention are ordered as $m_{H_1} \leq m_{H_2} \leq m_{H_3}$. The rotation matrix R diagonalising the neutral Higgs sector can be parametrised in terms of three mixing angles α_i ($i = 1, 2, 3$) as

$$
R = \begin{pmatrix} c_1 c_2 & s_1 c_2 & s_2 \\ -(c_1 s_2 s_3 + s_1 c_3) & c_1 c_3 - s_1 s_2 s_3 & c_2 s_3 \\ -c_1 s_2 c_3 + s_1 s_3 & -(c_1 s_3 + s_1 s_2 c_3) & c_2 c_3 \end{pmatrix}, \tag{24}
$$

where $s_i \equiv \sin \alpha_i$, $c_i \equiv \cos \alpha_i$, and, without loss of generality, the angles vary in the range

$$
-\frac{\pi}{2} \leq \alpha_i \leq \frac{\pi}{2}. \tag{25}
$$

We also define

$$
\tan \beta = \frac{v_2}{v_1} \tag{26}
$$

and identify

$$
v = \sqrt{v_1^2 + v_2^2}, \tag{27}
$$

where v is the SM VEV, $v \approx 246$ GeV.

In the C2HDM the three neutral Higgs boson masses are not independent. The third neutral Higgs mass is a dependent quantity and is obtained from the input parameters, cf. [251]. We choose two of the three neutral Higgs boson masses as input values and calculate the third one. The chosen input masses are called m_{H_i} and m_{H_j} with H_i per default denoting the lighter one, i.e. $m_{H_i} < m_{H_j}$. They denote any two of

the three neutral Higgs bosons among which we take one to be the 125 GeV SM-like scalar. We furthermore replace the three mixing angles $\alpha_{1,2,3}$ by two coupling values of H_i and by a matrix element of our rotation matrix. These are the squared H_i couplings to the massive gauge bosons V and to the top quarks t, $c_{H_i VV}^2$ and $c_{H_i tt}^2$, respectively, and the neutral mixing matrix entry R_{23}. We furthermore fix the sign of R_{13}, $\text{sg}(R_{13})$, to either $+1$ or -1 in order to lift the degeneracy that we introduce by specifying only the squared values of the H_i couplings. This choice of input parameters complies with the input parameters of the program code ScannerS that we will use for our parameter scans as explained below. We hence have the input parameter set

$$v, \quad \tan\beta, \quad c_{H_i VV}^2, \quad c_{H_i tt}^2, \quad R_{23}, \quad m_{H_i},$$
$$m_{H_j}, \quad m_{H^\pm} \quad \text{and} \quad \text{Re}(m_{12}^2). \tag{28}$$

One should notice here that in certain multi-Higgs scenarios, featuring flavour symmetries in both the Higgs and fermion sectors, the next-to-lightest scalars may predominantly couple to the light (first- or second-generation) quarks, thus, significantly altering their production and decay observables compared to conventional searches [252]. A comprehensive analysis of the multi-Higgs production channels in such models is a subject of a future work.

The N2HDM

We briefly introduce the N2HDM and refer to [59] for more details. The scalar potential of the N2HDM can be obtained from the 2HDM potential by adding a real singlet field Φ_S. In terms of the two $SU(2)_L$ Higgs doublets Φ_1 and Φ_2, defined in Eq. (23), and the singlet field, defined as

$$\Phi_S = v_S + \rho_S, \tag{29}$$

the N2HDM potential is given by

$$V_{\text{N2HDM}} = V_{\text{2HDM}} + \frac{1}{2}m_S^2\Phi_S^2 + \frac{\lambda_6}{8}\Phi_S^4$$
$$+ \frac{\lambda_7}{2}(\Phi_1^\dagger\Phi_1)\Phi_S^2 + \frac{\lambda_8}{2}(\Phi_2^\dagger\Phi_2)\Phi_S^2. \tag{30}$$

The above scalar potential is obtained by imposing two $\mathbb{Z}_2$ symmetries,

$$\Phi_1 \to \Phi_1, \quad \Phi_2 \to -\Phi_2, \quad \Phi_S \to \Phi_S \quad \text{and}$$
$$\Phi_1 \to \Phi_1, \quad \Phi_2 \to \Phi_2, \quad \Phi_S \to -\Phi_S. \tag{31}$$

The first (softly-broken) $\mathbb{Z}_2$ symmetry is the extension of the usual 2HDM $\mathbb{Z}_2$ symmetry to the N2HDM which, once extended to the Yukawa sector, will forbid FCNCs at tree level, implying four different N2HDM versions just like in the 2HDM, cf. Table 10. The second $\mathbb{Z}_2$ symmetry is an exact symmetry which will be spontaneously broken by the singlet VEV and as such does not allow the model to have a DM candidate. Other versions of the model choose parameters such that $v_S = 0$ yielding very interesting DM phenomenology,

but in the current work we will not consider these possibilities.

After EWSB, we have three neutral CP-even Higgs bosons $H_{1,2,3}$ with masses ranked as $m_{H_1} < m_{H_2} < m_{H_3}$, one neutral CP-odd boson A and a pair of charged Higgs bosons $H^\pm$. The physical states $H_{1,2,3}$ are obtained from the weak basis (ρ_1, ρ_2, ρ_S) by an orthogonal transformation R which is defined by 3 mixing angles $\alpha_{1,2,3}$ that are in the same range as in the C2HDM. After exploiting the minimisation conditions, we are left with twelve independent input parameters for the N2HDM. For the scan, we will again replace the three mixing angles $\alpha_{1,2,3}$ by the squared H_1 couplings to massive gauge bosons V and the top quarks t, $c_{H_1 VV}^2$ and $c_{H_1 tt}^2$, respectively, and the neutral mixing matrix element R_{23}, so that our input parameters read

$$\tan\beta \quad c_{H_1 VV}^2 \quad c_{H_1 tt}^2 \quad R_{23} \quad m_{H_1} \quad m_{H_2}$$
$$m_{H_3} \quad m_A \quad m_{H^\pm} \quad v, \quad v_s \quad \text{and} \quad m_{12}^2. \tag{32}$$

Like in the 2HDM, we fix $\text{sg}(R_{13})$ to either $+1$ or -1 in order to lift the introduced degeneracy through the squared values of the H_1 couplings.

The NMSSM

As a supersymmetric benchmark model, we consider the next-to minimal supersymmetric SM (NMSSM) [63–72]. It extends the two doublet fields $\hat{H}_u$ and $\hat{H}_d$ of the MSSM by a complex superfield $\hat{S}$. When the singlet field acquires a non-vanishing VEV, this not only solves the μ problem [253] but, compared to the MSSM, it also relaxes the tension on the stop mass values that need to be large for the SM-like Higgs boson mass value to be compatible with the measured 125.09 GeV. Indeed in supersymmetry the neutral Higgs masses are given in terms of the gauge parameters at tree level so that there is an upper mass bound on the lightest neutral scalar which, in the MSSM, is given by the Z boson mass. Substantial higher-order corrections to the Higgs boson mass are therefore required to obtain phenomenologically valid mass values for the SM-like Higgs boson. The additional singlet contribution to the tree-level mass of the lightest neutral Higgs boson shifts its mass to larger values compared to the MSSM prediction, thus no longer requiring large radiative corrections. The scale-invariant NMSSM superpotential that is added to the MSSM superpotential W^{MSSM} reads

$$W^{\text{NMSSM}} = -\lambda\hat{S}\hat{H}_u \cdot \hat{H}_d + \frac{\kappa}{3}\hat{S}^3 + W^{\text{MSSM}}, \quad \text{with}$$
$$W^{\text{MSSM}} = -y_t\widehat{Q}_3\widehat{H}_u\widehat{t}_R^c + y_b\widehat{Q}_3\widehat{H}_d\widehat{b}_R^c + y_\tau\widehat{L}_3\widehat{H}_d\widehat{\tau}_R^c, \tag{33}$$

where for simplicity we only included the third generation fermion superfields, given by the left-handed doublet quark $(\widehat{Q}_3)$ and lepton $(\widehat{L}_3)$ superfields, and the right-handed singlet quark $(\widehat{t}_R^c, \widehat{b}_R^c)$ and lepton $(\widehat{\tau}_R^c)$ superfields. The NMSSM-type couplings λ and κ are dimensionless and taken real since

we consider the CP-conserving NMSSM. The Yukawa couplings y_t, y_b, y_τ can always be taken real. The scalar part of $\hat{S}$ will develop a VEV $v_S/\sqrt{2}$, which dynamically generates the effective μ parameter $\mu_{\text{eff}} = \lambda v_S/\sqrt{2}$ through the first term in the superpotential. The second term, cubic in $\hat{S}$, breaks the Peccei-Quinn symmetry and thus avoids a massless axion, and W^{MSSM} contains the Yukawa interactions. The symplectic product $x \cdot y = \epsilon_{ij} x^i y^j$ $(i, j = 1, 2)$ is built by the antisymmetric tensor $\epsilon_{12} = \epsilon^{12} = 1$. The soft SUSY breaking Lagrangian reads

$$
\begin{aligned}
\mathcal{L}_{\text{soft,NMSSM}} = & -m_{H_u}^2 |H_u|^2 - m_{H_d}^2 |H_d|^2 - m_{\widetilde{Q}_3}^2 |\widetilde{Q}_3^2| \\
& -m_{\tilde{t}_R}^2 |\tilde{t}_R^2| - m_{\tilde{b}_R}^2 |\tilde{b}_R^2| - m_{\widetilde{L}_3}^2 |\widetilde{L}_3^2| \\
& -m_{\tilde{\tau}_R}^2 |\tilde{\tau}_R^2| + (y_t A_t H_u \cdot \widetilde{Q}_3 \tilde{t}_R^c - y_b A_b H_d \cdot \widetilde{Q}_3 \tilde{b}_R^c \\
& -y_\tau A_\tau H_d \cdot \widetilde{L}_3 \tilde{\tau}_R^c + \text{H.c.}) \\
& -\frac{1}{2} \left(M_1 \widetilde{B} \widetilde{B} + M_2 \sum_{a=1}^{3} \widetilde{W}^a \widetilde{W}_a + M_3 \sum_{a=1}^{8} \widetilde{G}^a \widetilde{G}_a + \text{H.c.} \right) \\
& -m_S^2 |S|^2 + (\lambda A_\lambda S H_d \cdot H_u - \frac{1}{3} \kappa A_\kappa S^3 + \text{H.c.}),
\end{aligned}
\tag{34}
$$

where again only the third generation of fermions and sfermions have been taken into account. The tilde over the fields denotes the complex scalar component of the corresponding superfields. The soft SUSY breaking gaugino parameters M_k $(k = 1, 2, 3)$ of the bino, wino and gluino fields $\widetilde{B}$, $\widetilde{W}$ and $\widetilde{G}$, as well as the soft SUSY breaking trilinear couplings A_x $(x = \lambda, \kappa, t, b, \tau)$ are in general complex, whereas the soft SUSY breaking mass parameters of the scalar fields, m_X^2 $(X = S, H_d, H_u, \widetilde{Q}, \tilde{u}_R, \tilde{b}_R, \widetilde{L}, \tilde{\tau}_R)$ are real. Since we consider the CP-conserving NMSSM, they are all taken real. In what follows, we will use conventions such that λ and $\tan \beta$ are positive, whereas κ, A_λ, A_κ and μ_{eff} are allowed to have both signs.

After EWSB, we expand the Higgs fields around their VEVs v_u, v_d, and v_S, respectively, which are chosen to be real and positive

$$
\begin{aligned}
H_d &= \begin{pmatrix} (v_d + h_d + i a_d)/\sqrt{2} \\ h_d^- \end{pmatrix}, \\
H_u &= \begin{pmatrix} h_u^+ \\ (v_u + h_u + i a_u)/\sqrt{2} \end{pmatrix}, \\
S &= \frac{v_s + h_s + i a_s}{\sqrt{2}}.
\end{aligned}
\tag{35}
$$

This leads to the mass matrices of the three scalars h_d, h_u, h_s, the three pseudoscalars a_d, a_u, a_s, and the charged Higgs states $h_u^\pm$, $h_d^\mp$, obtained from the second derivatives of the scalar potential. The mass matrix is diagonalised with orthogonal rotation matrices, mapping the gauge eigenstates to the mass eigenstates. These are the three neutral CP-even Higgs bosons H_1, H_2, H_3 that are ordered by ascending mass with $m_{H_1} \leq m_{H_2} \leq m_{H_3}$, the two CP-odd mass eigenstates A_1

and A_2 with $m_{A_1} \leq m_{A_2}$, and a pair of charged Higgs bosons $H^\pm$.

After applying the minimisation conditions, we choose as independent input parameters for the tree-level NMSSM Higgs sector the following,

$$
\lambda \; \kappa \; A_\lambda \; A_\kappa, \; \tan \beta = v_u/v_d \quad \text{and} \quad \mu_{\text{eff}} = \lambda v_s/\sqrt{2} .
\tag{36}
$$

Further parameters will become relevant upon inclusion of the higher-order corrections to the Higgs boson mass that are crucial to shift the SM-like Higgs boson mass to the measured value.

Scans and theoretical and experimental constraints
We performed the scans with the help of the program ScannerS [254–256] for all models except for the NMSSM. There are various scenarios with respect to which neutral Higgs boson takes the role of the SM-like Higgs which we will denote H_{SM} from now on. We distinguish the cases "light" where the lightest of the neutral Higgs bosons is SM-like ($H_1 \equiv H_{\text{SM}}$), "medium" with $H_2 \equiv H_{\text{SM}}$, and "heavy" with the heaviest being SM-like ($H_3 \equiv H_{\text{SM}}$). Note also that we restrict ourselves to the type I and II models. For all these models we apply the same theoretical constraints, which have different expressions for each model, requiring that all potentials are bounded from below, that perturbative unitarity holds and that the electroweak vacuum is the global minimum. In the C2HDM we use the discriminant from [257].

As for experimental constraints, we impose compatibility with the electroweak precision data by demanding the computed S, T and U values to be within 2σ of the SM fit [258], taking into account the full correlation among the three parameters. We require one of the Higgs bosons to have a mass of [259]

$$
m_{H_{\text{SM}}} = 125.09 \, \text{GeV},
\tag{37}
$$

and to behave SM-like. Compatibility with the Higgs signal data is checked through HiggsSignals version 2.6.1 [260] which is linked to ScannerS. We furthermore suppress interfering Higgs signals by forcing any other neutral scalar mass to deviate by more than ± 2.5 GeV from $m_{H_{\text{SM}}}$. Scenarios with neutral Higgs bosons that are close in mass are particularly interesting for non-resonant di-Higgs production as they may have discriminating power with respect to the SM case. The appearance of non-trivial interference effects requires, however, a dedicated thorough study that is beyond the focus of this study and is left for future work. We require 95% C.L. exclusion limits on non-observed scalar states by using HiggsBounds version 5.9.0 [261–263]. Additionally, we checked our sample with respect to the recent ATLAS analyses in the ZZ [231] and $\gamma\gamma$ [264] final states that were not yet included in HiggsBounds. Consistency with recent flavour constraints is ensured by testing for the compatibility with $\mathcal{R}_b$ [265,266] and $B \rightarrow X_s \gamma$ [266–

271] in the $m_{H^\pm} - \tan\beta$ plane (the code SuperIso [272] used for flavour physics is interfaced with ScannerS). For the non-supersymmetric type II models, we imposed the latest bound on the charged Higgs mass given in [271], $m_{H^\pm} \geq 800$ GeV for essentially all values of $\tan\beta$, whereas in the type I models this bound is much weaker and is strongly correlated with $\tan\beta$.

Lower values for $m_{H^\pm}$ allow, via electroweak precision constraints, different ranges for the masses of the neutral Higgs bosons, which will therefore affect our predictions for di-Higgs production.

In the C2HDM, we additionally have to take into account constraints on CP violation in the Higgs sector arising from electric dipole moment (EDM) measurements. Among these, the data from the EDM of the electron imposes the strongest constraints [273], with the current best experimental limit given by the ACME collaboration [274]. We demand compatibility with the values given in [274] at 90% C.L.

In the NMSSM, we use the program NMSSMCALC [275, 276] and compute the Higgs mass corrections up to $\mathcal{O}((\alpha_t + \alpha_\lambda + \alpha_\kappa)^2 + \alpha_t\alpha_s)$ [277–279] with on-shell renormalisation in the top/stop sector. We demand the computed SM-like Higgs boson mass to lie in the range 122 GeV...128GeV which accounts for the present typically applied theoretical error of 3 GeV [246]. We use HiggsBounds and HiggSignals to check for compatibility with the Higgs constraints. Furthermore, we omit parameter points with the following mass configurations for the lightest chargino $\tilde{\chi}_1^\pm$ and the lightest stop $\tilde{t}_1$,

$$m_{\tilde{\chi}_1^\pm} < 94 \text{ GeV}, \quad m_{\tilde{t}_1} < 1 \text{ TeV}, \tag{38}$$

to take into account lower limits on the lightest chargino and the lightest stop mass. The experimental limits given by the LHC experiments ATLAS and CMS rely on assumptions on the mass spectra and are often based on simplified models. The quotation of a lower limit therefore necessarily requires a scenario that matches the assumptions made by the experiments. For our parameter scan we therefore chose a conservative approach to apply limits that roughly comply with the recent limits given by ATLAS and CMS [280,281]. For further details of the Higgs mass computation and of the input parameters as well as their scan ranges, we refer to [279].

7.3.2 Multi-Higgs final states

In non-minimal Higgs models like the C2HDM, N2HDM, and NMSSM we can have multi-Higgs final states from cascade Higgs-to-Higgs decays. In the production of a SM-like plus non-SM-like Higgs final state, $H_{SM}\Phi$, we found that both the Higgs-to-Higgs decay of the SM-like Higgs or the non-SM-like one can lead to substantial final state rates. The largest next-to-leading-order (NLO) rates that we found above 10 fb, in the multi-Higgs final state, are summarised in

Table 11. In the C2HDM, we did not find NLO rates above 10 fb. We maintain the ordering of particles with regards to their decay chains, so that it becomes clear which Higgs boson decays into which Higgs pair. We give the rates in the $(6b)$ final state as they lead to the largest cross sections for all shown scenarios. In the following, we highlight a few benchmark scenarios from the table.

Non-SM-like Higgs search: di-Higgs beats single Higgs

In the following we present N2HDM-I and NMSSM scenarios with three SM-like Higgs bosons in the final states with H_1 being SM-like and with NLO rates above 10 fb. These benchmark points are special in the sense that the production of the non-SM-like Higgs boson H_2 from di-Higgs states beats, or is at least comparable to, its direct production. This appears in cases where the non-SM-like Higgs is singlet-like and/or is more down- than up-type like. The latter suppresses direct production from gluon fusion. The former suppresses all couplings to SM-like particles. In these cases the heavy non-SM-like Higgs boson might rather be discovered in the di-Higgs channel than in direct single Higgs production.

The input parameters for the N2HDM-I point are given in Table 12. With the values for the NLO $H_1 H_2$ cross section and the branching ratios BR($H_2 \to H_1 H_1$) and BR($H_1 \to b\bar{b}$) we get the following rate in the 6b final state,

$$\begin{aligned} &\sigma_{H_1 H_2}^{NLO} \times \text{BR}(H_2 \to H_1 H_1) \times \text{BR}(H_1 \to b\bar{b})^3 \\ &= 509 \cdot 0.37 \cdot 0.60^3 \text{ fb} = 40 \text{ fb}. \end{aligned} \tag{39}$$

We can compare this with direct H_2 production (we use the NNLO value calculated with SusHi [282–284]) in either the 4b final state from the $H_2 \to H_1 H_1$ decay,

$$\begin{aligned} &\sigma^{NNLO}(H_2) \times \text{BR}(H_2 \to H_1 H_1) \times \text{BR}(H_1 \to b\bar{b})^2 \\ &= 161 \cdot 0.37 \cdot 0.60^2 \text{ fb} = 21 \text{ fb}, \end{aligned}$$

$$\tag{40}$$

or direct H_2 production in the other dominant decay channel given by the WW final state,

$$\sigma^{NNLO}(H_2) \times \text{BR}(H_2 \to WW) = 161 \cdot 0.44 \text{ fb} = 71 \text{ fb}. \tag{41}$$

Note that the H_2 branching ratio into $(b\bar{b})$ is tiny. The second lightest Higgs boson H_2 has a significant down-type and large singlet admixture but only a small up-type admixture so that its production in gluon fusion is not very large[2] and also its decay branching ratios into a lighter Higgs pair are comparable to the largest decay rates into SM particles. In this case, the non-SM-like Higgs boson H_2 has better chances of being discovered in di-Higgs when compared to single Higgs channels. Note, that the W bosons still need to decay into

---

[2] The production in association with b quarks is very small for the small $\tan\beta$ value of this scenario.

Table 11 Upper: maximum rates for multi-Higgs final states given at NLO QCD in the heavy-top mass limit. The K-factor is given in the last column. In the third and fourth column we also give the mass values m_{Φ_1} and m_{Φ_2} of the non-SM-like Higgs bosons involved in the process, in the order of their appearance. Lower: in case of resonantly enhanced production the mass of the resonantly produced Higgs boson is given together with the next-to-next-to-leading order (NNLO) QCD production rate. More details on these points can be provided on request

Model	Mixed Higgs state	m_{Φ_1} [GeV]	m_{Φ_2} [GeV]	Rate [fb]	K-factor
N2HDM-I	$H_2 H_3 (\equiv H_{SM}) \to H_1 H_1 (b\bar{b}) \to (b\bar{b})(b\bar{b})(b\bar{b})$	98	41	15	1.95
	$H_2 H_1 (\equiv H_{SM}) \to H_1 H_1 (b\bar{b}) \to (b\bar{b})(b\bar{b})(b\bar{b})$	282	–	40	1.96
	$H_2 H_1 (\equiv H_{SM}) \to AA (b\bar{b}) \to (b\bar{b})(b\bar{b})(b\bar{b})$	157	73	33	2.05
	$H_1 H_2 (\equiv H_{SM}) \to (b\bar{b}) H_1 H_1 \to (b\bar{b})(b\bar{b})(b\bar{b})$	54	–	111	2.09
	$H_3 H_2 (\equiv H_{SM}) \to H_1 H_1 (b\bar{b}) \to (b\bar{b})(b\bar{b})(b\bar{b})$	212	83	8	1.93
N2HDM-II	$H_2 H_1 (\equiv H_{SM}) \to H_1 H_1 (b\bar{b}) \to (b\bar{b})(b\bar{b})(b\bar{b})$	271	–	3	1.87
NMSSM	$H_2 H_1 (\equiv H_{SM}) \to H_1 H_1 (b\bar{b}) \to (b\bar{b})(b\bar{b})(b\bar{b})$	319	–	11	1.90
	$H_2 H_1 (\equiv H_{SM}) \to A_1 A_1 (b\bar{b}) \to (b\bar{b})(b\bar{b})(b\bar{b})$	253	116	26	1.92

Model	Mixed Higgs state	$m_{res.}$ [GeV]	Res. rate [fb]
N2HDM-I	$H_2 H_3 (\equiv H_{SM}) \to H_1 H_1 (b\bar{b}) \to (b\bar{b})(b\bar{b})(b\bar{b})$	–	–
	$H_2 H_1 (\equiv H_{SM}) \to H_1 H_1 (b\bar{b}) \to (b\bar{b})(b\bar{b})(b\bar{b})$	441	39
	$H_2 H_1 (\equiv H_{SM}) \to AA (b\bar{b}) \to (b\bar{b})(b\bar{b})(b\bar{b})$	294	37
	$H_1 H_2 (\equiv H_{SM}) \to (b\bar{b}) H_1 H_1 \to (b\bar{b})(b\bar{b})(b\bar{b})$	229	119
	$H_3 H_2 (\equiv H_{SM}) \to H_1 H_1 (b\bar{b}) \to (b\bar{b})(b\bar{b})(b\bar{b})$	–	–
N2HDM-II	$H_2 H_1 (\equiv H_{SM}) \to H_1 H_1 (b\bar{b}) \to (b\bar{b})(b\bar{b})(b\bar{b})$	615	2
NMSSM	$H_2 H_1 (\equiv H_{SM}) \to H_1 H_1 (b\bar{b}) \to (b\bar{b})(b\bar{b})(b\bar{b})$	560	11
	$H_2 H_1 (\equiv H_{SM}) \to A_1 A_1 (b\bar{b}) \to (b\bar{b})(b\bar{b})(b\bar{b})$	518	26

Table 12 Di-Higgs beats single Higgs: N2HDM-I input parameters

m_{H_1} [GeV]	m_{H_2} [GeV]	m_{H_3} [GeV]	m_A [GeV]	$m_{H^\pm}$ [GeV]	$\tan\beta$
125.09	281.54	441.25	386.98	421.81	1.990

α_1	α_2	α_3	v_s [GeV]	$\mathrm{Re}(m_{12}^2)$ [GeV^2]
1.153	0.159	0.989	9639	29769

fermionic final states where additionally the neutrinos are not detectable so that the H_2 mass cannot be reconstructed.

The input parameters for the first NMSSM scenario that we discuss here are given in Table 13. We also specify in Table 14 the parameters required for the computation of the Higgs pair production cross sections through HPAIR.

Since H_2 is rather singlet-like, its production cross section through gluon fusion is small and also its decay branching ratios into SM-final states. The gluon fusion production cross section amounts to

$$\sigma^{NNLO}(H_2) = 13.54 \text{ fb.} \tag{42}$$

Its dominant branching ratio is given by the decay into $A_1 A_1$, reaching

$$\mathrm{BR}(H_2 \to A_1 A_1) = 0.887. \tag{43}$$

We hence get for direct H_2 production in the $A_1 A_1$ final state the rate

$$\sigma^{NNLO}(H_2) \times \mathrm{BR}(H_2 \to A_1 A_1) = 12.01 \text{ fb.} \tag{44}$$

On the other hand, we have for di-Higgs production of $H_1 H_2$ at NLO QCD where H_1 is the SM-like Higgs state,

$$\sigma^{NLO}(H_1 H_2) = 111 \text{ fb.} \tag{45}$$

With

$$\mathrm{BR}(H_1 \to b\bar{b}) = 0.539, \tag{46}$$

and the H_2 branching ratio into $A_1 A_1$ given above we hence have

$$\sigma^{NLO}(H_1 H_2) \times \mathrm{BR}(H_1 \to b\bar{b}) \\ \times \mathrm{BR}(H_2 \to A_1 A_1) = 53 \text{ fb.} \tag{47}$$

Table 13 Di-Higgs beats single Higgs: NMSSM input parameters required by `NMSSMCALC` for the computation of the NMSSM spectrum

λ	κ	A_λ [GeV]	A_κ [GeV]	μ_{eff} [GeV]	$\tan\beta$
0.593	0.390	296	5.70	200	2.815
$m_{H^\pm}$ [GeV]	M_1 [GeV]	M_2 [GeV]	M_3 [TeV]	A_t [GeV]	A_b [GeV]
505	989.204	510.544	2	-2064	-1246
$m_{\tilde{Q}_3}$ [GeV]	$m_{\tilde{t}_R}$ [GeV]	$m_{\tilde{b}_R}$ [GeV]	A_τ [GeV]	$m_{\tilde{L}_3}$ [GeV]	$m_{\tilde{\tau}_R}$ [GeV]
1377	1207	3000	-1575.91	3000	3000

Table 14 These input parameters and those given in the first line of Table 13 are required by `HPAIR` for the computation of the Higgs pair production cross sections. The total width of the charged Higgs boson is not required but given here for completeness $\Gamma_{H^\pm}^{\text{tot}} = 3.94$ GeV

m_{H_1} [GeV]	m_{H_2} [GeV]	m_{H_3} [GeV]	m_{A_1} [GeV]	m_{A_2} [GeV]
127.78	253	518	116	508
$\Gamma_{H_1}^{\text{tot}}$ [GeV]	$\Gamma_{H_2}^{\text{tot}}$ [GeV]	$\Gamma_{H_3}^{\text{tot}}$ [GeV]	$\Gamma_{A_1}^{\text{tot}}$ [GeV]	$\Gamma_{A_2}^{\text{tot}}$ [GeV]
$4.264 \, 10^{-3}$	0.466	3.145	$9.9 10^{-7}$	4.750
h_{11}	h_{12}	h_{13}	h_{21}	h_{22}
0.325	0.939	-0.112	0.234	0.034
h_{23}	h_{31}	h_{32}	h_{33}	a_{11}
0.971	0.916	-0.321	-0.209	-0.0063
a_{21}	a_{13}	a_{23}		
-0.0022	0.999	0.0067		

With

$$\text{BR}(A_1 \to b\bar{b}) = 0.704 \tag{48}$$

we then obtain in double Higgs production in the $6b$ final state the rate

$$\sigma^{\text{NLO}}(H_1 H_2)_{6b} = 53 \times 0.704^2 \text{ fb} = 26 \text{ fb.} \tag{49}$$

On the other hand, we have in single Higgs production for the $4b$ final state

$$\begin{aligned} \sigma^{\text{NNLO}}(H_2)_{4b} &= \sigma^{\text{NNLO}}(H_2) \times \text{BR}(H_2 \to A_1 A_1) \\ &\quad \times \text{BR}(A_1 \to b\bar{b})^2 \\ &= 13.54 \times 0.887 \times 0.704^2 \text{ fb} = 5.95 \text{ fb.} \end{aligned} \tag{50}$$

Note that direct H_2 production with subsequent decay into $W^+ W^-$ only reaches a rate of 1 fb. We clearly see that di-Higgs beats single Higgs production and the non-SM-like singlet-dominated state H_2 might be first discovered in di-Higgs production instead directly in single H_2 production through gluon fusion.

For the second NMSSM benchmark scenario that we present here the input parameters for `NMSSMCALC` and `HPAIR` are summarized in Tables 15 and 16. The singlet-like H_2 dominantly decays into an SM-like pair $H_1 H_1$, and in the $H_1 H_1$ final state we obtain the rate

$$\begin{aligned} \sigma^{\text{NNLO}}(H_2) \times \text{BR}(H_2 \to H_1 H_1) &= 134.95 \cdot 0.566 \text{ fb} \\ &= 76.38 \text{ fb.} \end{aligned} \tag{51}$$

With $\text{BR}(H_1 \to b\bar{b}) = 0.636$ this results in the $4b$ rate

$$\begin{aligned} &\sigma^{\text{NNLO}}(H_2) \times \text{BR}(H_2 \to H_1 H_1) \times \text{BR}^2(H_1 \to b\bar{b}) \\ &= 31.00 \text{ fb.} \end{aligned} \tag{52}$$

On the other hand, with $\text{BR}(H_2 \to b\bar{b}) = 0.103$, we have the $2b$ final state rate

$$\begin{aligned} \sigma^{\text{NNLO}}(H_2) \times \text{BR}(H_2 \to b\bar{b}) &= 134.95 \cdot 0.104 \text{ fb} \\ &= 14.03 \text{ fb.} \end{aligned} \tag{53}$$

The rate for direct H_2 production in the $4b$ final state via its decay into $H_1 H_1$ beats the one of direct H_2 production in the $2b$ final state by more than a factor of 2. Note finally that the $6b$ rate for H_2 production, through $H_1 H_2$ production and further H_2 decay into Higgs pairs, amounts to

$$\begin{aligned} &\sigma^{\text{NLO}}(H_1 H_2) \times \text{BR}(H_2 \to H_1 H_1) \times \text{BR}^3(H_1 \to b\bar{b}) \\ &= 75 \cdot 0.566 \cdot 0.636^3 \text{ fb} = 11 \text{ fb,} \end{aligned} \tag{54}$$

which is not much below the $2b$ final state rate.

Non-SM-like Higgs pair final states For non-SM-like Higgs pair production, we can have a large plethora of all possible Higgs pair combinations inducing final states with multiple Higgs bosons, two or three Higgs bosons in association with one or two gauge bosons, or also with a top-quark pair, resulting finally in multi-fermion, multi-photon or multi-fermion plus multi-photon final states (see e.g. Ref. [244]). We present a few selected interesting signatures from non-SM-like Higgs pair production in Table 17. More signatures and benchmark

Table 15 Di-Higgs beats single Higgs: NMSSM input parameters required by `NMSSMCALC` for the computation of the NMSSM spectrum

λ	κ	A_λ [GeV]	A_κ [GeV]	μ_{eff} [GeV]	$\tan\beta$
0.545	0.598	168	-739	258	2.255
$m_{H^\pm}$ [GeV]	M_1 [GeV]	M_2 [GeV]	M_3 [TeV]	A_t [GeV]	A_b [GeV]
548	437.872	498.548	2	-1028	1083
$m_{\tilde{Q}_3}$ [GeV]	$m_{\tilde{t}_R}$ [GeV]	$m_{\tilde{b}_R}$ [GeV]	A_τ [GeV]	$m_{\tilde{L}_3}$ [GeV]	$m_{\tilde{\tau}_R}$ [GeV]
1729	1886	3000	-1679.21	3000	3000

Table 16 These input parameters and those given in the first line of Table 13 are required by `HPAIR` for the computation of the Higgs pair production cross sections. The total width of the charged Higgs boson is not required but given here for completeness $\Gamma_{H^\pm}^{\text{tot}} = 5.503$ GeV

m_{H_1} [GeV]	m_{H_2} [GeV]	m_{H_3} [GeV]	m_{A_1} [GeV]	m_{A_2} [GeV]
123.20	319	560	545	783
$\Gamma_{H_1}^{\text{tot}}$ [GeV]	$\Gamma_{H_2}^{\text{tot}}$ [GeV]	$\Gamma_{H_3}^{\text{tot}}$ [GeV]	$\Gamma_{A_1}^{\text{tot}}$ [GeV]	$\Gamma_{A_2}^{\text{tot}}$ [GeV]
3.985×10^{-3}	0.010	4.207	6.399	6.913
h_{11}	h_{12}	h_{13}	h_{21}	h_{22}
0.419	0.909	0.015	0.187	-0.102
h_{23}	h_{31}	h_{32}	h_{33}	a_{11}
0.977	0.889	-0.407	-0.212	0.908
a_{21}	a_{13}	a_{23}		
-0.104	0.114	0.994		

points can be provided on request. As we can infer from the table, we can have high rates in non-SM-like Higgs pair production, e.g. up to 9 pb in the 4b final state from non-SM-like $H_1 H_1$ production in the N2HDM-I with $H_2 \equiv H_{\text{SM}}$ (marked by a '*' in Table 17).

7.3.2.1 Cascade decays with multiple Higgs final states
As already stated, in non-mimimal Higgs extensions, we can have Higgs-to-Higgs cascade decays that can lead to multiple Higgs final states. The largest rate at NLO QCD that we found, for a final state with more than three Higgs bosons, is given in the N2HDM-I, where we have

$$\sigma(pp \to H_2 H_2 \to H_1 H_1 H_1 H_1 \to 4(b\bar{b})) = 1.4 \text{ fb}. \quad (55)$$

The SM-like Higgs is H_1 and the K-factor for the NLO QCD production of $H_2 H_2$ is 1.82. Also in the NMSSM and C2HDM we can have multiple Higgs production but the rates are below 10 fb after the decays of the Higgs bosons. In the N2HDM, we can even produce up to eight Higgs bosons in the final states but the rates are too small to be measurable.

7.4 Constraints on the trilinear and quartic Higgs self-couplings at HL-LHC

P. Stylianou, G. Weiglein

7.4.1 Introduction

In the SM, the self-interactions of the Higgs boson depend on the form of the potential,

$$V(\Phi) = \lambda(\Phi^\dagger \Phi)^2 - \mu^2 \Phi^\dagger \Phi, \quad (56)$$

and are parameterised by λ and μ. The potential can be reparameterised in terms of the Higgs mass M_H and VEV v, which have been measured experimentally. However, a more complicated potential could be realised in nature, arising from models with a richer scalar sector, and measuring the Higgs self-couplings will thus provide concrete information on the exact shape beyond the SM ansatz. One should notice also that the Higgs self-interactions may, in general, receive large radiative corrections which are strongly sensitive to the existence of New Physics states coupled to the Higgs boson. For a systematic procedure of calculation of such corrections starting from the one-loop effective potential, see Ref. [285].

Deviations away from the SM values can be experimentally studied in the κ-framework, where for the self-interactions we define $\kappa_i = g_i / g_i^{\text{SM}}$ for $i = 3, 4$, and g_i^{SM} is the SM coupling at leading order. The production of a Higgs pair allows the direct probe of the trilinear coupling κ_3, and the ATLAS [5] and CMS [4] experiments provide limits on by combining the gluon fusion and weak boson fusion (WBF) production channels with different decays of the Higgs. ATLAS additionally includes information from

Table 17 Upper: selected rates for non-SM-like Higgs pair final states at NLO QCD. We specify the model, which of the Higgs bosons is the SM-like one, the signature and its rate as well as the K-factor. In the fourth column we also give the mass value m_Φ of the non-SM-like Higgs boson involved in the process. Lower: in case of resonantly enhanced cross sections, the mass of the resonantly produced Higgs boson is given together with the NNLO QCD production rate. Some scenarios contain two heavier Higgs bosons that can contribute to resonant production. All benchmark details can be provided on request

Model	SM-like Higgs	Signature	m_Φ [GeV]	Rate [fb]	K-factor
N2HDM-I	H_3	$H_1 H_1 \to (b\bar{b})(b\bar{b})$	41	14538	2.18
	H_3	$H_1 H_1 \to (4b); (4\gamma)$	41	4545 ; 700	2.24
	H_1	$AA \to (b\bar{b})(b\bar{b})$	75	6117	2.11
	H_1	$H_2 H_2 \to (b\bar{b})(b\bar{b})$	146	73	2.01
	H_2	$AA \to (b\bar{b})(b\bar{b})$	80	2875	2.13
	H_2	$AH_1 \to (b\bar{b})(b\bar{b})$	$m_A : 87$ $m_{H_1} : 91$	921	2.09
*	H_2	$H_1 H_1 \to (b\bar{b})(b\bar{b})$	47	8968	2.17
N2HDM-II	H_2	$H_1 H_1 \to (b\bar{b})(b\bar{b})$	44	1146	2.18
C2HDM-I	H_1	$H_2 H_2 \to (b\bar{b})(b\bar{b})$	128	475	2.07
	H_2	$H_1 H_1 \to (b\bar{b})(b\bar{b})$	66	814	2.16
	H_3	$H_1 H_1 \to (b\bar{b})(b\bar{b})$	84	31	2.09
NMSSM	H_1	$A_1 A_1 \to (b\bar{b})(b\bar{b})$	166	359	1.95
	H_1	$A_1 A_1 \to (\gamma\gamma)(\gamma\gamma)$	179	34	1.96
	H_2	$H_1 H_1 \to (b\bar{b})(b\bar{b})$	48	3359	2.18
	H_2	$A_1 A_1 \to (b\bar{b})(b\bar{b})$	54	1100	2.18
	H_1	$A_1 A_1 \to (t\bar{t})(t\bar{t})$	350	20	1.82

Model	Signature	$m_{\rm res.}$ [GeV]	res. rate [fb]	$m_{\rm res.}$ 2 [GeV]	res. rate 2 [fb]
N2HDM-I	$H_1 H_1 \to (b\bar{b})(b\bar{b})$	125.09	621	98	17137
	$H_1 H_1 \to (4b); (4\gamma)$	125.09	126; 19	94	5445; 839
	$AA \to (b\bar{b})(b\bar{b})$	1535	<0.1	323	482
	$H_2 H_2 \to (b\bar{b})(b\bar{b})$	360	76	–	–
	$AA \to (b\bar{b})(b\bar{b})$	178	3191	–	–
	$AH_1 \to (b\bar{b})(b\bar{b})$	–	–	–	–
	$H_1 H_1 \to (b\bar{b})(b\bar{b})$	588	22	125.09	997
N2HDM-II	$H_1 H_1 \to (b\bar{b})(b\bar{b})$	520	< 0.1	125.09	1330
C2HDM-I	$H_2 H_2 \to (b\bar{b})(b\bar{b})$	266	497	–	–
	$H_1 H_1 \to (b\bar{b})(b\bar{b})$	151	598	–	–
	$H_1 H_1 \to (b\bar{b})(b\bar{b})$	–	–	–	–
NMSSM	$A_1 A_1 \to (b\bar{b})(b\bar{b})$	552	31	453	332
	$A_1 A_1 \to (\gamma\gamma)(\gamma\gamma)$	796	< 0.01	444	34
	$H_1 H_1 \to (b\bar{b})(b\bar{b})$	882	<0.1	125.59	4173
	$A_1 A_1 \to (b\bar{b})(b\bar{b})$	676	< 0.1	122.99	1353
	$A_1 A_1 \to (t\bar{t})(t\bar{t})$	741	7	705	14

single-Higgs channels, where κ_3 enters at next-to-leading order, and provides the strongest limit of $\kappa_3 \in [-0.4, 6.3]$.

Triple Higgs production is sensitive to both the trilinear and quartic self-couplings and could enable establishing the first limit on κ_4, beyond theoretical constraints. However, it is known to suffer from small cross sections at the LHC. We motivate the possibility of large values of κ_3, κ_4 in

Sect. 7.4.2 and explore the potential constraints at HL-LHC in Sect. 7.4.3.

7.4.2 Theoretical motivation and perturbative unitarity

Theoretical bounds for κ_3 and κ_4 can be established by requiring perturbative unitarity to be satisfied [286]. Focusing on

the $HH \rightarrow HH$ scattering at tree level, which is the relevant channel to extract perturbative unitarity bounds for the self-couplings, the zeroth partial wave is given by

$$a^0 = \frac{3M_H^2\sqrt{s^2 - 4M_H^2 s}}{32\pi s(s - M_H^2)v^2}\left[\kappa_4(s - M_H^2) - 3\kappa_3^2 M_H^2 \right.$$
$$\left. + \frac{6\kappa_3^2 M_H^2(s - M_H^2)}{s - 4M_H^2}\log\left(\frac{s}{M_H^2} - 3\right)\right], \qquad (57)$$

and the requirement $|\text{Re}\left(a^0\right)| \leq 1/2$ gives the region that satisfies perturbative unitarity. For large values of s, a^0 depends only on κ_4 and yields a lower and upper bound on the quartic coupling, while for lower energies unitarity is violated depending on the value of κ_3, as shown in Fig. 46. The latter occurs at relatively low energies, so in practice we check that a particular value of κ_3 does not violate unitarity up to 10 TeV (this upper limit only matters for the corners of the contour at $\kappa_4 \sim 67$ and $|\kappa_3| \sim 9$). The current ATLAS bounds on $\kappa_3 \in [-0.4, 6.3]$, as well as the 95% combined ATLAS and CMS projection for the HL-LHC $\kappa_3 \in [0.1, 2.3]$ [8] are also shown.[3] The theoretical constraints on κ_3 are considerably stronger than on κ_4, which can be understood in terms of both an effective field theory prescription and concrete UV-models as discussed below.

A generic extension of the SM potential with higher dimensional operators included as a power expansion in inverse powers of a UV-scale Λ can be written as [288,289]

$$V_{\text{BSM}} = \frac{C_6}{\Lambda^2}\left(\Phi^\dagger\Phi - \frac{v^2}{2}\right)^3 + \frac{C_8}{\Lambda^4}\left(\Phi^\dagger\Phi - \frac{v^2}{2}\right)^4$$
$$+ \mathcal{O}\left(\frac{1}{\Lambda^6}\right). \qquad (58)$$

where the Higgs doublet can be expanded as $\Phi = \left(0, (v + H)/\sqrt{2}\right)$ and v, H are the vacuum expectation value and the 125 GeV Higgs, respectively. Parameterising the additional terms of the potential in this way ensures that κ_3 (κ_4) receives contributions only from dimension-six (dimension-six and -eight) operators but not ones of higher order. The coupling modifiers with this parameterisation are then given by

$$(\kappa_3 - 1) = \frac{C_6 v^2}{\lambda\Lambda^2},$$
$$(\kappa_4 - 1) = \frac{6C_6 v^2}{\lambda\Lambda^2} + \frac{4C_8 v^4}{\lambda\Lambda^4}. \qquad (59)$$

Requiring that dimension-eight operators vanish yields $(\kappa_4 - 1) \simeq 6(\kappa_3 - 1)$ (also shown as a line in Fig. 46) hinting

_____

[3] We note that the current bound is the observed one, with a best-fit value of $\kappa_3 = 3.0^{1.8}_{-1.9}$. Additionally the negative log-likelihood ratio as a function of κ_3 obtained by experiments is also asymmetric, implying that the central value does not correspond to the best-fit value [5,287].
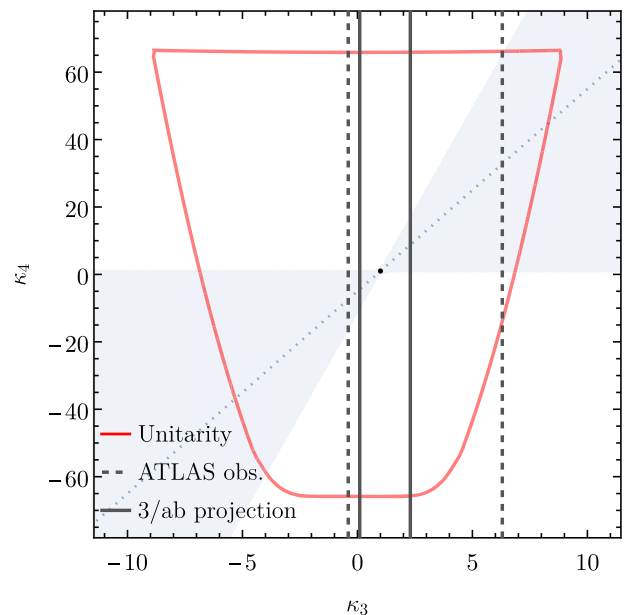
Fig. 46 Perturbative unitarity bounds for κ_3 and κ_4, as well as current experimental bounds (black dashed lines) and HL-LHC projections (black solid lines). The region where dimension-eight contributions to κ_4 are smaller than dimension-six is shown as a blue region, while the dotted blue line corresponds to $\kappa_4 - 1 \simeq 6(\kappa_3 - 1)$

that deviations on the quartic coupling can be more sizeable than the trilinear coupling, in-line with the weaker constraint of perturbative unitarity for κ_4. Relaxing the assumption of vanishing dimension-eight operators and requiring that the dimension-eight contribution to κ_4 is smaller than the dimension-six yields the condition $|(\kappa_4 - 1) - 6(\kappa_3 - 1)| < 6|\kappa_3 - 1|$.

As an example from a specific model, we focus on the Two-Higgs Doublet Model[4] and a specific benchmark point in the alignment limit from Ref. [290] that is currently not excluded by experiments. The particular benchmark point yields sizeable corrections to κ_3 at loop-level, and to show this we reproduce the one-loop result for κ_3 from Ref. [290] in Fig. 47, showing however also the the one-loop corrections to κ_4. Consistent with the effective approach and perturbative unitarity, κ_4 rises to significantly larger values than κ_3 hinting that if a deviation away from $\kappa_3 \sim 1$ is realised in nature, the deviation on $(\kappa_4 - 1)$ could in fact be much larger.

The correlation between κ_3 and κ_4 in the 2HDM (at one-loop) is also shown in Fig. 48 for different values of the scale $M = m_{12}/(c_\beta s_\beta)$ and m_A. The charged Higgs mass $m_{H^\pm}$ is kept equal to m_A which avoids 2HDM contributions to the oblique parameters S, T and U at one-loop level. A linear relation is maintained between the self-couplings for the particular parameter choices in the 2HDM and these values are within the region of well-behaved EFT framework with

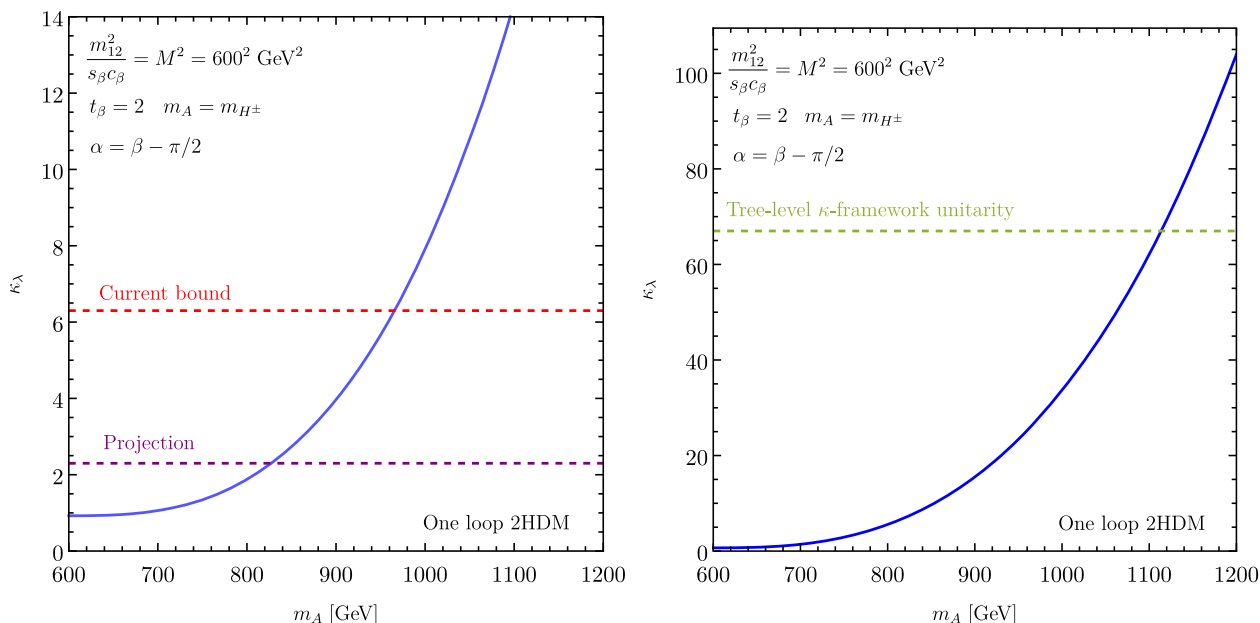**Fig. 47** One loop corrections to the trilinear coupling κ_3 (left) and to the quartic κ_4 (right). The scale $M = m_{12}/(c_\beta s_\beta)$ is fixed to $M = m_H = 600$ GeV and $m_A = m_{H^\pm}$ is varied. s_β, c_β and t_β correspond to $\sin\beta$, $\cos\beta$ and $\tan\beta$, respectively

higher order operators added to the potential. A non-linear approach (e.g. HEFT) would be required to study regions with small deviations of κ_3 but large κ_4 that do not lie in the well-behaved EFT shaded region. For the rest of this work we remain model-agnostic and use the κ-framework.

7.4.3 Triple Higgs at the HL-LHC

Setting limits on the self-couplings through triple Higgs production is a challenging task at the HL-LHC due to the small cross section rates and the difficult final states. To counter the former we focus on the dominant production through gluon fusion with on-shell Higgs bosons decaying to b-quarks and τ-leptons. In particular, we investigate the $6b$ final state with at least 5 tagged b-quarks and the $4b2\tau$ final state with at least 3 tagged b-quarks and 2 tagged τ leptons. The included background contamination for the $6b$ channel consists of multijet QCD events, while for the $4b2\tau$ we include $WWbbbb$ (including $ttbb$), $Zbbbb$, ttH ttZ and the $tttt$ production of the SM. Analyses with these final states have been previously performed for FCC-energies [35,38,50].

Events are generated using MADGRAPH [81,291][5] and a generation-level cut of 350 GeV is imposed on the minimum invariant mass of the process. Additionally, relaxed cuts are imposed on the transverse momentum p_T and pseudorapidity η of the b-quarks and τ-leptons: $p_T(b) > 30$ GeV, $p_T(\tau) > 10$ GeV, $|\eta(b)| < 2.5$ and $|\eta(\tau)| < 2.5$. Furthermore, at

Fig. 48 Correlation of κ_3 and κ_4 when $M = m_H$ and $m_A = m_{H^\pm}$ are varied. The solid lines correspond to particular values of M, while the purple area is the range of self-coupling values obtained for m_A, $M \in [0.3, 10]$ TeV. We also overlay blue shaded region of Fig. 46 and the gray region shows the area excluded by perturbative unitarity

least one pair of b-jets or τ-leptons should yield an invariant mass close to the SM Higgs mass, [110, 140] GeV. In order to include higher order effects, K-factors of 1.7 and 2 are applied on cross sections for signal [30] and background,

---

[5] We generate signal events for $pp \rightarrow hhh$ and subsequently decay them on-shell with MADSPIN [292].
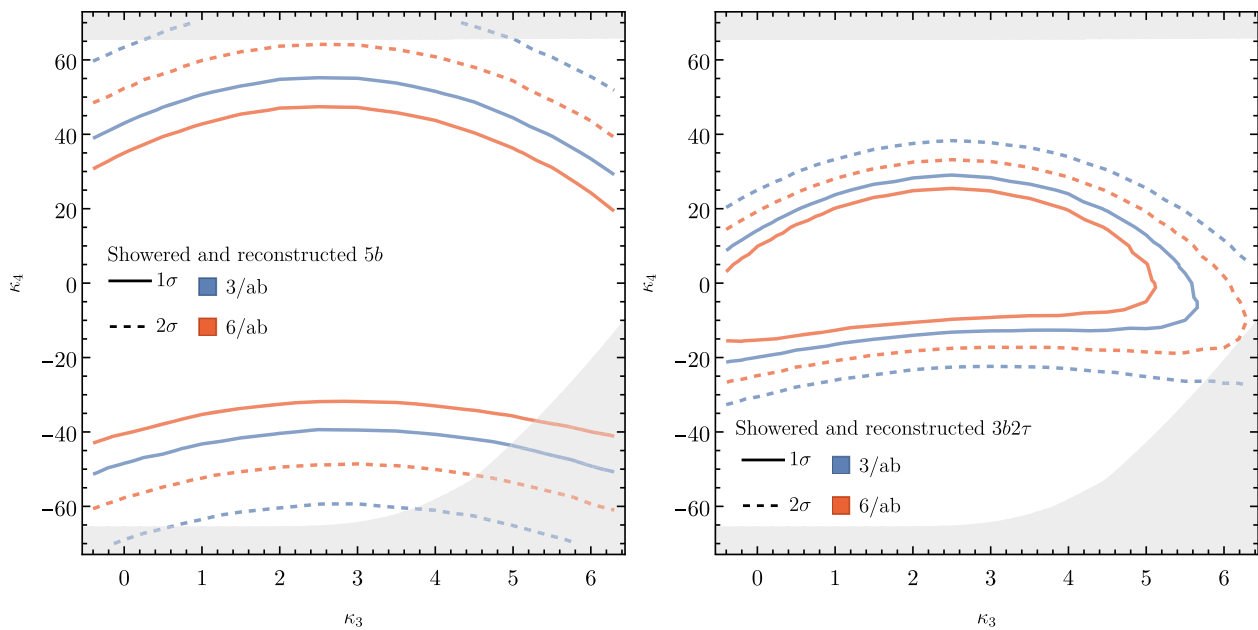
Fig. 49 The 1σ and 2σ bounds in the κ_3–κ_4 plane from the $6b$ analysis are shown on the left, while ones from the $4b2\tau$ analysis are shown on the right. The light gray area corresponds to the region excluded by unitarity

respectively. The tagging efficiencies for both b-quarks and τ leptons is assumed to be 0.8, and for the $4b2\tau$ analysis, at least one τ is assumed to decay hadronically.

To identify the appropriate signal region, a Graph Neural Network (GNN) with the EdgeConv [293] operation (similar to Refs. [294,295]) is trained on simulated signal data with $(\kappa_3, \kappa_4) = (1, 1)$ and background events. Nodes are added for b-tagged jets (and τ-tagged leptons), as well as pairs of b-quarks or τ-leptons that are close to the Higgs mass (for more details, see Ref. [32]). The features for each node are $[p_T, \eta, \phi, E, m, \text{PDGID}]$.

In the $6b$ analysis the network discriminates between two classes (signal and background), and the signal region is identified with a background rejection of ~ 0.4. We instead use multi-class classification for the $4b2\tau$, maintaining the different background contributions as different classes. The selection region is identified by requiring $P[WWbbbb] < 3\%$, $P[Zbbbb] < 10\%$ and $P[tt(H \to \tau\tau)] < 30\%$.

Based on the signal S and background events B in the signal region, we calculate the significance

$$Z = \sqrt{2\left((S + B)\ln\left(1 + \frac{S}{B}\right) - S\right)}. \qquad (60)$$

by assuming a HL-LHC luminosity of 3/ab and the resulting 1σ and 2σ contours for each channel are shown in Fig. 49, as well as the case of a combined ATLAS & CMS luminosity of 6/ab. Assuming no correlations, we additionally obtain the combined significance $Z_{\text{comb}} = \sqrt{Z_{5b}^2 + Z_{3b2\tau}^2}$, and show the relevant contours in Fig. 50.
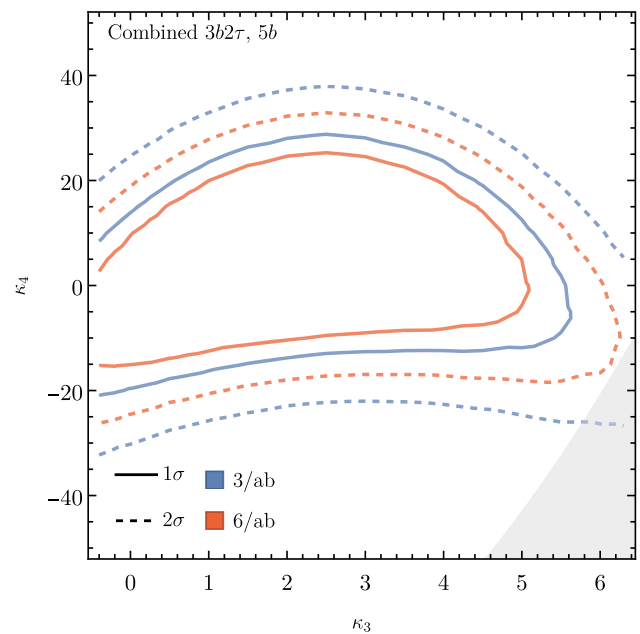
Fig. 50 The 1σ and 2σ bounds in the κ_3–κ_4 plane after a combination of the $6b$ and $4b2\tau$ analyses are shown. Perturbative unitarity is overlaid as a gray shaded area

7.4.4 Conclusions

Despite its low cross section rates, triple-Higgs production offers valuable insights into the Higgs self-couplings. The correlation between κ_3 and κ_4 can enable distinguishing between beyond the SM scenarios. A significant deviation

in κ_4 while maintaining consistency of κ_3 with the SM may suggest the presence of non-linear effects. Conversely, deviations in both couplings could align with expectations from certain specific models such as the 2HDM. Although sensitivity to κ_3 at HL-LHC will primarily come from di-Higgs production, incorporating HHH can still remain beneficial for combinations. Our findings suggest that triple-Higgs production at HL-LHC is expected to establish the first experimental constraints on κ_4 beyond theoretical bounds from perturbative unitarity.

7.5 Triple Higgs boson production with anomalous interactions

A. Papaefstathiou, G. Tetlalmatzi-Xolocotzi

7.5.1 Introduction

Novel Higgs boson interactions, to new or to SM particles, may arise at the electro-weak scale, but they may also appear at higher scales, $\mathcal{O}$(few TeV). If this is the case, we can parametrize our ignorance using a higher-dimensional effective field theory (EFT), see, e.g. [296–298]. Neglecting lepton-number violating operators, the lowest-dimensionality EFT that can be written down consists of $D = 6$ operators. Upon electro-weak symmetry breaking, the Higgs boson would acquire a VEV and these operators would result in several new interactions, as well modifications of the SM interactions of the Higgs boson. Several of the operators in the physical basis of the Higgs boson scalar (h) would then have coefficients that are correlated, according to $D = 6$ EFT. These correlations, however, may be broken by even higher-dimensional operators (e.g. $D = 8$), particularly if the new phenomena are closer to the electro-weak scale. Therefore, it may be beneficial to lean towards a more agnostic, and hence more phenomenological, approach and, while still remaining inspired by $D = 6$ EFT, consider fully uncorrelated, "anomalous" interactions of the Higgs boson with the SM. This is the approach that was pursued in [299].

7.5.2 Phenomenological Lagrangian for anomalous interactions

The implementation of this study further modifies the $D = 6$ EFT Lagrangian relevant to the Higgs boson's interactions, see, e.g. [300], to allow for uncorrelated, anomalous coefficients in the interactions. In addition, to match more closely

the LHC experimental collaboration definitions, we define the following phenomenological Lagrangian [301,302]:

$$
\begin{aligned}
\mathcal{L}_{\text{PhenoExp}} = & -\lambda_{\text{SM}} v \left(1 + d_3\right) h^3 - \frac{\lambda_{\text{SM}}}{4} \left(1 + d_4\right) h^4 \\
& + \frac{\alpha_s}{12\pi} \left(c_{g1} \frac{h}{v} - c_{g2} \frac{h^2}{2v^2} \right) G^a_{\mu\nu} G^{\mu\nu}_a \\
& - \left[\frac{m_t}{v} \left(1 + c_{t1}\right) \bar{t}_L t_R h + \frac{m_b}{v} \left(1 + c_{b1}\right) \bar{b}_L b_R h + \text{h.c.} \right] \\
& - \left[\frac{m_t}{v^2} c_{t2} \bar{t}_L t_R h^2 + \frac{m_b}{v^2} c_{b2} \bar{b}_L b_R h^2 + \text{h.c.} \right] \\
& - \left[\frac{m_t}{v^3} \left(\frac{c_{t3}}{2} \right) \bar{t}_L t_R h^3 + \frac{m_b}{v^3} \left(\frac{c_{b3}}{2} \right) \bar{b}_L b_R h^3 + \text{h.c.} \right],
\end{aligned}
$$

(61)

where we have taken $\lambda_{\text{SM}} \equiv m_h^2 / 2v^2$.

The CMS parametrization is then obtained by setting: $\kappa_\lambda = (1 + d_3)$, $k_t = c_{t1}$, $c_2 = c_{t2}$, $c_g = c_{g1}$, $c_{gg} = c_{2g}$ and the ATLAS parametrization by $c_{hhh} = (1 + d_3)$, $c_{ggh} = 2c_{g1}/3$, $c_{gghh} = -c_{g2}/3$ (see, e.g. [303]). The Lagrangian of Eq. 61 encapsulates the form of the interactions that we employ for the rest of our phenomenological analysis.

7.5.3 Monte Carlo event generation

The Lagrangian of Eq. 61 has been implemented in `MadGraph5_aMC@NLO` (MG5_aMC) [236,291], following closely the instructions for proposed code modifications found in [304].[6] These modifications essentially introduce tree-level diagrams in the form of fake "UV counter-terms", that are generated along with any loop-level diagrams, therefore allowing the calculation of interference terms between them, which are otherwise not technically possible. The model presented in this section, created through the procedure briefly outlined, has been fully validated by direct comparison to an implementation of Higgs boson pair production in $D = 6$ EFT in the `HERWIG 7` Monte Carlo, and by taking the limit of a heavy scalar boson for those vertices that do not appear in that process. See appendix B of [299] for further details of the latter effort. The necessary modifications to the `MG5_aMC` codebase,[7] as well as the model can be found in the public gitlab repository at [305].[8]

7.5.4 Phenomenological analysis

To obtain constraints on anomalous triple Higgs boson production at proton colliders, we have performed a hadron-

---

[6] Suggested by Valentin Hirschi.

[7] At present available for versions 2.9.15 and 3.5.0.

[8] It is interesting to note here that there exists a more comprehensive `MG5_aMC` treatment of one-loop computations in the standard-model effective field theory at $D = 6$ (dubbed "smeft@nlo") [306], which should directly map to the $D = 6$ limit of the present section.

level phenomenological analysis of the 6 b-jet final-state originating from the decays of all three Higgs bosons to $b\bar{b}$ quark pairs. We closely follow the analysis of Refs. [35,50]. Parton-level events have been generated using the MG5_aMC anomalous couplings implementation presented here, with showering, hadronization, and simulation of the underlying event, performed via the general-purpose HERWIG 7 Monte Carlo event generator [307–314]. The event analysis was performed via the HwSim framework addon to HERWIG 7 [315]. No smearing due to the detector resolution or identification efficiencies have been applied to the final objects used in the analysis, apart from a b-jet identification efficiency, discussed below.

The branching ratio of $h \to b\bar{b}$ will be modified primarily due to c_{t1}, c_{g1}, indirectly through modifications to the $h \to gg$ and $h \to \gamma\gamma$ branching ratios, and directly through c_{b1}. To take this effect into account, we employed the eHDECAY code [316]. The program eHDECAY includes QCD radiative corrections, and next-to-leading order EW corrections are only applied to the SM contributions. For further details, see Ref. [316]. We have performed a fit of the eHDECAY branching ratio $h \to b\bar{b}$, and we have subsequently normalized this to the latest branching ratio provided by the Higgs Cross Section Working Group's Yellow Report [131,140], BR($h \to b\bar{b}$) = 0.5824. The fit is then used to rescale the final cross section of $pp \to hhh \to (b\bar{b})(b\bar{b})(b\bar{b})$. The background processes containing Higgs bosons turned out to be subdominant with respect to the dominant QCD 6 b-jet and Z+jets backgrounds, and therefore we did not modify these when deriving the final cross sections.

For the generation of the backgrounds involving b-quarks *not* originating from either a Z or Higgs boson, we imposed the following generation-level cuts for the 100 TeV proton collider: $p_{T,b} > 30$ GeV, $|\eta_j| < 5.0$, and $\Delta R_{b,b} > 0.2$. The transverse momentum cut was lowered to $p_{T,b} > 20$ GeV for 13.6 TeV, except for the QCD 6 b-jet background, for which we produced the events inclusively, without any generation cuts.[9] The selection analysis was optimized considering as a main backgrounds the QCD-induced process $pp \to (b\bar{b})(b\bar{b})(b\bar{b})$, and the Z+jets process (represented by $Z + (b\bar{b})(b\bar{b})$), which we found to be significant at LHC energies.

The event selection procedure for our analyses proceeds as follows: as in [35], an event is considered if there are at least six b-tagged jets, of which only the six ones with the highest p_T are taken into account. A universal minimal threshold for the transverse momentum, $p_{T,b}$, of any of the

selected b-tagged jets is imposed. In addition a universal cut on their maximum pseudo-rapidity, $|\eta_b|$, is also applied. We subsequently make use of the observable:

$$\chi^{2,(6)} = \sum_{qr \in I} (m_{qr} - m_h)^2, \qquad (62)$$

where $I = \{jb_1jb_2, jb_3jb_4, jb_5jb_6\}$ is the set of all possible 15 pairings of 6-b tagged jets. Out of all the possible combinations we pick the one with the smallest value $\chi^{2,(6)}_{\min}$. The pairings of b-jets defining $\chi^{2,(6)}_{\min}$ constitute our best candidates for the reconstruction of the three Higgs bosons, h. Our studies have demonstrated that $\chi^{2,(6)}_{\min}$ is one of the most powerful observables to employ in signal versus background discrimination.

We further refine the discrimination power of the $\chi^{2,(6)}_{\min}$ variable by using the individual mass differences $\Delta m = |m_{qr} - m_h|$ in Eq. (62), sorting them out according to $\Delta m_{\min} < \Delta m_{\text{med}} < \Delta m_{\max}$, and imposing independent cuts on each of them. We also consider the transverse momentum $p_T(h^i)$ of each reconstructed Higgs boson candidate. These reconstructed particles are also sorted based on the value of $p_T(h^i)$, on which we then impose a cut. Besides the universal minimal threshold on $p_{T,b}$, introduced at the beginning of this section, we impose cuts on the three b-jets with the highest transverse momentum p_{T,b_i}, for $i = 1, 2, 3$. The set of cuts $p_{T,b_3} < p_{T,b_2} < p_{T,b_1}$ is the second most powerful discriminating observable in our list. Finally, we also considered two additional geometrical observables. The first of them is the distance between b-jets in each reconstructed Higgs boson $\Delta R_{bb}(h^i)$. The second one is the distance between the reconstructed Higgs bosons $\Delta R(h^i, h^j)$ themselves.

Our optimization process then proceeds as in [35,50]: we sequentially try different combination of cuts over the observables introduced above on our signal and background samples until we achieve a significance above 2 or when our number of Monte Carlo events is reduced so drastically that no meaningful statistical conclusions can be derived if this number becomes smaller (this happens for instance when for a given combination of cuts, we are left with less than 10 Monte Carlo events of signal or background).[10] The optimal set of cuts is shown in Table 18, and the resulting signal and background cross sections and number of events are shown in Table 19.

To employ the results of the SM analysis over the whole of the parameter space we are considering, we have performed a polynomial fit of the efficiency of the analysis on the signal,

---

[9] In general, the simulation of the QCD induced process $pp \to (b\bar{b})(b\bar{b})(b\bar{b})$ is one of the most challenging aspects of the phenomenological study. The samples are produced in parallel using OMNI cluster at the University of Siegen using the "gridpack" option available in MG5_aMC.

[10] Note the Poisson uncertainty on 10 Monte Carlo events is $\sim^{+2.3}_{-4.3}$, resulting in a worst-case scenario uncertainty of $\sim^{+23\%}_{-43\%}$ on our event rates. In practice, this only occurs for certain backgrounds, and given the rest of the uncertainties in the present phenomenological analysis, we have deemed this to be acceptable.

Table 18 Optimized cuts determined for the phenomenological analysis. The indices i, j can take the values $i, j = 1, 2, 3$. For the cut $\Delta R(h^i, h^j)$ the three pairings correspond to $(1, 2), (1, 3), (2, 3)$. The indexed elements should be read from left to right in increasing order. The last two rows refer to cuts over light jets

Optimized cuts		
Observable	13.6 TeV	100 TeV
$p_{T,b} >$	25.95 GeV	35.00 GeV
$|\eta_b| <$	2.3	3.3
$\Delta R_{bb} >$	0.3	0.3
$p_{T,b_i} >$	[25.95, 25.95, 25.95] GeV $i = 1, 2, 3$	[170.00, 135.00, 35.00] GeV
$\chi^{2,(6)} <$	27.0 GeV	26.0 GeV
$\Delta m_{\min, \text{med}, \max} <$	[100, 200, 300] GeV	[8, 8, 8] GeV
$\Delta R_{bb}(h^i) <$	[3.5, 3.5, 3.5]	[3.5, 3.5, 3.5]
$\Delta R(h^i, h^j) <$	[3.5, 3.5, 3.5]	[3.5, 3.5, 3.5]
$p_T(h^i) >$	[0.0, 0.0, 0.0] GeV	[200.0, 190.0, 20.0] GeV
$p_{T\text{jet}} >$	25 GeV	25 GeV
$|\eta_{\text{jet}}| <$	4.0	4.0

Table 19 The lists of processes considered during our phenomenological analysis, along with their respective cross sections to the 6 b-jet final state. The efficiencies $\varepsilon_{\text{analysis}}$ and number of events $N_{\mathcal{L}}^{\text{cuts}}$, correspond to those obtained after applying the set of cuts given in Table 18. A b-jet identification efficiency of 0.85 (for each b-jet) has also been applied to obtain the number of events. For the HL-LHC we considered an integrated luminosity of $\mathcal{L} = 3000$ fb^{-1}, and for the FCC-hh a luminosity of $\mathcal{L} = 20$ ab^{-1}. To approximate higher-order corrections, a K-factor $K = 2$ has been included for all processes, with respect to the leading-order cross section. The background processes that are shown to be initiated via "pp" constitute the LO (tree-level) contributions, whereas those marked with "LI" represent loop-induced contributions that form NLO corrections. Since they do not interfere with the LO processes, they have been generated separately. If a Z boson is not stated in the process definition, the $(b\bar{b})$ has a QCD origin

Process	$\sigma_{\text{NLO}}(6\,b-\text{jet})$ [fb]	$\varepsilon_{\text{analysis}}$	$N^{\text{cuts}}_{3 \times 10^3 \text{ fb}^{-1}}$
LHC analysis (13.6 TeV)			
hhh(SM)	1.97×10^{-2}	0.12	2.77
QCD $(b\bar{b})(b\bar{b})(b\bar{b})$	6136.12	1.00×10^{-5}	69.67
$pp \to Z(b\bar{b})(b\bar{b})$	61.80	0.0045	318.17
$pp \to ZZ(b\bar{b})$	2.16	0.0059	14.3
$pp \to hZ(b\bar{b})$	0.45	0.0159	8.1
$pp \to hhZ$	0.0374	0.034	1.45
$pp \to hh(b\bar{b})$	0.0036	0.028	0.11
LI $gg \to hZZ$	0.143	0.022	3.62
LI $gg \to ZZZ$	0.124	0.013	1.76
LI $gg \to hhZ$	0.0458	0.047	2.42

Process	$\sigma_{\text{NLO}}(6\,b-\text{jet})$ [fb]	$\varepsilon_{\text{analysis}}$	$N^{\text{cuts}}_{20 \text{ ab}^{-1}}$
FCC-hh analysis (100 TeV)			
hhh(SM)	1.14	0.0115	98.90
QCD $(b\bar{b})(b\bar{b})(b\bar{b})$	56.66×10^3	1.12×10^{-5}	4777.71
$pp \to Z(b\bar{b})(b\bar{b})$	1285.37	3.04×10^{-5}	294.63
$pp \to ZZ(b\bar{b})$	49.01	2.02×10^{-5}	7.48
$pp \to hZ(b\bar{b})$	9.87	3.04×10^{-5}	2.26
$pp \to hhZ$	0.601	5.95×10^{-4}	2.70
$pp \to hh(b\bar{b})$	0.096	8.095×10^{-5}	$\ll 1$
LI $gg \to hZZ$	8.28	1.62×10^{-4}	10.12
LI $gg \to ZZZ$	6.63	4.05×10^{-5}	2.03
LI $gg \to hhZ$	2.65	2.54×10^{-4}	5.07

$\varepsilon_{\text{analysis}}(hhh)$, at various, randomly-chosen, combinations of anomalous coefficient values. In combination with the fits of the cross section, and the fit of the branching ratio of the Higgs boson to $(b\bar{b})$, we can estimate the number of events at a given luminosity, for a given collider for any parameter-space point within the anomalous coupling picture, which we dub $S(\{c_i\})$.

The main results of our two-dimensional analysis over the (c_{t3}, d_4)-plane are shown in Figs. 51 and 52. In particular, Fig. 51 shows the potential "evidence" and "discovery" regions (3σ and 5σ, respectively) for triple Higgs boson production at the high-luminosity LHC on the left (13.6 TeV with 3000 fb^{-1} of integrated luminosity), and at a FCC-hh (100 TeV, with 20 ab^{-1}) on the right. Evidently, very large modifications to the quartic self-coupling are necessary for discovery of triple Higgs boson production at the HL-LHC, ranging from $d_4 \sim 125$ for $c_{t3} \sim -8$, to $d_4 \sim \pm 40$ for $c_{t3} \sim 0$ and then down to $d_4 \sim -200$ for $c_{t3} \sim 12$. The situation is greatly improved, as expected, at the FCC-hh, where the range of d_4 is reduced to $d_4 \sim 40$ for $c_{t3} \sim -1.5$, and to $d_4 \sim -20$ for $c_{t3} \sim 1.0$. It is interesting to note that the whole of the parameter space with $c_{t3} \gtrsim 1.0$, or with $c_{t3} \lesssim -1.5$ is discoverable, at the FCC-hh at 5σ. For the potential 68% (1σ) and 95% C.L. (2σ) constraints of Fig. 52, the situation is slightly more encouraging for the HL-LHC, with the whole region of $d_4 \gtrsim 40$ or $d_4 \lesssim -60$ excluded at 95% C.L.. The corresponding region at 68% C.L. is $d_4 \gtrsim 20$ and $d_4 \lesssim -30$. For c_{t3}, it is evident that all the region $c_{t3} \lesssim -2$ and $c_{t3} \gtrsim 5$ will be excluded at 95% C.L. and $c_{t3} \lesssim -1$, $c_{t3} \gtrsim 4$ at 68% C.L.. On the other hand, the FCC-hh will almost be able to exclude the whole positive region of d_4 for any value of c_{t3} at 68% C.L.. This will potentially be achievable if combined with other Higgs boson triple production final states. For the c_{t3} coupling, both the constraints reach the $\mathcal{O}$(few 10%) level for any value of d_4.

The one-dimensional analysis' results, presented in Tables 20 and 21, for the "evidence" and "discovery" potential, and exclusion limits, respectively, reflect the above conclusions. For instance, it is clear by examining Table 20, that the HL-LHC will only see evidence of triple Higgs boson production in the 6 b-jet final state only if d_4 has modifications of $|d_4| \sim \mathcal{O}$(few 10), and will only discover it if $|d_4| \sim \mathcal{O}(100)$. On the other hand, there could be evidence or discovery of Higgs boson triple production if $|c_{t3}| \sim \mathcal{O}(1-10)$. The 1σ and 2σ exclusion regions are much tighter, as expected, with $|d_4| \sim \mathcal{O}(10)$ at 1σ or 2σ at the HL-LHC, improving somewhat at the FCC-hh, and $|c_{t3}| \sim \mathcal{O}(0.1 - 1)$, both at the HL-LHC and FCC-hh.

7.5.5 Conclusions

The results of our study demonstrate the importance of including additional contributions, beyond the modifications to the self-couplings, when examining multi-Higgs boson

production processes, and in particular triple Higgs boson production. We are looking forward to a more detailed study for the HL-LHC, conducted by the ATLAS and CMS collaborations, including detector simulation effects, and the full correlation between other channels. From the phenomenological point of view, improvements will arise by including additional final states, e.g. targeting the process $pp \rightarrow hhh \rightarrow (b\bar{b})(b\bar{b})(\tau^+\tau^-)$, or by performing an analysis that leverages machine learning techniques to maximize significance.[11] In summary, we believe that the triple Higgs boson production process should constitute part of a full multi-dimensional fit, within the anomalous couplings picture.

7.6 Probing the Higgs potential through gravitational waves

R. Pasechnik

7.6.1 Cosmological phase transitions

At very early times, the Universe rapidly went through a so-called electroweak (EW) phase transition into a ground state in which almost all elementary particles became massive through interaction with the Higgs field. It is also believed that in the course of this transition the observed matter–antimatter asymmetry has been created through a mechanism widely known as EW baryogenesis. A strongly first-order phase transition manifests, similarly to the boiling of water, as a violent process of bubble nucleation away from thermal equilibrium. Such a process is realised either via quantum tunneling through the potential barrier determined by instanton solutions (at low temperatures) [317,318], or through thermal jumps over the barrier (at high temperatures). The dynamics of both types of processes can be described as a classical motion in Euclidean space governed by the three-dimensional action:

$$\hat{S}_3(\hat{\phi}, T) = 4\pi \int_0^\infty dr \, r^2 \left\{ \frac{1}{2}\left(\frac{d\hat{\phi}}{dr}\right)^2 + V_{\text{eff}}(\hat{\phi}, T)\right\}, \quad (63)$$

where $\hat{\phi}$ is a classical solution of the equation of motion found as the path in the configuration (field) space that minimizes the action [319,320], and the thermal effective potential of the underlined theory [321,322]

$$V_{\text{eff}}(\hat{\phi}, T) = V_0 + V_{\text{CW}} + \Delta V(T) + V_{\text{ct}}, \quad (64)$$

that consists of the tree-level potential V_0 of a given model, the Coleman–Weinberg potential generated by radiative corrections at zero temperature V_{CW}, the thermal corrections $\Delta V(T)$, and the counter-term potential V_{ct}.

A phase transition is characterised by the critical temperature T_c, at which a local minimum of $V_{\text{eff}}(T)$ evolves to

---

[11] This approach was taken in [32] at the HL-LHC for modifications of the Higgs boson's self-couplings.
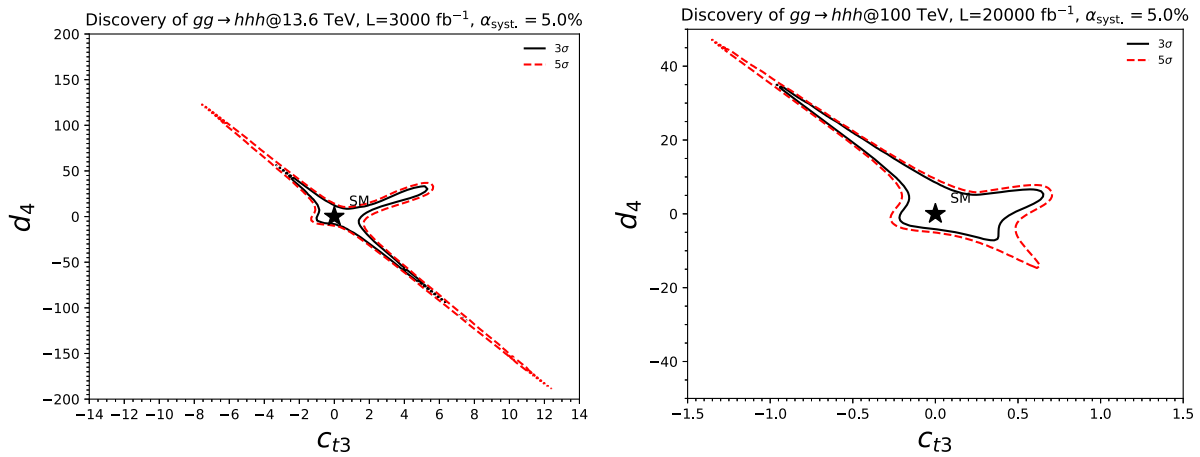
Fig. 51 The 3σ evidence (black solid) and 5σ discovery (red dashed) curves on the (c_{t3}, d_4)-plane for triple Higgs boson production at 13 TeV/3000 fb^{-1} (left), and 100 TeV/20 ab^{-1} (right), marginalized over the c_{t2} and d_3 anomalous couplings. Note the differences in the axes ranges at each collider
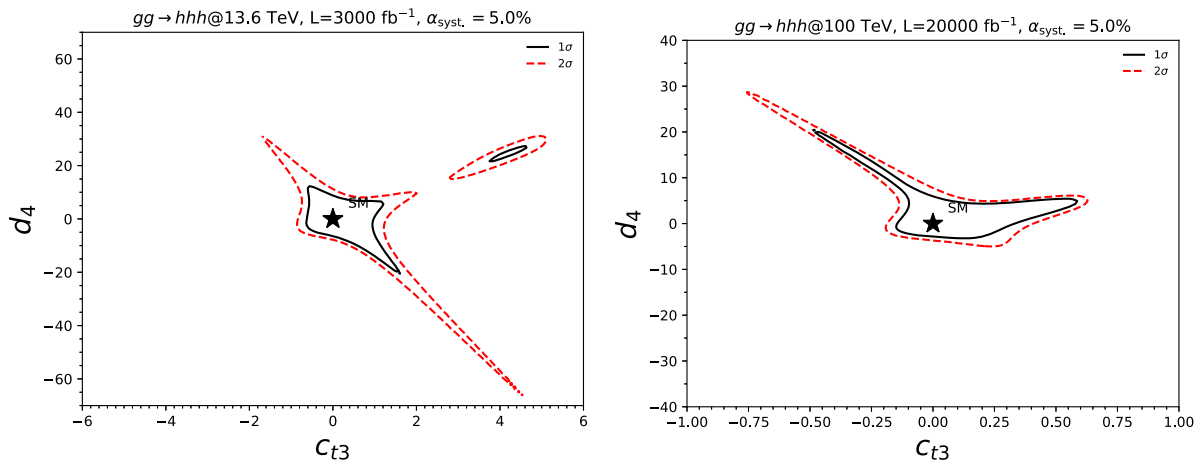

Fig. 52 The 68% C.L. (1σ, black solid) and 95% C.L (2σ, red dashed) limit on the (c_{t3}, d_4)-plane for triple Higgs boson production at 13 TeV/3000 fb^{-1} (left), and 100 TeV/20 ab^{-1} (right), marginalized over the c_{t2} and d_3 anomalous couplings. Note the differences in the axes ranges at each collider

Table 20 The 3σ evidence and 5σ discovery limits on for triple Higgs boson production, for the c_{t3} and d_4 coefficients at 13 TeV/3000 fb^{-1}, and 100 TeV/20 ab^{-1}, marginalized over c_{t2}, d_3 and either d_4, or c_{t3}

	HL-LHC 3σ	HL-LHC 5σ	FCC-hh 3σ	FCC-hh 5σ
d_4	[−28.0, 41.7]	[−99.5, 152.9]	[−24.9, 20.8]	[−40.8, 23.1]
c_{t3}	[−2.1, 5.5]	[−7.1, 11.3]	[−0.8, 0.6]	[−1.2, 0.7]

Table 21 The 68% C.L. (1σ) and 95% C.L (2σ) limits on c_{t3} and d_4 for triple Higgs boson production at 13 TeV/3000 fb^{-1}, and 100 TeV/20 ab^{-1}, marginalized over c_{t2}, d_3 and either d_4, or c_{t3}

	HL-LHC 68%	HL-LHC 95%	FCC-hh 68%	FCC-hh 95%
d_4	[−6.6, 12.4]	[−10.0, 21.3]	[−3.9, 10.5]	[−10.6, 18.8]
c_{t3}	[−0.6, 1.1]	[−0.9, 3.6]	[−0.1, 0.3]	[−0.4, 0.6]

become equal to its global one, and by the transition rate [323,324]

$$\Gamma(T) \approx T^4 \left(\frac{\hat{S}_3}{2\pi T}\right)^{3/2} e^{-\hat{S}_3/T}. \tag{65}$$

At $T < T_c$, the nucleation process becomes effective due to large thermal fluctuations. The nucleation temperature T_n is then found requiring as a point in cosmological history when a single true vacuum bubble nucleates per cosmological horizon satisfying,

$$\int_{T_n}^{T_c} \frac{dT}{T} \frac{\Gamma(T)}{H^4} = 1,$$
$$H^2 = \frac{g_*(T)\pi^2 T^4}{90 M_{\text{Pl}}^2} + \frac{\Delta V_{\text{vac}}}{3 M_{\text{Pl}}^2}, \tag{66}$$

in terms of the Hubble rate $H = H(T)$ including both the radiation (first term) and vacuum density ΔV_{vac} (second term) contributions [325], and the effective number of relativistic d.o.f. in the considered epoch at a temperature T is denoted as $g_*(T)$. Here, M_{Pl} is the Planck mass. For practical purposes, it is particularly useful to define a percolation temperature $T_* < T_n < T_c$ at which about 34% of the Universe has transited to the true (stable) vacuum [326], i.e.

$$I(T_*) = 0.34,$$
$$I(T) = \frac{4\pi v_b^3}{3} \int_T^{T_c} \frac{\Gamma(T')dT'}{T'^4 H(T')} \left(\int_T^{T'} \frac{d\tilde{T}}{H(\tilde{T})}\right)^3, \tag{67}$$

Eventually, the bubbles of the energetically favoured vacuum state take over giving rise to today's Universe where the EW symmetry is broken.

The energy budget of a first-order phase transition, and hence its effective strength, is typically characterised by difference in the trace anomaly between the two (initial metastable i and final stable f) phases or vacua relative to the radiation density of the universe ρ_γ at the nucleation epoch $T = T_*$ [327,328]

$$\alpha = \frac{1}{\rho_\gamma}\left[\Delta V - \frac{T}{4}\left(\frac{\partial \Delta V}{\partial T}\right)\right], \quad \Delta V = V_i - V_f,$$
$$\rho_\gamma = g_*(T_*)\frac{\pi^2}{30}T_*^4, \tag{68}$$

where $V_i \equiv V_{\text{eff}}(\phi^i, T_*)$ and $V_f \equiv V_{\text{eff}}(\phi^f, T_*)$ are the effective potential values in the two phases, respectively. Besides, α one also considers the inverse time scale of the phase transition defined in units of the cosmological horizon time-scale given by $H(T)$ as

$$\frac{\beta}{H} = T_* \frac{\partial}{\partial T}\left(\frac{\hat{S}_3}{T}\right)\bigg|_{T_*}. \tag{69}$$

7.6.2 Primordial gravitational waves: a window into New Physics

The bubble nucleation process triggers ripples in space-time through bubble collisions, sound-waves and turbulence in the cosmic plasma contributing to the gravitational-wave background. A large amount of energy released in the phase transition over a very short time scale could be sufficient to produce primordial gravitational waves potentially observable today [329]. The key observable is the energy-density of the gravitational radiation per logarithmic frequency found as (see for instance Refs. [330–332] and references therein)

$$h^2\Omega_{\text{GW}}(f) \equiv \frac{h^2}{\rho_c}\frac{\partial \rho_{\text{GW}}}{\partial \log f}$$
$$= h^2\Omega_{\text{GW}}^{\text{peak}}\left(\frac{4}{7}\right)^{-\frac{7}{2}}\left(\frac{f}{f_{\text{peak}}}\right)^3\left[1 + \frac{3}{4}\left(\frac{f}{f_{\text{peak}}}\right)\right]^{-\frac{7}{2}}, \tag{70}$$

in terms of the known critical density of the modern Universe ρ_c as well as the peak-frequency f_{peak} and the peak-amplitude $h^2\Omega_{\text{GW}}^{\text{peak}}$ of the gravitational signal. The latter quantities can be parameterised in terms of the basic phase transition characteristics T_*, α and β/H as well as the bubble wall velocity v_w (see Refs. [333,334] for explicit formulas). Hence, the measurement of primordial gravitational waves is often considered as an indirect way to probe the Higgs potential at temperatures close to the EW phase transition epoch in the early Universe [334,335].

Observable consequences of the EW phase transition in cosmology are strongly connected to the structure of the Higgs potential. A large ongoing effort in the literature is devoted to analysis of an interplay between direct probes of the Higgs potential (such as e.g. Higgs boson pair and triple-Higgs production etc) at high-energy particle colliders and indirect probes of the EW phase transition in the early Universe using primordial gravitational waves (for such a discussion, see e.g. Refs. [334,336–353] and references therein). Existing and planned gravitational-wave facilities, hence, offer a plethora of new opportunities to explore many different New Physics scenarios in a way that is complementary to direct observations at particle colliders [329] (for a recent review, see e.g. Ref. [354] and references therein). For the recent measurements of the stochastic gravitational waves' background by NANOGrav and its implications for New Physics, see e.g. Ref. [355] and references therein.

The LHC or its high-luminosity upgrade HL-LHC are expected to provide the data sufficient for a consistent measurement of the Higgs boson self-coupling depending on whether or not the Higgs potential is minimal [21,356]. On the other hand, the next generation, space-based, gravitational-wave experiment LISA [357] will have a

large enough sensitivity to probe the stochastic gravitational-wave background of the Universe sourced by the EW phase transition for the first time [333,334]. The recent approval of LISA Phase B2 on January 25, 2024, has marked the start of its hardware implementation, with the launch expected in mid-2030s. Thus, we live in a historic moment when the collider data from terrestrial measurements such as LHC can be combined with the astrophysical data from space-based gravitational-wave experiments such as LISA to uncover the true dynamics of the EW phase transition and thereby to probe possible variants of New Physics beyond the Standard Model (BSM).

It is well-known that in the SM featuring the minimal Higgs sector, the EW phase transition is a continuous second-order transformation between the EW-symmetric and EW-broken phases. As result, neither the observed baryon asymmetry nor primordial gravitational waves can be produced in this case. These and other well-known shortcomings of the SM (such as a lack of CP violation required by baryogenesis, the absence of a neutrino mass generation mechanism and of a suitable particle Dark Matter candidate) have historically been the strongest points favouring New Physics still waiting for its direct experimental observation.

Typical New Physics scenarios feature additional states coupled to the Higgs field. These affect the shape of the effective Higgs potential which strongly depends on temperature, such that it is important to probe it at different epochs of cosmic evolution. Indeed, the curvature of the Higgs potential is determined by the measured Higgs mass (m_h) and triple-Higgs self-coupling (λ_{hhh}) whose value as a function of quartic Higgs coupling (λ_{hhhh}) is known in the SM but may change in BSM theories e.g. via radiative corrections involving non-SM particles. A systematic and generic way of deriving the effective Higgs self-interactions starting from the one-loop effective potential has been advised in Ref. [285]. A precision measurement of both λ_{hhh} (e.g. through Higgs pair production) and λ_{hhhh} (through triple Higgs production) is instrumental for probing the influence of BSM physics on the Higgs potential and, hence, for the physics of EW phase transition. Such a measurement is one of the key reasons for LHC upgrades as well as for building new collider facilities at the high-energy frontier.

Characteristics of the phase transitions and the corresponding spectrum of primordial gravitational waves in a particular model strongly depend on the thermal effective Higgs potential, which is determined by the particle spectrum of the model and their interactions with the Higgs boson. Many SM extensions feature very complicated, non-minimal Higgs potentials as is the case, for instance, in composite Higgs and supersymmetric theories which also provide an explanation for Dark Matter and yield the Higgs boson mass protected from large radiative corrections. For the purpose of detailed exploration of the EW phase transition, instead of considering the full UV-complete models, it is more consistent to utilise simplified TeV-scale effective field theory (EFT) approximations to them focusing only on a few operators and states relevant below a TeV energy scale such as popular 2HDMs and a scalar singlet-extended SM.

At high temperatures, additional sub-TeV scalar states and their interactions with the Higgs boson effectively induce a barrier between the initial and final phases in the Higgs vacuum, thus, enabling the EW phase transition to become first-order which, along with the enhanced CP violation, is a vital part of the EW baryogenesis mechanism [358]. Indeed, adding a single EW-singlet field at EW scale is already enough to trigger a first-order phase transition that is sufficiently strong for efficient EW baryogenesis [359]. Knowing the effective Higgs potential at finite temperatures, it is rather straightforward to compute the phases of the theory at a given temperature and such characteristics of transitions between them as the strength of the transition (usually attributed to the released latent heat), the bubble nucleation and percolation temperatures and the duration of a given phase transition. The latter, in turn, determine the spectrum of the produced gravitational waves, although still with significant uncertainties (see e.g. Ref. [360]).

7.6.3 Constraining Higgs self-interactions with gravitational waves: the case of Majoron EFT

One of the simplest SM extensions – a singlet scalar extended SM – provides a rich playground for studies of the impact of extra scalar states and interactions on the shape of the effective Higgs potential at finite temperatures, the phase transition dynamics and the related production of primordial gravitational waves.[12] For recent studies of the interplay between the collider signatures and gravitational wave signals in the real singlet scalar extended SM, see e.g. Refs. [343,345,349,364] and references therein. In what follows, we elaborate on such an interplay for a complex singlet scalar extended SM representing another simplest and popular class of BSM scenarios having important implications for both Dark Matter physics and neutrino mass generation (see e.g. Refs. [359,360,365,366]).

The potential of complex-singlet extended model possesses a global softly-broken U(1) symmetry, and the Higgs weak-doublet H and a complex EW-singlet σ can have a non-zero charge under this symmetry. Such a potential provides a basis for the so-called Majoron model [367–369] where the global U(1) is extended to the lepton sector (thus, considered to be the lepton number symmetry) with additional Majorana

---

[12] For earlier works exploring the rich vacuum structure, phase transitions and gravitational wave signatures in extended models featuring more complicated scalar sectors, see e.g. Refs. [346,361–363] and references therein.

neutrinos giving rise to the neutrino mass generation via an inverse seesaw mechanism.

The simplest renormalisable (dimension-4) variant of the Majoron model that assumes no UV completion does not yield primordial gravitational waves detectable by LISA simultaneously with featuring a suitable Dark Matter candidate [370]. Unknown UV physics at a large seesaw scale Λ, however, can generate higher-dimensional operators in the low-energy EFT that may enhance the potential barrier between false and true vacua. The emergence of a first-order EW phase transition induced by a dimension-six $\propto (HH^\dagger)^3$ operator in the effective Higgs potential has been studied in Refs. [371–373]. In the case of Majoron EFT, this occurs without immediately conflicting with the invisible Higgs decay constraints for light Majorons [338].

Considering the contribution from the U(1)-preserving dimension-six operators, the potential of such a Majoron EFT valid at energies below the cutoff scale Λ reads:

$$V_0(H,\sigma) = V_{\text{SM}}(H) + V_{\text{4D}}(H,\sigma) \\ + V_{\text{6D}}(H,\sigma) + V_{\text{soft}}(\sigma), \tag{71}$$

where

$$V_{\text{SM}}(H) = \mu_h^2 H^\dagger H + \lambda_h (H^\dagger H)^2,$$
$$V_{\text{4D}}(H,\sigma) = \mu_\sigma^2 \sigma^\dagger \sigma + \lambda_\sigma (\sigma^\dagger \sigma)^2 + \lambda_{\sigma h} H^\dagger H \sigma^\dagger \sigma,$$
$$V_{\text{6D}}(H,\sigma) = \frac{\delta_0}{\Lambda^2}(H^\dagger H)^3 + \frac{\delta_2}{\Lambda^2}(H^\dagger H)^2 \sigma^\dagger \sigma \tag{72}$$
$$+ \frac{\delta_4}{\Lambda^2} H^\dagger H (\sigma^\dagger \sigma)^2 + \frac{\delta_6}{\Lambda^2}(\sigma^\dagger \sigma)^3,$$
$$V_{\text{soft}}(\sigma) = \frac{1}{2}\mu_b^2 \left(\sigma^2 + \sigma^{*2}\right).$$

In the real field basis, H and σ are found as follows

$$H = \frac{1}{\sqrt{2}} \begin{pmatrix} \omega_1 + i\omega_2 \\ \phi_h + h + i\eta \end{pmatrix},$$
$$\sigma = \frac{1}{\sqrt{2}} \left(\phi_\sigma + h' + iJ\right), \tag{73}$$

in terms of the classical-field configurations ϕ_h and ϕ_σ, the corresponding radial fluctuations h and h', and Goldstone bosons $\omega_{1,2}$, η effectively "eaten up" by $W^\pm$ and Z bosons, and Majoron J staying physical in the spectrum. The latter acquires its pseudo-Goldstone mass via a soft $U(1) \to \mathbb{Z}_2$ breaking mass term $V_{\text{soft}}(\sigma)$ and may play a role of Dark Matter. Further details of the mass spectrum, parameter space and the finite-temperature effective potential in this model can be found in Ref. [338].

As was mentioned above, the strong first-order EW phase transitions originate due to a sizeable trilinear coupling of the SM-like Higgs boson h_1 determining a potential barrier between the false and true Higgs vacua. At one-loop level, it receives contributions from the top quark t, heavy neutrinos

N and the second CP-even Higgs boson h_2 loops, i.e.

$$\lambda_{h_1 h_1 h_1} = \lambda_{h_1 h_1 h_1}^{(0)} + \frac{1}{16\pi^2}\left(\lambda_{h_1 h_1 h_1}^t + \lambda_{h_1 h_1 h_1}^N + \lambda_{h_1 h_1 h_1}^{h_2}\right) \tag{74}$$

with explicit expression found in Ref. [338].

In a general parameter scan of Ref. [338], one extracts the Lagrangian parameters $\lambda_{\sigma h}$, λ_σ, λ_h, μ_b and δ_6 in terms of five physical observables serving as input parameters – two CP-even scalar masses, $m_{h_1} \simeq 125$ GeV and $m_{h_2} = [60\ldots1000]$ GeV, the scalar mixing angle α_h (bounded by $|\sin\alpha_h| < 0.24$), the mass of the pseudo-Goldstone Majoron state m_J, and the Higgs branching ratio into Majorons $\text{Br}(h_1 \to JJ)$. Additional parameters varied in the scan are the EFT cut-off scale $\Lambda = [10\ldots1000]$ TeV, the Majoron VEV $v_\sigma = [100\ldots1000]$ GeV, light neutrino mass scale $m_\nu < 0.1$ eV, as well as the magnitudes of the remaining dimension-6 operators $\delta_{0,2,4}$ chosen to be within wide ranges consistent with perturbativity of the corresponding quartic couplings in the EFT potential (72). In the original work of Ref. [338], the parameter ranges were chosen to generically comply with the LHC constraints on $\kappa_\lambda \lesssim 6.5$ [4] (see Table 3 for the existing CMS and ATLAS bounds in various channels) and on the branching ratio of invisible Higgs decays $\text{BR}(h_1 \to JJ) < 0.18$ from Ref. [374]. The current ATLAS bound on the latter observable is somewhat tighter, $\text{BR}(h_1 \to JJ) < 0.107$ [375], which may not impact the conclusions of Ref. [338] in a significant manner. Besides, the case of a light Majoron has been considered, with $m_J < 100$ keV, that might, under certain conditions, play a role of Dark Matter candidate.

The main results of the restricted parameter scan are highlighted in Fig. 53 where the correlations of the the trilinear Higgs coupling modifier κ_λ with the mass of the second CP-even Higgs boson mass h_2 (left) and with the scalar CP-even mixing parameter $\sin\alpha_h$ (right) are shown for parameter space points that provide a strongly first-order phase transition [338]. In this restrictive scan, the dimension-six Higgs operator has been omitted $\delta_0 = 0$ to showcase the importance of Higgs-singlet portal interactions encoded in δ_2 and δ_4. For such points, the strength of the phase transition takes maximal values $\alpha \gtrsim 0.1$ while the inverse duration is minimised $10 \lesssim \beta/H \lesssim 100$. The color scale represents the maximal value of the induced cosmic gravitational wave spectrum $h^2\Omega_{\text{GW}}^{\text{peak}}$. Here, the magenta points, with the ballpark localised at $100 \lesssim m_{h_2}/\text{GeV} \lesssim 250$ and $0 \lesssim \kappa_\lambda \lesssim 2$, represent gravitational wave signals strong enough to be potentially detectable at the future LISA [357], BBO [376,377] and DECIGO [378,379] facilities.
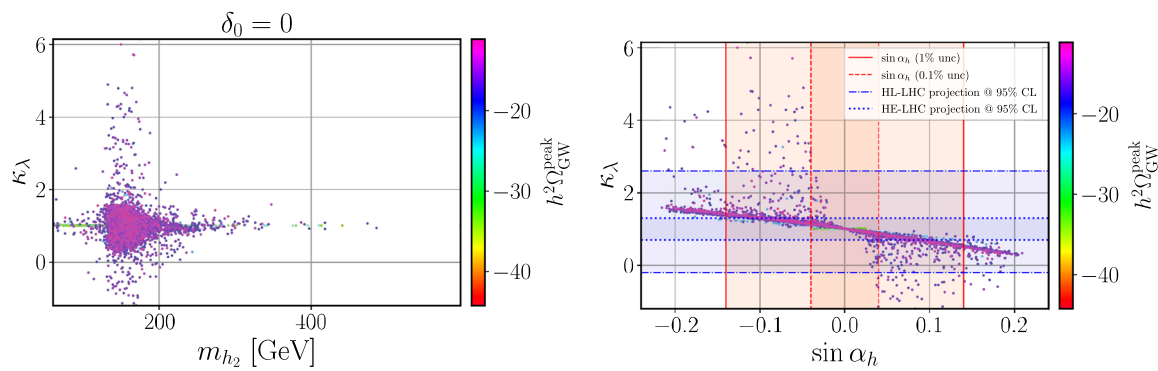
$\delta_0 = 0$

Fig. 53 Left panel: correlation between the trilinear Higgs coupling modifier κ_λ and the mass of the second CP-even Higgs boson mass h_2. Right panel: correlation between κ_λ and the scalar CP-even mixing $\sin \alpha_h$. Only points featuring a strongly first-order phase transition are shown. In both panels, the peak-amplitude of the resulting primordial gravitational wave spectrum is presented in the color scale, and $\delta_0 = 0$ has been imposed in a restrictive parameter scan. From Ref. [338]

7.6.4 Conclusions

The same operators that enhance the strength of the phase transition also contribute to the Higgs-pair, triple-Higgs and the associated (with an additional scalar) Higgs production channels. These observables of the Higgs sector provide a direct access to the Higgs vacuum structure and, thus, to dynamics of the phase transitions. The future measurements of these channels at the LHC, its forthcoming upgrades and future colliders can be cross-correlated with possible observations of primordial gravitational waves enabling to efficiently constrain New Physics at a TeV scale [340,350,380–382]. Moreover, correlations with other measurements such as the searches for $A \to ZH$ (with $H \to t\bar{t}$) in the case of 2HDMs [339] or for deviations from the SM prediction in the W boson mass in the case of scalar-triplet extensions [383] provide other possible probes for parameter space domains in multi-scalar models that feature strong first-order EW phase transitions.

Figure 53 (right) provides a good example illustration of the interplay between collider and gravitational wave measurements. In particular, the power of such an interplay can be understood considering the measurements of the CP-even scalar mixing angle α_h (red vertical lines) [384] and the Higgs trilinear coupling κ_λ (blue horizontal lines) [385] at the forthcoming LHC upgrades and future colliders. Hence, already in the example of Majoron EFT discussed above, one notices that correlations between collider and gravitational-wave observables may pose significant constraints on New Physics models that feature portal-type couplings between the Higgs boson and BSM scalars.

8 Simulation and parton level Monte Carlo/simplified models

A. Papaefstathiou, T. Robens, R. Zhang

In Sect. 2, we discussed the current state of the art and open points for the simulation of triple Higgs final states following SM predictions, also addressing available Monte Carlo tools for both signal and background. Here, in turn, we describe the available tools for double resonance enhanced triple Higgs production in new physics scenarios. We briefly elaborate on of the currently available tools that focusses on a simple production and decay chain. In addition, we point to possible pitfalls that can arize from an oversimplified approach in scenarios where additional features of a particular UV realization are important.

8.1 Introduction

We here focus on resonance-enhanced triple scalar production, i.e. scenarios that allow for onshell production of the form

$$p\, p \to h_3 \to h_1\, h_2 \to h_1\, h_1\, h_1, \tag{75}$$

where we assumed mass a hierarchy $M_3 \geq M_2 \geq M_1$. Basically all new physics scenarios that contain at least 4 scalar fields in the gauge eigenbasis (we here count complex degrees of freedom separately) can provide such scenarios. The simplest realization is however the extension of the scalar potential by a complex or, equivalently, two real singlets, see e.g. [386] for early work.

In case the above decay chain is dominant, the following parameters are minimally needed to describe the above process:

Table 22 The correspondence between the parameters defined by Eqs. (76) and (77) and those in the `MadGraph5_aMC@NLO` model

Parameter	MadGraph5_aMC@NLO
λ_{ijk}	Kijk
λ_{ijkl}	Kijkl
κ_i	ki
Particle	
h_1	h
h_2	eta0
h_3	iota0

M_1, M_2, M_3; Γ_1, Γ_2, Γ_3; $g_{h_3 t \bar{t}}$, λ_{123}, λ_{112},

where λ_{ijk} denote triple scalar couplings. If decays of the triple scalar states are specified, in principle also coupling modifications of the h_{125} to the respective final states are still allowed within a range of $\kappa \geq 0.96$, see e.g. [233], and should be included in the parameter list. Note that for a specific UV complete realization the widths are not free parameters.

8.2 Current model version

The phenomenological Lagrangian described by the `MadGraph5_aMC@NLO` model, found at [387], contains scalar interactions of the form:

$$V \supset \sum_{i,j,k} \lambda_{ijk} h_i h_j h_k + \sum_{i,j,k,l} \lambda_{ijkl} h_i h_j h_k h_l, \tag{76}$$

where $i, j, k, l = 1, 2, 3$ correspond to the three physical scalar particles present in the model, h_1, h_2, h_3.

The couplings of the scalars to the rest of the SM particles are SM-like and are each re-scaled by a single parameter κ_i:

$$g_{h_i XX} = g_{hXX}^{\text{SM}} \kappa_i, \tag{77}$$

where $i = 1, 2, 3$.

If we identify h_1 with the SM-like Higgs boson, then $m_1 \simeq 125$ GeV and $\kappa_1 \lesssim 1$, and $\kappa_{2,3} \simeq 0$, following experimental constraints steming from the SM-like Higgs boson signal strength measurements.

This model has been implemented into `MadGraph5_aMC@NLO` with the input parameters defined by Eqs. (76) and (77), where the correspondence to the input parameters of the `MadGraph5_aMC@NLO` is given in Table 22.

In addition, the masses of the new particles can be entered as free parameters. Note that this requires to use autowidth for

consistency reasons, otherwise the rates given by the Monte Carlo run can be non physical.[13]

As a caution, we want to emphasize that a randomly set of parameters does not guarantee that a realistic UV-complete model exists that can be mapped on the corresponding values. The above model also does not allow for non-uniform rescaling of couplings to SM particles, as e.g. present in new physics scenarios with additional doublets. In the current implementation, the important sum rule [388] should always be obeyed:

$$\sum_i \kappa_i^2 = 1. $$

8.3 Enhancement of number of free parameters/more physical description

In general, if a process in the form of Eq. (75) is targeted, it is clear that various channels can contribute to the final state $h_i h_i h_i$. In particular, all possible intermediate indices can appear

$$p \, p \rightarrow h_i \rightarrow h_j h_1 \rightarrow h_1 h_1 h_1, \tag{78}$$

where $\{i, j, k\} \in \{1, 2, 3\}$. In such a scenario, in principle all κ_i and $\lambda_{ij1}/\lambda_{j11}$ are needed as input parameters. While the above model allows for an inclusion of all these choosing arbitrary values, the total number of free parameters that needs to be taken into account is increased by 12, including the additional couplings $g_{h_{1/2} t \bar{t}}$.

8.4 Possible pitfalls

Clearly, possible pitfalls can occur when the process specified in Eq. (75) is no longer dominant. In this case, obviously a process can still be generated that corresponds to the one above, and used for cut optimization and, if applicable, training of neural networks or similar tools, but the correct mapping to a UV complete theory might then require recasting methods. One way to identify such scenarios is e.g. the case where

$$p \, p \rightarrow h_1 \rightarrow h_1 h_1 \rightarrow h_1 h_1 h_1$$

with intermediate off-shell particles is large.

We have considered such a scenario in the TRSM, with the following input parameters [389]:

$$M_2 = 550 \text{ GeV}, \qquad M_3 = 700 \text{ GeV},$$
$$\theta_{hs} = -0.002826, \qquad \theta_{hx} = 0.04424, \qquad \theta_{sx} = 0.8908,$$
$$v_s = 739.2 \text{ GeV}, \qquad v_x = 152.3 \text{ GeV}. \tag{79}$$

---

[13] While using an arbitrary width might be corrected by rescaling in case the process of Eq. (75) is dominant, it immediately starts to fail once more physical descriptions of the production process are used. See discussion below for details.
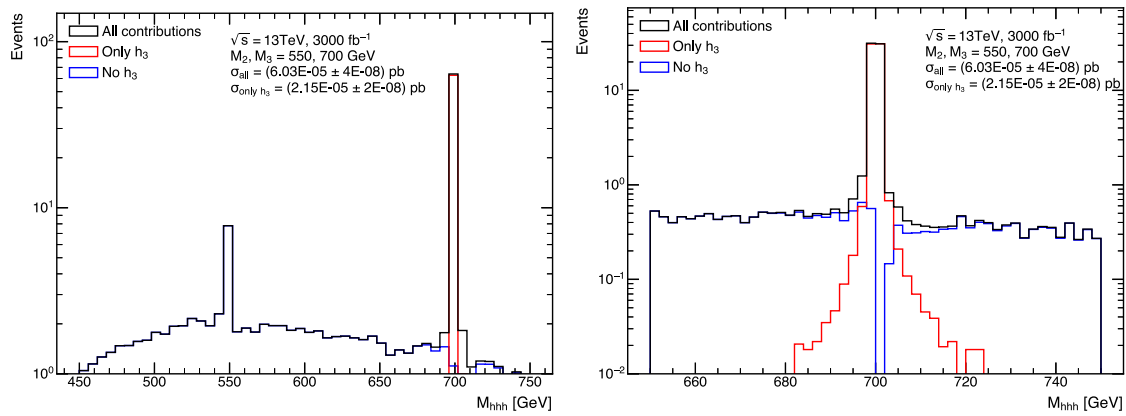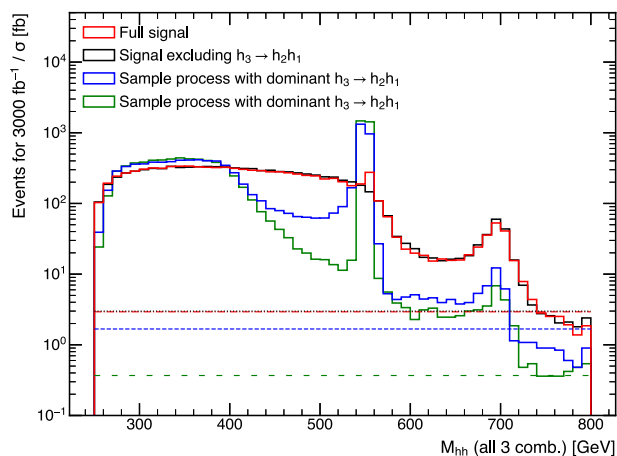
Fig. 54 Comparison of M_{hhh} invariant mass distributions for the point in Eq. (79), for full process *(black)*, process excluding contributions from (75) *(blue)*, and contributions via the dominant process (75) only *(orange)*, for the whole mass region *(left)* as well as zoomed in into the relevant mass region *(right)*. Events are shown for 13 TeV and 3000 fb^{-1}. Bin size is 6 GeV and 2 GeV, respectively
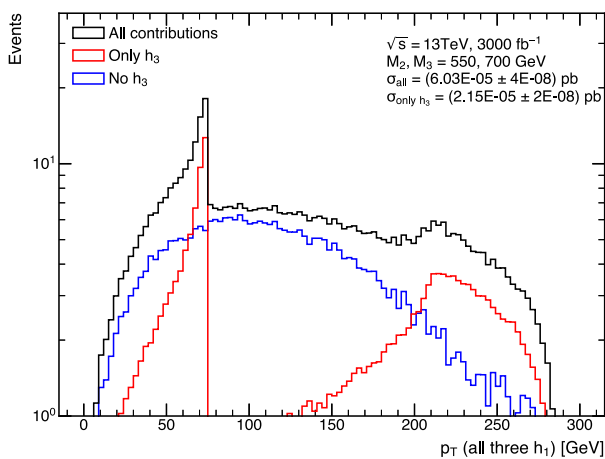
Fig. 55 Comparison of $p_\perp$ distributions for all scalars for the point in Eq. (80), for full process *(black)*, process excluding contributions from (75) *(blue)*, and contributions via the dominant process (75) only *(orange)*. Events are shown for 13 TeV and 3000 fb^{-1}. Bin size is 3 GeV

For this parameter point, the cross section for the total process without intermediate state specification is given by $\sigma_{tot} = 0.06031(4)$ fb; specifying the intermediate state as given above leads to $\sigma_{h_3} = 0.02151(2)$ fb at 13 TeV; in this scenario, although onshell production is possible, the double resonance enhanced process only contributes to about 40 % of the total cross section.

We display the respective distributions in the triple scalar invariant mass as well as the $p_\perp$ of all scalars in Figs. 54 and 55, respectively.

For the mass distribution, we see that in the region around the peak the full process and the target process render the same distributions. However, off the mass peak the second

obviously neglects additional contributions. Similarly, the $p_\perp$ distributions also differ between the two descriptions.

Another interesting parameter point is a scenario where the target process only contributes about 6 % of the total cross section, and dominant contributions instead stem from

$$p\,p \;\rightarrow\; h_3 \;\rightarrow\; h_3\,h_1 \;\rightarrow\; h_1\,h_1\,h_1$$

where again the intermediate particles can be offshell. An example of such a scenario is the point specified by

$$
\begin{aligned}
M_2 &= 550 \text{ GeV}, \quad M_3 = 700 \text{ GeV}, \\
\theta_{hs} &= 0.06232, \quad \theta_{hx} = 0.2773, \\
\theta_{sx} &= 0.1150, \\
v_s &= 269.2 \text{ GeV}, \quad v_x = 173.1 \text{ GeV}.
\end{aligned}
\tag{80}
$$

For this scenario, the M_{hhh} distribution will feature a peak at $\sim$ 700 GeV, as around 90% of the process is mediated via h_3 production. However, the hh invariant mass distribution will look different. As an example, in Fig. 56 we show the corresponding contributions for the above point with and without the original target process given by Eq. (75), and in addition compare it to two sample processes where h_3 clearly dominates.

It is obvious that the above points are just examples, and it could very well be that in regions of parameter space with large rates the decay chain given by Eq. (75) is always dominant. However, depending on the models parameter space many other processes of the form given by Eq. (78) can appear that lead to different distributions in the parameter space of a UV complete model.

Fig. 56 Comparison of M_{hh} invariant mass distributions for the point in Eq. (80), for full process *(red)*, process excluding contributions from (75) *(black)*, and two other parameter point where $\gtrsim 90\%$ stem from (75) *(blue, green)*, normalized to the respective cross sections. The lines signify 1 event at $\mathcal{L}_{int} = 3000\,\text{fb}^{-1}$ for 13 TeV. Bin size is 10 GeV

9 Summary and open questions

J. Konigsberg, G. Landsberg, T. Robens

After the discovery of a particle with properties consistent with those of the Higgs boson of the electroweak Standard Model, all parameters of the scalar sector are now known in principle. However, to determine whether the scalar sector that is realized in Nature indeed corresponds to the one of the SM, both the triple (κ_3) and quartic (κ_4) scalar couplings of this Higgs boson need to be determined with sufficient precision. While κ_3 can be determined in the observation of processes leading to di-Higgs final states (see e.g. [21] for a concise overview), κ_4 is only accessible at leading order in processes with triple Higgs final states.

Di-Higgs production is nearly exclusively sensitive to κ_3, while triple Higgs production is sensitive to both κ_3 and κ_4. A full determination of the Higgs potential is only possible through the combined measurement of these couplings. The cross section for triple Higgs production at hadron colliders, within the Standard Model, is known up to NNLO in QCD and ranges from $\mathcal{O}\left(10^{-1}\text{fb}\right)$ at 14 TeV to $\mathcal{O}$ (fb) at 100 TeV colliders [30]. These cross sections predict very small signal yields even at the highest energy colliders, and are several hundred times smaller than those for di-Higgs production. Therefore, a first attempt at discovering triple Higgs processes could be made by considering new physics scenarios with significantly enhanced production rates with respect to SM predictions. Even though these processes could include final states with different kinematic distributions from SM ones, they provide a very good testing ground for various experimental analysis strategies. But importantly, the possi-

bility of discovering new physics in itself merits deliberate searches for such scenarios.

In this workshop, we addressed various such new physics models that extend the SM scalar sector and that can potentially result in observable signal yields at hadron colliders. Importantly, we also discussed in depth the experimental challenges, and the corresponding tools and techniques needed, in searching for these processes. Such new physics models include additional scalars produced in conjunction with Higgs bosons, resulting in multi-Higgs processes with additional resonances that can be searched for experimentally due to their striking, and diverse, topologies. An example of such models in which, in addition to the discovered Higgs boson, two new real singlet scalars are introduced is the TRSM model, for which different regions of mass phase-space (for the three scalars involved) can yield signals large enough for potential discovery at the HL-LHC. In general, the extended scalar sector is broadly interesting and, for example, has potential connections to dark matter, hierarchies in the quark mass sector, or even electroweak baryogenesis. The message is that such multi-scalar searches should be pursued, both in model-dependent and model-independent fashions.

In terms of how to purse triple Higgs searches, it is illustrative to see where we are with the di-Higgs pursuits. The current expected sensitivity to di-Higgs production, by CMS and ATLAS, using each about 140 fb^{-1} of data from Run 2, is in the range of $2.5-2.9$ times the predicated rate of the SM. The main final state channels contributing to these searches are: $b\bar{b}b\bar{b}$, $b\bar{b}\tau^+\tau^-$, and $b\bar{b}\gamma\gamma$. With doubling of the Run 2 data in Run 3 and a possible combination of the results from the ATLAS and CMS experiments, it is possible that a 3-σ evidence for di-Higgs production can be achieved at the LHC in the next couple of years. At the HL-LHC, with the techniques developed now and in future, and with the expected 3000 fb^{-1} of data, observation of di-Higgs production is achievable.

There were extensive discussion of these techniques at the workshop, that are also applicable to triple Higgs searches. Because the Higgs decay to b-quark pairs is the largest ($\sim 58\%$), focusing on final states that contain at least four b-quarks, from the decay of two of the three Higgs bosons, is the most promising path to larger signal yields and background reduction. A price in the efficiency in the detection of b-jets is nonetheless paid in order to reduce fakes while enhancing the signal. To alleviate that, the decay of the third boson, in addition to considering the $b\bar{b}$ mode, can also include non-b jets, such as hadronically decaying tau leptons, jets from the W^+W^-, or from gg decay modes. The main analysis components of these searches are: the triggers used to capture as much signal as possible, the b-tagging algorithms, the topological reconstruction of the event, the modeling of the multi-jet QCD background, and the algorithms for signal extraction. All of these elements have benefited significantly

from the fast pace of machine learning developments that have now become integral to advanced analyses.

Implementing b-tagging and full event reconstruction algorithms in the triggers is paramount to maintaining trigger rates reasonably low, while recording as much signal as possible. Access to low level detector information at the earliest levels of the trigger paths is, and will continue to be, critical so that ML techniques can be implemented in fast hardware such as field-programmable gate array (FPGA) and GPU based engines. Flavor-tagging algorithms have evolved tremendously from the early days in which silicon tracking detectors were first used in hadron colliders. The continuous evolution of silicon tracker technology, combined with ML techniques, nowadays results in algorithms that can identify b-jets with an efficiency of $\sim 80\%$ and a fake rate at the 10^{-2} level. Similar ML algorithms have also been extremely useful in charm-tagging and in the identification of tau lepton hadronic decays, all relevant in triple Higgs searches.

The complexity of these multi-object final states, with potentially multiple resonances, lends itself further to a broad usage of ML techniques. Event-wide ML algorithms have proven to be extremely effective in discerning signal from background at the event selection stage and, very importantly, in modeling QCD background using data-driven techniques, as this is an important component of the systematic uncertainty in the searches. At the end stage of the analyses, dedicated ML algorithms focus on signal extraction in specific signal regions. In di-Higgs and in triple Higgs searches, be them from SM processes or not, there are regions of phase space in which, due to the large boost of the particles involved, the final state jets are close together and merge. Experiments use ML algorithms to discern whether jet event activity in large fiducial cones is from decays of boosted objects such as bosons or top quarks. ML algorithms have also been developed to identify whether the merged jets originate from heavy flavor. In any given multi-jet process events can be categorized as fully resolved – with all final state jets far away enough from each others, as semi-merged – with some of the jets closely merged, and as fully merged in which every jet is merged with another. Techniques to optimize the categorization and consequent utilization of the appropriate analysis techniques for each case are important, with the ultimate sensitivity being the deciding figure of merit. A complication in signal event reconstruction stems from additional jets from pileup interactions, and from initial and final state radiation, and these need to be included in the event reconstruction ML algorithms.

Another important area addressed in the workshop was the intricacy of theoretical challenges and recent advancements in reaching higher orders of precision in QCD calculations of hadronic processes. These are important in establishing predictions of signal cross sections, including accurate kinematical differential distributions. Related to this, the Monte Carlo generators modeling of multi-jet processes has become more and more critical as ML algorithms need to be trained using very large simulated samples of background multi-jet events that are modeled as accurately as possible.

In conclusion, the HHH workshop held in Dubrovnik last Summer brought together theorists and experimentalists to a dedicated forum in which the discussions proceeded with intense focus and great camaraderie. As reflected in this white paper, the projection of everyone's knowledge and experience onto the triple Higgs landscape has helped establish an initial stage of common understandings and a road map on how to pursue the detection of HHH final states at hadron colliders. It is clear at the moment that this is no easy feat, but history is such that over a decade ago just the observation of $H \to b\bar{b}$ decay was considered very far from achievable. That was established. Nowadays evidence for di-Higgs production may already be within reach in the next couple of years. In the near future the HL-LHC will deliver enormous amounts of data to experiments over a long period of time. We should remain confident that continuous, and significant, improvements on every aspect of the ingredients that make up these quests will be made. Beyond that, there is the promise of a future 100 TeV collider, where the SM HHH production cross section increases by a factor of 60 or so, and rough estimates, at this stage, predict almost reaching evidence for this process with 30 ab^{-1} of data. History shows this is bound to get better and better. It is an exciting time to push on this frontier.

Author contributions Shown are the participants of the HHH Workshop in Dubrovnik, where the Whitepaper was initiated. The following authors are visible on the attached picture: Hannah Arnold, Vuko Brigljevic, Maggie Chen, Tristan du Pree, Dinko Ferencek, Benjamin Fuks, Sanmay Ganguly, Osama Karkout, Marina Kolosova, Jacobo Konigsberg, Greg Landsberg, Bingxuan Liu, Brian Moser, Andreas Papaefstathiou, Roman Pasechnik, Tania Robens, Marko Stamenkovic, Panagiotis Stylianou, Tatjana Susa, Gilberto Tetlalmatzi-Xolocotzi, Giulia Zanderighi.

References

1. G. Aad et al., Observation of a new particle in the search for the Standard Model Higgs boson with the ATLAS detector at the LHC. Phys. Lett. B **716**, 1–29 (2012). arXiv:1207.7214

2. S. Chatrchyan et al., Observation of a new boson at a mass of 125 GeV with the CMS experiment at the LHC. Phys. Lett. B **716**, 30–61 (2012). arXiv:1207.7235

3. G. Aad et al. A detailed map of Higgs boson interactions by the ATLAS experiment ten years after the discovery. Nature, **607**(7917), 52–59 (2022). arXiv:2207.00092. [Erratum: Nature **612**, E24 (2022)]

4. A. Tumasyan et al., A portrait of the Higgs boson by the CMS experiment ten years after the discovery. Nature **607**(7917), 60–68 (2022). arXiv:2207.00043

5. G. Aad et al., Constraints on the Higgs boson self-coupling from single- and double-Higgs production with the ATLAS detector using pp collisions at s=13 TeV. Phys. Lett. B **843**, 137745 (2023). arXiv:2211.01216

6. R. Contino et al. Physics at a 100 TeV pp collider: Higgs and EW symmetry breaking studies (2016). arXiv:1606.09408. CERN-TH-2016-113

7. A. Abada et al., FCC physics opportunities: future circular collider conceptual design report volume 1. Eur. Phys. J. C **79**(6), 474 (2019)

8. M. Cepeda et al., Report from Working Group 2. CERN Yellow Rep. Monogr. **7**, 221–584 (2019). arXiv:1902.00134

9. P. Azzi et al., Report from Working Group 1: standard model physics at the HL-LHC and HE-LHC. CERN Yellow Rep. Monogr. **7**, 1–220 (2019). arXiv:1902.04070

10. T. Plehn, M. Rauch, The quartic Higgs coupling at hadron colliders. Phys. Rev. D **72**, 053008 (2005). arXiv:hep-ph/0507321

11. T. Binoth, S. Karg, N. Kauer, R. Ruckl, Multi-Higgs boson production in the Standard Model and beyond. Phys. Rev. D **74**, 113008 (2006). arXiv:hep-ph/0608057

12. A. David, A. Denner, M. Duehrssen, M. Grazzini, C. Grojean, G. Passarino, M. Schumacher, M. Spira, G. Weiglein, M. Zanetti, LHC HXSWG interim recommendations to explore the coupling structure of a Higgs-like particle (2012). arXiv:1209.0040

13. J.R. Andersen et al., Handbook of LHC Higgs Cross Sections: 3. Higgs Properties (2013). arXiv:1307.1347

14. S. Profumo, M.J. Ramsey-Musolf, G. Shaughnessy, Singlet Higgs phenomenology and the electroweak phase transition. JHEP **08**, 010 (2007). arXiv:0705.2425

15. G.C. Branco, P.M. Ferreira, L. Lavoura, M.N. Rebelo, M. Sher, J.P. Silva, Theory and phenomenology of two-Higgs-doublet models. Phys. Rep. **516**, 1–102 (2012). arXiv:1106.0034

16. J.R. Espinosa, T. Konstandin, F. Riva, Strong electroweak phase transitions in the standard model with a singlet. Nucl. Phys. B **854**, 592–630 (2012). arXiv:1107.5441

17. S. Profumo, M.J. Ramsey-Musolf, C.L. Wainwright, P. Winslow, Singlet-catalyzed electroweak phase transitions and precision Higgs boson studies. Phys. Rev. D **91**(3), 035018 (2015). arXiv:1407.5342

18. T. Robens, T. Stefaniak, Status of the Higgs singlet extension of the standard model after LHC Run 1. Eur. Phys. J. C **75**, 104 (2015). arXiv:1501.02234

19. A.G. Akeroyd et al., Prospects for charged Higgs searches at the LHC. Eur. Phys. J. C **77**(5), 276 (2017). arXiv:1607.01320

20. T. Robens, T. Stefaniak, J. Wittbrodt, Two-real-scalar-singlet extension of the SM: LHC phenomenology and benchmark scenarios. Eur. Phys. J. C **80**(2), 151 (2020). arXiv:1908.08554

21. J. Alison et al., Higgs boson potential at colliders: status and perspectives. Rev. Phys. **5**, 100045 (2020). arXiv:1910.00012

22. A.H. Ajjath, S. Hua-Sheng, N^3LO+N^3LL QCD improved Higgs pair cross sections. JHEP **02**, 067 (2023). arXiv:2209.03914

23. Combination of searches for non-resonant and resonant Higgs boson pair production in the $b\bar{b}\gamma\gamma$, $b\bar{b}\tau^+\tau^-$ and $b\bar{b}b\bar{b}$ decay channels using pp collisions at $\sqrt{s}$ = 13 TeV with the ATLAS detector (2021). ATLAS-CONF-2021-052

24. Snowmass White Paper Contribution: Physics with the Phase-2 ATLAS and CMS Detectors (2022) ATL-PHYS-PUB-2022-018

25. Snowmass White Paper Contribution: Physics with the Phase-2 ATLAS and CMS Detectors (2022). CMS-PAS-FTR-22-001

26. G. Degrassi, P.P. Giardino, F. Maltoni, D. Pagani, Probing the Higgs self coupling via single Higgs production at the LHC. JHEP **12**, 080 (2016). arXiv:1607.04251

27. M. Gorbahn, U. Haisch, Indirect probes of the trilinear Higgs coupling: $gg \rightarrow h$ and $h \rightarrow \gamma\gamma$. JHEP **10**, 094 (2016). arXiv:1607.03773

28. W. Bizon, M. Gorbahn, U. Haisch, G. Zanderighi, Constraints on the trilinear Higgs coupling from vector boson fusion and associated Higgs production at the LHC. JHEP **07**, 083 (2017). arXiv:1610.05771

29. F. Maltoni, D. Pagani, A. Shivaji, X. Zhao, Trilinear Higgs coupling determination via single-Higgs differential measurements at the LHC. Eur. Phys. J. C **77**(12), 887 (2017). arXiv:1709.08649

30. D. de Florian, I. Fabre, J. Mazzitelli, Triple Higgs production at hadron colliders at NNLO in QCD. JHEP **03**, 155 (2020). arXiv:1912.02760

31. B. Fuks, J.H. Kim, S.J. Lee, Probing Higgs self-interactions in proton-proton collisions at a center-of-mass energy of 100 TeV. Phys. Rev. D **93**(3), 035026 (2016). arXiv:1510.07697

32. P. Stylianou, G. Weiglein, Constraints on the trilinear and quartic Higgs couplings from triple Higgs production at the LHC and beyond. Eur. Phys. J. C **84**(4), 366 (2024). arXiv:2312.04646

33. W. Bizoń, U. Haisch, L. Rottoli, Constraints on the quartic Higgs self-coupling from double-Higgs production at future hadron colliders. JHEP **10**, 267 (2019). arXiv:1810.04665

34. S. Borowka, C. Duhr, F. Maltoni, D. Pagani, A. Shivaji, X. Zhao, Probing the scalar potential via double Higgs boson production at hadron colliders. JHEP **04**, 016 (2019). arXiv:1811.12366

35. A. Papaefstathiou, G. Tetlalmatzi-Xolocotzi, M. Zaro, Triple Higgs boson production to six b-jets at a 100 TeV proton collider. Eur. Phys. J. C **79**(11), 947 (2019). arXiv:1909.09166

36. A. Papaefstathiou, K. Sakurai, Triple Higgs boson production at a 100 TeV proton-proton collider. JHEP **02**, 006 (2016). arXiv:1508.06524

37. C.-Y. Chen, Q.-S. Yan, X. Zhao, Y.-M. Zhong, Z. Zhao, Probing triple-Higgs productions via 4b2γ decay channel at a 100 TeV hadron collider. Phys. Rev. D **93**(1), 013007 (2016). arXiv:1510.04013

38. B. Fuks, J.H. Kim, S.J. Lee, Scrutinizing the Higgs quartic coupling at a future 100 TeV proton–proton collider with taus and b-jets. Phys. Lett. B **771**, 354–358 (2017). arXiv:1704.04298

39. W. Kilian, S. Sun, Q.-S. Yan, X. Zhao, Z. Zhao, New Physics in multi-Higgs boson final states. JHEP **06**, 145 (2017). arXiv:1702.03554

40. C.G. Lester, D.J. Summers, Measuring masses of semiinvisibly decaying particles pair produced at hadron colliders. Phys. Lett. B **463**, 99–103 (1999). arXiv:hep-ph/9906349

41. A. Barr, C. Lester, P. Stephens, m(T2): the truth behind the glamour. J. Phys. G **29**, 2343–2363 (2003). arXiv:hep-ph/0304226

42. A.J. Barr, S.T. French, J.A. Frost, C.G. Lester, Speedy Higgs boson discovery in decays to tau lepton pairs: h→tau, tau. JHEP **10**, 080 (2011). arXiv:1106.2322

43. A.J. Barr, B. Gripaios, C.G. Lester, Measuring the Higgs boson mass in dileptonic W-boson decays at hadron colliders. JHEP **07**, 072 (2009). arXiv:0902.4864

44. A.J. Barr, M.J. Dolan, C. Englert, M. Spannowsky, Di-Higgs final states augMT2ed-selecting hh events at the high luminosity LHC. Phys. Lett. B **728**, 308–313 (2014). arXiv:1309.6318

45. S.F. King, M. Mühlleitner, R. Nevzorov, K. Walz, Discovery prospects for NMSSM Higgs bosons at the high-energy large hadron collider. Phys. Rev. D **90**(9), 095014 (2014). arXiv:1408.1120

46. R. Costa, M. Mühlleitner, M.O.P. Sampaio, R. Santos, Singlet extensions of the standard model at LHC Run 2: benchmarks and comparison with the NMSSM. JHEP **06**, 034 (2016). arXiv:1512.05355

47. U. Ellwanger, M. Rodriguez-Vazquez, Simultaneous search for extra light and heavy Higgs bosons via cascade decays. JHEP **11**, 008 (2017). arXiv:1707.08522

48. S. Baum, N.R. Shah, Two Higgs doublets and a complex singlet: disentangling the decay topologies and associated phenomenology. JHEP **12**, 044 (2018). arXiv:1808.02667

49. S. Baum, N.R. Shah, K. Freese, The NMSSM is within reach of the LHC: mass correlations & decay signatures. JHEP **04**, 011 (2019). arXiv:1901.02332

50. A. Papaefstathiou, T. Robens, G. Tetlalmatzi-Xolocotzi, Triple Higgs boson production at the large hadron collider with two real singlet scalars. JHEP **05**, 193 (2021). arXiv:2101.00037

51. C. Englert, M. Fairbairn, M. Spannowsky, P. Stylianou, S. Varma, Sensing Higgs boson cascade decays through memory. Phys. Rev. D **102**(9), 095027 (2020). arXiv:2008.08611

52. T. Robens, Two-real-singlet-model benchmark planes. Symmetry **15**(1), 27 (2023). arXiv:2209.10996

53. T.D. Lee, A theory of spontaneous T violation. Phys. Rev. D **8**, 1226–1239 (1973)

54. G.C. Branco, M.N. Rebelo, The Higgs mass in a model with two scalar doublets and spontaneous CP violation. Phys. Lett. B **160**, 117–120 (1985)

55. S. Weinberg, Unitarity constraints on CP nonconservation in Higgs exchange. Phys. Rev. D **42**, 860–866 (1990)

56. I.F. Ginzburg, M. Krawczyk, P. Osland, Two Higgs doublet models with CP violation, in *International Workshop on Linear Colliders (LCWS 2002)*, pp. 703–706 (2002). arXiv:hep-ph/0211371

57. D. Fontes, M. Mühlleitner, J.C. Romão, R. Santos, J.P. Silva, J. Wittbrodt, The C2HDM revisited. JHEP **02**, 073 (2018). arXiv:1711.09419

58. C.-Y. Chen, M. Freid, M. Sher, Next-to-minimal two Higgs doublet model. Phys. Rev. D **89**(7), 075009 (2014). arXiv:1312.3949

59. M. Muhlleitner, M.O.P. Sampaio, R. Santos, J. Wittbrodt, The N2HDM under theoretical and experimental scrutiny. JHEP **03**, 094 (2017). arXiv:1612.01309

60. I. Engeln, M. Mühlleitner, J. Wittbrodt, N2HDECAY: Higgs boson decays in the different phases of the N2HDM. Comput. Phys. Commun. **234**, 256–262 (2019). arXiv:1805.00966

61. R. Barbieri, S. Ferrara, C.A. Savoy, Gauge models with spontaneously broken local supersymmetry. Phys. Lett. B **119**, 343 (1982)

62. M. Dine, W. Fischler, M. Srednicki, A simple solution to the strong CP problem with a harmless axion. Phys. Lett. B **104**, 199–202 (1981)

63. J.R. Ellis, J.F. Gunion, H.E. Haber, L. Roszkowski, F. Zwirner, Higgs bosons in a nonminimal supersymmetric model. Phys. Rev. D **39**, 844 (1989)

64. M. Drees, Supersymmetric models with extended Higgs sector. Int. J. Mod. Phys. A **4**, 3635 (1989)

65. U. Ellwanger, M.R. de Traubenberg, C.A. Savoy, Particle spectrum in supersymmetric models with a gauge singlet. Phys. Lett. B **315**, 331–337 (1993). arXiv:hep-ph/9307322

66. U. Ellwanger, M.R. de Traubenberg, C.A. Savoy, Higgs phenomenology of the supersymmetric model with a gauge singlet. Z. Phys. C **67**, 665–670 (1995). arXiv:hep-ph/9502206

67. U. Ellwanger, M.R. de Traubenberg, C.A. Savoy, Phenomenology of supersymmetric models with a singlet. Nucl. Phys. B **492**, 21–50 (1997). arXiv:hep-ph/9611251

68. T. Elliott, S.F. King, P.L. White, Unification constraints in the next-to-minimal supersymmetric standard model. Phys. Lett. B **351**, 213–219 (1995). arXiv:hep-ph/9406303

69. S.F. King, P.L. White, Resolving the constrained minimal and next-to-minimal supersymmetric standard models. Phys. Rev. D **52**, 4183–4216 (1995). arXiv:hep-ph/9505326

70. F. Franke, H. Fraas, Neutralinos and Higgs bosons in the next-to-minimal supersymmetric standard model. Int. J. Mod. Phys. A **12**, 479–534 (1997). arXiv:hep-ph/9512366

71. M. Maniatis, The next-to-minimal supersymmetric extension of the standard model reviewed. Int. J. Mod. Phys. A **25**, 3505–3602 (2010). arXiv:0906.0777

72. U. Ellwanger, C. Hugonie, A.M. Teixeira, The next-to-minimal supersymmetric standard model. Phys. Rep. **496**, 1–77 (2010). arXiv:0910.1785

73. A. Banfi, G.P. Salam, G. Zanderighi, Infrared safe definition of jet flavor. Eur. Phys. J. C **47**, 113–124 (2006). arXiv:hep-ph/0601139

74. M. Cacciari, G.P. Salam, G. Soyez, The anti-k_t jet clustering algorithm. JHEP **04**, 063 (2008). arXiv:0802.1189

75. A. Banfi, G.P. Salam, G. Zanderighi, Accurate QCD predictions for heavy-quark jets at the Tevatron and LHC. JHEP **07**, 026 (2007). arXiv:0704.2999

76. M. Czakon, A. Mitov, R. Poncelet, Infrared-safe flavoured anti-k_T jets. JHEP **04**, 138 (2023). arXiv:2205.11879

77. R. Gauld, A. Huss, G. Stagnitto, Flavor identification of reconstructed hadronic jets. Phys. Rev. Lett. **130**(16), 161901 (2023). arXiv:2208.11138

78. S. Caletti, A.J. Larkoski, S. Marzani, D. Reichelt, Practical jet flavour through NNLO. Eur. Phys. J. C **82**(7), 632 (2022). arXiv:2205.01109

79. F. Caola, R. Grabarczyk, M.L. Hutt, G.P. Salam, L. Scyboz, J. Thaler, Flavored jets with exact anti-kt kinematics and tests of infrared and collinear safety. Phys. Rev. D **108**(9), 094010 (2023). arXiv:2306.07314

80. F. Buccioni, J.-N. Lang, J.M. Lindert, P. Maierhöfer, S. Pozzorini, H. Zhang, M.F. Zoller, OpenLoops 2. Eur. Phys. J. C **79**(10), 866 (2019). arXiv:1907.13071

81. J. Alwall, R. Frederix, S. Frixione, V. Hirschi, F. Maltoni, O. Mattelaer, H.S. Shao, T. Stelzer, P. Torrielli, M. Zaro, The automated computation of tree-level and next-to-leading order differential cross sections, and their matching to parton shower simulations. JHEP **07**, 079 (2014). arXiv:1405.0301

82. S. Actis, A. Denner, L. Hofer, J.-N. Lang, A. Scharf, S. Uccirati, RECOLA: REcursive computation of one-loop amplitudes. Comput. Phys. Commun. **214**, 140–173 (2017). arXiv:1605.01090

83. P. Nason, A new method for combining NLO QCD with shower Monte Carlo algorithms. JHEP **11**, 040 (2004). arXiv:hep-ph/0409146

84. S. Frixione, B.R. Webber, Matching NLO QCD computations and parton shower simulations. JHEP **06**, 029 (2002). arXiv:hep-ph/0204244

85. H.A. Chawdhry, M.L. Czakon, A. Mitov, R. Poncelet, NNLO QCD corrections to three-photon production at the LHC. JHEP **02**, 057 (2020). arXiv:1911.00479

86. S. Kallweit, V. Sotnikov, M. Wiesemann, Triphoton production at hadron colliders in NNLO QCD. Phys. Lett. B **812**, 136013 (2021). arXiv:2010.04681

87. H.A. Chawdhry, M. Czakon, A. Mitov, R. Poncelet, NNLO QCD corrections to diphoton production with an additional jet at the LHC. JHEP **09**, 093 (2021). arXiv:2105.06940

88. S. Badger, M. Czakon, H.B. Hartanto, R. Moodie, T. Peraro, R. Poncelet, S. Zoia, Isolated photon production in association with a jet pair through next-to-next-to-leading order in QCD. JHEP **10**, 071 (2023). arXiv:2304.06682

89. M. Czakon, A. Mitov, R. Poncelet, Next-to-next-to-leading order study of three-jet production at the LHC. Phys. Rev. Lett., **127**(15), 152001 (2021). arXiv:2106.05331. [Erratum: Phys. Rev. Lett. **129**, 119901 (2022)]

90. H.B. Hartanto, R. Poncelet, A. Popescu, S. Zoia, Next-to-next-to-leading order QCD corrections to Wbb̄ production at the LHC. Phys. Rev. D **106**(7), 074016 (2022). arXiv:2205.01687

91. L. Buonocore, S. Devoto, S. Kallweit, J. Mazzitelli, L. Rottoli, C. Savoini, Associated production of a W boson and massive bottom quarks at next-to-next-to-leading order in QCD. Phys. Rev. D **107**(7), 074032 (2023). arXiv:2212.04954

92. S. Catani, S. Devoto, M. Grazzini, S. Kallweit, J. Mazzitelli, C. Savoini, Higgs boson production in association with a top-antitop quark pair in next-to-next-to-leading order QCD. Phys. Rev. Lett. **130**(11), 111902 (2023). arXiv:2210.07846

93. L. Buonocore, S. Devoto, M. Grazzini, S. Kallweit, J. Mazzitelli, L. Rottoli, C. Savoini, Precise predictions for the associated production of a W boson with a top-antitop quark pair at the LHC. Phys. Rev. Lett. **131**(23), 231901 (2023). arXiv:2306.16311

94. S. Hoeche, F. Krauss, M. Schonherr, F. Siegert, QCD matrix elements + parton showers: the NLO case. JHEP **04**, 027 (2013). arXiv:1207.5030

95. T. Gehrmann, S. Hoche, F. Krauss, M. Schonherr, F. Siegert, NLO QCD matrix elements + parton showers in e^+e^- –> hadrons. JHEP **01**, 144 (2013). arXiv:1207.5031

96. R. Frederix, S. Frixione, Merging meets matching in MC@NLO. JHEP **12**, 061 (2012). arXiv:1209.6215

97. K. Hamilton, P. Nason, C. Oleari, G. Zanderighi, Merging H/W/Z + 0 and 1 jet at NLO with no merging scale: a path to parton shower + NNLO matching. JHEP **05**, 082 (2013). arXiv:1212.4504

98. V.S. Fadin, V.A. Khoze, A.D. Martin, Interference radiative phenomena in the production of heavy unstable particles. Phys. Rev. D **49**, 2247–2256 (1994)

99. A.A. Penin, Two-loop photonic corrections to massive Bhabha scattering. Nucl. Phys. B **734**, 185–202 (2006). arXiv:hep-ph/0508127

100. A. Mitov, S. Moch, The singular behavior of massive QCD amplitudes. JHEP **05**, 001 (2007). arXiv:hep-ph/0612149

101. T. Becher, K. Melnikov, Two-loop QED corrections to Bhabha scattering. JHEP **06**, 084 (2007). arXiv:0704.3582

102. T. Engel, C. Gnendiger, A. Signer, Y. Ulrich, Small-mass effects in heavy-to-light form factors. JHEP **02**, 118 (2019). arXiv:1811.06461

103. G. Wang, T. Xia, L.L. Yang, X. Ye, On the high-energy behavior of massive QCD amplitudes (2023). arXiv:2312.12242

104. M.A. Samuel, J.R. Ellis, M. Karliner, Comparison of the Pade approximation method to perturbative QCD calculations. Phys. Rev. Lett. **74**, 4380–4383 (1995). arXiv:hep-ph/9503411

105. J.R. Ellis, M. Karliner, M.A. Samuel, A prediction for the four loop beta function in QCD. Phys. Lett. B **400**, 176–181 (1997). arXiv:hep-ph/9612202

106. V. Elias, F.A. Chishtie, T.G. Steele, Pade improvement of hadronic Higgs decays. J. Phys. G **26**, 1239–1254 (2000). arXiv:hep-ph/0004140

107. R. Gröber, A. Maier, T. Rauh, Top quark mass effects in $gg \rightarrow ZZ$ at two loops and off-shell Higgs boson interference. Phys. Rev. D **100**(11), 114013 (2019). arXiv:1908.04061

108. J. Davies, R. Gröber, A. Maier, T. Rauh, M. Steinhauser, Top quark mass dependence of the Higgs boson-gluon form factor at three loops. Phys. Rev. D, **100**(3), 034017 (2019). arXiv:1906.00982. [Erratum: Phys. Rev. D **102**, 059901 (2020)]

109. R. Harlander, M. Kramer, M. Schumacher, Bottom-quark associated Higgs-boson production: reconciling the four- and five-flavour scheme approach (2011). arXiv:1112.3478

110. M. Cacciari, M. Greco, P. Nason, The p_T spectrum in heavy-flavour hadroproduction. JHEP **05**, 007 (1998). arXiv:hep-ph/9803400

111. M. Dasgupta, F.A. Dreyer, K. Hamilton, P.F. Monni, G.P. Salam, G. Soyez, Parton showers beyond leading logarithmic accuracy. Phys. Rev. Lett. **125**(5), 052002 (2020). arXiv:2002.11114

112. M. van Beekveld, S. Ferrario Ravasio, K. Hamilton, G.P. Salam, A. Soto-Ontoso, G. Soyez, R. Verheyen, PanScales showers for hadron collisions: all-order validation. JHEP **11**, 020 (2022). arXiv:2207.09467

113. Z. Nagy, D.E. Soper, A parton shower based on factorization of the quantum density matrix. JHEP **06**, 097 (2014). arXiv:1401.6364

114. J.R. Forshaw, J. Holguin, S. Plätzer, Building a consistent parton shower. JHEP **09**, 014 (2020). arXiv:2003.06400

115. F. Herren, S. Höche, F. Krauss, D. Reichelt, M. Schoenherr, A new approach to color-coherent parton evolution. JHEP **10**, 091 (2023). arXiv:2208.06057

116. S. Ferrario Ravasio, K. Hamilton, A. Karlberg, G.P. Salam, L. Scyboz, G. Soyez, Parton showering with higher logarithmic accuracy for soft emissions. Phys. Rev. Lett. **131**(16), 161906 (2023). arXiv:2307.11142

117. Z. Nagy, D.E. Soper, Parton showers with more exact color evolution. Phys. Rev. D **99**(5), 054009 (2019). arXiv:1902.02105

118. K. Hamilton, R. Medves, G.P. Salam, L. Scyboz, G. Soyez, Colour and logarithmic accuracy in final-state parton showers. JHEP **03**(041), 041 (2021). arXiv:2011.10054

119. J.R. Forshaw, J. Holguin, S. Plätzer, Rings and strings: a basis for understanding subleading colour and QCD coherence beyond the two-jet limit. JHEP **05**, 190 (2022). arXiv:2112.13124

120. J.M. Campbell et al. Event Generators for High-Energy Physics Experiments, in *Snowmass 2021* (2022). arXiv:2203.11110

121. A.J. Larkoski, I. Moult, B. Nachman, Jet substructure at the large hadron collider: a review of recent advances in theory and machine learning. Phys. Rep. **841**, 1–63 (2020). arXiv:1709.04464

122. R. Kogler et al., Jet substructure at the large hadron collider: experimental review. Rev. Mod. Phys. **91**(4), 045003 (2019). arXiv:1803.06991

123. S. Marzani, G. Soyez, M. Spannowsky, *Looking inside jets: an introduction to jet substructure and boosted-object phenomenology*, vol. 958. Springer (2019). arXiv:1901.10342

124. F.A. Dreyer, G.P. Salam, G. Soyez, The lund jet plane. JHEP **12**, 064 (2018). arXiv:1807.04758

125. I. Moult, L. Necib, J. Thaler, New angles on energy correlation functions. JHEP **12**, 153 (2016). arXiv:1609.07483

126. P.T. Komiske, E.M. Metodiev, J. Thaler, Energy flow networks: deep sets for particle jets. JHEP **01**, 121 (2019). arXiv:1810.05165

127. Q. Huilin, L. Gouskos, ParticleNet: jet tagging via particle clouds. Phys. Rev. D **101**(5), 056019 (2020). arXiv:1902.08570

128. F.A. Dreyer, Q. Huilin, Jet tagging in the Lund plane with graph networks. JHEP **03**, 052 (2021). arXiv:2012.08526

129. D.Y. Shao, C.S. Li, H.T. Li, J. Wang, Threshold resummation effects in Higgs boson pair production at the LHC. JHEP **07**, 169 (2013). arXiv:1301.1245

130. D. de Florian, J. Mazzitelli, Higgs pair production at next-to-next-to-leading logarithmic accuracy at the LHC. JHEP **09**, 053 (2015). arXiv:1505.07122

131. D. de Florian et al., Handbook of LHC Higgs Cross Sections: 4. Deciphering the Nature of the Higgs Sector (2016). arXiv:1610.07922

132. A. Shmakov, M.J. Fenton, T.-W. Ho, S.-C. Hsu, D. Whiteson, P. Baldi, SPANet: generalized permutationless set assignment for particle physics using symmetry preserving attention. SciPost Phys. **12**(5), 178 (2022). arXiv:2106.03898

133. G. Aad et al., Search for nonresonant pair production of Higgs bosons in the bb̄bb̄ final state in pp collisions at s=13 TeV with the ATLAS detector. Phys. Rev. D **108**(5), 052003 (2023). arXiv:2301.03212

134. A. Tumasyan et al., Search for Higgs boson pair production in the four b quark final state in proton-proton collisions at s=13 TeV. Phys. Rev. Lett. **129**(8), 081802 (2022). arXiv:2202.09617

135. A. Tumasyan et al., Search for nonresonant pair production of highly energetic higgs bosons decaying to bottom quarks. Phys. Rev. Lett. **131**(4), 041803 (2023). arXiv:2205.06667

136. G. Aad et al., Search for the non-resonant production of Higgs boson pairs via gluon fusion and vector-boson fusion in the $b\bar{b}\tau^+\tau^-$ final state in proton-proton collisions at $\sqrt{s} = 13$ TeV with the ATLAS detector (2023). ATLAS-CONF-2023-071

137. A. Tumasyan et al., Search for nonresonant Higgs boson pair production in final state with two bottom quarks and two tau leptons in proton-proton collisions at s=13 TeV. Phys. Lett. B **842**, 137531 (2023). arXiv:2206.09401

138. G. Aad et al., Studies of new Higgs boson interactions through nonresonant HH production in the $b\bar{b}\gamma\gamma$ final state in pp collisions at $\sqrt{s} = 13$ TeV with the ATLAS detector. JHEP **01**, 066 (2024). arXiv:2310.12301

139. A.M. Sirunyan et al., Search for nonresonant Higgs boson pair production in final states with two bottom quarks and two photons in proton-proton collisions at $\sqrt{s} = 13$ TeV. JHEP **03**, 257 (2021). arXiv:2011.12373

140. CERN, Yellow Report webpage (2016). https://twiki.cern.ch/twiki/bin/view/LHCPhysics/CERNYellowReportPageBR

141. R.L. Workman et al., Review of particle physics. PTEP, **2022**, 083C01 (2022)

142. A. Papaefstathiou, G. Tetlalmatzi-Xolocotzi, M. Zaro, Triple Higgs boson production to six b-jets at a 100 TeV proton collider. Eur. Phys. J. C **79**(11), 947 (2019). arXiv:1909.09166

143. R. Contino et al. Physics at a 100 TeV pp collider: Higgs and EW symmetry breaking studies (2016). arXiv:1606.09408

144. B. Fuks, J.H. Kim, S.J. Lee, Scrutinizing the Higgs quartic coupling at a future 100 TeV proton-proton collider with taus and b-jets. Phys. Lett. B **771**, 354–358 (2017). arXiv:1704.04298

145. F. Maltoni, E. Vryonidou, M. Zaro, Top-quark mass effects in double and triple Higgs production in gluon-gluon fusion at NLO. JHEP **11**, 079 (2014). arXiv:1408.6542

146. G. Aad et al., Search for the non-resonant production of Higgs boson pairs via gluon fusion and vector-boson fusion in the $b\bar{b}\tau^+\tau^-$ final state in proton-proton collisions at $\sqrt{s} = 13$ TeV with the ATLAS detector (2024). arXiv:2404.12660

147. Z. Gillis, B. Moser, L. Rottoli, P. Windischhofer, Addendum to: constraints on the quartic Higgs self-coupling from double-Higgs production at future hadron colliders (2024). arXiv:2402.03463

148. P. Agrawal, D. Saha, L.-X. Xu, J.-H. Yu, C.P. Yuan, Determining the shape of the Higgs potential at future colliders. Phys. Rev. D **101**(7), 075023 (2020). arXiv:1907.02078

149. M.J. Dolan, C. Englert, N. Greiner, M. Spannowsky, Further on up the road: $hhjj$ production at the LHC. Phys. Rev. Lett. **112**, 101802 (2014). arXiv:1310.1084

150. L.-S. Ling, R.-Y. Zhang, W.-G. Ma, L. Guo, W.-H. Li, X.-Z. Li, NNLO QCD corrections to Higgs pair production via vector boson fusion at hadron colliders. Phys. Rev. D **89**(7), 073001 (2014). arXiv:1401.7754

151. M.J. Dolan, C. Englert, N. Greiner, K. Nordstrom, M. Spannowsky, $hhjj$ production at the LHC. Eur. Phys. J. C **75**(8), 387 (2015). arXiv:1506.08008

152. F. Bishara, R. Contino, J. Rojo, Higgs pair production in vector-boson fusion at the LHC and beyond. Eur. Phys. J. C **77**(7), 481 (2017). arXiv:1611.03860

153. E. Arganda, C. Garcia-Garcia, M.J. Herrero, Probing the Higgs self-coupling through double Higgs production in vector boson scattering at the LHC. Nucl. Phys. B **945**, 114687 (2019). arXiv:1807.09736

154. G. Aad et al., Search for the $HH \rightarrow b\bar{b}b\bar{b}$ process via vector-boson fusion production using proton-proton collisions at $\sqrt{s} = 13$ TeV with the ATLAS detector. JHEP **07**, 108 (2020). arXiv:2001.05178

155. A. Dainese, M. Mangano, A.B. Meyer, A. Nisati, G. Salam, M.A. Vesterinen, (eds.), *Report on the Physics at the HL-LHC, and Perspectives for the HE-LHC. Report number CERN-2019-007*, CERN Yellow Reports: Monographs, vol. 7. CERN (2019)

156. F. Kling et al., Maximizing the significance in Higgs boson pair analyses. Phys. Rev. D **95**, 035026 (2017). arXiv:1607.07441

157. J.M. Butterworth, A.R. Davison, M. Rubin, G.P. Salam, Jet substructure as a new Higgs search channel at the LHC. Phys. Rev. Lett. **100**, 242001 (2008). arXiv:0802.2470

158. A. Abdesselam et al., Boosted objects: a probe of beyond the standard model physics. Eur. Phys. J. C **71**, 1661 (2011). arXiv:1012.5412

159. A. Butter et al., The machine learning landscape of top taggers. SciPost. Phys. **7**, 014 (2019). arXiv:1902.09914

160. L Borgonovi, S. Braibant, B. Di Micco, E. Fontanesi, P. Harris, C. Helsens, D. Jamin, M.L. Mangano, G. Ortona, M. Selvaggi, A. Sznajder, M. Testa, M. Verducci, Higgs measurements at FCC-hh. Technical report, CERN, Geneva (2018)

161. F. Scarselli, M. Gori, A.C. Tsoi, M. Hagenbuchner, G. Monfardini, The graph neural network model. IEEE Trans. Neural Netw. **20**(1), 61 (2009)

162. P.W. Battaglia, R. Pascanu, M. Lai, D. Rezende, K. Kavukcuoglu, Interaction Networks for Learning about Objects, Relations and Physics (2016). arXiv:1612.00222

163. Y. Wang, Y. Sun, Z. Liu, S.E. Sarma, M.M. Bronstein, J.M. Solomon, Dynamic graph CNN for learning on point clouds. ACM Trans. Graph. (2019). arXiv:1801.07829

164. J. Lin, M. Freytsis, I. Moult, B. Nachman, Boosting $H \rightarrow b\bar{b}$ with machine learning. JHEP **10**, 101 (2018). arXiv:1807.10768

165. E.A. Moreno et al., JEDI-net: a jet identification algorithm based on interaction networks. Eur. Phys. J. C **80**, 58 (2020). arXiv:1908.05318

166. E.A. Moreno et al., Interaction networks for the identification of boosted $H \rightarrow b\bar{b}$ decays. Phys. Rev. D **102**, 012010 (2020). arXiv:1909.12285

167. E. Bernreuther, T. Finke, F. Kahlhoefer, M. Krämer, A. Mück, Casting a graph net to catch dark showers. SciPost. Phys. **10**(2), 046 (2021). arXiv:2006.08639

168. A.M. Sirunyan et al., Identification of heavy, energetic, hadronically decaying particles using machine-learning techniques. JINST **15**, P06005 (2020). arXiv:2004.08262

169. J. Shlomi, P. Battaglia, J.-R. Vlimant, Graph neural networks in particle physics. Mach. Learn. Sci. Technol. **2**, 021001 (2021). arXiv:2007.13681

170. J. Duarte, J.-R. Vlimant, Graph neural networks for particle tracking and reconstruction, in *Artificial Intelligence for High Energy Physics*, ed. by P. Calafiura, D. Rousseau, K. Terao (World Scientific, 2022), p. 387. arXiv:2012.01249

171. S. Thais, P. Calafiura, G. Chachamis, G. DeZoort, J. Duarte, S. Ganguly, M. Kagan, D. Murnane, M.S. Neubauer, K. Terao, Graph Neural Networks in Particle Physics: Implementations, Innovations, and Challenges, in *2022 Snowmass Summer Study* (2022). arXiv:2203.12852

172. J. Gilmer, S.S. Schoenholz, P.F. Riley, O. Vinyals, G.E. Dahl, Neural Message Passing for Quantum Chemistry, in *ICML* (2017). arXiv:1704.01212

173. A.M. Sirunyan et al., Inclusive search for highly boosted Higgs bosons decaying to bottom quark-antiquark pairs in proton-proton collisions at $\sqrt{s} = 13$ TeV. JHEP **12**, 085 (2020). arXiv:2006.13251

174. A.M. Sirunyan et al., A search for the standard model Higgs boson decaying to charm quarks. JHEP **03**, 131 (2020). arXiv:1912.01662

175. Nonresonant pair production of highly energetic Higgs bosons decaying to bottom quarks. CMS Physics Analysis Summary CMS-PAS-B2G-22-003 (2022)

176. S. Banerjee, C. Englert, M.L. Mangano, M. Selvaggi, M. Spannowsky, hh + jet production at 100 TeV. Eur. Phys. J. C **78**(4), 322 (2018). arXiv:1802.01607

177. J. de Favereau, C. Delaere, P. Demin, A. Giammanco, V. Lemaître, A. Mertens, M. Selvaggi, DELPHES 3, a modular framework for fast simulation of a generic collider experiment. JHEP **02**, 057 (2014). arXiv:1307.6346

178. Delphes FCC Physic events varXiv:0.2 (2022). http://fcc-physics-events.web.cern.ch/fcc-physics-events/Delphesevents_fcc_v02.php

179. M. Cacciari, G.P. Salam, G. Soyez, FastJet user manual. Eur. Phys. J. C **72**, 1896 (2012). arXiv:1111.6097

180. A.J. Larkoski, S. Marzani, G. Soyez, J. Thaler, Soft drop. JHEP **05**, 146 (2014). arXiv:1402.2657

181. J. Thaler, K. Van Tilburg, Identifying boosted objects with N-subjettiness. JHEP **03**, 015 (2011). arXiv:1011.2268

182. D.P. Kingma, J. Ba, Adam: a method for stochastic optimization, in *3rd International Conference on Learning Representations, ICLR 2015, San Diego, CA, USA, May 7–9, 2015, Conference Track Proceedings*, ed. by Y. Bengio, Y. LeCun (2015). arXiv:1412.6980

183. F.A.D. Bello, S. Ganguly, E. Gross, M. Kado, M. Pitt, L. Santi, J. Shlomi, Towards a computer vision particle flow. Eur. Phys. J. C **81**(2), 107 (2021). arXiv:2003.08863

184. J. Pata, J. Duarte, J.-R. Vlimant, M. Pierini, M. Spiropulu, MLPF: efficient machine-learned particle-flow reconstruction using graph neural networks. Eur. Phys. J. C **81**(5), 381 (2021). arXiv:2101.08578

185. J. Pata, J. Duarte, F. Mokhtar, E. Wulff, J. Yoo, J.-R. Vlimant, M. Pierini, M. Girone, Machine learning for particle flow reconstruction at CMS. J. Phys. Conf. Ser. **2438**(1), 012100 (2023). arXiv:2203.00330

186. J. Guo, J. Li, T. Li, R. Zhang, Boosted Higgs boson jet reconstruction via a graph neural network. Phys. Rev. D **103**(11), 116025 (2021). arXiv:2010.05464

187. Mass regression of highly-boosted jets using graph neural networks. CMS Detector Performance Note CMS-DP-2021-017 (2021)

188. F. Mokhtar, R. Kansal, D. Diaz, J. Duarte, J. Pata, M. Pierini, J.-R. Vlimant, Explaining machine-learned particle-flow reconstruction, in *4th Machine Learning and the Physical Sciences Workshop at the 35th Conference on Neural Information Processing Systems* (2021). arXiv:2111.12840

189. A. Bogatskiy, B. Anderson, J.T. Offermann, M. Roussi, D.W. Miller, R. Kondor, Lorentz Group Equivariant Neural Network for Particle Physics, in *Proceedings of the 37th International Conference on Machine Learning*, *Proceedings of Machine Learning Research*, ed. by H. Daumé III, A. Singh, vol. 119, p. 992. PMLR (2020). arXiv:2006.04780

190. A. Bogatskiy et al., Symmetry Group Equivariant Architectures for Physics. In *2022 Snowmass Summer Study* (2022). arXiv:2203.06153

191. The ATLAS Collaboration, Jet reconstruction and performance using particle flow with the ATLAS Detector. Eur. Phys. J. C **77**(7), 466 (2017). arXiv:1703.10485

192. The ATLAS Collaboration, ATLAS flavour-tagging algorithms for the LHC Run 2 pp collision dataset. Eur. Phys. J. C **83**(7), 681 (2023). arXiv:2211.16345

193. The ATLAS Collaboration, Fast b-tagging at the high-level trigger of the ATLAS experiment in LHC Run 3. JINST **18**(11), P11006 (2023). arXiv:2306.09738

194. The ATLAS Collaboration, Measurement of the $t\bar{t}$ cross section and its ratio to the Z production cross section using pp collisions at $\sqrt{s}$=arXiv:13.6 TeV with the ATLAS detector. Phys. Lett. B **848**, 138376 (2024). arXiv:2308.09529

195. Performance of the Run 3 ATLAS b-tagging algorithms. Technical Report FTAG-2022-004, CERN (2022)

196. Jet Flavour Tagging With GN1 and DL1d. Generator dependence, Run 2 and Run 3 data agreement studies. Technical Report FTAG-2023-01, CERN (2023)

197. Neural Network Jet Flavour Tagging with the Upgraded ATLAS Inner Tracker Detector at the High-Luminosity LHC. Technical Report ATL-PHYS-PUB-2022-047, CERN, Geneva (2022)

198. Graph Neural Network Jet Flavour Tagging with the ATLAS Detector. Technical Report ATL-PHYS-PUB-2022-027, CERN, Geneva (2022)

199. E. Bols, J. Kieseler, M. Verzetti, M. Stoye, A. Stakia, Jet flavour classification using DeepJet. JINST **15**(12), P12012 (2020). arXiv:2008.10519

200. Performance of the DeepJet b tagging algorithm using 41.9/fb of data from proton-proton collisions at 13TeV with Phase 1 CMS detector. Technical Report CMS-DP-2018-058 (2018)

201. A.M. Sirunyan et al., Identification of heavy-flavour jets with the CMS detector in pp collisions at 13 TeV. JINST **13**(05), P05011 (2018). arXiv:1712.07158

202. Adversarial training for b-tagging algorithms in CMS. Technical Report CMS-DP-2022-049 (2022)

203. I. Goodfellow, Y. Bengio, A. Courville. Deep Learning (MIT Press, 2016). http://www.deeplearningbook.org

204. I.J. Goodfellow, J. Shlens, C. Szegedy, Explaining and harnessing adversarial examples (2015). arXiv:1412.6572

205. A. Tumasyan et al., A new calibration method for charm jet identification validated with proton-proton collision events at $\sqrt{s}$ =13 TeV. JINST **17**(03), P03014 (2022). arXiv:2111.03027

206. H. Qu, C. Li, S. Qian, Particle Transformer for Jet Tagging (2022). arXiv:2202.03772

207. A. Vaswani, N. Shazeer, N. Parmar, J. Uszkoreit, L. Jones, A.N. Gomez, L. Kaiser, I. Polosukhin, Attention Is All You Need, in *31st International Conference on Neural Information Processing Systems* (2017). arXiv:1706.03762

208. Transformer models for heavy flavor jet identification. Technical Report CMS-DP-2022-050 (2022)

209. Variable Radius, Exclusive-k_T, and Center-of-Mass Subjet Reconstruction for Higgs($\to b\bar{b}$) Tagging in ATLAS. Technical Report ATL-PHYS-PUB-2017-010, CERN, Geneva (2017)

210. DeXTer: Deep Sets based Neural Networks for Low-p_T $X \to b\bar{b}$ Identification in ATLAS. Technical Report ATL-PHYS-PUB-2022-042, CERN, Geneva (2022)

211. The ATLAS Collaboration, Optimisation of large-radius jet reconstruction for the ATLAS detector in 13 TeV proton–proton collisions. Eur. Phys. J. C **81**(4), 334 (2021). arXiv:2009.04986

212. Transformer Neural Networks for Identifying Boosted Higgs Bosons decaying into $b\bar{b}$ and $c\bar{c}$ in ATLAS. Technical Report ATL-PHYS-PUB-2023-021, CERN, Geneva (2023)

213. A.M. Sirunyan et al., Identification of heavy, energetic, hadronically decaying particles using machine-learning techniques. JINST **15**(06), P06005 (2020). arXiv:2004.08262

214. G. Louppe, M. Kagan, K. Cranmer, Learning to Pivot with Adversarial Networks (2016). arXiv:1611.01046

215. J. Dolen, P. Harris, S. Marzani, S. Rappoccio, N. Tran, Thinking outside the ROCs: designing decorrelated taggers (DDT) for jet substructure. JHEP **05**, 156 (2016). arXiv:1603.00027

216. Y. Wang, Y. Sun, Z. Liu, S.E. Sarma, M.M. Bronstein, J.M. Solomon, Dynamic graph cnn for learning on point clouds (2019) arXiv:1801.07829

217. Identification of highly Lorentz-boosted heavy particles using graph neural networks and new mass decorrelation techniques. Technical Report CMS-DP-2020-002 (2020)

218. The ATLAS Collaboration, Configuration and performance of the ATLAS b-jet triggers in Run 2. Eur. Phys. J. C **81**(12), 1087 (2021). arXiv:2106.03584

219. Performance of Run 3 HLT b-tagging with fast tracking. Technical report (2022). All figures are available at https://twiki.cern.ch/twiki/bin/view/AtlasPublic/BJetTriggerPublicResults

220. Performance of the ParticleNet tagger on small and large-radius jets at High Level Trigger in Run 3. Technical Report CMS-DP-2023-021 (2023)

221. Novel strategy targeting HH and HHH production at High Level Trigger in Run 3. Technical Report CMS-DP-2023-050 (2023)

222. B-Jet Trigger Performance in Run 2. Technical Report CMS-DP-2019-042 (2019)

223. Performance of top triggers in Run 2. Technical Report CMS-DP-2019-026 (2019)

224. Performance of tau lepton reconstruction at High Level Trigger using 2022 data from the CMS experiment at CERN. Technical Report CMS-DP-2023-024 (2023)

225. A. Tumasyan et al., Identification of hadronic tau lepton decays using a deep neural network. JINST **17**, P07023 (2022). arXiv:2201.08458

226. Performance of jets and missing transverse momentum reconstruction at the High Level Trigger using Run 3 data from the CMS Experiment at CERN. Technical Report CMS-DP-2023-016 (2023)

227. A.M. Sirunyan et al., Combination of searches for Higgs boson pair production in proton-proton collisions at $\sqrt{s} = 13$ TeV. Phys. Rev. Lett. **122**(12), 121803 (2019). arXiv:1811.09689

228. M. Aaboud et al., Search for pair production of Higgs bosons in the $b\bar{b}b\bar{b}$ final state using proton-proton collisions at $\sqrt{s} =$ 13 TeV with the ATLAS detector. JHEP **01**, 030 (2019). arXiv:1804.06174

229. A.M. Sirunyan et al., Search for resonant pair production of Higgs bosons decaying into bottom quark-antiquark pairs in proton-proton collisions at 13 TeV. JHEP **08**, 152 (2018). arXiv:1806.03548

230. G. Aad et al., Combination of searches for Higgs boson pairs in pp collisions at $\sqrt{s} =$13 TeV with the ATLAS detector. Phys. Lett. B **800**, 135103 (2020). arXiv:1906.02025

231. G. Aad et al., Search for heavy resonances decaying into a pair of Z bosons in the $\ell^+\ell^-\ell'^+\ell'^-$ and $\ell^+\ell^-\nu\bar{\nu}$ final states using 139 fb^{-1} of proton-proton collisions at $\sqrt{s} = 13$ TeV with the ATLAS detector. Eur. Phys. J. C **81**(4), 332 (2021). arXiv:2009.14791

232. A. Tumasyan et al., Search for a heavy Higgs boson decaying into two lighter Higgs bosons in the $\tau\tau$bb final state at 13 TeV. JHEP **11**, 057 (2021). arXiv:2106.10361

233. T. Robens, Two-Real-Singlet Model Benchmark Planes—A Moriond Update, in *57th Rencontres de Moriond on QCD and High Energy Interactions* (2023). arXiv:2305.08595

234. T. Robens, TRSM benchmark planes—EPS-HEP2023 update. *PoS* EPS-HEP2023:055 (2024). arXiv:2310.18045

235. A. Papaefstathiou. `MadGraph5_aMC@NLO` model for standard model + two extra scalar particles (2023). https://gitlab.com/apapaefs/twoscalar

236. J. Alwall, M. Herquet, F. Maltoni, O. Mattelaer, T. Stelzer, MadGraph 5: going beyond. JHEP **06**, 128 (2011). arXiv:1106.0522

237. E. Conte, B. Fuks, G. Serret, MadAnalysis 5, a user-friendly framework for collider phenomenology. Comput. Phys. Commun. **184**, 222–256 (2013). arXiv:1206.1599

238. A.M. Sirunyan et al., Combination of searches for Higgs boson pair production in proton-proton collisions at $\sqrt{s} = 13$ TeV. Phys. Rev. Lett. **122**(12), 121803 (2019). arXiv:1811.09689

239. G. Aad et al., Combination of searches for Higgs boson pairs in pp collisions at $\sqrt{s} =$13 TeV with the ATLAS detector. Phys. Lett. B **800**, 135103 (2020). arXiv:1906.02025

240. A.M. Sirunyan et al., Search for a new scalar resonance decaying to a pair of Z bosons in proton-proton collisions at $\sqrt{s} = 13$ TeV. JHEP, **06**, 127 (2018). arXiv:1804.01939. [Erratum: JHEP **03**, 128 (2019)]

241. M. Aaboud et al., Search for heavy resonances decaying into WW in the $e\nu\mu\nu$ final state in pp collisions at $\sqrt{s} = 13$ TeV with the ATLAS detector. Eur. Phys. J. C **78**(1), 24 (2018). arXiv:1710.01123

242. HL-LHC prospects for diboson resonance searches and electroweak vector boson scattering in the $WW/WZ \to \ell\nu qq$ final state. Technical Report ATL-PHYS-PUB-2018-022, CERN, Geneva (2018)

243. M. Aaboud et al., Search for Higgs boson pair production in the $WW^{(*)}WW^{(*)}$ decay channel using ATLAS data recorded at $\sqrt{s} = 13$ TeV. JHEP **05**, 124 (2019). arXiv:1811.11028

244. P.M. Ferreira, J. Gonçalves, A.P. Morais, A. Onofre, R. Pasechnik, V. Vatellis, Collider phenomenology of new neutral scalars in a flavored multi-Higgs model. Phys. Rev. D **107**(9), 095041 (2023). arXiv:2211.10109

245. H. Abouabid, A. Arhrib, D. Azevedo, J. El Falaki, P.M. Ferreira, M. Mühlleitner, R. Santos, Benchmarking di-Higgs production in various extended Higgs sector models. JHEP **09**, 011 (2022). arXiv:2112.12515

246. P. Slavich et al., Higgs-mass predictions in the MSSM and beyond. Eur. Phys. J. C **81**(5), 450 (2021)

247. R. Grober, M. Muhlleitner, M. Spira, Higgs pair production at NLO QCD for CP-violating Higgs sectors. Nucl. Phys. B **925**, 1–27 (2017). arXiv:1705.05314

248. A. Ordell, R. Pasechnik, H. Serôdio, F. Nottensteiner, Classification of anomaly-free 2HDMs with a gauged U(1)' symmetry. Phys. Rev. D **100**(11), 115038 (2019). arXiv:1909.05548

249. A. Ordell, R. Pasechnik, H. Serôdio, Anomaly-free 2HDMs with a gauged abelian symmetry and two generations of right-handed neutrinos. Phys. Rev. D **102**(3), 035016 (2020). arXiv:2006.08676

250. S.L. Glashow, S. Weinberg, Natural conservation laws for neutral currents. Phys. Rev. D **15**, 1958 (1977)

251. A.W. El Kaffas, P. Osland, O.M. Ogreid, CP violation, stability and unitarity of the two Higgs doublet model. Nonlinear Phenom. Complex Syst. **10**, 347–357 (2007). arXiv:hep-ph/0702097

252. J.E. Camargo-Molina, T. Mandal, R. Pasechnik, J. Wessén, Heavy charged scalars from $c\bar{s}$ fusion: a generic search strategy applied to a 3HDM with U(1) × U(1) family symmetry. JHEP **03**, 024 (2018). arXiv:1711.03551

253. J.E. Kim, H.P. Nilles, The mu problem and the strong CP problem. Phys. Lett. B **138**, 150–154 (1984)

254. R. Coimbra, M.O.P. Sampaio, R. Santos, ScannerS: constraining the phase diagram of a complex scalar singlet at the LHC. Eur. Phys. J. C **73**, 2428 (2013). arXiv:1301.2599

255. R. Costa, R. Guedes, M.O.P. Sampaio, R. Santos, ScannerS project (2014). http://scanners.hepforge.org

256. M. Mühlleitner, M.O.P. Sampaio, R. Santos, J. Wittbrodt, ScannerS: parameter scans in extended scalar sectors. Eur. Phys. J. C **82**(3), 198 (2022). arXiv:2007.02985

257. I.P. Ivanov, J.P. Silva, Tree-level metastability bounds for the most general two Higgs doublet model. Phys. Rev. D **92**(5), 055017 (2015). arXiv:1507.05100

258. M. Baak, J. Cúth, J. Haller, A. Hoecker, R. Kogler, K. Mönig, M. Schott, J. Stelzer, The global electroweak fit at NNLO and prospects for the LHC and ILC. Eur. Phys. J. C **74**, 3046 (2014). arXiv:1407.3792

259. G. Aad et al., Combined measurement of the Higgs boson mass in pp collisions at $\sqrt{s}$ = 7 and 8 TeV with the ATLAS and CMS experiments. Phys. Rev. Lett. **114**, 191803 (2015). arXiv:1503.07589

260. P. Bechtle, S. Heinemeyer, O. Stål, T. Stefaniak, G. Weiglein, *HiggsSignals*: Confronting arbitrary Higgs sectors with measurements at the Tevatron and the LHC. Eur. Phys. J. C **74**(2), 2711 (2014). arXiv:1305.1933

261. P. Bechtle, O. Brein, S. Heinemeyer, G. Weiglein, K.E. Williams, HiggsBounds: confronting arbitrary Higgs sectors with exclusion bounds from LEP and the Tevatron. Comput. Phys. Commun. **181**, 138–167 (2010). arXiv:0811.4169

262. P. Bechtle, O. Brein, S. Heinemeyer, G. Weiglein, K.E. Williams, HiggsBounds 2.0.0: confronting neutral and charged Higgs sector predictions with exclusion bounds from LEP and the Tevatron. Comput. Phys. Commun. **182**, 2605–2631 (2011). arXiv:1102.1898

263. P. Bechtle, O. Brein, S. Heinemeyer, O. Stål, T. Stefaniak, G. Weiglein, K.E. Williams, HiggsBounds − 4: improved tests of extended Higgs sectors against exclusion bounds from LEP, the tevatron and the LHC. Eur. Phys. J. C **74**(3), 2693 (2014). arXiv:1311.0055

264. G. Aad et al., Search for resonances decaying into photon pairs in 139 fb^{-1} of pp collisions at $\sqrt{s}$=13 TeV with the ATLAS detector. Phys. Lett. B **822**, 136651 (2021). arXiv:2102.13405

265. H.E. Haber, H.E. Logan, Radiative corrections to the Z b anti-b vertex and constraints on extended Higgs sectors. Phys. Rev. D **62**, 015011 (2000). arXiv:hep-ph/9909335

266. O. Deschamps, S. Descotes-Genon, S. Monteil, V. Niess, S. T'Jampens, V. Tisserand, The two Higgs doublet of type II facing flavour physics data. Phys. Rev. D **82**, 073012 (2010). arXiv:0907.5135

267. F. Mahmoudi, O. Stal, Flavor constraints on the two-Higgs-doublet model with general Yukawa couplings. Phys. Rev. D **81**, 035016 (2010). arXiv:0907.1791

268. T. Hermann, M. Misiak, M. Steinhauser, $\bar{B} \to X_s\gamma$ in the two Higgs doublet model up to next-to-next-to-leading order in QCD. JHEP **11**, 036 (2012). arXiv:1208.2788

269. M. Misiak et al., Updated NNLO QCD predictions for the weak radiative B-meson decays. Phys. Rev. Lett. **114**(22), 221801 (2015). arXiv:1503.01789

270. M. Misiak, M. Steinhauser, Weak radiative decays of the B meson and bounds on $M_{H^\pm}$ in the Two-Higgs-Doublet Model. Eur. Phys. J. C **77**(3), 201 (2017). arXiv:1702.04571

271. M. Misiak, A. Rehman, M. Steinhauser, Towards $\overline{B} \to X_s\gamma$ at the NNLO in QCD without interpolation in m$_c$. JHEP **06**, 175 (2020). arXiv:2002.01548

272. A. Arbey, F. Mahmoudi, G. Robbins, SuperIso Relic v4: a program for calculating dark matter and flavour physics observables in Supersymmetry. Comput. Phys. Commun. **239**, 238–264 (2019). arXiv:1806.11489

273. S. Inoue, M.J. Ramsey-Musolf, Y. Zhang, CP-violating phenomenology of flavor conserving two Higgs doublet models. Phys. Rev. D **89**(11), 115023 (2014). arXiv:1403.4257

274. J. Baron et al., Order of magnitude smaller limit on the electric dipole moment of the electron. Science **343**, 269–272 (2014). arXiv:1310.7534

275. J. Baglio, R. Gröber, M. Mühlleitner, D.T. Nhung, H. Rzehak, M. Spira, J. Streicher, K. Walz, NMSSMCALC: a program package for the calculation of loop-corrected Higgs boson masses and decay widths in the (Complex) NMSSM. Comput. Phys. Commun. **185**(12), 3372–3391 (2014). arXiv:1312.4788

276. S.F. King, M. Muhlleitner, R. Nevzorov, K. Walz, Exploring the CP-violating NMSSM: EDM constraints and phenomenology. Nucl. Phys. B **901**, 526–555 (2015). arXiv:1508.03255

277. M. Mühlleitner, D.T. Nhung, H. Rzehak, K. Walz, Two-loop contributions of the order $mathcalO$ ($\alpha_t\alpha_s$) to the masses of the Higgs bosons in the CP-violating NMSSM. JHEP **05**, 128 (2015). arXiv:1412.0918

278. T.N. Dao, R. Gröber, M. Krause, M. Mühlleitner, H. Rzehak, Two-loop $\mathcal{O}$ (α_t^2) corrections to the neutral Higgs boson masses in the CP-violating NMSSM. JHEP **08**, 114 (2019). arXiv:1903.11358

279. T.N. Dao, M. Gabelmann, M. Mühlleitner, H. Rzehak, Two-loop $\mathcal{O}((\alpha_t + \alpha_\lambda + \alpha_\kappa)^2)$ corrections to the Higgs boson masses in the CP-violating NMSSM. JHEP **09**, 193 (2021). arXiv:2106.06990

280. ATLAS Collaboration, SUSY Summary Plots June 2021. ATL-PHYS-PUB-2021-019 (2021)

281. CMS Collaboration, CMS Summary Plots 13 TeV. https://twiki.cern.ch/twiki/bin/view/CMSPublic/PhysicsResultsSUS#Run_2_Summary_plots_13_TeV

282. R.V. Harlander, S. Liebler, H. Mantler, SusHi: a program for the calculation of Higgs production in gluon fusion and bottom-quark annihilation in the Standard Model and the MSSM. Comput. Phys. Commun. **184**, 1605–1617 (2013). arXiv:1212.3249

283. S. Liebler, Neutral Higgs production at proton colliders in the CP-conserving NMSSM. Eur. Phys. J. C **75**(5), 210 (2015). arXiv:1502.07972

284. R.V. Harlander, S. Liebler, H. Mantler, SusHi Bento: beyond NNLO and the heavy-top limit. Comput. Phys. Commun. **212**, 239–257 (2017). arXiv:1605.03190

285. J.E. Camargo-Molina, A.P. Morais, R. Pasechnik, M.O.P. Sampaio, J. Wessén, All one-loop scalar vertices in the effective potential approach. JHEP **08**, 073 (2016). arXiv:1606.07069

286. T. Liu, K.-F. Lyu, J. Ren, H.X. Zhu, Probing the quartic Higgs boson self-interaction. Phys. Rev. D **98**(9), 093004 (2018). arXiv:1803.04359

287. Constraints on the Higgs boson self-coupling with combination of single and double Higgs boson production (2023)

288. F. Boudjema, E. Chopin, Double Higgs production at the linear colliders and the probing of the Higgs selfcoupling. Z. Phys. C **73**, 85–110 (1996). arXiv:hep-ph/9507396

289. F. Maltoni, D. Pagani, X. Zhao, Constraining the Higgs self-couplings at e^+e^- colliders. JHEP **07**, 087 (2018). arXiv:1802.07616

290. H. Bahl, J. Braathen, G. Weiglein, New constraints on extended Higgs sectors from the trilinear Higgs coupling. Phys. Rev. Lett. **129**(23), 231802 (2022). arXiv:2202.03453

291. V. Hirschi, O. Mattelaer, Automated event generation for loop-induced processes. JHEP **10**, 146 (2015). arXiv:1507.00020

292. P. Artoisenet, R. Frederix, O. Mattelaer, R. Rietkerk, Automatic spin-entangled decays of heavy resonances in Monte Carlo simulations. JHEP **03**, 015 (2013). arXiv:1212.3460

293. Y. Wang, Y. Sun, Z. Liu, S.E. Sarma, M.M. Bronstein, J.M. Solomon, Dynamic Graph CNN for Learning on Point Clouds (2018). arXiv:1801.07829

294. O. Atkinson, A. Bhardwaj, S. Brown, C. Englert, D.J. Miller, P. Stylianou, Improved constraints on effective top quark interactions using edge convolution networks. JHEP **04**, 137 (2022). arXiv:2111.01838

295. Anisha, O. Atkinson, A. Bhardwaj, C. Englert, P. Stylianou, Quartic gauge-Higgs couplings: constraints and future directions. JHEP **10**, 172 (2022). arXiv:2208.09334

296. W. Buchmuller, D. Wyler, Effective Lagrangian analysis of new interactions and flavor conservation. Nucl. Phys. B **268**, 621–653 (1986)

297. B. Grzadkowski, M. Iskrzynski, M. Misiak, J. Rosiek, Dimension-six terms in the Standard Model Lagrangian. JHEP **10**, 085 (2010). arXiv:1008.4884

298. J. Elias-Miro, J.R. Espinosa, E. Masso, A. Pomarol, Higgs windows to new physics through d=6 operators: constraints and one-loop anomalous dimensions. JHEP **11**, 066 (2013). arXiv:1308.1879

299. A. Papaefstathiou, G. Tetlalmatzi-Xolocotzi, Multi-Higgs Boson Production with Anomalous Interactions at Current and Future Proton Colliders (2023). arXiv:2312.13562

300. F. Goertz, A. Papaefstathiou, L.L. Yang, J. Zurita, Higgs boson pair production in the D=6 extension of the SM. JHEP **04**, 167 (2015). arXiv:1410.3471

301. A. Carvalho, M. Dall'Osso, T. Dorigo, F. Goertz, C.A. Gottardo, M. Tosi, Higgs pair production: choosing benchmarks with cluster analysis. JHEP **04**, 126 (2016). arXiv:1507.02245

302. M. Capozi, G. Heinrich, Exploring anomalous couplings in Higgs boson pair production through shape analysis. JHEP **03**, 091 (2020). arXiv:1908.08923

303. A. Carvalho, HH combinations and parameterscans (2022). https://indico.cern.ch/event/1001391/timetable/#32-hh-combination-and-paramete

304. V. Hirschi, Computing the interference of loop-induced diagrams with a tree-level background with MadEvent in MG5_aMC (2016). https://cp3.irmp.ucl.ac.be/projects/madgraph/wiki/LoopInducedTimesTree

305. A. Papaefstathiou, G. Tetlalmatzi-Xolocotzi, A. Tonero, Triple Higgs Boson Production in a Higgs Effective Theory (2023). https://gitlab.com/apapaefs/multihiggs_loop_sm

306. C. Degrande, G. Durieux, F. Maltoni, K. Mimasu, E. Vryonidou, C. Zhang, Automated one-loop computations in the standard model effective field theory. Phys. Rev. D **103**(9), 096024 (2021). arXiv:2008.11743

307. M. Bahr et al., Herwig++ physics and manual. Eur. Phys. J. C **58**, 639–707 (2008). arXiv:0803.0883

308. S. Gieseke et al., Herwig++ 2.5 Release Note (2011). arXiv:1102.1672

309. K. Arnold et al., Herwig++ 2.6 Release Note (2012). arXiv:1205.4902

310. J. Bellm et al., Herwig++ 2.7 Release Note (2013). arXiv:1310.6877

311. J. Bellm et al., Herwig 7.0/++ 3.0 release note. Eur. Phys. J. C **76**(4), 196 (2016). arXiv:1512.01178

312. J. Bellm et al., Herwig 7.1 Release Note (2017). arXiv:1705.06919

313. J. Bellm et al., Herwig 7.2 release note. Eur. Phys. J. C **80**(5), 452 (2020). arXiv:1912.06509

314. G. Bewick et al., Herwig 7.3 Release Note (2023). arXiv:2312.05175

315. A. Papaefstathiou, The HwSim analysis package for HERWIG 7. https://gitlab.com/apapaefs/hwsim

316. R. Contino, M. Ghezzi, C. Grojean, M. Mühlleitner, M. Spira, eHDECAY: an implementation of the Higgs effective Lagrangian into HDECAY. Comput. Phys. Commun. **185**, 3412–3423 (2014). arXiv:1403.3381

317. A.D. Linde, Decay of the false vacuum at finite temperature. Nucl. Phys. B **216**, 421 (1983). [Erratum: Nucl. Phys. B **223**, 544 (1983)]

318. M. Dine, R.G. Leigh, P.Y. Huet, A.D. Linde, D.A. Linde, Towards the theory of the electroweak phase transition. Phys. Rev. D **46**, 550–571 (1992). arXiv:hep-ph/9203203

319. S.R. Coleman, The fate of the false vacuum. 1. Semiclassical theory. Phys. Rev. D **15**, 2929–2936 (1977). [Erratum: Phys. Rev. D **16**, 1248 (1977)]

320. C.L. Wainwright, CosmoTransitions: computing cosmological phase transition temperatures and bubble profiles with multiple fields. Comput. Phys. Commun. **183**, 2006–2013 (2012). arXiv:1109.4189

321. M. Quiros, Finite temperature field theory and phase transitions, in *ICTP Summer School in High-Energy Physics and Cosmology*, pp. 187–259 (1999). arXiv:hep-ph/9901312

322. D. Curtin, P. Meade, H. Ramani, Thermal resummation and phase transitions. Eur. Phys. J. C **78**(9), 787 (2018). arXiv:1612.00466

323. J. Ellis, M. Lewicki, V. Vaskonen, Updated predictions for gravitational waves produced in a strongly supercooled phase transition. JCAP **11**, 020 (2020). arXiv:2007.15586

324. J. Ellis, M. Lewicki, M. Merchand, J.M. No, M. Zych, The scalar singlet extension of the Standard Model: gravitational waves versus baryogenesis. JHEP **01**, 093 (2023). arXiv:2210.16305

325. V. Brdar, A.J. Helmboldt, J. Kubo, Gravitational waves from first-order phase transitions: LIGO as a window to unexplored seesaw scales. JCAP **02**, 021 (2019). arXiv:1810.12306

326. J. Ellis, M. Lewicki, J.M. No, On the maximal strength of a first-order electroweak phase transition and its gravitational wave signal. JCAP **04**, 003 (2019). arXiv:1809.08242

327. M. Hindmarsh, S.J. Huber, K. Rummukainen, D.J. Weir, Numerical simulations of acoustically generated gravitational waves at a first order phase transition. Phys. Rev. D **92**(12), 123009 (2015). arXiv:1504.03291

328. M. Hindmarsh, S.J. Huber, K. Rummukainen, D.J. Weir, Shape of the acoustic gravitational wave power spectrum from a first order phase transition. Phys. Rev. D **96**(10), 103520 (2017). arXiv:1704.05871. [Erratum: Phys. Rev. D **101**, 089902 (2020)]

329. A. Kosowsky, M.S. Turner, R. Watkins, Gravitational waves from first order cosmological phase transitions. Phys. Rev. Lett. **69**, 2026–2029 (1992)

330. C. Caprini, R. Durrer, Gravitational wave production: a strong constraint on primordial magnetic fields. Phys. Rev. D **65**, 023517 (2001). arXiv:astro-ph/0106244

331. D.G. Figueroa, M. Hindmarsh, J. Urrestilla, Exact scale-invariant background of gravitational waves from cosmic defects. Phys. Rev. Lett. **110**(10), 101302 (2013). arXiv:1212.5458

332. M. Hindmarsh, Sound shell model for acoustic gravitational wave production at a first-order phase transition in the early Universe. Phys. Rev. Lett. **120**(7), 071301 (2018). arXiv:1608.04735

333. C. Caprini et al., Detecting gravitational waves from cosmological phase transitions with LISA: an update. JCAP **03**, 024 (2020). arXiv:1910.13125

334. C. Caprini, R. Jinno, M. Lewicki, E. Madge, M. Merchand, G. Nardini, M. Pieroni, A.R. Pol, V. Vaskonen, Gravitational waves from first-order phase transitions in LISA: reconstruction pipeline and physics interpretation (2024). arXiv:2403.03723

335. P. Auclair et al., Cosmology with the laser interferometer space antenna. Living Rev. Relativ. **26**(1), 5 (2023). arXiv:2204.05434

336. O. Karkout, A. Papaefstathiou, M. Postma, G. Tetlalmatzi-Xolocotzi, J. van de Vis, T. du Pree, Triple Higgs boson production and electroweak phase transition in the two-real-singlet model (2024). arXiv:2404.12425

337. A. Ahriche, S. Kanemura, M. Tanaka, Gravitational waves from phase transitions in scale invariant models. JHEP **01**, 201 (2024). arXiv:2308.12676

338. A. Addazi, A. Marcianò, A.P. Morais, R. Pasechnik, J. Viana, H. Yang, Gravitational echoes of lepton number symmetry breaking with light and ultralight Majorons. JCAP **09**, 026 (2023). arXiv:2304.02399

339. T. Biekötter, S. Heinemeyer, J.M. No, K. Radchenko, M.O.O. Romacho, G. Weiglein, First shot of the smoking gun: probing the electroweak phase transition in the 2HDM with novel searches for $A \to ZH$ in $\ell^+\ell^- t\bar{t}$ and $\nu\nu b\bar{b}$ final states. JHEP **01**, 107 (2024). arXiv:2309.17431

340. T. Biekötter, S. Heinemeyer, J.M. No, M.O. Olea-Romacho, G. Weiglein, The trap in the early Universe: impact on the interplay between gravitational waves and LHC physics in the 2HDM. JCAP **03**, 031 (2023). arXiv:2208.14466

341. T. Biekötter, S. Heinemeyer, J.M. No, M.O. Olea, G. Weiglein, Fate of electroweak symmetry in the early Universe: non-restoration and trapped vacua in the N2HDM. JCAP **06**, 018 (2021). arXiv:2103.12707

342. J.E. Camargo-Molina, R. Enberg, J. Löfgren, A new perspective on the electroweak phase transition in the Standard Model Effective Field Theory. JHEP **10**, 127 (2021). arXiv:2103.14022

343. A. Alves, D. Gonçalves, T. Ghosh, H.-K. Guo, K. Sinha, Di-Higgs blind spots in gravitational wave signals. Phys. Lett. B **818**, 136377 (2021). arXiv:2007.15654

344. A. Eichhorn, J. Lumma, J.M. Pawlowski, M. Reichert, M. Yamada, Universal gravitational-wave signatures from heavy new physics in the electroweak sector. JCAP **05**, 006 (2021). arXiv:2010.00017

345. A. Alves, D. Gonçalves, T. Ghosh, H.-K. Guo, K. Sinha, Di-Higgs production in the 4b channel and gravitational wave complementarity. JHEP **03**, 053 (2020). arXiv:1909.05268

346. A.P. Morais, R. Pasechnik, Probing multi-step electroweak phase transition with multi-peaked primordial gravitational waves spectra. JCAP **04**, 036 (2020). arXiv:1910.00717

347. F.P. Huang, Z. Qian, M. Zhang, Exploring dynamical CP violation induced baryogenesis by gravitational waves and colliders. Phys. Rev. D **98**(1), 015014 (2018). arXiv:1804.06813

348. M. Chala, M. Ramos, M. Spannowsky, Gravitational wave and collider probes of a triplet Higgs sector with a low cutoff. Eur. Phys. J. C **79**(2), 156 (2019). arXiv:1812.01901

349. A. Alves, T. Ghosh, H.-K. Guo, K. Sinha, Resonant di-Higgs production at gravitational wave benchmarks: a collider study using machine learning. JHEP **12**, 070 (2018). arXiv:1808.08974

350. P. Huang, A.J. Long, L.-T. Wang, Probing the electroweak phase transition with Higgs factories and gravitational waves. Phys. Rev. D **94**(7), 075008 (2016). arXiv:1608.06619

351. K. Hashino, M. Kakizaki, S. Kanemura, T. Matsui, Synergy between measurements of gravitational waves and the triple-Higgs coupling in probing the first-order electroweak phase transition. Phys. Rev. D **94**(1), 015005 (2016). arXiv:1604.02069

352. K. Hashino, M. Kakizaki, S. Kanemura, P. Ko, T. Matsui, Gravitational waves and Higgs boson couplings for exploring first order phase transition in the model with a singlet scalar field. Phys. Lett. B **766**, 49–54 (2017). arXiv:1609.00297

353. M. Kakizaki, S. Kanemura, T. Matsui, Gravitational waves as a probe of extended scalar sectors with the first order electroweak phase transition. Phys. Rev. D **92**(11), 115007 (2015). arXiv:1509.08394

354. P. Athron, C. Balázs, A. Fowlie, L. Morris, W. Lei, Cosmological phase transitions: from perturbative particle physics to gravitational waves. Prog. Part. Nucl. Phys. **135**, 104094 (2024). arXiv:2305.02357

355. A. Afzal et al., The NANOGrav 15 yr data set: search for signals from new physics. Astrophys. J. Lett. **951**(1), L11 (2023). arXiv:2306.16219

356. Measurement prospects of the pair production and self-coupling of the Higgs boson with the ATLAS experiment at the HL-LHC (2018)

357. P. Amaro-Seoane et al., Laser Interferometer Space Antenna (2017). arXiv:1702.00786

358. A.D. Sakharov, Violation of CP invariance, C asymmetry, and baryon asymmetry of the universe. Pisma Zh. Eksp. Teor. Fiz. **5**, 32–35 (1967)

359. J.R. Espinosa, M. Quiros, Novel effects in electroweak breaking from a hidden sector. Phys. Rev. D **76**, 076004 (2007). arXiv:hep-ph/0701145

360. F.F. Freitas, G. Lourenço, A.P. Morais, A. Nunes, J. Olívia, R. Pasechnik, R. Santos, J. Viana, Impact of SM parameters and of the vacua of the Higgs potential in gravitational waves detection. JCAP **03**(03), 046 (2022). arXiv:2108.12810

361. T. Vieu, A.P. Morais, R. Pasechnik, Electroweak phase transitions in multi-Higgs models: the case of trinification-inspired THDSM. JCAP **07**, 014 (2018). arXiv:1801.02670

362. X. Wang, F.P. Huang, X. Zhang, Gravitational wave and collider signals in complex two-Higgs doublet model with dynamical CP-violation at finite temperature. Phys. Rev. D **101**(1), 015015 (2020). arXiv:1909.02978

363. C. Bonilla, A.E. Carcamo Hernandez, J. Goncalves, K.N. Vishnudath, A.P. Morais, R. Pasechnik, Gravitational waves from a scotogenic two-loop neutrino mass model (2023). arXiv:2305.01964

364. A. Beniwal, M. Lewicki, J.D. Wells, M. White, A.G. Williams, Gravitational wave, collider and dark matter signals from a scalar singlet electroweak baryogenesis. JHEP **08**, 108 (2017). arXiv:1702.06124

365. A. Ashoorioon, T. Konstandin, Strong electroweak phase transitions without collider traces. JHEP **07**, 086 (2009). arXiv:0904.0353

366. D. Gonçalves, A. Kaladharan, W. Yongcheng, Electroweak phase transition in the 2HDM: collider and gravitational wave complementarity. Phys. Rev. D **105**(9), 095041 (2022). arXiv:2108.05356

367. Y. Chikashige, R.N. Mohapatra, R.D. Peccei, Are there real goldstone bosons associated with broken lepton number? Phys. Lett. B **98**, 265–268 (1981)

368. J. Schechter, J.W.F. Valle, Neutrino decay and spontaneous violation of lepton number. Phys. Rev. D **25**, 774 (1982)

369. M.C. Gonzalez-Garcia, J.W.F. Valle, Fast decaying neutrinos and observable flavor violation in a new class of majoron models. Phys. Lett. B **216**, 360–366 (1989)

370. A. Addazi, A. Marcianò, A.P. Morais, R. Pasechnik, R. Srivastava, J.W.F. Valle, Gravitational footprints of massive neutrinos and lepton number breaking. Phys. Lett. B **807**, 135577 (2020). arXiv:1909.09740

371. F.P. Huang, Y. Wan, D.-G. Wang, Y.-F. Cai, X. Zhang, Hearing the echoes of electroweak baryogenesis with gravitational wave detectors. Phys. Rev. D **94**(4), 041702 (2016). arXiv:1601.01640

372. C. Grojean, G. Servant, J.D. Wells, First-order electroweak phase transition in the standard model with a low cutoff. Phys. Rev. D **71**, 036001 (2005). arXiv:hep-ph/0407019

373. C. Delaunay, C. Grojean, J.D. Wells, Dynamics of non-renormalizable electroweak symmetry breaking. JHEP **04**, 029 (2008). arXiv:0711.2511

374. A. Tumasyan et al., Search for invisible decays of the Higgs boson produced via vector boson fusion in proton-proton collisions at s=13 TeV. Phys. Rev. D **105**(9), 092007 (2022). arXiv:2201.11585

375. G. Aad et al., Combination of searches for invisible decays of the Higgs boson using 139 fb−1 of proton-proton collision data at s=13 TeV collected with the ATLAS experiment. Phys. Lett. B **842**, 137963 (2023). arXiv:2301.10731

376. J. Crowder, N.J. Cornish, Beyond LISA: exploring future gravitational wave missions. Phys. Rev. D **72**, 083005 (2005). (**gr-qc/0506015**)

377. V. Corbin, N.J. Cornish, Detecting the cosmic gravitational wave background with the big bang observer. Class. Quantum Gravity **23**, 2435–2446 (2006). (**gr-qc/0512039**)

378. N. Seto, S. Kawamura, T. Nakamura, Possibility of direct measurement of the acceleration of the universe using 0.1-Hz band laser interferometer gravitational wave antenna in space. Phys. Rev. Lett. **87**, 221103 (2001). (**astro-ph/0108011**)

379. S. Isoyama, H. Nakano, T. Nakamura, Multiband gravitational-wave astronomy: observing binary inspirals with a decihertz detector, B-DECIGO. PTEP **2018**(7), 073E01 (2018). arXiv:1802.06977

380. P. Basler, M. Krause, M. Muhlleitner, J. Wittbrodt, A. Wlotzka, Strong first order electroweak phase transition in the CP-conserving 2HDM revisited. JHEP **02**, 121 (2017). arXiv:1612.04086

381. P. Basler, M. Mühlleitner, J. Wittbrodt, The CP-violating 2HDM in light of a strong first order electroweak phase transition and implications for Higgs pair production. JHEP **03**, 061 (2018). arXiv:1711.04097

382. K. Hashino, R. Jinno, M. Kakizaki, S. Kanemura, T. Takahashi, M. Takimoto, Selecting models of first-order phase transitions using the synergy between collider and gravitational-wave experiments. Phys. Rev. D **99**(7), 075011 (2019). arXiv:1809.04994

383. A. Addazi, A. Marciano, A.P. Morais, R. Pasechnik, H. Yang, CDF II W-mass anomaly faces first-order electroweak phase transition. Eur. Phys. J. C **83**(3), 207 (2023). arXiv:2204.10315

384. A. Papaefstathiou, T. Robens, G. White, Signal strength and W-boson mass measurements as a probe of the electro-weak phase transition at colliders—Snowmass White Paper, in *Snowmass 2021* (2022). arXiv:2205.14379

385. D. Gonçalves, T. Han, F. Kling, T. Plehn, M. Takeuchi, Higgs boson pair production at future hadron colliders: from kinematics to dynamics. Phys. Rev. D **97**(11), 113004 (2018). arXiv:1802.04319

386. V. Barger, P. Langacker, M. McCaskey, M. Ramsey-Musolf, G. Shaughnessy, Complex singlet extension of the Standard Model. Phys. Rev. D **79**, 015018 (2009). arXiv:0811.0393

387. A. Papaefstathiou, MadGraph5_aMC@NLO model for standard model + two extra scalar particles (2023). https://gitlab.com/apapaefs/twoscalar_generic/

388. J.F. Gunion, H.E. Haber, J. Wudka, Sum rules for Higgs bosons. Phys. Rev. D **43**, 904–912 (1991)

389. T. Robens, R. Zhang, in preparation